Left Atrial Appendage Segmentation and Analysis in Cardiovascular CT Images

Leventić, Hrvoje

HRVOJE LEVENTIĆ

LEFT ATRIAL APPENDAGE SEGMENTATION AND ANALYSIS IN CARDIOVASCULAR CT IMAGES

GHENT UNIVERSITY

JOSIP JURAJ STROSSMAYER UNIVERSITY OF OSIJEK

LEFT ATRIAL APPENDAGE SEGMENTATION AND ANALYSIS IN CARDIOVASCULAR CT IMAGES

Segmentacija i analiza lijevog srčanog aurikula iz kardiovaskularnih CT snimaka
Segmentatie en analyse van het linker hartoor in cardiovasculaire CT-afbeeldingen

HRVOJE LEVENTIĆ

Department of Software Engineering
Faculty of Electrical Engineering, Computer Science and Information Technology Osijek
Josip Juraj Strossmayer University of Osijek

Department of Telecommunications and Information Processing
Faculty of Engineering and Architecture
Ghent University

December 2018

Hrvoje Leventić
Left Atrial Appendage Segmentation and Analysis in Cardiovascular CT Images, Joint Doctoral Thesis,

DEGREES:
Doctor of Computer Science Engineering
Doctor of Electrical Engineering, branch Communications and Informatics

SUPERVISOR [UNIOS] :
Prof. Irena Galić, PhD

SUPERVISORS [UGENT] :
Prof. Aleksandra Pižurica, PhD
Dr. Danilo Babin

MEMBERS OF THE JURY:

prof. dr. sc. Robert Cupec (University of Osijek, chairman)
prof. dr. ir. Filip De Turck (Ghent University, co-chairman)
prof. dr. ir. Patrick Segers (Ghent University, secretary)
prof. dr. ir. Aleksandra Pižurica (Ghent University, supervisor)
dr. ir. Danilo Babin (Ghent University, supervisor)
prof. dr. sc. Irena Galić (University of Osijek, supervisor)
prof. dr. sc. Sven Lončarić (University of Zagreb)
prof. dr. md. Lazar Velicki (University of Novi Sad)

AFFILIATIONS:

Department of Software Engineering (ZPI)
FERIT, J. J. Strossmayer University of Osijek
Department of Telecommunications and Information Processing (TELIN),
FEA, Ghent University

For instance, on the planet Earth, man had always assumed that he was more intelligent than dolphins because he had achieved so much—the wheel, New York, wars and so on—whilst all the dolphins had ever done was muck about in the water having a good time. But conversely, the dolphins had always believed that they were far more intelligent than man—for precisely the same reasons.

— Douglas Adams, *Hitchhiker's Guide to the Galaxy*

It is known that there are an infinite number of worlds, simply because there is an infinite amount of space for them to be in. However, not every one of them is inhabited. Therefore, there must be a finite number of inhabited worlds. Any finite number divided by infinity is as near to nothing as makes no odds, so the average population of all the planets in the Universe can be said to be zero. From this it follows that the population of the whole Universe is also zero, and that any people you may meet from time to time are merely the products of a deranged imagination.

— *Douglas Adams,* Hitchhiker's Guide to the Galaxy

ACKNOWLEDGMENTS

This work would never have been carried out without the help and support of colleagues, friends and family. I would like to express my gratitude to the following people:

First and foremost, I would like to thank my advisers, Prof. dr. ir. Aleksandra Pižurica, Prof. dr. sc. Irena Galić, and especially dr. ir. Danilo Babin for the opportunity to conduct research in attractive research field of image processing. I would also like to thank them for numerous constructive discussions about my research topic and for allowing me a great freedom in following my interests.

I would like to thank prof. dr. md. Lazar Velicki and dr. md. Dan Devos for providing medical expertise. I would also like to thank prof. dr. ir. Wilfried Philips for his invitations to TELIN, which started this cooperation. On that same note, I am very grateful to Dean of my Faculty prof. dr. sc. Drago Žagar, for approving all my travels, conferences and the Joint doctorate agreement. Thank you to dr. ir. Jan Aelterman for his help.

Big thank you to my friend and cimer dr. sc. Krešimir Romić. I would also like to thank all my colleagues and ex- colleagues for creating a nice atmosphere that makes work pleasant.

Finally, I would like to thank my family and relatives for their love and support.

SUMMARY

Cardiovascular diseases are the main cause of death both in Europe and globally. Predominantly the elderly population suffers from cardiovascular diseases, especially in the developed countries, while at the same time the world population is getting older. Globally, number of people above 60 is estimated to more than double in thirty years from now. Thus, any improvements in the methods for diagnosis, treatment and prevention of cardiovascular diseases will significantly increase the quality of life and reduce the cost of treatment.

Atrial fibrillation is a cardiovascular disease which mostly affects the elderly population and it drastically increases the risk of stroke. The disease is caused when the disorganized electrical signals in the upper heart chambers overwhelm the normal electrical signals propagating through the electrical pathways in the heart. This chaotic electrical activity causes asynchronous contractions and the heart beats outside of the regular sinus rhythm. The asynchronous contractions impede the exchange of blood through the chambers, preventing the complete filling and emptying of the chambers. The blood pools in the chambers, enabling the formation of thrombi. When the thrombi become dislodged and enter the blood circulation (becoming thromboemboli), they can cause stroke. Estimates show that over 90% of strokes caused by cardiovascular diseases are caused by the thromboemboli formed in the left atrial appendage (LAA), small pouch-like structure protruding from the left atrium.

A novel percutaneous procedure called the left atrial appendage occlusion has recently been approved for the reduction of the risk of stroke in patients suffering from atrial fibrillation. During the procedure a device called the occluder is placed in the neck of the left atrial appendage, effectively closing it off from the rest of the heart and stopping the blood flow through the LAA. Several occluder device types are available on the market from different manufacturers. Each occluder device type comes in several predefined sizes. Physicians choose a device of the correct size according to each patient's anatomy. Physicians have to be able to determine the accurate anatomical measurement in order to be able to properly size the device.

Advancements in the development of medical imaging modalities, such as computed tomography (CT) or magnetic resonance imaging (MRI), have enabled the acquisition of detailed three-dimensional images of the patients cardiovascular anatomy. Physicians can determine detailed anatomical characteristics of patients' cardiovascular

anatomy from such three-dimensional images. The images can be used for pre-procedural planning of the procedures, reducing the time spent on administering the procedure and reducing the complication rate of the procedure. For example, even though percutaneous LAA occlusion can be administered without the prior CT scan, reports have noted a decrease in total time required for the administration as well as a decrease in the complications during the procedure if the pre-procedural CT has been administered. Additionally, the patients prefer the pre-procedural CT scan to the pre-procedural transesophageal echocardiography (TEE), despite the increased irradiation during the imaging. Currently, physicians perform the pre-procedural planning with CT in two main ways: either (1) they measure the patients anatomy directly in 2D slices, or (2) they analyse the 3D model of the LAA. Direct analysis of the 2D slices, even when using the multi-planar reconstruction (MPR), is subjective and error-prone. Certain characteristics of the LAA can be determined differently depending on the plane of the reconstruction, while determining them from the 3D visualization of the LAA is less error-prone and less subjective. Thus, accurate 3D segmentation methods of the LAA are very important for pre-procedural planning.

This thesis is focused on the segmentation and the analysis in the cardiovascular CT images in order to reduce the time physicians spend on the pre-procedural planning of the LAA occlusion procedure. The final goal of the thesis is to present the methods which will enable the physicians to – with minimal interaction – determine the feasibility of the procedure for the patient, segment the LAA and determine the location for the placement of the device. The main scientific contributions of this thesis are the three novel methods for the LAA segmentation and analysis, which could improve the pre-procedural planning of the occlusion. All presented methods require minimal interaction, as the physician only has to select two parameters in the input CT image: a single pixel (seed point) marking the location of the appendage in one of the slices and a single parameter (threshold) value. Both parameters are intuitive to trained medical users.

One of the most important scientific contributions of this work is the method for the centerline detection through the appendage. The detected centerline stretches from the seed point in the appendage to the center of the left atrium. The proposed method detects a centerline in the 3D image by tracking the voxels with the largest radius of the maximum inscribed spheres. The detected centerline is used as an input to the two subsequent methods: the LAA segmentation method and the LAA orifice localization method. However, the reason for the centerline detection is not only to use it as an input in the subsequent methods. The detected centerline allows us to determine the length of

the appendage, which is an important parameter for the sizing of the device and an exclusion criteria for a certain types of devices (the ratio of the width and the length of the appendage determines the exclusion criterion for the Watchman and LARIAT devices). Currently the length is determined by a direct measurement in the transesophageal echocardiography (TEE) imaging during the procedure, by a direct measurement in CT slices using the MPR, and finally by specialized software where the physician manually selects the points on the centerline. Our proposed method detects the centerline using only one seed point. Finally, the length of the appendage is calculated from the detected centerline.

The second key contribution of this work is the method for the segmentation of the left atrial appendage based on the detected centerline. Left atrial appendage segmentation methods are proving to be increasingly clinically important because they enable the use of different techniques for the pre-procedural planning. One of the most important appendage characteristics is the type of the morphology, which is an exclusion criterion for the procedure in certain types of morphologies. The morphology can be simply determined visually by the physician from the 3D model of the LAA. Determining the morphology type from the 2D slices is error-prone, since the appendage looks differently depending on the angle of the MPR reconstruction. Additionally, accurate segmentation allows for the simple determination of the volume of the appendage, which is another factor in determining the risk of stroke. Finally, proliferation of the 3D printing in the pre-procedural planning, combined with the availability of the accurate LAA segmentation methods, allows the physicians to 3D print the model of the heart and the appendage and correctly determine the correct size of the device prior to the procedure.

The proposed segmentation method gradually grows the region marked by the detected centerline and accurately extracts the region containing the LAA and most of the left atrium from an initial mask image created by thresholding the input image. The extraction of the appendage together with the left atrium (LA) area around the appendage allows better understanding of the appendage in the context of the surrounding atrial anatomy (e.g. position and direction of the appendage and proximity to blood vessels). The main advantage of the proposed method is the robustness to the selected threshold value and to the leaks occurring in the mask image. Currently, to the best of our knowledge, very few LAA segmentation methods are available on the market, while the standard region growing methods used in the interactive segmentation software are not robust to leaks after thresholding.

The third major scientific contribution of the thesis is the method for the localization of the LAA ostium which uses the detected centerline to determine the plane in 3D space delineating the left atrium from the appendage in the segmentation result from the previous method. The shape of the LAA ostium, determined in the segmented image by intersection with the delineation plane, is an important factor in choosing the type of the device used for the occlusion. Certain types of ostia also indicate a greater risk of peri-device leakage of the blood. Currently, the ostium shape is determined visually in the 2D slices using the double oblique view – MPR centered in the neck of the appendage. By using the proposed method, the physician does not have to modify the MPR planes manually, as the ostium plane is determined by the intersection of the segmented LAA and the determined delineation plane. The ostium shape directly indicates the sizing of the device to be used for the procedure.

All three proposed methods are validated against the ground truth segmentations manually created by two medical experts (a radiologist and a cardiosurgeon). The methods achieve large overlap coefficients against the ground truth segmentations. Finally, we have developed an application which enables the physician to visualize the LAA from the input image and easily calculate the required parameters for the procedure. Our work in this area resulted in two published papers in journals in the Science Citation Index and appeared in proceedings of four international conferences.

SAMENVATTING

Hart- en vaatziekten zijn de belangrijkste doodsoorzaak in de Europese Unie en zelfs wereldwijd. Hart- en vaatziekten treffen voornamelijk de oudere bevolking, vooral in ontwikkelde landen waar de vergrijzing meer en meer voelbaar wordt. Het aantal bejaarden (60 jaar en ouder) zal naar schatting rond het midden van de eeuw verdrievoudigd zijn. Daarom zal elke verbetering in diagnose, behandeling en preventie van hart- en vaatziekten de levenskwaliteit van ouderen aanzienlijk verbeteren en behandelingskosten verlagen.

Atriale fibrillatie is een cardiovasculaire aandoening die vooral de oudere bevolking treft en het risico op een beroerte drastisch verhoogt. De ziekte manifesteert zich wanneer de normale elektrische signalen die zich voortplanten door de elektrische paden in het hart worden overweldigd. Als gevolg van die chaotische elektrische signalen slaat het hart dan buiten het normale sinusritme. Asynchrone contracties belemmeren vervolgens de uitwisseling van bloed doorheen de hartkamers, waardoor het vullen en ledigen van de kamers wordt voorkomen. Het bloed verzamelt zich in de kamers, waardoor de vorming van trombi mogelijk wordt. De trombi kunnen losraken en in de bloedsomloop terechtkomen (waardoor trombo-embolie ontstaat). Dergelijke trombo-embolieën veroorzaken vaak een beroerte. Schattingen tonen aan dat meer dan 90beroertes veroorzaakt door hart- en vaatziekten wordt veroorzaakt door de trombo-embolie gevormd in het linker hartoor (LAA), een klein buidelachtig aanhangsel dat uitsteekt uit het linker atrium.

Recent is een nieuwe percutane procedure, genaamd occlusie van het linker atrium, goedgekeurd voor het verminderen van het risico op een beroerte bij patiënten die lijden aan atriale fibrillatie. Tijdens de procedure wordt een apparaat, de occluder, geplaatst in de nek van het linker hartoor, waardoor die effectief wordt afgesloten van de rest van het hart en de bloedstroom door de LAA wordt gestopt. Verschillende occluder-apparaten, van verschillende fabrikanten, zijn momenteel op de markt. Elk occluderapparaat wordt geleverd in verschillende grootten. Artsen kiezen een occluder van de geschikte grootte volgens de anatomie van de patiënt. Artsen moeten in staat zijn om via een correcte anatomische meting te bepalen welke occluder het best geschikt is.

Vooruitgang in medische beeldvorming, zoals computertomografie (CT) of magnetische resonantiebeeldvorming (MRI), hebben het mogelijk gemaakt gedetailleerde driedimensionale beelden te maken

van de cardiovasculaire anatomie van een patiënt. Die beelden kunnen worden gebruikt voor planning van procedures, waardoor het tijdsbestek van de procedure wordt verkort en de complicatieratio van de procedure wordt verlaagd. Hoewel de percutane LAA-occlusie kan worden toegediend zonder de voorafgaande CT-scan, is in de literatuur een verlaging van de proceduretijd en aantal complicaties gerapporteerd wanneer wel een pre-procedurale CT-scan is gebeurd. Patiënten geven bovendien vaak de voorkeur aan een pre-procedurale CT-scan, ondanks de bestraling die daarmee gepaard gaat. Momenteel voeren artsen de pre-procedurele planning met CT uit op twee manieren: ofwel (1) meten ze de anatomie van de patiënt in 2D-slices, ofwel (2) analyseren ze een 3D-model van de LAA. Directe analyse van de 2D-slices, zelfs bij gebruik van de multi-planaire reconstructie (MPR), is echter subjectief en foutgevoelig: afhankelijk van het gekozen reconstructievlak kunnen LAA kenmerken er anders uitzien, terwijl het bepalen op basis van de 3D LAA-visualisatie minder foutgevoelig en minder subjectief is. Daarom zijn nauwkeurige 3D-segmentatiemethoden van de LAA erg belangrijk voor pre-procedurele planning.

Dit proefschrift richt zich op de automatische segmentatie en analyse van cardiovasculaire CT-beelden om de tijd te verminderen die artsen besteden aan pre-procedurele planning van de LAA-occlusieprocedure. Het uiteindelijke doel van dit proefschrift is om methoden te presenteren die de artsen in staat stellen om - met minimale interactie - de haalbaarheid van de procedure voor een patiënt te bepalen, de LAA te segmenteren en de locatie voor de plaatsing van het hulpmiddel te bepalen. De wetenschappelijke bijdragen van dit proefschrift zijn drie nieuwe methoden voor de LAA-segmentatie en analyse, die de pre-procedurele planning van de occlusie kunnen verbeteren. Alle voorgestelde methoden vereisen minimale interactie van de gebruiker: enkel het plaatsen van een seedpunt in het aanhangsel en het kiezen van een drempelwaarde.

Onze eerste wetenschappelijke bijdrage is een methode voor middellijndetectie van de LAA. De gedetecteerde middellijn strekt zich uit van het startpunt in het aanhangsel tot het midden van het linkeratrium. De voorgestelde methode detecteert een middellijn in het 3D-beeld door die voxels te volgen met de grootste straal van de maximaal ingeschreven bollen. De gedetecteerde middellijn wordt gebruikt als invoer voor de twee volgende methoden: de LAA-segmenteringsmethode en de LAA-meetlocatiemethode. De motivatie voor het ontwikkelen van middenlijndetectie is niet alleen om deze te gebruiken als invoer voor andere methoden. De gedetecteerde middellijn stelt ons bovendien ook in staat om de lengte van het aanhangsel te bepalen. Die lengte is een belangrijke parameter bij de dimensionering van de occluder

en een uitsluitingscriterium voor bepaalde soorten apparaten (de verhouding tussen de breedte en de lengte van het aanhangsel bepaalt de uitsluitingscriteria voor de Watchman- en LARIAT-apparaten). Momenteel wordt de lengte bepaald ofwel door directe metingen m.b.v. transesofageale echocardiografie (TEE) beeldvorming tijdens de procedure ofwel door directe meting in CT-slices met behulp van de MPR ofwel met gespecialiseerde software waarbij de arts handmatig punten op de middellijn aanduidt. Onze voorgestelde methode detecteert de middellijn automatisch vanaf één gegeven startpunt. De lengte van het aanhangsel wordt dan berekend op basis van de automatisch gedetecteerde middellijn.

Onze tweede wetenschappelijke bijdrage is een methode voor segmentatie van het linker hartoor op basis van een gegeven middellijn. Deze segmentatiemethode is waarschijnlijk de belangrijkste bijdrage van dit proefschrift omdat ze alternatieve technieken voor de pre-procedurele planning mogelijk maakt. Een van de belangrijkste LAA-kenmerken is de morfologie, een uitsluitingscriterium is voor de procedure. De morfologie kan eenvoudig visueel worden bepaald door de arts uit het 3D-model van de LAA. Het bepalen van het morfologietype uit de 2D-slices is foutgevoelig, omdat het voorkomen van het aanhangsel afhankelijk is van de hoek van de MPR-reconstructie. Nauwkeurige automatische segmentatie vereenvoudigt de volumemeting van het LAA, wat een andere kenmerk is voor het bepalen van het risico op een beroerte. Ten slotte stelt de opkomst van 3D-printen in de pre-procedurele planning, gecombineerd met nauwkeurige LAA-segmentatiemethoden, artsen in staat om een model van het hart en het aanhangsel in 3D te printen. Hierop kan de juiste maat van de occluder voorafgaand aan de procedure worden vastgesteld.

De voorgestelde segmentatiemethode laat iteratief het gebied groeien dat wordt gemarkeerd door de gedetecteerde middellijn. Zo onderscheidt de methode het gebied met de LAA en het grootste deel van het linkeratrium van andere gebieden uit de maskerafbeelding die is bekomen door het ingevoerde beeld te segmenteren met een eenvoudige drempelwaarde. Het belangrijkste voordeel van de voorgestelde methode is robuustheid tegenover geselecteerde drempelwaarden en lekken die typisch optreden in het maskerbeeld. Op dit moment bestaan, voor zover wij weten, weinig specifieke LAA-segmentatiemethoden. Standaard interactieve segmentatiesoftware, gebaseerd op regio-groeimethoden is dan weer niet robuust tegen lekken na drempelsegmentatie.

Onze derde wetenschappelijke bijdrage is een methode voor de lokalisatie van het LAA-ostium. Deze methode gebruikt de gedetecteerde middellijn om het afbakeningsvlak te bepalen dat het linkeratrium van het LAA scheidt in 3D-ruimte. De vorm van het LAA-ostium, i.e.

de doorsnede van het gesegmenteerde LAA met afbakeningsvlak, is een belangrijke factor bij het kiezen van het type occluder: Bepaalde typen ostia duiden op een groter risico op peri-device leakage (PDL). Momenteel wordt de ostiumvorm visueel bepaald in de 2D-slices, met behulp van de "double oblique" weergave - MPR gecentreerd in de nek van het aanhangsel. Dankzij de voorgestelde methode hoeft de arts de MPR-vlakken niet meer handmatig aan te duiden. De ostiumvorm geeft een directe indicatie van de vereiste grootte van het occluderapparaat dat voor de procedure moet worden gebruikt.

De drie voorgestelde methoden zijn gevalideerd op basis een grondwaarheid die handmatig werd gecreëerd door twee medische experts (een radioloog en een hartchirurg). De methoden vertonen grote overlapcoëfficiënten met de grondwaarheid. Ten slotte hebben we een applicatie ontwikkeld waarmee de arts de LAA kan visualiseren vanuit een invoerbeeld en waarmee die ook eenvoudig de vereiste parameters voor een procedure kan berekenen. Ons werk resulteerde in twee gepubliceerde tijdschriftartikelen opgenomen in de Science Citation Index en vier artikelen als bijdrage aan internationale conferenties.

SAŽETAK

Kardiovaskularne bolesti su glavni uzročnik smrti u Europskoj uniji te jedan od glavnih uzročnika smrti globalno. Nadalje, kardiovaskularne bolesti primarno pogađaju stariju populaciju, pogotovo u zemljama razvijenog svijeta. Brojne projekcije pokazuju kako će se populacija svijeta starija od 60 godina (osobe treće životne dobi) do sredine stoljeća udvostručiti. Samim time povećat će se i negativan utjecaj kardiovaskularnih bolesti na globalno stanovništvo. Kvalitetne metode dijagnosticiranja, liječenja i prevencije kardiovaskularnih bolesti mogu značajno povećati kvalitetu života osoba treće životne dobi i smanjiti troškove liječenja.

Fibrilacija atrija je kardiovaskularna bolest koja drastično povećava rizik od moždanog udara, a posebno pogađa upravo stariju populaciju te se smatra kako je odgovorna za oko petinu moždanih udara. Fibrilacija atrija je kardiovaskularna bolest koja nastaje zbog poremećaja u električnim putevima u srcu, kada zbog kaotičnih električnih signala srce kuca van regularnog sinusnog ritma. Zbog asinkronih kontrakcija koje se odvijaju van regularnog srčanog ritma, dolazi do nepotpune izmjene krvi pri prolasku kroz srce. Zbog zadržavanja krvi u pretklijetkama može nastati tromb. Ukoliko se takav tromb otkine dolazi do tromboembolizma te ulaskom takvog tromboembolija u krvotok može nastati moždani udar. Procjenjuje se kako preko 90% tromboembolija koji izazovu moždani udar nastaje u aurikulu lijeve srčane pretklijetke (engl. *left atrial appendage (LAA)*), maloj *vrećastoj* strukturi koja izlazi iz lijeve pretklijetke.

Radi smanjenja rizika od moždanog udara kod pacijenata koji pate od fibrilacije atrija uvedena je nova neinvazivna procedura – perkutana okluzija lijevog srčanog aurikula. Ovom procedurom postavlja se uređaj u aurikul lijeve srčane pretklijetke koji će zatvoriti aurikul i tako zaustaviti protok krvi kroz njega. Postoji nekoliko proizvođača okludera, uređaja kojima se provodi zatvaranje (*okluzija*) LAA, a svaki proizvođač nudi svoj tip uređaja u više varijanti različitih dimenzija. Svakom pacijentu tijekom provođenja procedure odabire se uređaj čije dimenzije odgovaraju anatomiji tog pacijenta. Za odabir točne dimenzije okludera potrebno je poznavati anatomiju lijevog atrija te detaljne anatomske karakteristike aurikula.

Napretkom u razvoju medicinskih modaliteta snimanja, kao što je kompjuterizirana tomografija (CT) ili magnetska rezonanca (MRI), moguće je dobiti detaljne trodimenzionalne snimke kardiovaskularne anatomije pacijenta. Detaljne anatomske karakteristike aurikula pojedi-

nog pacijenta mogu se odrediti iz takvih trodimenzionalnih snimaka. Pred-operativno planiranje provedbe okluzije pomoću CT snimki pacijenta može značajno ubrzati provedbu same procedure, kao i omogućiti rano prepoznavanje pacijenata kod kojih provedba okluzije nije moguća. Trenutno se preoperativno planiranje pomoću CT snimaka provodi na dva osnovna način: mjerenjem anatomskih dimenzija direktno u 2D presjecima u CT snimci te analizom 3D modela LAA. Direktna analiza LAA korištenjem 2D presjeka, čak i ako se koristi više-ravninska rekonstrukcija (engl. *MPR*) je subjektivna i podložna pogrešci. Određene značajke aurikula je puno lakše odrediti iz 3D modela te je postojanje metoda koje mogu odrediti preciznu segmentaciju aurikula vrlo bitno za planiranje provedbe okluzije.

Ova disertacija se fokusira na segmentaciju i analizu kardiovaskularnih CT snimaka kako bi omogućili liječnicima lakše planiranje provedbe okluzije LAA. Konačni cilj metoda predstavljenih u ovoj disertaciji je, uz minimalnu interakciju liječnika, segmentirati LAA i predložiti lokaciju za postavljanje okludera. Predstavljena su tri izvorna znanstvena doprinosa – nove metode računalne obrade CT snimki – čija primjena može olakšati i ubrzati proces planiranja provedbe okluzije. Sve predstavljene metode zahtijevaju samo dva ulazna podatka od liječnika: postavljanje u ulaznu CT snimku jedne početne točke (engl. *seed point*) unutar aurikula te odabir vrijednosti jednog parametra (intenzitet praga) za tu snimku. Oba parametra su intuitivna obučenim medicinskim korisnicima.

Prvi znanstveni doprinos je metoda za određivanje centralne linije kroz aurikul, od početne odabrane točke do centra lijeve pretklijetke. Predložena metoda traži put u 3D slici od početne točke prateći voksele duž središta LAA dok ne dođe do centra lijeve pretklijetke. Određena centralna linija se koristi kao ulaz u naredne korake – metodu za segmentaciju te metodu za određivanje lokacije ostiuma LAA. Ipak, bitno je napomenuti kako je centralna određena centralna linija sama po sebi bitan rezultat za određivanje mogućnosti provođenja okluzije. Na primjer, duljina centralne linije predstavlja duljinu LAA, a duljina LAA u odnosu na širinu je indikacija za korištenje Watchman i LARIAT okluder uređaja. Trenutno se duljina LAA određuje mjerenjem u prikazu transesofagealne ehokardiografije (engl. *TEE*) tijekom provođenja same procedure, direktnim mjerenjem u 2D presjecima CT snimke nakon određivanja pogodnog kuta za MPR, te konačno specijaliziranim softverom koji omogućuje ručno određivanje centralne linije postavljanjem više točaka u 2D presjeke. Naša predložena metoda omogućuje detekciju centralne linije iz samo jedne početne točke. Iz određene centralne linije možemo jednostavno izračunati i prikazati liječniku duljinu LAA, što će pomoći liječniku planiranje provođenja procedure okluzije.

Drugi znanstveni doprinos ove disertacije je metoda za segmentaciju aurikula lijeve srčane pretklijetke bazirana na detektiranoj centralnoj liniji. Segmentacija LAA je vjerojatno najbitniji rezultat predloženih metoda, omgućujući različite primjene u planiranju provedbe procedure okluzije. Među najbitnijim značajkama aurikula koje je moguće direktno odrediti vizualizacijom segmentacije je tip morfologije aurikula, koji utječe na mogućnost provedbe procedure. Postoji četiri različita tipa morfologije, a svaki od njih indicira različit rizik od pojave moždanog udara. U različitim kutevima MPR rekonstrukcije LAA izgleda kao da ima drugačiji tip morfologije, dok je iz 3D modela puno lakše točno odrediti tip morfologije. Nadalje, iz precizne segmentacije moguće je odrediti i volumen aurikula u odnosu na volumen lijevog atrija, veličinu koja također ukazuje na rizik od moždanog udara. Posljednjih godina, popularizacijom 3D printanja za predoperativno planiranje, precizne metode segmentacije su posebno dobile na važnosti. Iz precizne segmentacije LAA moguće je isprintati 3D model u stvarnoj veličini, na kojem se može uživo isprobati odabrana veličina okludera s obzirom na anatomiju pacijenta.

Predložena metoda za segmentaciju vrši segmentaciju iterativnim rastom regije određene detektiranom centralnom linijom. Metoda iz binarne maske (određene pomoću vrijednosti praga koju je postavio korisnik) izdvaja regiju koja sadrži LAA i većinu lijeve pretklijetke. Izdvajanjem i područja pretklijetke u okolici aurikula liječniku omogućujemo bolje razumijevanje anatomije aurikula u kontekstu lokalne anatomije pretklijetke (npr. poziciju i smjer aurikula u zidu atrija, blizinu plućnih vena i slično). Glavna odlika metode je robusnost na odabranu vrijednost praga i na curenje (engl. *leaks*) koje se pojavljuje u maskiranoj slici. Trenutno na tržištu postoji vrlo malen broj metoda za segmentaciju LAA, dok standardne metode rasta regije koje se koriste za interaktivnu segmentaciju često nisu robusne na curenje.

Treći znanstveni doprinos ovog rada predstavlja metoda za lokalizaciju ostiuma LAA koja korištenjem određene centralne linije i segmentiranog aurikula određuje ravninu presjeka koja odvaja aurikul od pretklijetke. Oblik presjeka LAA u području ostiuma, koji se dobije presjekom segmentiranog aurikula i određene ravnine presjeka, definira oblik ostiuma LAA. Oblik ostiuma također indicira koji je tip uređaja moguće koristiti za provođenje okluzije. Trenutno se oblik ostiuma određuje vizualno iz odgovarajućeg 2D presjeka nakon prilagodbe prikaza presjeka korištenjem MPR (*double oblique* prikaz centriran u ostium LAA). Korištenjem predložene metode liječnik ne mora ručno prilagođavati MPR rekonstrukciju, već se ona određuje automatski iz presjeka segmentiranog LAA i određene ravnine presjeka. Oblik ostiuma također određuje maksimalni i minimalni promjer ostiuma, koji

direktno utječu na veličinu uređaja za okluziju koji će se koristiti za provedbu okluzije.

Sve tri predstavljene metode validirane su na *ground-truth* segmentacijama koje su ručno kreirala dva medicinska stručnjaka (radiolog i kardiokirurg) te postižu visoke koeficijente poklapanja s ručnim segmentacijama. Konačno, razvili smo i aplikaciju koja korištenjem navedenih metoda omogućuje liječniku lakše planiranje provođenja okluzije. Rezultati dobiveni tijekom istraživačkog rada u području obrade kardiovaskularnih snimaka, osim što su rezultirali ovom disertacijom, objavljeni su i u dva rada u časopisima indeksiranim u Science Citation Index te četiri rada na međunarodnim znanstvenim konferencijama.

CONTENTS

LIST OF FIGURES

LIST OF TABLES

ALGORITHMS

ACRONYMS

AAM Active Appearance Model

ACM Active Contour Model

ACPS adaptive control point status

ADF adaptive diffusion flow

AF atrial fibrillation

ANN artificial neural network

ASM Active Shape Model

AV atrioventricular

CART classification and regression trees

CCTA coronary CT angiography

CLT common left trunk

CNN convolutional neural network

CTA computed tomography angiography

CT computed tomography

CVD cardiovascular disease

CVS Cardiovascular system

DOF degree of freedom

FCM Fuzzy C-means clustering

FDA Food and Drug Administration

FFD free-form deformation

GCV great cardiac vein

GVF gradient vector flow

LAAO left atrial appendage occlusion

LAA left atrial appendage

LACM localizing region-based active contour

LARM locally affine registration method

LASC Left Atrium Segmentation Challenge

LA left atrium

LCX left circumflex artery

LIPV left inferior pulmonary vein

LOM ligament of Marshall

LSPV left superior pulmonary vein

LVEF left ventricular ejection fraction

LV left ventricle

MACE major adverse cardiac event

MAS multi-atlas segmentation

MI mutual information

MPR multi-planar reconstrution

MRI magnetic resonance imaging

MSL Marginal Space Learning

NMI normalized mutual information

NN neural network

PA pulmonary artery

PCA principal component analysis

PDE partial differential equation

PV pulmonary vein

RA right atrium

RIPV right inferior pulmonary vein

RMPV right middle pulmonary vein

ROI region of interest

RSPV right superior pulmonary vein

RV right ventricle

SAC Shape-constrained Active Contour

SPF signed pressure force

SSM statistical shape models

SVM support vector machines

TEE transesophageal echocardiography

UI user interface

WHO World Health Organization

WHS whole heart segmentation

1 INTRODUCTION

Cardiovascular diseases (CVD) have been identified as the leading cause of death in the developed world [130, 183]. Diagnosis and treatment of cardiovascular diseases (CVDs) has significantly improved in recent years due to the advances in cardiovascular imaging technologies. However, fast and accurate extraction of clinically relevant data from cardiovascular images still presents a challenge. Clinically relevant data is necessary for both the diagnosis of CVDs and for the planning of medical procedures. The field where researchers develop methods and algorithms for extraction of such data from medical images is called medical image analysis. This thesis is focused on cardiovascular image analysis for the purpose of stroke prevention.

The methods presented in this thesis are aimed to aid physicians in planning and execution of a procedure that reduces the risk of stroke – the left atrial appendage (LAA) occlusion. We present three novel methods that facilitate the pre-procedural planning of the occlusion procedure: the method for the detection of the LAA centerline, the method for the centerline-based LAA segmentation and the method for the localization of the LAA orifice. The research work reported in this thesis appeared in two journals in the Science Citation Index and four proceedings of international conferences.

1.1 CARDIOVASCULAR IMAGE ANALYSIS

Cardiovascular image analysis is the process of extracting the meaningful and relevant data to support the CVD diagnosis and therapy. Recent advances in computational power have enabled new types of methods for interpretation of medical images. Until recently, most physicians performed the diagnosis by visual inspection of 2D images. This involved interpreting the images on a slice-by-slice basis, even when the imaging was performed in three dimensions. Necessary measurements were often taken manually on 2D slices. The precision, quality and the amount of data in medical images have increased along with the increase in available computational power. Today, physicians routinely perform advanced medical imaging procedures which often result in multidimensional medical images — 4D images (consist of 3D images acquired in different time frames during an examination, e.g. during different phases of a cardiac cycle) and increasingly 5D images (the term used for images consisting of 4D images acquired during

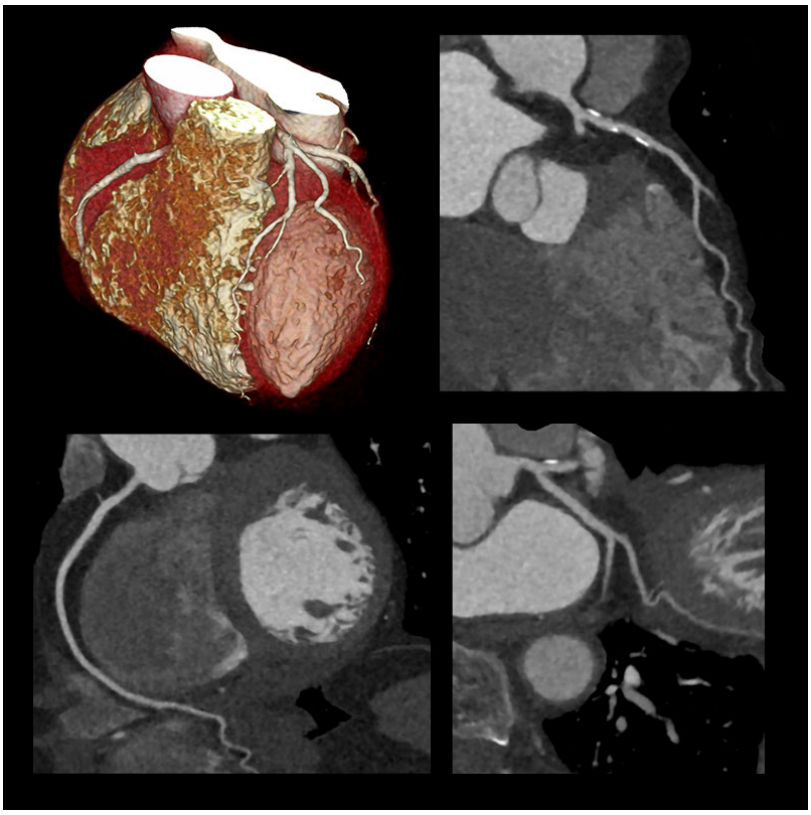

Figure 1.1: Four panel view of cardiac CT imaging. Panels show: 3D rendering of the heart (top left), axial (bottom left), sagital (top right) and coronal (bottom right) views. Image source: LaBarbera and Donnino [93]

several examinations). Visual inspection and interpretation of such multidimensional images is a time-consuming process. Fortunately, developments in the medical image analysis field have followed the advances in both the imaging and the computational power. A large number of advanced medical image analysis and visualization methods are available today. Using these methods physicians can quickly and accurately interpret the images, set the diagnosis and plan the necessary treatments. Figure 1.1 shows an example of a four-panel view of a cardiac CT image.

There are an increasing number of methods which extract clinically relevant information from the images and present it to physicians in an intuitive way. The most often used imaging modalities for the CVD diagnosis are ultrasound, cardiovascular CT imaging and MRI. Each modality has its advantages and disadvantages which will be explained in detail in the later chapters. The methods presented in this thesis will focus on the CT images, which are at the present the most frequently used imaging modality for high resolution cardiovascular anatomic imaging [62, 115].

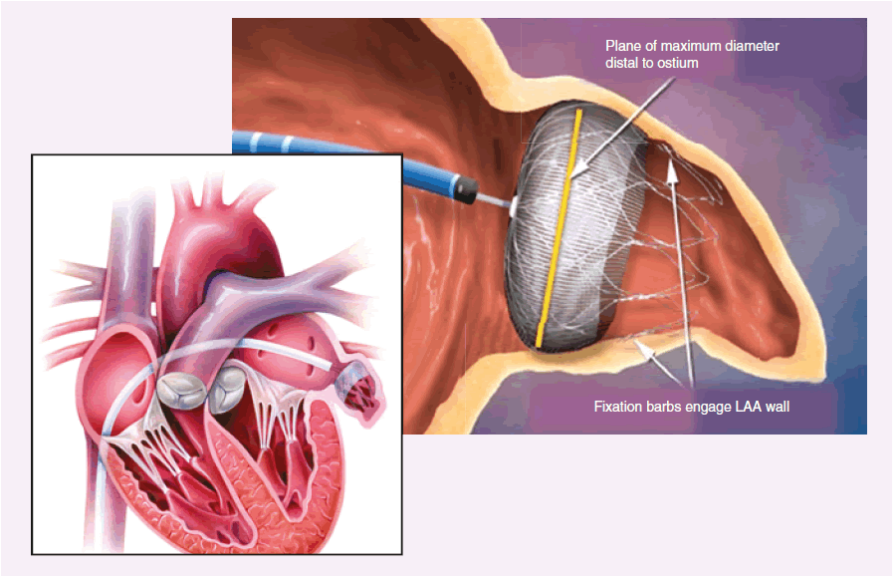

Figure 1.2: The location of the LAA in the heart and the placement of the Watchman occluder in the neck of the LAA. Image source: Whisenant and Lindley [180]

1.2 STROKE PREVENTION

The main goal of this thesis is to propose a collection of image processing methods for helping physicians plan the procedure aimed at reducing the risk of stroke. Stroke is the third leading cause of death worldwide [183], accounting for about a third of all deaths caused by cardiovascular diseases. One of the cardiovascular diseases which is a main risk factor for stroke is the atrial fibrillation [57, 181]. Atrial fibrillation manifests as the asynchronous chaotic contractions of the atria. Due to the disorganized electrical signals in the heart, the atrium fibrillates – contracts outside the standard regular sinus rhythm of the heart. Incomplete and improperly timed contractions of the atria cause the blood to pool in the atria, enabling the formation of a blood clot. If such a clot becomes dislodged it can enter the bloodstream and cause a stroke. It is estimated that around 20% of all strokes are caused by atrial fibrillation [24]. Additionally, the majority of strokes caused by non-rheumatic atrial fibrillation is thought to originate in the left atrial appendage (LAA). Left atrial appendage is a small pouch-like structure protruding from the wall of the left atrium, located between the mitral anulus and the root of the left pulmonary veins [25].

The blood flow through the LAA can be closed off with a novel percutaneous procedure called the left atrial appendage occlusion (LAAO). During the procedure, the physician deploys a device inside the neck of LAA which closes the blood flow through the appendage, preventing the blood clot from exiting the appendage and entering the

circulatory system. Figure 1.2 on the left shows the catheter entering the right heart through the femoral vein, passing from the right heart to the left through the interatrial septum and deploying the occluder device inside the LAA. The right side of the figure shows the device firmly placed in the neck of the appendage.

Multiple occluder devices are available on the market, each with their own set of requirements about the LAA anatomy. In order to be able to choose the device of the correct type and size for the patient's anatomy, the physicians need to be able to perform accurate measurements of the heart and the appendage. Currently, most physiscians perform the occlusion without the pre-procedural CT imaging, sizing the device with measurements obtained from standard fluoroscopy and TEE modalities. However, there is a growing trend of using pre-procedural CT imaging to plan the procedure and to guide the sizing of the device. The benefits of the pre-procedural CT scanning, compared to standard pre-procedural TEE evaluation, include better prediction of the appropriate device size [158, 176], and better determination of patient's suitaility for the procedure [176]. Still, even physicians that do use pre-procedural CT evaluation rarely use specialized software to plan the occlusion. They often perform measurements directly in 2D slices of different MPR views. Very few software packages focused on the pre-procedural planning of the left atrial appendage occlusion are available on the market, due to the relative novelty of the procedure (it has only been FDA approved in 2015). The goal of this thesis is the development of a pre-procedural planning software capable of automating certain parts of the planning workflow (using the methods proposed in later chapters) and in turn reducing the time required for the pre-procedural planning.

1.2.1 *Clinical goals*

This thesis presents new signal and image processing approaches to support the planning of the LAA occlusion. From the point of view of the clinical application, the following requirements have to be met: the user interaction should be minimal; accurate segmentation has to be guaranteed, along with the proper visualization; and the results should be presented in such a way that the physician can easily calculate the parameters of the LAA needed for the planning of the occlusion procedure. Some of the most important parameters to the physician are:

1. type of the appendage morphology,
2. maximal and minimal diameters of the ostium,
3. length of the appendage,

4. volume of the appendage.

The performance of the methods should be fast enough to represent an improvement over the manual analysis of the images.

1.3 NOVELTIES AND CONTRIBUTIONS

In this thesis we develop three novel methods for medical image processing to support the planning of the occlusion procedure. The proposed methods are:

1. The method for the detection of the centerline through the appendage. This method is semi-automatic. It requires only one seed point and a threshold value. The centerline is important for the determination of the length of the appendage.

2. An accurate method for the left atrial appendage segmentation based on the detected centerline. Thorough validation against the ground truth segmentations by two medical experts showed an excellent performance of this method. The segmentation step is crucial for determining the appendage morphology, as well as for the volume calculation.

3. The method for the localization of the LAA orifice. This method localizes the orifice of the appendage and proposes the location for the occluder placement. The locations proposed by the method are very close to the locations determined by a medical expert.

1.4 ORGANIZATION OF THE THESIS

This section present an overview of the content of the various chapters of the thesis.

CHAPTER 2: MEDICAL BACKGROUND. In this chapter we introduce the medical background concerning the left atrial appendage and the left atrial appendage occlusion. We cover the most common cardiovascular diseases and their causes and effects on the patients' health. Special focus is given to stroke prevention techniques, especially the left atrial appendage occlusion procedure. We give an overview of the cardiovascular anatomy with special focus on the left atrium and the left atrial appendage. Several occluder devices are currently available on the market. The devices are available in a range of predetermined sizes (diameters). For every patient, the physician chooses a device of the correct size according to patient's anatomy. Several medical imaging modalities are routinely used before, during and after the

occlusion procedure. We explain their advantages and disadvantages in the context of the occlusion procedure. The methods for planning the occlusion procedure presented in this thesis use the coronary CT angiography (CCTA) images for both the evaluation of the patient's suitability for the procedure, as well as the pre-procedural device sizing. The CCTA pre-procedural planning demonstrated certain advantages which are described in the chapter.

CHAPTER 3: CURRENT SEGMENTATION APPROACHES. This chapter covers the current state-of-the-art approaches for cardiovascular segmentation from medical images. The covered methods are aimed at extracting necessary anatomical information about the heart to aid physicians in diagnosis and treatment of cardiovascular diseases. In terms of underlying methods the available state-of-the-art approaches can be divided into four categories: partial differential equation-based methods, graph-cuts methods, clustering and classification methods and model-based methods. The methods with the highest performance often combine more than one approach. Historically, most of the methods were heuristical in nature. Nowdays, most of the methods are based on some kind of machine learning, due to the rise in the available computing power since the beginning of the decade. However, cardiovascular segmentation is not inherently suited for machine learning algorithms as the sizes of individual images are very large (3D and often even 4D images). Consequently, sample sizes of most datasets are very small (datasets with more than 100 individual images are rarely reported in the literature). Thus, most of the machine learning-based approaches are specially designed to handle that limitation. Approaches most commonly used in the image processing in the last few years, such as deep neural networks, are rarely used for this purpose, even though several approaches have been presented in the last few years. Nevertheless, specialized machine learning algorithms, such as the marginal space learning algorithm, are still among the top performers in the field.

The approaches for the segmentation and analysis of the left atrial appendage are a lot less researched. To the best of our knowledge, only a few methods for the LAA segmentation have been published, most of them semi-automatic. We have found only few automatic LAA segmentation methods. The lack of development in the area pointed us to the existence of real clinical needs, in turn providing the motivation for the development of the methods proposed in this thesis.

CHAPTER 4: CENTERLINE EXTRACTION In this chapter we introduce our novel method for the detection of the left atrial appendage centerline. The method for centerline detection is based on tracking

the voxels with the largest radius of maximum inscribed sphere. The tracking step detects voxels in path between the seed point and the center of left atrium. The extraction step extracts the centerline from the set of tracked voxels using the skeletonization approach. The purpose of the detected centerline is twofold: while the centerline is useful to determine the length of the appendage, it is also used as as an input to the subsequent methods presented in the thesis. The validation of the extraction method is performed by measuring the Hausdorff distance between the centerline created by a medical professional and the centerline detected with our method.

CHAPTER 5: CENTERLINE BASED LAA SEGMENTATION In this chapter we present our method for the centerline based LAA segmentation. The proposed method performs the growing of a region determined by the centerline. The method is designed to grow the region towards the border regions of the anatomy, segmenting the border regions of the LAA in the process. We also explain the method's robustness to leaks and the selected threshold value. The chapter also presents the results of the validation of the method and discusses the demonstrated segmentation results.

CHAPTER 6: LOCALIZATION OF THE LAA ORIFICE In this chapter we describe our novel method for the localization of the LAA orifice. The method determines the location of the orifice by analysing the cross-sectional areas along the centerline. We explain in the chapter the process of searching for minimal cross-sectional areas along the centerline and present our novel algorithm called weighted rising slopes, which localizes the orifice. Finally, we explain how the results are validated and what are the clinical implications thereof.

CHAPTER 7: CONCLUSIONS The final chapter states the global conclusions of the thesis and points to some directions for further research continuing on this work.

2

MEDICAL BACKGROUND

In this chapter we introduce the medical background concerning the cardiovascular system. We will give a short overview of the heart anatomy and the anatomy of the cardiovascular system. We will explain common cardiovascular diseases and the often-used treatment procedures. Cardiovascular diseases are diseases which are affecting the heart and the cardiovascular system. Main clinical manifestations of cardiovascular diseases can be split into three groups: the manifestations affecting the heart and the cardiovascular system, the manifestations affecting the brain and the cerebrovascular system and the manifestations affecting the lower limbs. We will predominantly focus on the cerebrovascular manifestations of the cardiovascular diseases – mainly the cardiovascular diseases as the common cause of stroke and the methods for stroke prevention. The sections on stroke and stroke prevention will explain the role of the atrial fibrillation as the main cause of stroke from cardiovascular diseases.

2.1 CARDIOVASCULAR SYSTEM

In this section we give a brief overview of the Cardiovascular system (CVS) including the anatomical properties of the heart and the vessels. The cardiovascular system is also often called the circulatory system. The CVS is a system of organs which enables the blood to circulate throughout the body, delivering oxygen and transporting nutrients [1]. The parts composing the cardiovascular system are: the heart, blood vessels and blood. The structure and the function of the circulatory system is adapted to its primary function: to continuously deliver oxygen and nutrients to every cell of the person's body [131]. Cells use the delivered oxygen to generate the energy sources needed for all the functions of the body. Additional functions of the CVS (according to [1]) are: the transportation of the metabolic waste products and CO_2 to organs which eliminate them from the body; distribution of water, electrolytes and hormones; cooperation with the immune system and thermoregulation.

The heart is the main *driver* of the CVS , a muscular pump driving the blood through the blood vessels to the rest of the body. The heart is divided into the left and the right side, with each side containing two chambers, an atrium and a ventricle. Both chambers are mostly composed of cardiac muscle cells. The atria have thin muscle walls

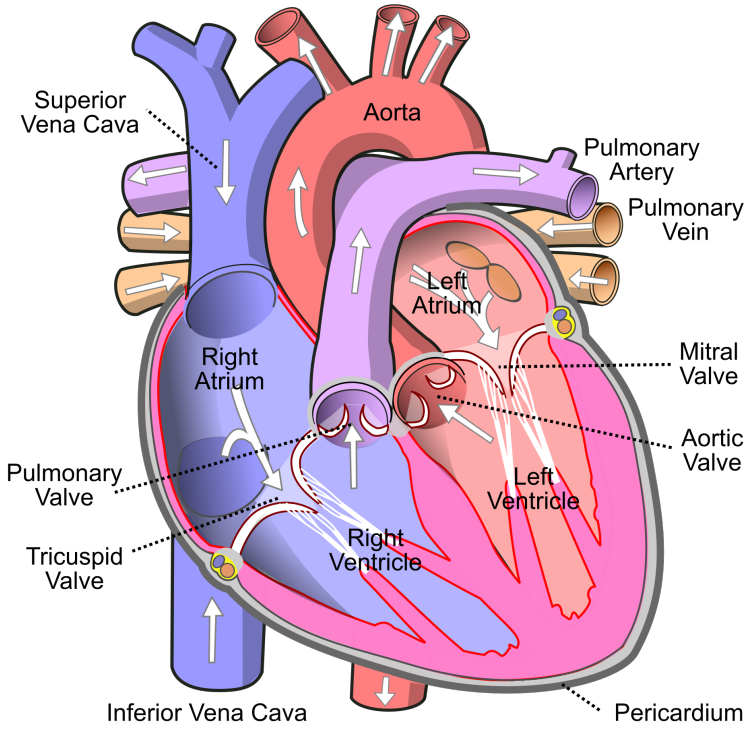

Figure 2.1: Diagram of the human heart. Image source: Wikimedia [144]

and their primary function is to fill or *prime* the ventricles. The ventricles drive the blood collected from the atria to the rest of the body through the forceful constriction of their thick muscle walls. Figure 2.1 illustrates the heart anatomy, with the four chambers in the center of the figure.

Let's observe the blood flow starting from the left ventricle (LV), the largest chamber in the heart, at the moment when it's full of blood collected from the left atrium (LA). The mitral valve is closed, preventing the return of the blood to the left atrium and ensuring the unidirectional flow of blood trough the heart. The LV muscle walls forcefully constrict, creating an increased pressure that drives the blood out of the LV and into the body. As the pressure rises, the aortic valve opens and the contraction expels the blood from the LV into the aorta. Aorta is the largest artery in the body and the first blood vessel of the systemic circulation (also called the systemic circuit). The period of the ventricular contraction (and the transferring of the blood into the aorta) is called the systole, while the maximal pressure during the systole is called the systolic pressure. During the systole the blood is pushed through the aorta and the aorta distends due to its elasticity. After the blood ejection from the LV the aortic valve closes and the LV relaxes. This period of relaxation is called the diastole. During the diastole the blood continues to flow through the aorta because

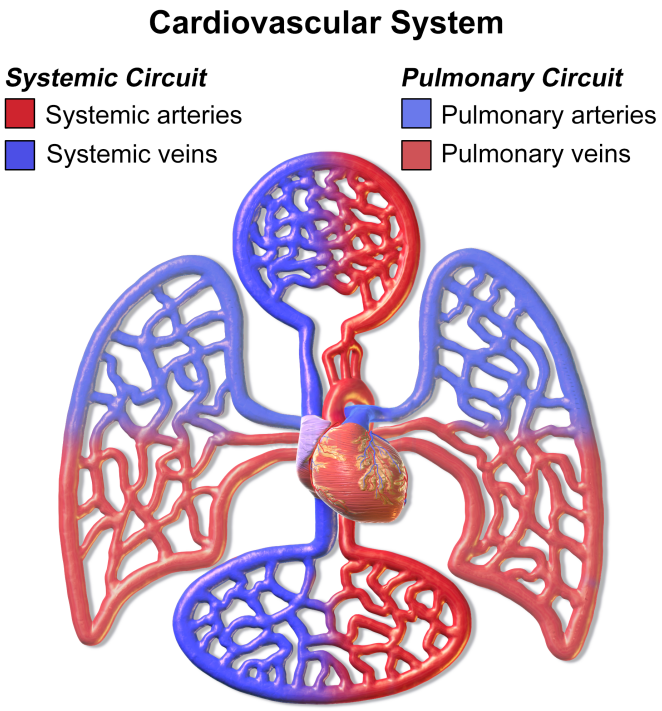

Figure 2.2: Cardiovascular circulation. The image shows the heart, the systemic and the pulmonary circulations. Image source: Wikimedia [16]

the *elastic recoil* of the aorta continues to exert pressure on the blood. This residual pressure is called the diastolic pressure and it gradually decreases during the diastole, until it reaches its minimal level. For a textbook person (typical 70kg 20-25 years old male [131]) the systolic pressure is around $120mmHg$, the diastolic pressure (at its minimal level) is around $80mmHg$ and the difference between the two is called the pulse pressure.

The blood pressure creates the blood flow from the aorta into the major arteries. The blood flows through the arteries into different parts of the body. The Figure 2.2 shows the illustration of the circulatory system. As visible in the figure, the major arteries divide carrying the arterial blood rich in oxygen and nutrients to different organs or body regions (illustrated in dark red). These arteries further subdivide into increasingly smaller vessels: muscular arteries subdivide into arterioles (arteries with diameters of $< 100\mu m$), which further subdivide into the smallest vessels called the capillaries. The capillaries form a dense network within all body tissues, performing the exchange of the gasses, delivering nutrients and collecting waste from the tissues. The capillaries progressively merge into larger vessels – venules, which in turn converge to become veins, which finally join together to become one of the two main veins in the body, the superior and the inferior venae cavae. The transition from the arterial to the venous blood is

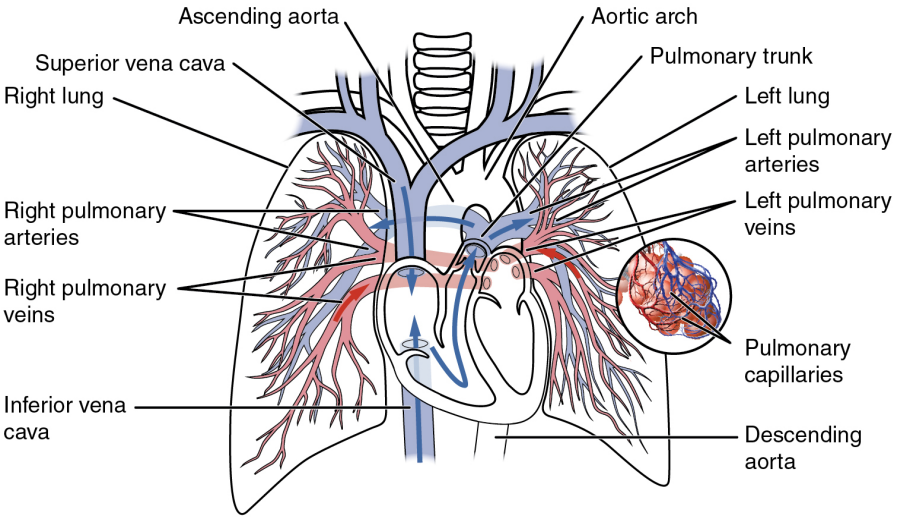

Figure 2.3: Illustration of the pulmonary circuit. Image source: Wikimedia [133]

illustrated in the Figure 2.2 by a transition from the dark red to the dark blue color. The superior and inferior venae cavae are shown as the two largest dark blue vessels, returning the de-oxygenated blood to the heart from the upper and lower body, respectively.

The blood returning to the heart through the venae cavae enters the right atrium (RA). The right atrium serves the same function as the left atrium, collecting the blood from the venae cavae and filling the right ventricle (RV) through the tricuspid valve (Figure 2.1). The right ventricle (same as the left ventricle) expels the blood collected from the atrium to the pulmonary artery, starting the pulmonary circulation. The contractions of left and the right heart occur simultaneously: both atria contract simultaneously – pushing the blood to their respective ventricles, while both ventricles contract simultaneously – pushing the blood to their respective circulations.

Pulmonary circulation is shown in the Figure 2.3. Pulmonary arteries, carrying the de-oxygenated blood from the heart to the lungs, are shown in light blue. Pulmonary circulation is shorter and has a much lower pressure than the systemic circulation. The arteries progressively subdivide in the lungs, forming the pulmonary capillary network, which performs the exchange of gasses and the oxygenation of the blood. Oxygenated blood passes through the capillary network, which progressively merges into larger vessels, with the blood finally returning to the heart through the pulmonary veins (red vessels in Figure 2.3). The pulmonary veins carry the oxygenated blood back to the left atrium, which pumps it into the left ventricle, from where the next systemic cycle begins.

2.1.1 *Heart anatomy*

The heart has four chambers – two atria and two ventricles – divided into two groups, often referred to as the left and right heart [1]. The chambers of the left heart are the left atrium (LA) and the left ventricle (LV), while the chambers of the right heart are the right atrium (RA) and the right ventricle (RV). The atria (the receiving chambers) receive the blood from the veins and fill the ventricles (the discharging chambers), which push the blood out through the arteries. The ventricles are filled with the blood from the atria through the atrioventricular (AV) valves (the mitral or bicuspid valve between the LA and the LV and the tricuspid valve between the RA and the RV). The AV valves are passive and open depending on the pressure inside the chambers. When the pressure in the atria exceeds the ventricular pressure, the AV valves open. Similarly, when the pressure in the ventricles exceed the pressure in the atria, the AV valves close. However, to prevent them from being everted during systole (when the ventricular pressure is at its highest), the valves are attached to the capillary muscles in the ventricles by fine cords (lat. *chordae tendineae*). This prevents the return of the blood to the atria, ensuring that the blood flow is always unidirectional.

During systole the ventricles contract, the pressure inside the ventricles rises and the semilunar valves between the ventricles and the atria open, allowing the blood flow into the arteries. The blood from the left ventricle drains through the aortic semilunar valve into the aorta, while the blood from the right ventricle drains through the pulmonary semilunar valve into the pulmonary artery. These valves are also passive, closing at the end of systole, when the pressure inside the ventricles drops below the pressure inside the arteries.

The filling of the ventricles occurs during the diastole, when the AV valves are open. Initiation of the heartbeat starts the atria contraction which completes the filling of the ventricles. When the ventricles start the contraction, the ventricular pressure quickly increases and the AV valves close, preventing the return of the blood to the atria. When the ventricular pressure exceeds the arterial pressure, the semilunar valves open and the blood ejects from the ventricles and into the arteries. As the blood leaves the ventricles and the systole ends, the ventricular pressure drops and the semilunar valves get closed by the backflow of the blood from the arteries.

The heart muscle – the generator of the force necessary for the contraction of the heart– is called the myocardium. The heart muscle is located inside the walls of the heart chambers. The walls of the atria are thin and the force generation during the contraction of the atria is relatively low, because the ventricles are mostly empty at the

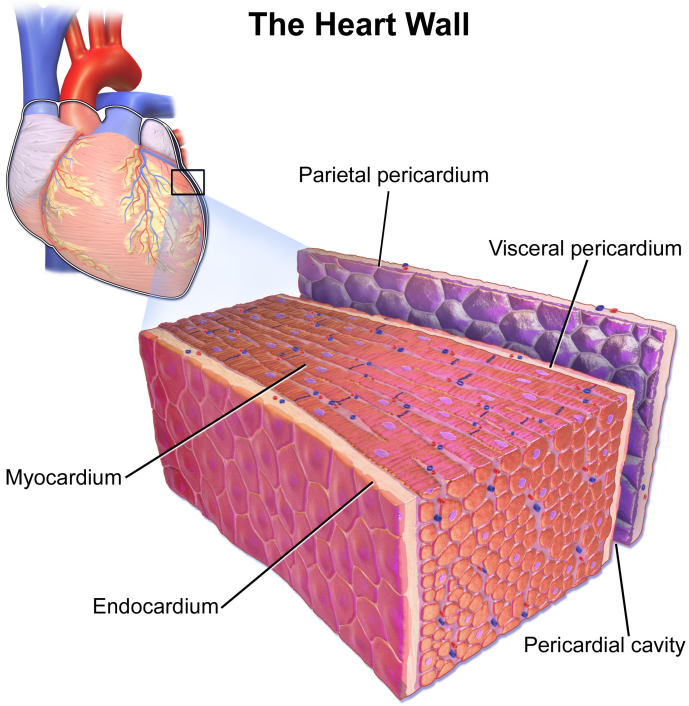

Figure 2.4: Illustration of the heart wall. Image source: Medical gallery of Blausen Medical 2014 [17]

time of atrial contraction. The walls of the ventricles are a lot thicker because the force required to push the blood to the rest of the body is a lot higher. We stated previously that the pulmonary circulation has much lower pressure than the systemic circulation, thus the RV has to generate less force than the LV. Consequently, the muscle walls of the RV are thinner than the muscle walls of the LV. The left ventricle has the greatest wall thickness of all heart chambers. The whole heart is surrounded by the paricardium, a thin sac which protects the heart and prevents excessive enlargement. The space between the heart and the pericardium is called the pericardial space or the pericardial cavity and it contains the interstitial fluid which acts as a lubricant. The Figure 2.4 illustrates the composition of the heart wall. The myocardium itself is surrounded by two layers: the endocardium on the inside of the chambers and the epicardium on the outside.

The heart muscle – myocardium – works very hard to supply the rest of the body with nutrients and oxygen. However, the myocardium itself also needs the oxygen and the energy to be able to work. Coronary circulation supplies the myocardium (as well as the other parts of the heart) with oxygen and necessary nutrients. Coronary circulation consists of the coronary arteries which supply the oxygenated blood to the heart, and the cardiac veins which drain away the de-oxygenated blood. Figure 2.5 show the illustration of the coronary circulation with coronary arteries labeled in red text. The heart gets its blood supply

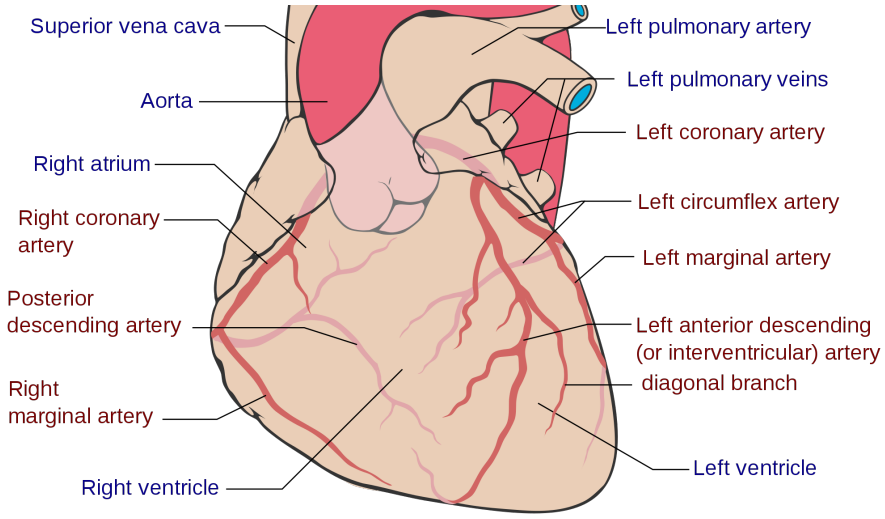

Figure 2.5: Illustration of coronary arteries with coronary arteries labeled in red text and other landmarks labeled in blue text. Image source: Wikimedia [110]

from two coronary arteries, the left and right coronary artery, extending from the aortic sinuses – the dilations in the wall of the aorta just superior of the aortic valve. The two pulmonary arteries branch into a number of smaller arteries along the heart. The right coronary artery runs along the right heart, eventually dividing into the right posterior descending artery and the right marginal artery. The left coronary artery runs for a short length (approx. 2cm) before dividing into the left circumflex artery, the left marginal artery and the left anterior descending artery. The de-oxygenated blood returns to the right atrium via the coronary sinus and anterior cardiac veins. Coronary arteries are functionally end arteries, meaning that the blockage of a coronary artery generally results in the death of the heart tissue supplied by that artery [70]. Thus, the blockage of coronary arteries often results in myocardial infarction [191] which will be explained in more detail in the later sections.

Posterior in biology and medicine refers to the back side of things – the opposite of anterior, which refers to the front side [122]

2.1.2 *Left atrium*

In this subsection we explain in more detail the anatomy of the left atrium. The left atrium the most posteriorly located of all the heart chambers [68]. Relative to the right atrium, the left atrial chamber is both more superiorly and more posteriorly located. The walls of the left atrium are slightly ticker than the walls of the right atrium. It's primary function is to collect the blood from the lungs during systole and modulate the filling of the ventricle during the diastole [18]. The left atrium receives oxygenated blood from the lungs through the pulmonary veins (PVs). Normal inflow of the blood through PVs is

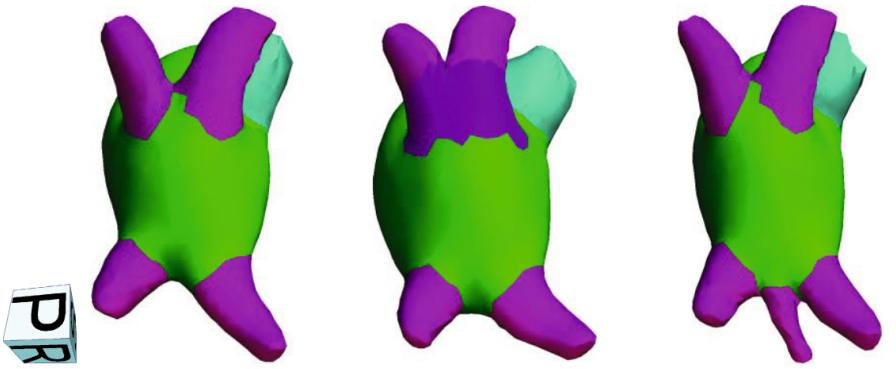

Figure 2.6: Variations in the anatomy of pulmonary veins. Images show the left atrial body (green), pulmonary veins (violet) and the LAA (mint green). Left: *typical* variation. Middle: CLT. Right: RMPV. Image source: Kutra et al. [92]

continuous and non-pulsatile, while the output of the heart is pulsatile (due to ventricular contractions). Without the atria, the venous inflow to the heart would be interrupted during the ventricular systole. Four essential characteristics of the atrium [6] enable the uninterrupted venous inflow:

- The veins entering the atria have no inlet valves which interrupt the blood flow during the atrial contractions;
- During the atrial systole, the venous blood flows uninterrupted through the atria into the ventricle. This is facilitated by incomplete atrial contractions which do not impede the atrial inflow.
- Tied to the above item, the gentle atrial contractions do not create significant back pressure which will impede the blood inflow.
- Finally, the timing of the atrial contractions results in the atrium that is relaxed before the start of the ventricular contraction, allowing it to accept the venous inflow without interruption.

ostium (pl. ostia): a mouthlike opening in a bodily part (as a fallopian tube or a blood vessel) [121]

The pulmonary veins enter the left atrium from the posterior side. *Typically*, the left atrium has four pulmonary veins joining the LA on each side through individual ostia [92]. The left superior pulmonary vein (LSPV) and the left inferior pulmonary vein (LIPV) connect to the LA from the left posterior side, while the right superior pulmonary vein (RSPV) and the right inferior pulmonary vein (RIPV) connect to the LA from the right posterior side. This *typical* four ostia pattern occurs in around 60% of the patients [117]. Diverging from the *typical* pattern, there are possible anatomical variations on both the left and the right side. The most common variations are either: the common left trunk (CLT) on the left side or the right middle pulmonary vein (RMPV) on the right side. However, patients with simultaneous variations on

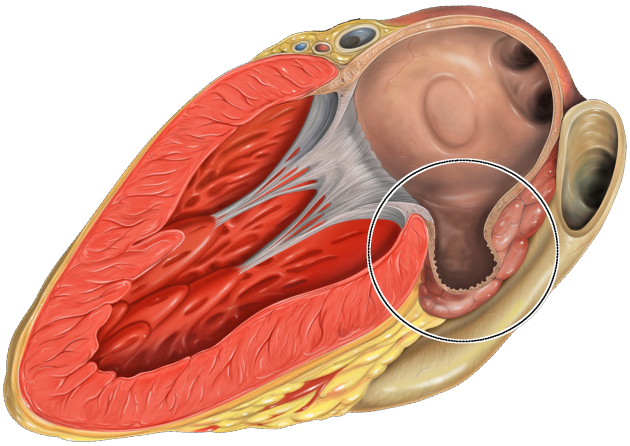

Figure 2.7: Left atrial appendage anatomy. Image show a cross-section of the left atrium and the left ventricle, with the left atrial appendage marked by a black-white circle. Image source: Wikimedia [111]

both sides are very rare. The CLT variation is characterized by both left PVs merging in the proximity of the LA body and entering the LA through a single ostium. Configurations where the distance from the ostium to the bifurcation is less than 1cm are called the short CLT and occur in about 10% of the patients [117]. The CLT occurs in about 4 to 8 % of the patients. Both the *typical* configuration and the short CLT are considered normal [82]. The RMPV configuration manifests with an additional PV joining the right side of the LA body with a separate ostium. This kind of configuration is found more often, in about 13% to 24% of the patients. The Figure 2.6 shows the examples of the described PV configurations.

2.1.3 *Left atrial appendage*

Due to the focus of this thesis on the left atrial appendage, in this section we explain in more detail the anatomy of the left atrial appendage. The left atrial appendage is a small pouch-like structure located in the wall of the left atrium [25], most often next the mitral annulus (the anatomical junction between the LA and the LV). The illustration of the LAA is shown in the Figure 2.7 in a circle. It is still somewhat unclear what is the function of the LAA. For a long time it was thought that the LAA is a relatively insignificant part of the heart [15], being a remnant of the development during gestation [4]. Currently, it is thought that the LAA functions as a decompression chamber during left ventricular systole and other periods of heightened atrial pressure [4]. It is also thought to contribute towards the left atrial reservoir and contractile functions [166]. However, it seems that the LAA has additional functions related to the neurohormonal regulation [12, 94].

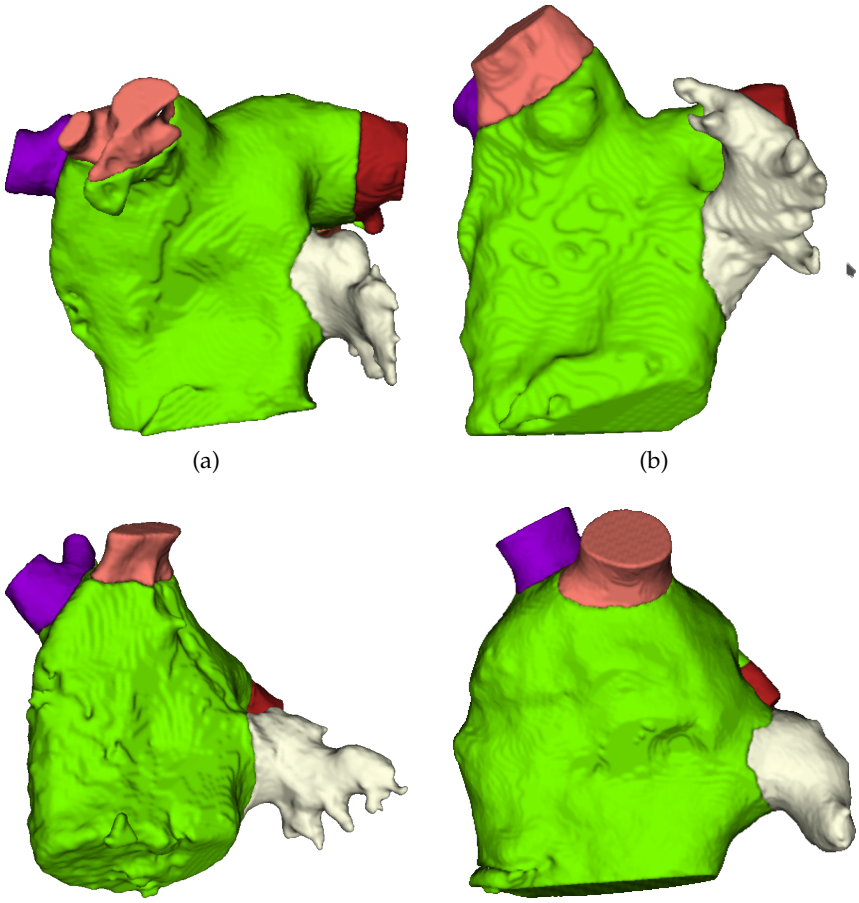

Figure 2.8: Renderings of LAAs (white) in posterior view with the left atrium (green) and pulmonary veins visible. Segmentation results from the LASC datasets [167] segmented with [197]

Nonetheless, we do know that there are real pathological concerns associated with its structure [15]. Primary concern is the increased possibility of the thrombus formation inside the LAA in patients with atrial fibrillation [63, 135, 181]. The role of the LAA in the increased risk of stroke in patients with atrial fibrillation will be explained in more detail in sections 2.3 and 2.3.1. For now, we will focus on the anatomical characteristics of the LAA.

LOCATION As stated previously, the LAA is a pouch-like structure in the wall of left atrium. The LAA is located within the confines of the pericardium in close relation to the free wall of the left ventricle [4]. The LAA comes in various shapes and sizes [24], but most often it is a long, tubular, hooked, finger-like structure protruding from the main body of the LA. There is a lot of variation in the size, shape and relationship of the LAA to other parts of the heart. Most often the appendage

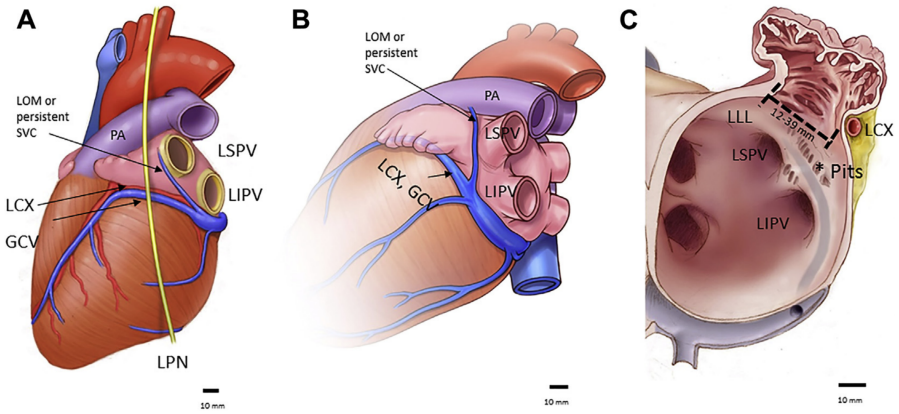

Figure 2.9: LAA location relative to other blood vessels. The posterior aspect of the LAA lies close to left-side pulmonary veins (LSPV and LIPV) and ligament of Marshall (LOM). Figures A and B show the relation of the superior aspect of the LAA to the left pulmonary artery (PA) and the relation of the inferior aspect to the left circumflex artery (LCX) and the great cardiac vein (GCV). On the endocardial aspect (C), the LAA ostium and the LSPV ostium are divided by the left lateral ridge (LLL). Image source: Naksuk et al. [128].

extends between the anterior and the lateral walls of the atrium. Even though its tip is most often directed anterosuperiorly, it's not uncommon for it to be directed laterally and backward. The superior part of the appendage is often located proximal to left pulmonary artery (PA) (Figure 2.9). The appendage is trabeculated, with muscle bars mostly running parallel to each other, resulting in a comb-like appearance. However, its wall are remarkably thin ($1mm$) [128]. From the outside (Figure 2.8), the appendage looks like a tubular, slightly flattened structure with crenellation, ending with a pointed tip. It can often have one or more bends in the structure [13]. The neck of the appendage is located in close proximity to the left circumflex artery (LCX).

OSTIUM There is often no clear boundary between the atrium and the appendage, thus the ostium can be defined somewhat arbitrary. Budge et al. [24] defines it by the curvature of the geometry on the junction between the atrium and the appendage. However, the junction between the LAA and the atrium can be defined by a narrowing in the LAA neck [13, 175]. This definition, albeit somewhat imprecise, is often used in the literature. In that case, most appendages have a well-defined orifice which opens to the body of the appendage. Figure 2.10 shows the view from inside of the left atrium looking down the appendage.

Wang et al. [179] performed a quantitative study of the LAA on 612 CT images, classifying the ostial relationship to the LSPV into three

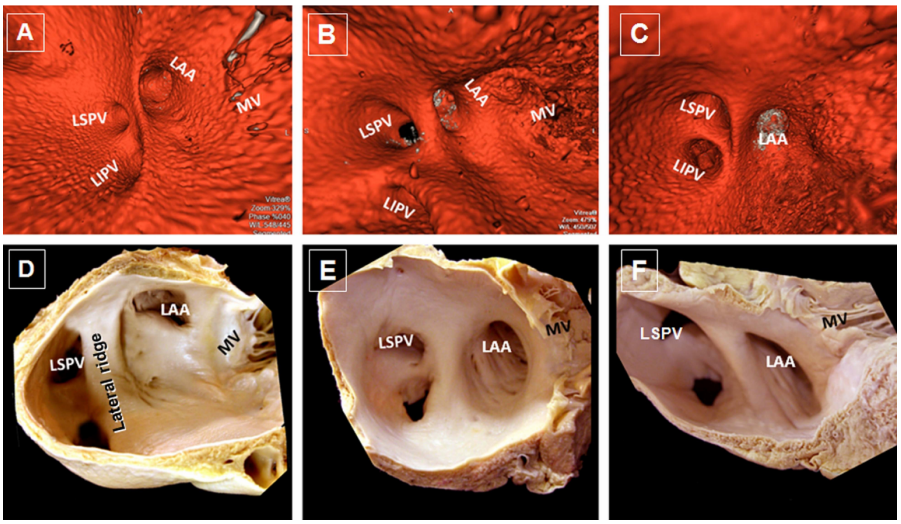

Figure 2.10: LAA view from the inside. Endoluminal CT (top row) and post-mortem (bottom row) views of the lateral wall of the right atrium, showing the ostial relationship of the left superior pulmonary vein (LSPV) and the LAA . In most cases the LAA is located either at the same level (B) or anterosuperior (A) to the LSPV ostium. The thickness of the lateral ridge between the LAA and the PVs varies between patients, while in rare cases there is no ridge between them. Image source: Cabrera et al. [25].

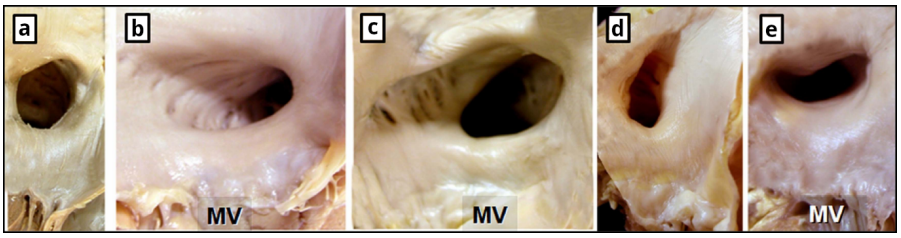

Figure 2.11: Morphological shape of LAA ostium: round (a), oval (b), triangular (c), water drop-like (d) and foot-like (e). Image source: Cabrera et al. [25].

groups: the high type (Figure 2.10 left), the mid type (Figure 2.10 middle) and the low type (Figure 2.10 right). Mid type (58.1% cases) and the high type (30.2% cases) are the more common cases, while the low type configuration was present in only 11.7% of cases.

Looking from the inside, the shape of the LAA orifice can also vary significantly. Wang et al. also classified the orifice shape into 5 categories:

- oval shape present in 68.9%,
- foot-like shape present in 10%,
- triangular shape present in 7.7%,
- water drop-like shape present in 7.7%, and finally

Table 2.1: Criteria for defining the LAA lobes. Reprinted from Veinot et al. [171].

Criteria for an LAA lobe according to [171]	
(1)	it was a visible outpouching from the main tubular body of the LAA, usually demarcated by an external crease;
(2)	it was internally capable of admitting a 2-mm probe (ie, it was not simply a tag of external adipose tissue);
(3)	it was occasionally but not necessarily associated with a change in direction of the main tubular body of the LAA;
(4)	it could lie in a different anatomic plane than the main tubular body; and
(5)	by definition, the LAA must have at least one lobe (ie, a tubular body with a blind-ending sac).

- round shape present in 5.7% of the patients.

Figure 2.11 shows the postmortem specimens of the orifice shape categories. The shape of the orifice is important for the planning of the occlusion procedure and is usually defined by two measure: the long diameter (the maximal diameter in the orifice) and the short diameter (perpendicular to short long diameter). Orifice dimensions also vary significantly, with a long diameter ranging from 10mm to 40mm [165]. Interestingly, Wang et al. [179] determined the orifice dimensions in CCTA images in both the 2D oblique and the 3D views, and found an average difference in dimensions between the two modalities of almost 5mm (average long diameter of $26.5 \pm 5.8mm$ and $21.7 \pm 5.7mm$ in 2D oblique and 3D view, respectively).

SHAPE Another large study of postmortem hearts by Veinot et al. [171] analyzed the morphology of the normal LAAs and defined the lobes with the criteria shown in the Table 2.1. Analysis on 500 postmortem hearts of all ages, according to the above criteria, has found that the appendage with two lobes is the most common (54% cases), followed by 3 lobes (23%), 1 lobe (20%) and 4 lobes (3%). They haven't found any significant age- or sex-related differences in morphologies.

The shape of the LAA can vary significantly and the number of lobes, while it is a useful measure in itself, is not enough to describe the variations in the morphology. Thus, Wang et al. [179] proposed to classify the LAA morphology into four types:

- Chicken-wing — the most common morphology type present in 48% of patients. This morphological type is characterized by

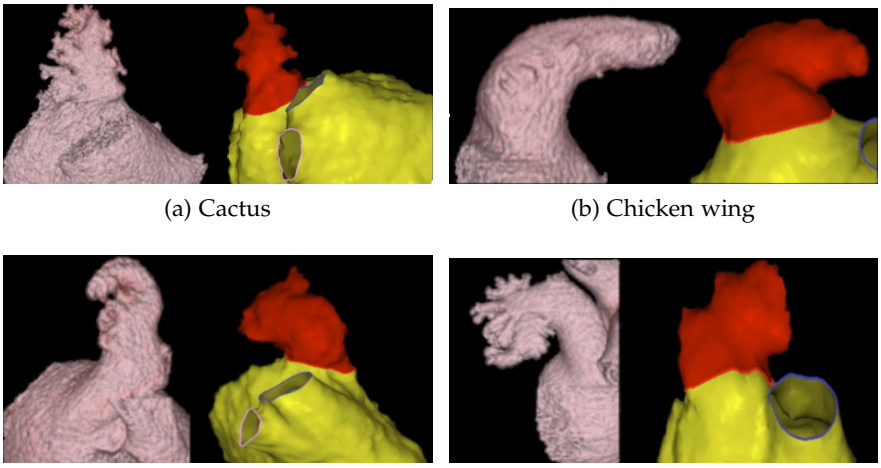

(a) Cactus (b) Chicken wing

(c) Windsock (d) Cauliflower

Figure 2.12: Types of LAA morphology. Each subfigure shows the rendering of a CT dataset (left) and an MRI dataset (right). Image source: Di Biase et al. [42].

a dominant lobe that has an obvious bend in its proximal or middle part. The distal part often folds back on itself. May have secondary lobes.

- Cactus — found in 30% of patients and characterized by a central dominant lobe, from which secondary lobes extend in both superior and inferior direction.
- Windsock — present in 19% of patients and also characterized by a dominant lobe as a primary structure, from which secondary or even tertiary lobes can arise in inferior direction.
- Cauliflower — rarest morphological type (3%) and most often associated with embolic events. Often characterized by its short overall length and lack of a dominant lobe.

The proposed classification was derived from a sample of 612 patients' CT images. Population consisted of patients both with and without non-valvular atrial fibrillation. The examples of the proposed morphology types are depicted in the Figure 2.12. The original criteria for the morphology classification is reprinted in the table 2.2. Additionally, Wang et al. [179] determined the average dimensions of the appendage necessary for the occlusion procedure. The approximate LAA length for the orifice to the LAA apex of the primary lobe was measured at $48 \pm 12.1mm$. The appendage volume was $8.8 \pm 5.6mL$. Obvious bend in the primary lobe was observed in the majority of patients (73.2%, $n = 448$). The angle of the first bend, observed from 2D axial slices, was measured at 97.6 ± 20.3○, while the distance from the orifice to the first bend was $14.1 \pm 4.0mm$.

Table 2.2: Criteria for each morphology type. Table from Wang et al. [179].

LAA with obvious bend	
1	*The ChickenWing LAA* is an anatomy whose main characteristic is an obvious bend in the proximal or middle part of the dominate lobe or folding back of the LAA anatomy on itself at some distance from the perceived LAA ostium. This LAA type may vary with or without secondary lobes or twigs, with the different measured distance to this bend as well as with the different orientation (anterior, superior, inferior, etc.) of the bend relative to the main lobe.
LAA without obvious bend	
2	*The WindSock LAA* is an anatomy in which 1 dominant lobe of sufficient length is the primary structure. Variations of this LAA type arise with the location and number of secondary or even tertiary lobes arising from the dominate lobe in inferior direction.
3	*The Cauliflower LAA* is an anatomy whose main characteristic is an LAA that has limited overall length with more complex internal characteristics. Variations of this LAA type are demonstrated by a more irregular shape of the perceived LAA ostium (oval vs. round), the number of significant lobes present and lack of 1 dominate lobe and the close proximity of internal separations or prominent pectinate ridges to the perceived LAA ostium.
4	*The Cactus LAA* is an anatomy whose main characteristic is a dominant central lobe with secondary lobes extending from the central lobe in both superior and inferior directions. Variations of this type relate to the number, location and orientation of the secondary lobes. This type of LAA may present like a fork with a dominant lobe and with 2 or 3 secondary lobes at the top of LAA.

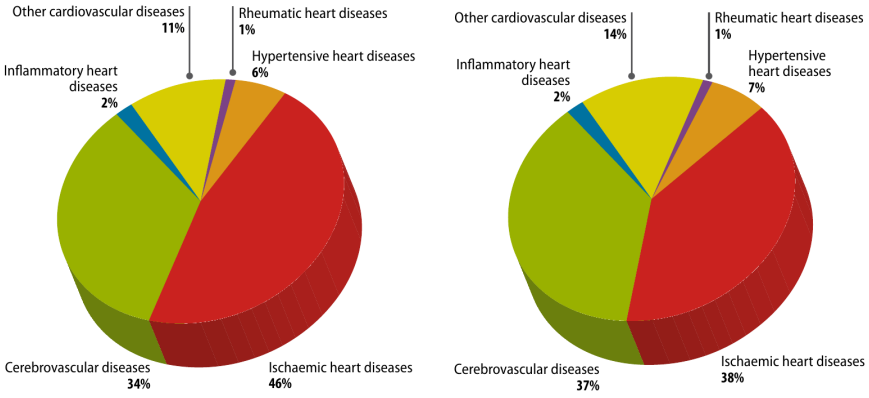

Figure 2.13: Distribution of deaths for males (left) and females (right) due to six common types of cardiovascular diseases. Image source: World Health Organization (WHO) [174].

2.2 CARDIOVASCULAR DISEASES

This section gives a short overview of major cardiovascular diseases (CVDs). Cardiovascular diseases kill more people every year than any other cause: with an estimated 17.9 million deaths in 2016, CVDs account for 31% of all worldwide deaths [183]. The term cardiovascular diseases refers to a group of disorders which include diseases of the heart, vascular diseases and diseases of blood vessels.

World Health Organization divides the diseases into two groups: diseases due to atherosclerosis and other cardiovascular diseases [174]. Cardiovascular diseases due to atherosclerosis are:

- ischaemic heart disease or coronary artery disease — disease of the blood vessels supplying the heart muscle (e.g. heart attack);
- cerebrovascular disease — disease of the blood vessels supplying the brain (e.g. stroke);
- diseases of the aorta and arteries — including hypertension and peripheral vascular disease (disease of blood vessels supplying the arms and legs);

Other major cardiovascular diseases include:

- congenital heart disease — malformations of heart structure existing at birth;
- rheumatic heart disease — damage to the heart muscle and heart valves from rheumatic fever, caused by streptococcal bacteria;
- cardiomyopaties — disorders of the heart muscle;
- cardiac arrhythmias – disorders of the electrical conduction system of the heart.

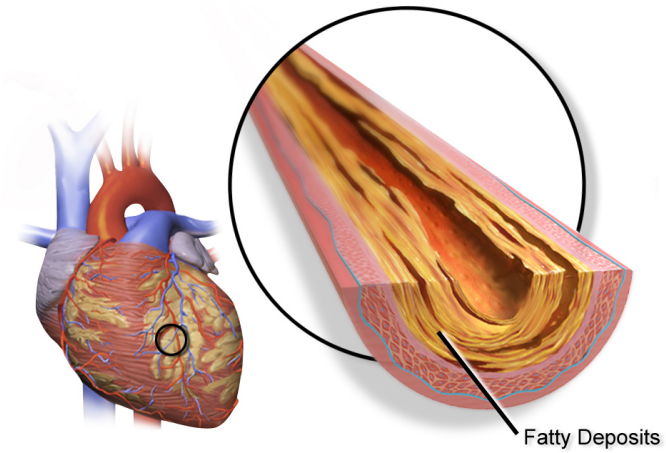

Figure 2.14: Blood flow obstruction due to build-up of fatty deposits in coronary vessels. Image source: Wikimedia [17].

Figure 2.13 shows the distribution of deaths from six main categories of cardiovascular diseases among males and females (WHO report in [172]). Among the CVD-induced deaths, most people die because of ischemic heart diseases, with the cerebrovascular diseases (stroke) following closely at the second place. These two diseases alone account for about 85% of all CVD induced deaths.

2.2.1 *Atherosclerosis*

Atherosclerosis is a disease affecting the blood vessels, which results in ischemic heart disease (heart attack) and cerebrovascular disease (stroke). Heart attacks and strokes are usually acute events which occur due to the obstruction of blood supply to the heart or the brain. The obstruction of the vessels supplying the heart can result in reduced blood flow to the heart tissue (ischemia) or a complete prevention of the blood flow so that the heart tissue dies (infarction). The prevention of blood supply to the brain is called a stroke. These cardiac events are often called major adverse cardiac events (MACEs) and include nonfatal stroke, nonfatal myocardial infarction and cardiovascular death [211]. Both myocardial infarction and stroke commonly occur due to thromboembolism – the blocking of the blood flow through the vessel by a blood clot originating somewhere else in the circulatory system.

Major underlying cause of MACE is a build-up of fatty deposits on the inner walls of blood vessels (Figure 2.14) due to atherosclerosis. Atherosclerosis is a long lasting disease, developing gradually over many years. Fatty material and cholesterol are gradually deposited inside the lumen of blood vessels, causing the lumen to become narrow.

lumen (pl. lumina): inside space of a tubular structure, such as an artery or intestine [109]

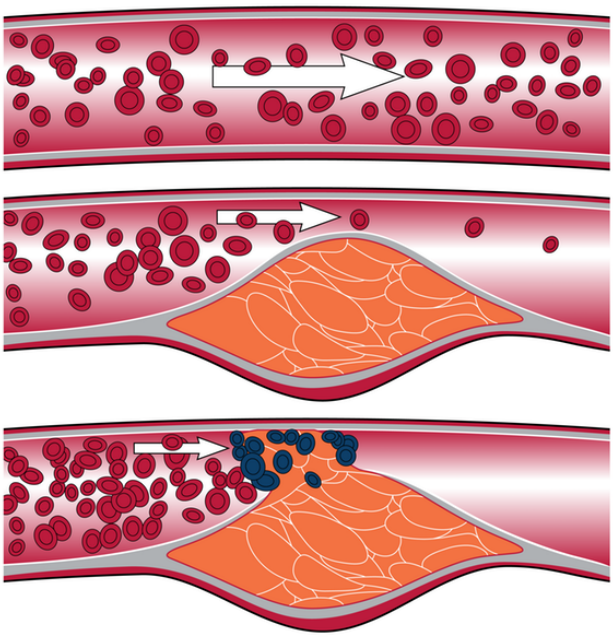

Figure 2.15: Development of coronary artery disease and forming of a blood clot after rupture. Top: Healthy artery. Middle: Diseased artery with plaque deposits. Bottom: The plaque ruptures, forming a blood clot and preventing the blood flow. Image source: Albert.io [71].

Additionally, while healthy blood vessels are flexible and elastic, over time the walls in the vessels can harden, making them less pliable. Consequently, all these effects can make it harder for the blood to flow through the vessel.

Certain types of plaque are vulnerable to rupture due to external stress, triggering the formation of a blood clot which obstructs the blood flow through the vessel [50]. (Figure 2.15). If the blood clot forms in a narrow vessel, such as coronary arteries or brain arteries, it can prevent the blood flow and cause a heart attack or a stroke.

2.2.2 *Rheumatic heart disease*

Rheumatic fever is a common cause of heart disease which predominantly affects children and adolescents living in poverty. Acute rheumatic fever is caused by an abnormal response of the body to infection with streptococcal bacteria. The infection usually begins as a pharyngitis or tonsillitis and, if left untreated, develops into a fever that primarily affects the heart, joints and central nervous system. The inflammation and scarring cause by the fever can damage the heart muscle and heart valves [173], leading to rheumatic heart disease.

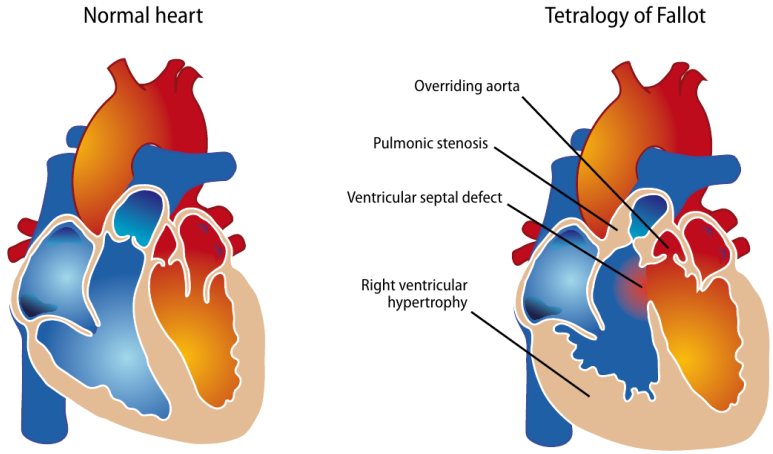

Figure 2.16: Congenital heart disease. Left: Healty heart. Right: Heart suffering from tetralogy of Fallot. Image source: Wikimedia [17].

2.2.3 *Congenital heart disease*

Congenital heart disease is an important cause of childhood morbidity and mortality worldwide, being the leading cause of birth defects and the second leading cause of death in infants. It manifests as a defect in the structure and function of the heart due to abnormal heart development before birth [174]. Birth defects can be caused by genetical factors, as well as behavioral and environmental factors [174].

Congenital heart diseases are usually divided into *cyanotic* and *non-cyanotic*, depending on whether the defect in the heart causes mixing of blood between the two sides of the heart [174]. Figure 2.16 shows an example of a cyanotic disease — tetralogy of Fallot — where several congenital defects are found together and the mixing of the blood between left and right ventricle does occur. Ventricular septal defect is the most common type of congenital heart defect, where the blood communicates between the left and the right ventricle. Figure 2.17a shows atrial septal defect, another common defect characterized by a hole in the septum between the atria [29]. Some defects, such as coarctation of the aorta (Figure 2.17b), may not cause problems for many years, while other defect may require immediate medical attention or surgery.

2.2.4 *Cardiomyopaty*

Cardiomyopaties refers to disorders of heart muscle, where the heart muscle becomes enlarged, thick, or rigid. In rare cases, the muscle tissue is replaced with scar tissue. The disease can be both acquired (develops over time due to another disease, condition or factor) and inherited [129]. Often the cause of the disease is not known. Usually,

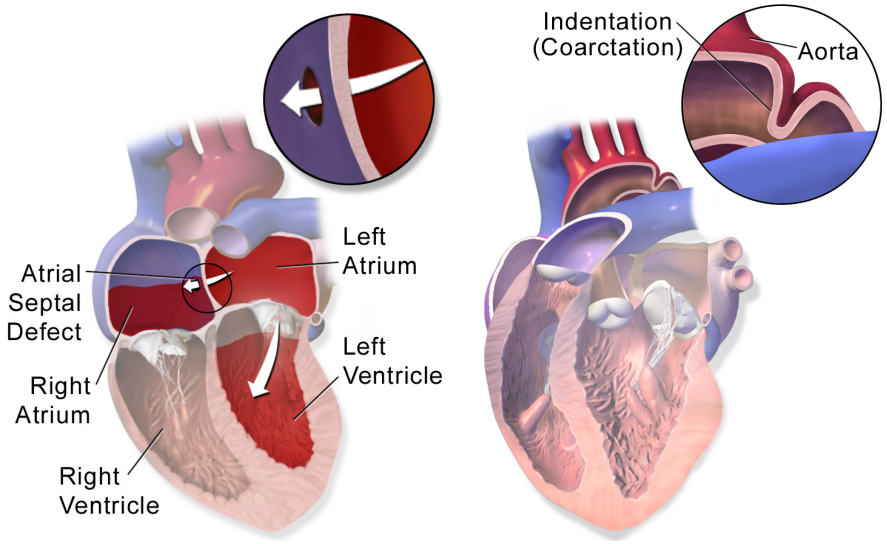

(a) atrial septal defect (b) coarctation of the aorta

Figure 2.17: Congenital heart defects. Image source: Wikimedia [17].

as the disease worsens, the heart becomes weaker. Weaker heart is less capable of pumping the blood through the body and maintaining a regular electrical rhythm. This can cause many complications, such as heart failure, arrhythmia, heart valve problems and similar [129]. Some patients that have cardiomyopathy do not show any symptoms and do not require treatment, while in others the disease develops quickly and causes serious complications. It can affect people of any age (although some age groups are more susceptible) and affects both sexes equally.

2.2.5 *Cardiac arrhythmia*

Heart's electrical system initiates and regulates the beating of the heart (Figure 2.19). Each heartbeat is controlled by an electrical impulse originating in the sinoatrial node in the right atrium of the heart [65]. Under normal conditions, sinoatrial node generates such electrical impulses regularly, between 60 and 100 times per minute. Each impulse propagates through the heart's conduction pathways, causing the contraction of the tissues. Initially, the impulse causes both of the atria to contract. Next, the impulse travels down through the conduction pathways, where it reaches and activates the atrioventricular node. Normally, the atrioventricular node is the only electrical connection between the atria and the ventricles. Here, the impulse slows down for a very short period of time. The impulse then continues down the pathways, via the atrioventricular bundle (called bundle of His) into the ventricles. The bundle of His divides into left and right bundle

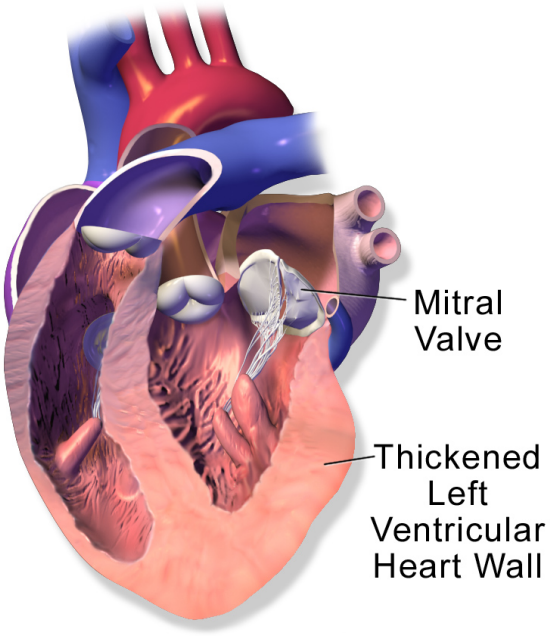

Figure 2.18: Hypertrophic cardiomyopaty is characterized by thickening of the left ventricular heart wall. Image source: Wikimedia [17].

branches, which are used to propagate the impulse to the left and right ventricles. Finally, while traveling the bundle branches, the impulse spreads through Purkinje fibers to the myocardium of the ventricle, causing the muscle tissue of the ventricle to contract.

Contraction of the ventricle generates the force required to eject blood out of the heart and to the rest of the body. Each contraction of the ventricle represents one heartbeat. The atrium contracts a fraction of a second before the ventricle and fills the ventricle with blood. This is possible because the impulse is delayed in the atrioventricular node, before it reaches the ventricle.

Abnormal electrical activity in the heart is known as cardiac arrhythmia. The irregular heartbeat due to arrhythmia can be too fast (tachycardia) or too slow (bradycardia). Arrhythmia can also be classified by site of origin, into: atrial arrhythmia, junctional arrhythmia, and ventricular arrhythmia [157]. Sometimes cardiac arrhythmia is life threatening and requires immediate medical care, sometimes it may give rise to palpitations and finally, sometimes it does not show symptoms at all.

Atrial fibrillation is a common type of arrhythmia, characterized by uncoordinated activation of atrial contractions, outside of the normal heart rhythm [85]. According to the above classification, atrial fibrillation can be classified as an atrial tachycardia. Atrial fibrillation is correlated to the deterioration of mechanical function of the heart and

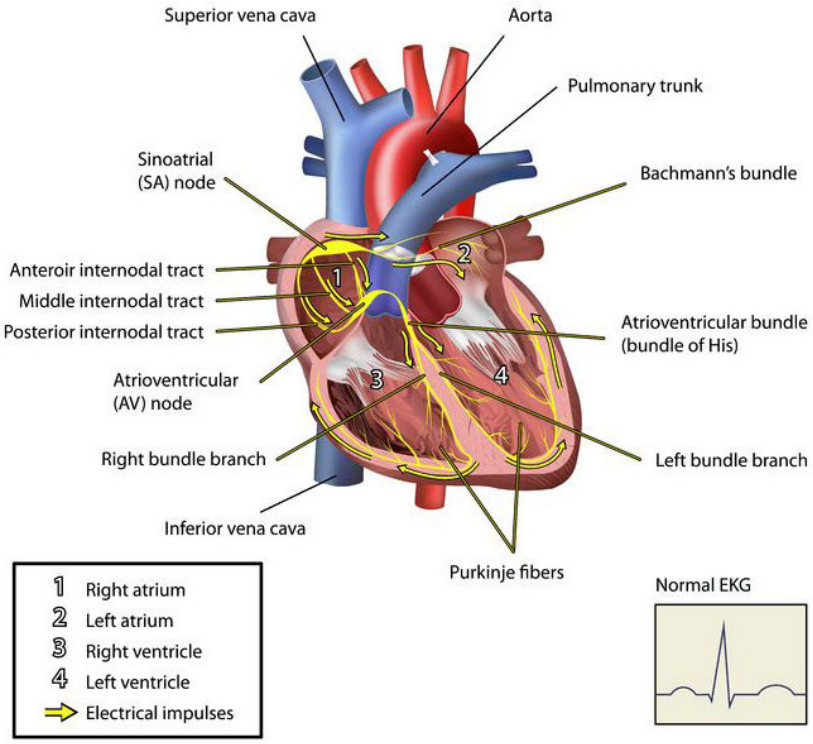

Figure 2.19: Electrical system of the heart. Image source: Medical Center Rochester [65].

commonly associated with stroke and congestive heart failure [85]. Atrial fibrillation drastically increases the risk of stroke.

While a detailed overview of all arrhythmias is outside the scope of this thesis, in the next section on stroke prevention we will describe the atrial fibrillation in more detail.

2.3 STROKE PREVENTION

Cardiovascular diseases (CVD) disproportionately affect the elderly population [132]. Stroke is the second leading cause of death globally, being responsible for around third of all deaths from CVDs [183]. For the last two decades the rate of new strokes, when adjusted for age, has steadily declined in the whole European Union [49]. However, the population in all of EU is aging [55] and the percentage of the population over 65 years of age is rising. Due to the strong association between stroke risk and age, the number of stroke incidents continues to rise. *The Burden of Stroke in Europe* report [49] quantified the effects of stroke on the EU economy:

> In 2015, direct healthcare costs alone added up to €20 billion in the EU, while indirect costs of stroke due to the opportunity cost of informal care by family and friends

> and lost productivity caused by morbidity or death were estimated to be another €25 billion.

The same report identified two most important risk factors for stroke as high blood pressure and atrial fibrillation (AF). Throughout this thesis we will focus on the stroke prevention due to atrial fibrillation. Specifically, the proposed methods aid the physicians in planning of percutaneous LAA occlusion – the procedure which is shown to drastically reduce the risk of stroke due to atrial fibrillation.

2.3.1 *Atrial Fibrillation*

Atrial fibrillation is an important risk factor for stroke – responsible for almost 20% of all strokes [24] and for the majority of cardioemoblic strokes [89]. Most cardioembolic strokes are the result of thromboemboli originating in the LAA. The disease manifests as arrhythmia, when the normal regular rhythm of the heart becomes irregular, due to disorganized electrical signals in the atria.

In a normal, healthy heart, the atria contract a fraction of a second before the ventricles, as the contracting impulses travel first through the atria and then, through the AV node, to the ventricles (Figure 2.19). With atrial fibrillation, the chaotic electrical activity causes asynchronous contractions of the atria – quivering or fibrillation – as the atria contract quickly and unevenly, instead of pumping rhythmically and forcefully [119]. The ventricles also beat rapidly, but slower than the atria, as AV node does not let all the impulses through to the ventricles. This prevents the heart chambers from filling and emptying properly.

Without effective blood pumping, the blood can sometimes pool in the heart and form a blood clot. Pieces can break off from a clot, forming thromboemboli, which can be passed from one chamber to the next and enter the circulatory system. When the clot ends up in a brain artery, it can stop the blood flow to the brain and cause a stroke. Estimates show that over 33 million people worldwide suffer from atrial fibrillation [34], as it is the most common type of arrhythmia. The disease predominantly affects the older population. Consequently, the number of people suffering from atrial fibrillation is expected to increase due to the increase in age of population, especially in the countries of the developed world [85, 208].

The most common method for stroke prevention in patients with atrial fibrillation is anticoagulation therapy. Anticoagulants block the activity of coagulation factors, reducing the body's ability to form blood clots. Anticoagulation therapy reduces the risk of stroke by $\sim 60\%$ [63]. However, patients often have contraindications to anticoagulation therapy, patients with higher risk of stroke are more likely

to have such contraindications [135] and nearly 40% of patients do not receive such therapy because of them [137].

2.3.2 *Left atrial appendage closure*

Left atrial appendage closure is an alternative stroke prevention method for patients with contraindications to anticoagulation therapy. It has recently been approved for clinical use by Food and Drug Administration in USA [137]. The procedure demonstrated non-inferiority to anticoagulation therapy [11, 69, 150] while avoiding most of the contraindications.

There are several LAA occlusion devices currently on the market available for the procedure, but their availability varies in different parts of the world. According to the American College of Cardiology [137] the only device approved by the Food and Drug Administration (FDA) for percutaneous LAA closure in the USA is the WATCHMAN device (Boston Scientific; Natick, MA). WATCHMAN is also the most extensively studied device to date through the PROTECT AF trial [149]. Two other popular devices for LAA closure are: PLAATO [125, 135] which was available in Europe, but is discontinued, and Amplatzer Cardiac Plug [140, 170] which is available in Europe, Canada and other parts of the world.

Left atrial appendage closure procedure is performed by percutaneously deploying the occluder device to the neck of the appendage. The device stops the blood flow between left atrium and LAA and prevents the trombi formed in the LAA from leaving the LAA and causing stroke. Closure devices are available in several predefined sizes. Physicians choose an appropriately sized device for each patient. Selection of the correctly sized device requires accurate measurements of the appendage. Usually, the measurements are obtained either from a CT image or during the TEE examination. However, for selecting the device of an appropriate size, the measurements obtained from CCTA images have shown to be superior to measurements derived from other modalities [56, 158, 185]. The work of Cabrera et al. [25] presents the complete list of 27 anatomic and imaging landmarks that determine the feasibility of LAA occlusion. However, the most important anatomic LAA measurements for the closure procedure are:

- diameter/circumference of the LAA orifice,
- shape of LAA orifice,
- LAA length and volume,
- maximal length of the dominant LAA lobe,

- type of LAA morphology.

All of the above measurements can be adequately determined from an accurate LAA segmentation. The type of the morphology can be easily determined from a visualized 3D rendering, while in 2D the process is error prone. In 2D, the LAA can appear as a different morphology type depending on the viewing angle of the reconstruction. LAA morphology is among the most important parameters that determine the feasibility of the LAA closure procedure and likelihood of post-procedural complications [25].

2.4 CONCLUSION

In this chapter we gave a broad overview of the cardiovascular anatomy, the functioning of the cardiovascular system and the cardiovascular pathology. Especially, we aimed to introduce the medical concepts necessary for understanding the need for the left atrial appendage segmentation methods. While reviewing the necessary medical background, we focused on the stroke prevention techniques, the role of the atrial fibrillation and the left atrial appendage in increasing the risk of stroke, and finally the percutaneous left atrial appendage occlusion procedure – a novel method for reducing the risk of stroke in patients with atrial fibrillation. The left atrial appendage occlusion procedure, despite being only recently approved by the FDA, is experiencing a steep rise in popularity, as the number of performed procedures rises and the costs drop. Although the procedure can be carried out without the pre-procedural CT scan using only the transesophageal echocardiography (TEE), the use of the CT based pre-procedural planning workflow reduces the time spent performing the procedure and increases the patient satisfaction. In order to effectively perform the pre-procedural planning and choose the device of the correct size, more sophisticated algorithms are required that can quickly and with minimal interaction determine accurate measurements of the LAA and surrounding structures.

3

SEGMENTATION APPROACHES

This chapter reviews major state-of-the-art image segmentation approaches in cardiovascular anatomy with the special focus on left atrial appendage segmentation. The available approaches can be divided according to part of the heart anatomy they are focused on: methods focused primarily on the segmentation of the whole heart (all four chambers) and the methods focused on the segmentation of the left atrium or the left atrial appendage. Alternatively, categorization can be made based on the type of computational approaches used in the methods, as was done in the review paper by Kang et al. [80]. We also make such a categorization based on the predominant computational and image processing concepts, and we review where appropriate the anatomical aspects too.

This chapter is organized in the following manner. First, we present an overview of the cardiovascular segmentation methods divided into categories according to the computational approach used. The methods are based on the four main approaches presented in the following subsections: methods based on partial differential equations (PDEs) in Section 3.1; methods based on graph-cuts in Section 3.2; model-based methods in Section 3.3; and methods based on clustering and classification in Section 3.4. In each of these sections we will explain the methods for the whole heart segmentation, including the methods for extraction of the heart as a whole from the images as well as the methods which will segment the chambers separately. Next, we give an overview of methods focused solely on the segmentation of the left atrial appendage – the main focus of the thesis. Some of the presented methods focus on the segmentation of the left atrium, with the LAA being an integral part of the left atrium. Finally, the Section 3.6 provides a short recap of the content of this chapter.

3.1 PDE-BASED SEGMENTATION METHODS

Image segmentation methods based on partial differential equations (PDEs) rely on the concept of an evolving contour. The evolution of the contour is performed by deforming the contour from the initial to the final position. Seminal work of Kass et al. [83] introduced the Active Contour Models (ACMs) also known as *Snakes*, one of the most widely used PDE-based approaches. Active contour models can be divided

in two main groups: the edge-based models and the region-based models.

The boundary of the object in the edge-based ACMs is identified using the image gradient. The advantage of the edge-based model is primarily in the ease of obtaining the final segmentation – object boundary identification from image gradient is intuitive even to non-technical users. The main drawback is the dependence of the final result on the initial contour. On the other hand, the region-based contour model uses a statistical approach to segment the region of interest from the background. This type of method calculates the optimal match of a model to the image which minimizes some kind of energy functional. This type of method is less dependent on the initial contour and more resistant to the noise in images, but obtains lower results when the objects in the image are heterogeneous.

3.1.1 *Active contour model*

The work of Kass et al. [83] introduced the energy minimization concept in their Active Contour Model (ACM) approach. The approach is based on the evolving curve, defined in the image domain, which is deformed (evolves) under the influence of internal and external forces. Internal forces try to control the smoothness of the curve during the deformation. External forces attract the curve towards the salient features in the image. The energy function controlling the deformation is defined as:

$$E_{\text{total}} = \int_0^1 \left[E_{\text{internal}}(x(y)) + E_{\text{external}}(x(y))\right] dy \tag{3-1}$$

where $x(y)$ is the contour, E_{internal} represents the internal energy and E_{external} represents the external energy function. The internal energy function is defined as:

$$E_{\text{internal}} = \int_0^1 \left[a\left|x'(y)\right|^2 + b\left|x''(y)\right|^2\right] dy \tag{3-2}$$

where a is weight parameter which controls tension, b is weight parameter for stiffness control and $x'(y)$, $x''(y)$ are first and second derivatives of the contour with the respect to $x(y)$. The external energy function is defined as:

$$E_{\text{external}} = \int_0^1 P(x(y))dy \tag{3-3}$$

where P is a scalar potential function defined in the image domain. For energy minimization, contour $x(y)$ has to satisfy Euler-Lagrange equation:

$$ax'(y) - by''(s) - \nabla(P)(x(y)) = 0 \tag{3-4}$$

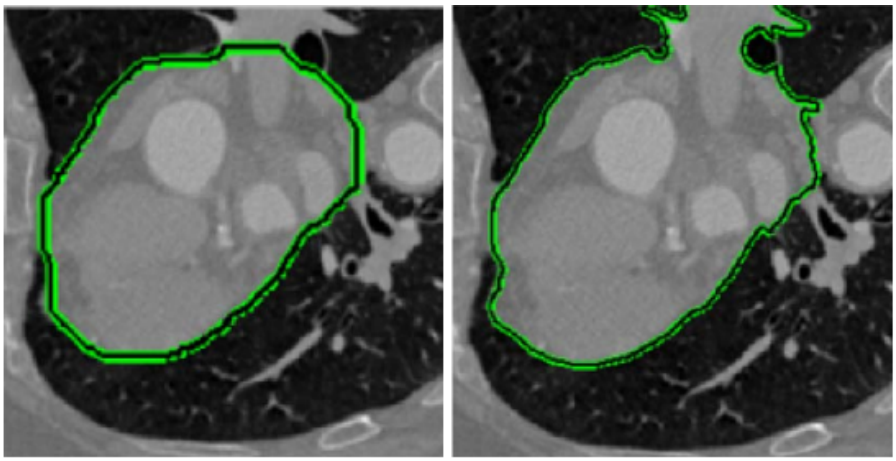

Figure 3.1: Active contour-based whole heart segmentation. Figure shows the initial contour (left) and the final result after contour evolution (right). Image source: Bai et al. [10].

where ∇ is gradient operator.

The work proposed by Bai and Li [10] performs the whole heart segmentation using the original *Snakes* approach proposed by Kass [83]. Figure 3.1 shows one slice from the resulting segmentation. The work performs the evolution of the initial contour, where the seed points for the initialization of the contour were obtained using watershed segmentation. The use of the ACM enables the iterative deformation of the initial contour until it conforms to the heart boundaries in the image. Additionally, one way to overcome the limitations of the explicit boundary identification approach is to combine the region and boundary information.

Lankton et al. [95] have proposed a novel concept of localizing region-based active contour (LACM) in order to deal with the intensity inhomogeneities. Their method enables the segmentation of objects with discontinuous and heterogeneous boundaries by using the approach based on probability of appearance of certain regions in the image. This is especially important for cardiac segmentation. In images acquired at a cardiac phase when the mitral valves are open, the contrasted blood is freely flowing from the atrium to the ventricle. The result is the lack of boundary between the atrium and the ventricle. This lack of boundary confuses the edge-based ACMs.

To overcome this problem, Wu et al. [184] proposed an adaptive diffusion flow (ADF) model. Later, Zhou et al. [204] merged these two approaches (the LACM and the ADF models) by using both the localizing region and the edge-based intensity information to perform the segmentation. Two main advantages of the Zhou approach are: (1) the ability of the model to handle both the weak edges and the intensity inhomogeneities; and (2) robustness to the contour initialization. Fig-

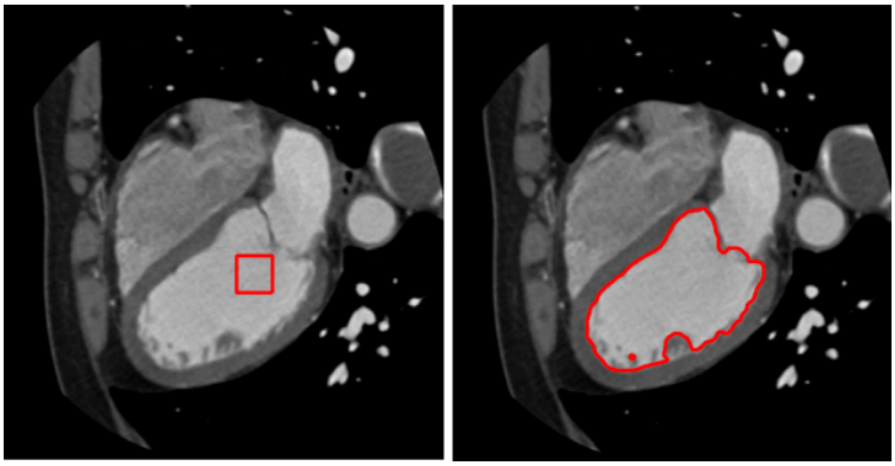

Figure 3.2: Active contour-based whole heart segmentation combining LACM and ADF with the initial contour (left) and the final resulting contour (right) in one CT slice. In this case, despite the closed mitral valve, the boundary in the image defined by the mitral area is still a rather weak one. Nonetheless, the method successfully segments the LV, demonstrating robustness to the contour initialization. Image source: Wu et al. [184].

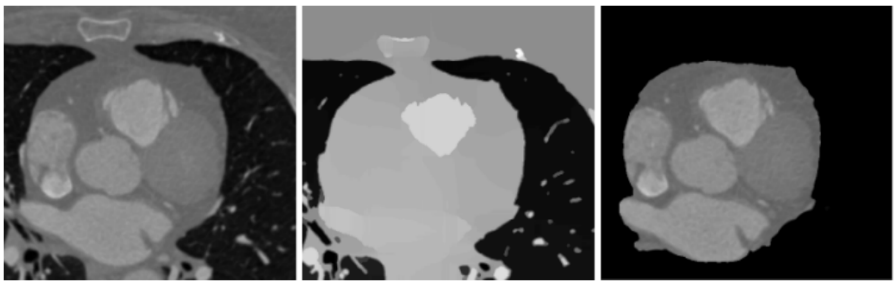

Figure 3.3: The initial slice (left), the smoothed image after the diffusion (middle) and the final masked image (right). Image source: Livada et al. [102].

ure 3.2 shows the example of the left ventricle segmentation using this approach.

Another relatively novel approach proposed by Soomro et al. [161] implements a region-based ACM which takes both the local and global information into account. Energy functional guiding the evolution is implemented using the signed pressure force (SPF) function. This approach diverges from the approaches presented above by using the level sets for evolution. The SPF function in the Soomro's approach drives the evolution of the zero level set curve towards the object boundary. The use of the Gaussian kernel instead of traditional reinitialization approach gives the benefit of regularizing the level set curve while removing the computationally expensive reinitialization step. The example of the approach is shown in Figure 3.4.

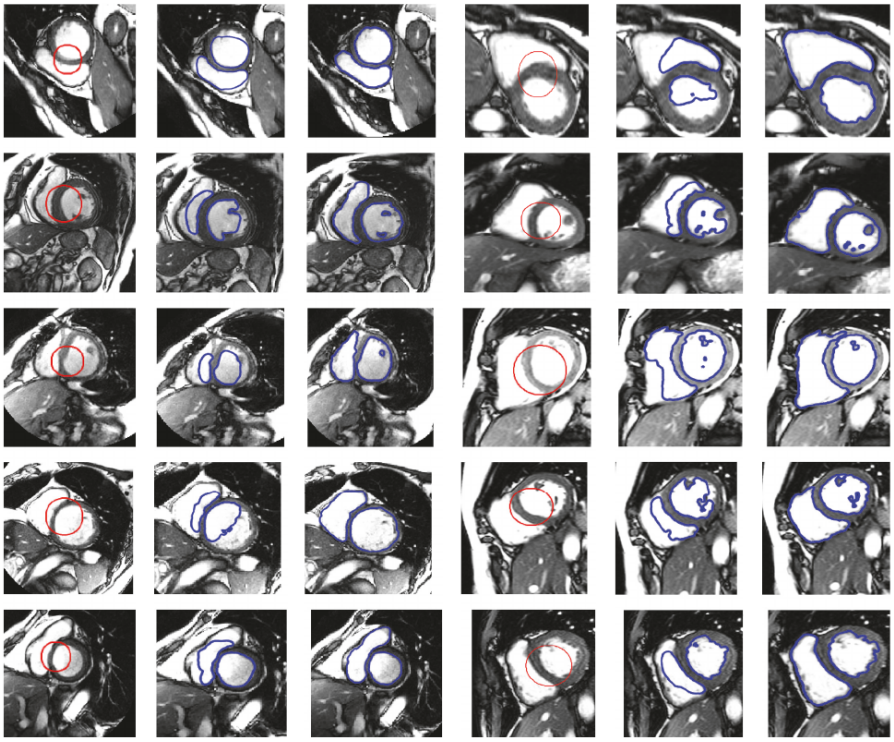

Figure 3.4: Region-based ACM segmentation of the left and right ventricles by Soomro et al. [161] (Image source). Figure shows (by columns from left to right): original slices from MICCAI 2012 database [143] with the initial contour (first and fourth columns); intermediate results (second and fifth columns) and the final resulting contours (third and sixth columns)

Our previous approach for heart segmentation [102] used Perona-Malik nonlinear diffusion [142] in pre-processing phase for edge enhancement and noise removal. The segmentation is performed in the enhanced image, where the detected boundary serves as a mask for the original image. An example is shown in Figure 3.3. We also proposed additional noise removal approaches [97, 98] to improve the segementation results.

Approach proposed by Koopert et al. [88] combined the traditional active contour method with feature function based on Lorenz et al. approach [105] for the epicardial and endocardial atrial wall segmentation. Daoudi et al. [39] presented an automatic segmentation method of the left atrium based on active contour model with gradient vector flow (GVF). The gradient vector flow (GVF) was proposed by Xu and Prince [186, 187] as an improvement of the traditional ACM when handling the convergence in the concave regions. Through the GVF, Daoudi et al. introduced a new external force which defines a vector diffusion equation in order to diffuse the gradient of the edge map extracted from the image. The initialization in their approach is per-

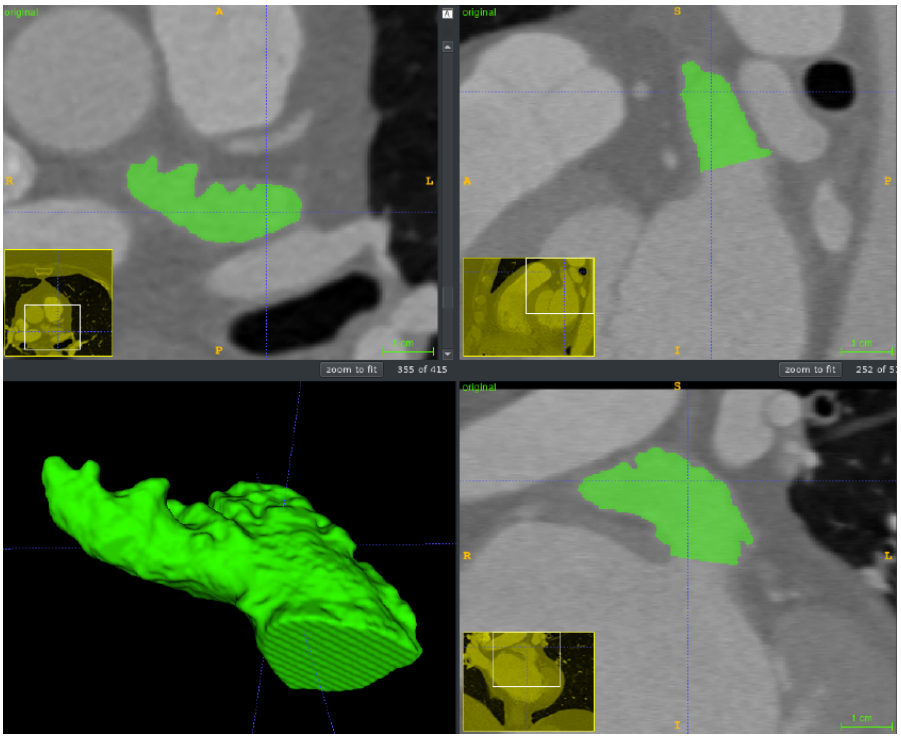

Figure 3.5: Interactive segmentation of the LAA using the ITK-SNAP software package. Initial segmentation was performed using the Snakes algorithm implemented in the ITK-SNAP package. The refinement was performed using the paintbrush tool.

formed after the pre-processing step which performs the adaptive histogram equalization. In their approach the proposed gradient vector flow (GVF) is one of the main driving forces which attracts the model to the enhanced borders in the equalized image.

3.1.2 *Geodesic active contour model*

In their seminal work on geodesic active contours, Caselles et al. [27, 28] introduced the idea of the Euclidean curve shortening and the use of level sets for the contour evolution. The main advantage of this approach is the implicit parameterization which can automatically handle the changes in the topology. Their use of geometric flow for the deformation of the curve was subsequently adapted by Sethian et. al. [3, 159]. This combination of the level set representation, combined with the geodesic active contours, has become the basis for a large number of segmentation methods [30, 138, 139], some of which will be explained in more detail in the next section.

Appleton [7] proposed a method for the automatic left ventricle segmentation using geodesic active contours by selecting the closed curves in every slice which are most likely to identify the myocardium.

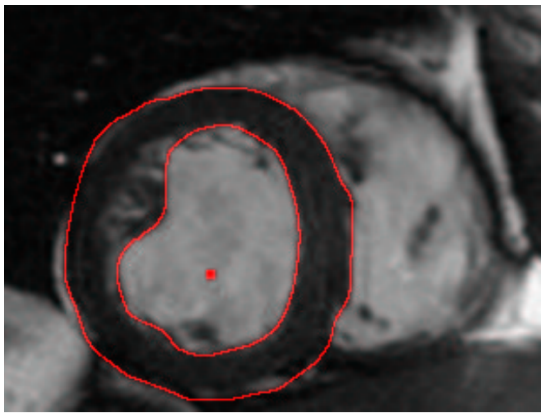

Figure 3.6: Geodesic active contour-based left ventricle segmentation Image source: Appleton et al. [7].

Figure 3.6 shows the segmentation result in one MRI slice. While the method segments clear borders exceptionally well, the strength of the approach is in handling the indistinct fuzzy boundaries and background clutter. The main source of error is the inclusion of papillary muscle fibers.

Finally, widely used in the medical imaging community is the work of Yushkevich et al. [194, 195]. Their work on the ITK-SNAP software package (Figure 3.5) represents one of the most widely distributed implementations of the geodesic active contours in a software package. The ITK-SNAP package was also used by our medical experts for all ground truth segmentations.

3.1.3 *Chan-Vase model*

The contour evolution in the classical active contour models is constrained by the image gradient. Thus, such methods work best for the objects where edges are defined by image gradients. In order to accommodate for this limitation, the seminal work of Chan and Vese [30] introduced an active contour model without stopping edge function. Their approach uses the Mumford-Shah functional [127] for controlling the evolution of the contour. Simply stated, the Mumford-Shah functional handles differently the smoothness of the region at object boundary and the smoothness of the region outside the boundary, allowing the segmentation of object with weak edges.

One direct application of the Chan-Vese model to the heart segmentation is proposed by Kang et al. [81]. Their approach segments the left and right heart from the image in several steps: first it detects the volume of interest in the preprocessed image (smoothing), next it determines the seed points by geometric analysis using the prior anatomical knowledge of the heart, and then the coarse segmentation

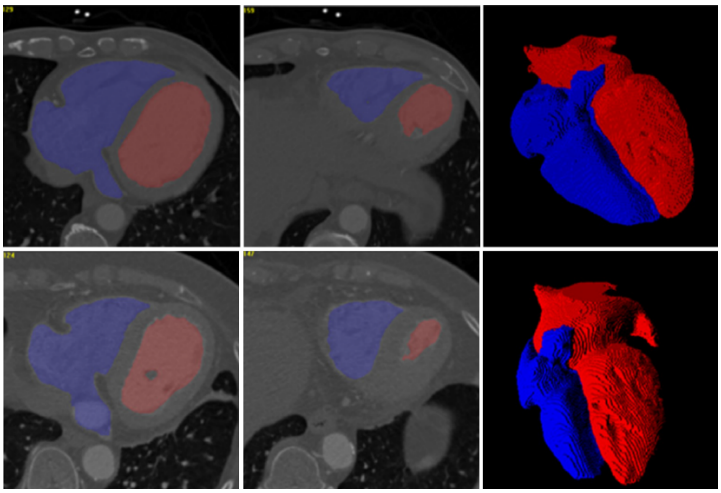

Figure 3.7: Whole heart segmentation in CT images using the Chan-Vese active contour model. Image source: Kang et al. [81].

using the power watershed segmentation separates the left from the right heart. Finally, the active contour model without edges refines the coarse segmentation. Figure 3.7 shows the segmentation results. Similar approach for whole heart segmentation is proposed by Rousseau and Bourgault [152].

3.2 GRAPH TECHNIQUES

Variety of graph techniques for image segmentation have been proposed during the years, some of which are graph-cuts, minimum spanning trees, shortest path etc. Graph-cuts techinque, commonly used for the segmentation in medical images, was originally introduced by Greig et al. [60]. The adaptation of the method by Boykov and Jolly [19, 20] introduced graph optimization algorithm as the combination of max-flow and min-cut. The adaptated is commonly used for boundary and region segmentation in N-dimensional data. The starting goal of the method was to automatically identify the object (marked by one or more seed points) from the background. The background contains hard and soft constrains to obtain the information about the region.

The requirement for the initialization with seed point prevents the graph-cuts method (in its original form) from being fully automatic. However, medical image segmentation methods often deterime seed points according to the prior anatomical knowledge. Very efficient approach for fully automatic whole heart segmentation using graph-cuts technique is proposed by Funka-Lea [54]. Their approach determines the seed points within the heart by computing the weighted volumetric barycenter. The determined seed point is then used by the

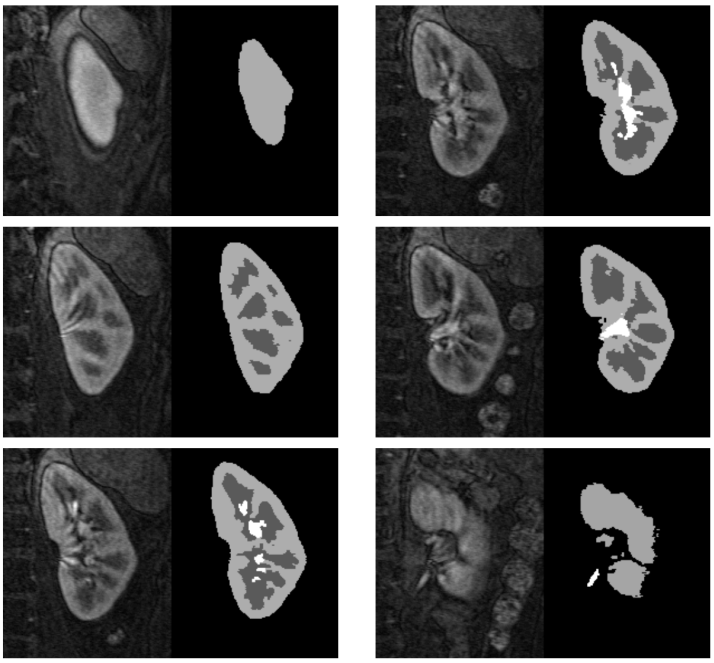

Figure 3.8: Graph-cuts based kidney segmentation in 3D angio MRI. Image source: Boykov et al. [20].

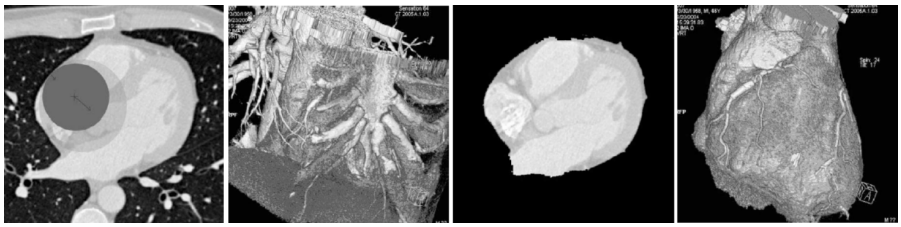

Figure 3.9: The graph-cuts based segmentation of the whole heart. Figure shows the expansion of the balloon within the heart. From left to right: initialized balloon, original heart volume, inflated balloon and resulting segmentation. Image source: Funka-Lea et al. [54].

graph-cut algorithm to determine the ellipsoid of the maximum volume (called the *balloon*) containing the heart region. The segmentation is performed by inflating the balloon and limiting its inflation where it touches the heart wall. The segmentation stops when the balloon cannot be inflated any further. Results of whole heart segmentation proposed in [54] are shown in Figure 3.9.

Grosgeorge et al. [61] proposed the method based on a statistical shape model obtained with principal component analysis (PCA). This approach presents the shapes of the RV with distance maps to their contour. The use of distance maps improves the performance of the landmark detection and matching. The method computes the PCA to describe the shape variations. The user registers the resulting shape model onto the image and the graph-cut refines the segmentation. Figure 3.10 shows the resulting segmentation in several MRI slices.

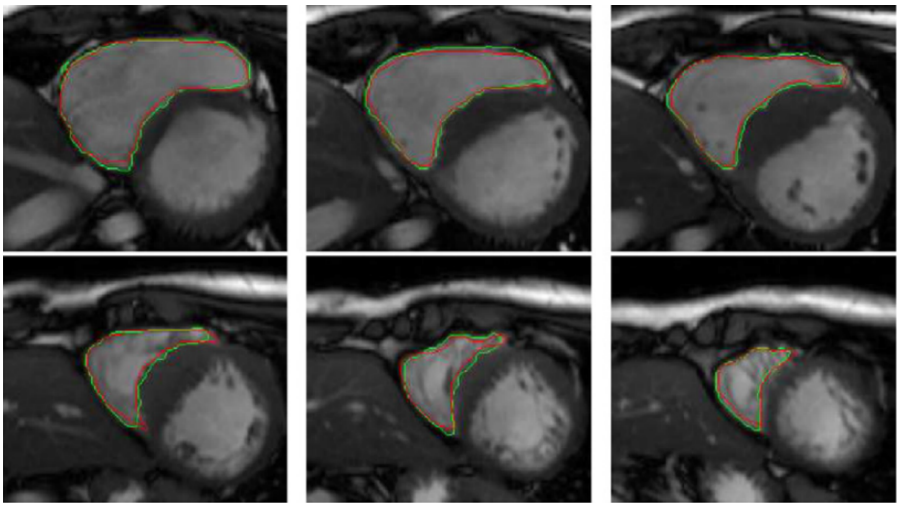

Figure 3.10: Graph-cuts for the purpose of right ventricle segmentation in MRI image. Image source: Grosgeorge [61].

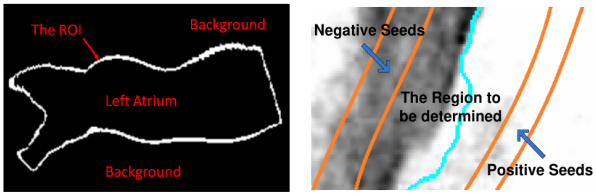

Figure 3.11: Seed placement for graph-cuts based refinement of the LA segmentation. Left: The detected region of interest (ROI) of the left atrium. Right: distribution of positive and negative seeds in the image. Image source: Yang et al. [189].

Similar method was proposed by Jolly [78] for the segmentation of the left ventricle. This method works on both CT and MRI images. Deng et al. [40] adapted the approach for the segmentation of the aorta.

The graph-cuts method can also be used for the segmentation refinement. Yang et al. [189] used the graph-cuts approach to refine the already segmented left atrium in C-arm CT images. First, the left atrium was segmented using the Marginal Space Learning approach (described in detail in section 3.4.4), then the region growing method was used for construction of graphs within the regions of interest. Finally, the graph-cuts optimization segments the voxels missed by the previous algorithm. Newly segmented voxels are assigned to different parts of the left atrium. Usually the graph-cuts methods are computationally expensive, but Yang et al. achieved the average runtime of 5 seconds with the described algorithm. Figure 3.11 shows the automatic seed placement for graph-cuts refinement of the LA. Figure 3.12 shows the results pre- and post-refinement.

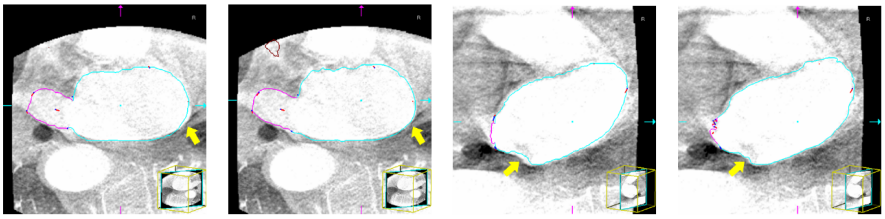

Figure 3.12: Segmentation result before and after graph-cuts based refinement of the left atrium segmentation. Image source: Yang et al. [189].

3.3 MODEL-BASED SEGMENTATION TECHNIQUES

Model-based segmentation techniques can be thought of as a group of techniques where the segmentation approach is based on using a predefined geometric model. The methods deform the model to match the locations of the extracted image features. Usually the first step for this type of method is the creation of the geometric model from the set of training data. In the next step the created model is matched to a new image. Being created from the training data, the model usually encapsulates some prior knowledge about anatomical structures which have to be segmented. The matching of a model to the new image is performed by a parametric deformation, in order to match the model to the detected features of the image. Thus, the goals of the model-based techniques are twofold: (1) extraction of features from the image and (2) generating the model with the best fit to the extracted features. Deforming the model to match the new image can be seen as an optimization problem, where the goal is to find the best model parameters for a given image.

We divide the deformation strategy into two main categories: techniques modifying the model shape parameters (deformable models), and techniques deforming the shape's embedding space (registration).

3.3.1 *Active Shape Model*

The Active Shape Models (ASMs)-based methods employ an iterative algorithm to detect the object of interest in an image. The iterative algorithm is similar to the one used in active contour models, but instead of evolving a contour, here we evolve a predefined model. Additionally, ASMs can only deform to fit the data consistent with the training set data [37].

Let vector of shape parameters $\mathbf{b}$ describe the object in an image, transforming it from model coordinate frame to the image coordinate

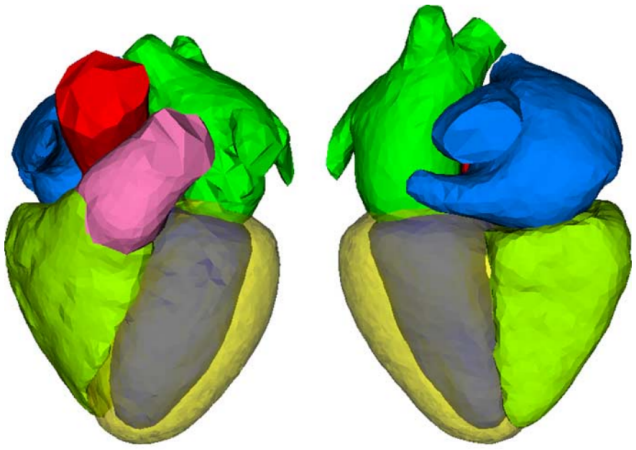

Figure 3.13: Visualization of the surface of the mean mesh prior to deformation. Image source: Ecabert et al. [47].

frame. Let T be the transformation function. The position of the model points $\mathbf{X}$ in the image can be defined as:

$$\mathbf{X} = T_{\mathbf{X_t Y_t \Phi s}}(\overline{\mathbf{X}} + \mathbf{\Phi b}) \tag{3-5}$$

where $\mathbf{X_t}$, $\mathbf{Y_t}$, $\mathbf{\Phi}$ and $\mathbf{s}$ are shape parameters which describe similarity transformation, orientation and scale of the points, respectively.

The iterative deformation algorithm performs the fitting in three main steps:

1. For each point of the model X_i, search the neighborhood pixels around the point and find the best match for $X_i^{'}$;
2. Update the shape parameters according to 3-5, determining the best fit to the newly found points;
3. Repeat until convergence.

Points of the model do not have to be placed on the locally strongest edge. Instead, they can represent a weaker secondary edge or some other image structure. This can often complicate the matching process. There are three most often used approaches for matching which can handle this problem. We can either build statistical models of the image structure around the point, we can find the points which most closely match the points from the training set model, or we can treat the matching as a classification task.

A fully automatic model-based segmentation approach was proposed by Ecabert et al. [46, 47], which introduced the progressive increase in the deformation degrees-of-freedom, increasing segmentation accuracy and improving the convergence. Additionally, they replaced the commonly used PCA-based initialization step with the piecewise affine transformation. The model used for the method was

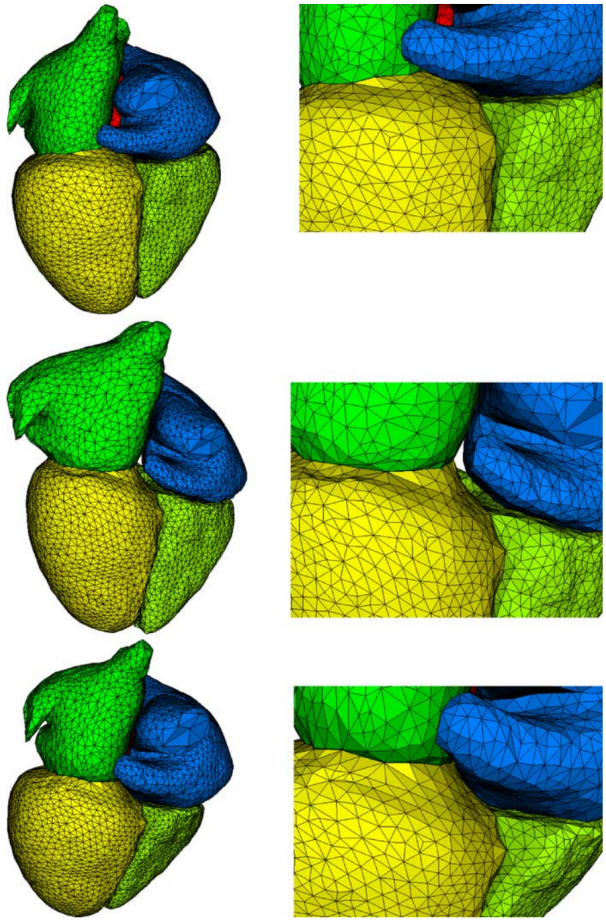

Figure 3.14: Vertex distribution in the mesh of the four-chamber heart model. First row shows the mean mesh prior to deformation, while second and third rows show the model after fitting to CT datasets. Models were deformed with piecewise affine transformation. The meshes remain regular even after the deformation. Image source: Ecabert et al. [47].

constructed as a four-chamber heart model, created from manually segmented ground truth images. Figure 3.15 shows the flowchart of the proposed segmentation method. An improvement to the method was proposed in [48], where the segmentation using the four-chamber heart model was improved by adding meshes of the great vessels to the original model. First, the main heart region of interest was detected using the generalized Hough transform. Afterwards, the method performs segmentation by adapting the four-chamber heart model to the chambers in the extracted region of interest using the ASM. Figure 3.16 shows the results of the segmentation using the proposed method.

The work of Zhao et al. [196] proposed the improvements to the standard ASM approach in terms of outliers sensitivity by using RANSAC [51] for the robust transformation estimation. Their work

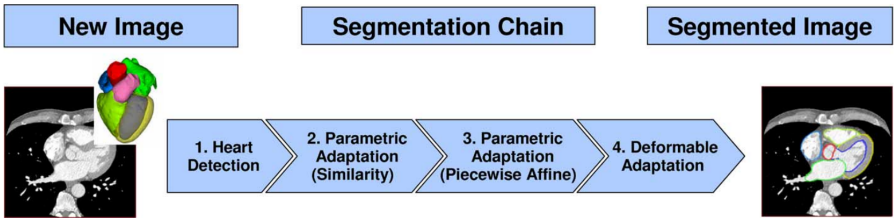

Figure 3.15: Automatic model-based segmentation flow example. Image source: Ecabert et al. [47].

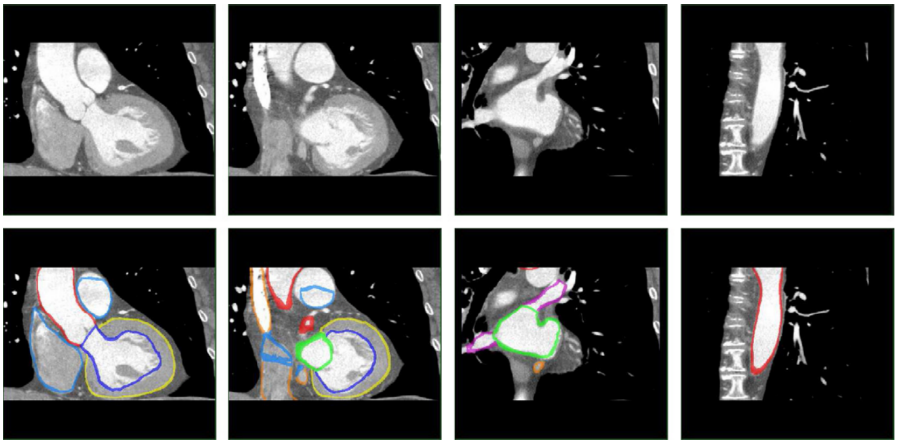

Figure 3.16: Segmentation results of the four-chamber heart model-based segmentation method. Image source: Ecabert et al. [48].

also introduced active contour-based model deformation called Shape-constrained Active Contour (SAC). The SAC evolves the model as if it were a contour, while retaining the prior knowledge about the shape of the model.

Ordas et al. [134] proposed a method for heart segmentation based on ASM which is able to perform automatic delineation of the training set, overcoming common practical limitation in building statistical shape models. Inspired by work of Rueckert et al. [153] they used algorithm based on free-form deformations (FFDs) and normalized mutual informations (NMIs) as shown in Figure 3.17. The model building algorithm has shown to be convergent, but suffered from severe performance penalties. Both the required computational time and the processing power were high. Ma et al. [112] proposed the use of Haar classifier for the localization of the heart ROI in input images. This approach treats the matching as a classification task, where the pre-built ASM is initialized on the detected ROI.

Finally, the work of Fritz et al. [52, 53] extracts the left ventricular functional parameters from the prior segmentation, obtained with region-growing. Figure 3.18 illustrates the workflow of the method [52]. The center of the ventricle coordinate system and the z-axis (Figure 3.18a) are determined from the pre-processed region-growing

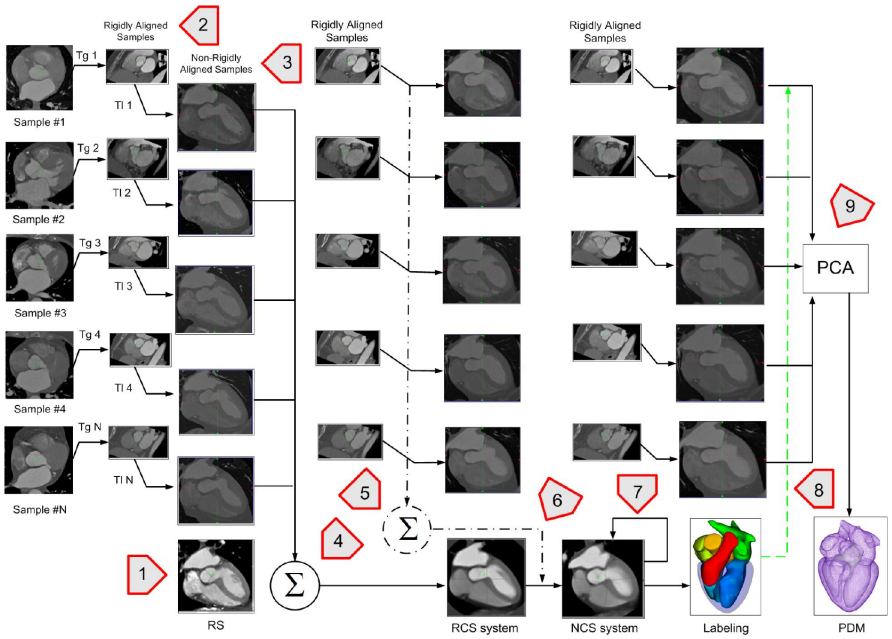

Figure 3.17: The algorithm for the shape model construction. Image source: Ordas et al. [134].

segmentation of the LV. A model is placed in the ventricle coordinate system along the short-axis with the model points in parallel short-axis slices (Figure 3.18b). The model geometry uses 72 rays per short-axis slice (Figure 3.18c shows a simplified view with only 4 rays per slice). Model points are in spherical coordinates at the base and the apex. Fitting of the model is based on local gray values along the rays in the model. The resulting segmentation is shown in Figure 3.18d. The novelty of their approach in [53] is in concatenating models of left and right ventricle into a single vector, and in turn segmenting both chambers simultaneously. This concatenation demonstrated superior results than segmenting each chamber independently.

3.3.2 *Active Appearance Model*

The concept of Active Appearance Models (AAMs) is an extension of Active Shape Model (ASM) which takes into account the texture information in the image. The concept was first introduced by Cootes et al. [35, 36]. The main advantage of the AAM over ASM is in the fact that the ASM is scanning only lines when searching for the best match, while AAM searches the complete volume. The additional information contained in the texture of the image results in improved fitting accuracy. However, this additional information results in the significant increase in computation time.

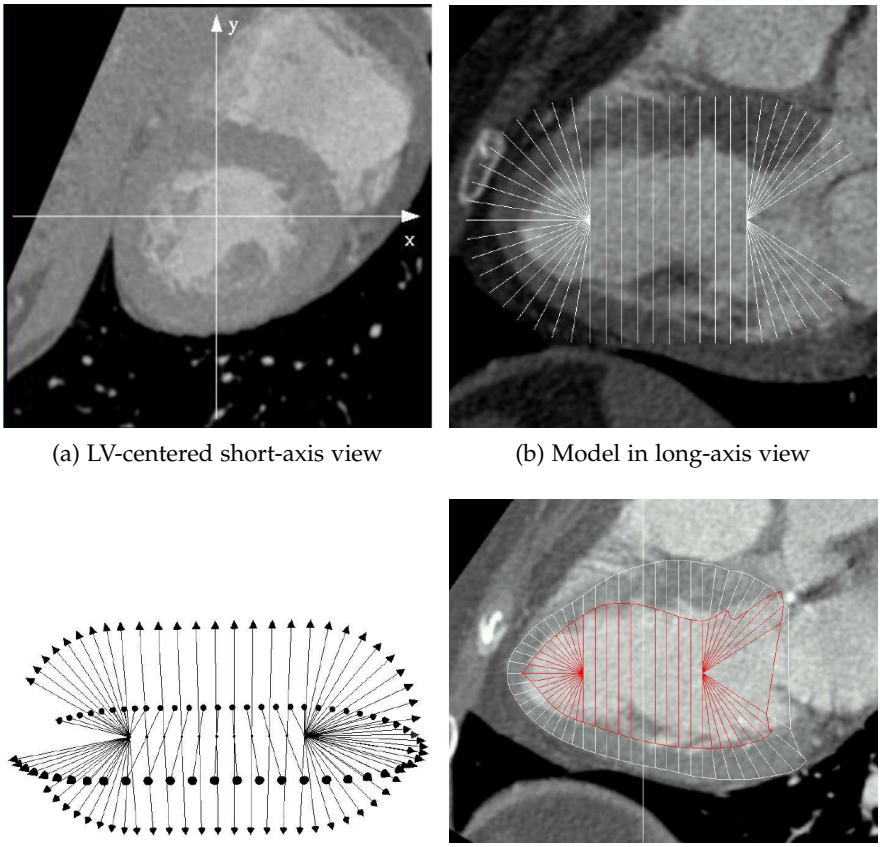

(a) LV-centered short-axis view

(b) Model in long-axis view

(c) Model

(d) Resulting fit in long-axis view

Figure 3.18: Segmentation of the left ventricle using the ASM fitting with prior region-growing pre-processing step. Image source: Fritz et al. [52].

The AAMs treat the matching as an optimization problem where the main objective is to minimize the difference between a new image and the training set model image. A difference vector is defined as:

$$\delta \mathbf{I} = \mathbf{I}_i - \mathbf{I}_m \tag{3-6}$$

where $\mathbf{I}_i$ represents a vector of intensity values in the new image and $\mathbf{I}_m$ represents a vector of intensity values of the current image model. The quality of the match is represented with the magnitude of the difference vector, defined as:

$$\Delta = |\delta \mathbf{I}|^2 \tag{3-7}$$

Finding the best match between the new image and the model is performed by minimizing the value of Δ.

Originally, AAMs were only defined in two-dimensional domain, but the work by Mitchell et al. [124] generalized it to three-dimensional spaces. The work of Stegman and Pedersen [163] introduced the bi-temporal model which could calculate the left ventricular ejection

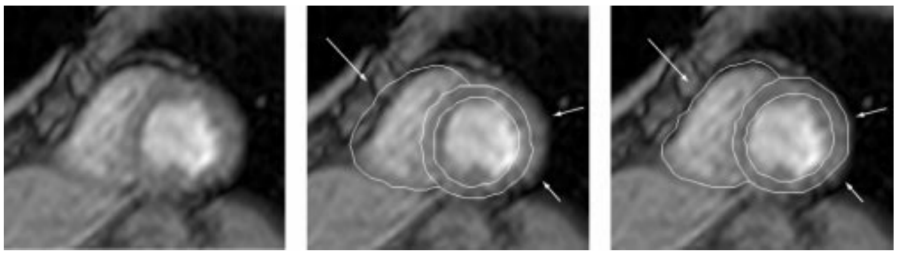

Figure 3.19: Model fitting using the conventional AAM and multistage hybrid ASM/AAM approach. Left: Original slice. Middle: Conventional AAM results in a good gray level appearance fit, but the border positioning accuracy is low (arrows). Right: Multistage hybrid ASM/AAM demonstrates a significant improvement in the accuracy. Image source: Mitchell et al. [123].

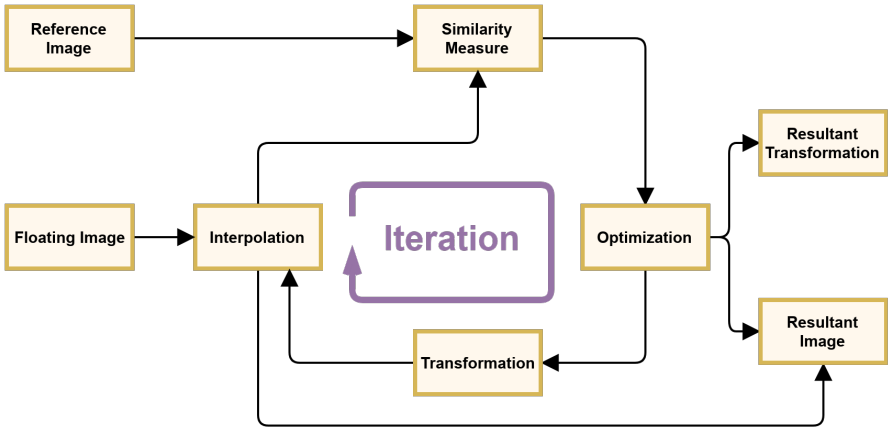

Figure 3.20: Flowchart of the registration process.

fraction (LVEF). The model combines the shape and the appearance information from the end-diastole and end-systole phases. The LVEF calculations are performed on the subsampled data (128x128 pixels), due to the computational complexity of the model. Finally, Mitchell et al. [123] introduced a combined approach which incorporates the advantages of both the ASM and the AAM. The approach is developed as a multistage framework in which AAM guaranteed better convergence while ASM improved boundary segmentation. Comparison of the hybrid approach results compared to the conventional AAM is shown in Figure 3.19.

3.3.3 *Registration and Atlas-based Segmentation*

Image registration represents the process of mapping points in one image (floating image) to equivalent points in another image (reference image) [154]. In the context of medical images, the mapping between equivalent points means the mapping between the points in the same

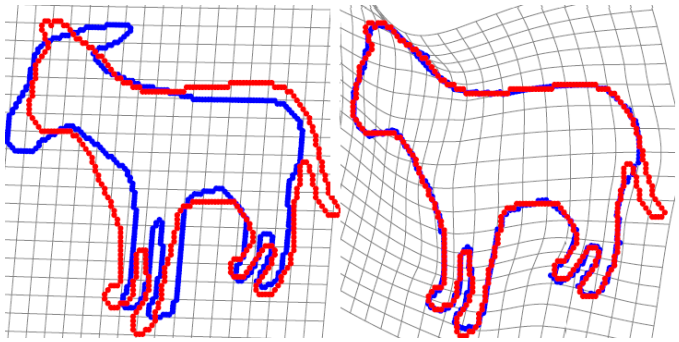

Figure 3.21: Illustration of the registration process. The process finds a transformation of the image space such that the transformed image spatially corresponds to the reference image. Image source: Rouhanni et al. [151].

anatomical position. Image registration process is shown in Figure 3.20. The registration process is an iterative approach searching for the best transformation of the floating image which maximizes the similarity between the reference image and the floating image. The cost function calculates the similarity between the *transformed image* (interpolated floating image after transformation) and the reference image, i.e. the quality of the mapping. The similarity between the reference image and the transformed image is directly affected by the transformation model and the interpolation method. The optimization method guides the search for the transformation which provides the best mapping (highest similarity) between the two images. Figure 3.21 illustrates the registration process.

Most often used interpolation methods are nearest-neighbour, linear and B-spline interpolation. The accuracy of the chosen interpolation method is in the direct relation with the computational cost of the method. Nearest-neighbour interpolation is computationally the fastest while being the least accurate method. On the other hand, the B-spline interpolation is the most accurate while being the most computationally expensive method. Linear interpolation provides a good trade-off between the two requirements.

Transformation model estimates the spatial difference between the images. We can divide them according to their most important characteristic – linearity – into three groups: linear, non-linear and locally affine transformations. Linear transformations maintain the global shape of objects in the image. Depending on the number of degrees of freedom (DOFs), we can divide the linear transformations for three-dimensional problems into following groups:

1. *rigid transformation* defined with six degrees of freedom,
2. *similarity transformation* defined with nine degrees of freedom, and

3. *affine transformation* defined with fifteen degrees of freedom.

The linear transformations are computationally efficient, but provide limited accuracy for images with local deformations.

Non-linear transformations (also called non-rigid or deformable) can handle objects with local deformations due to a much higher number of degrees of freedom than the linear transformations. However, higher number of DOFs directly results in a drastic increase in the computational complexity, making the registration process a time-consuming and computationally demanding task.

Locally affine transformations combine the advantages of both linear and non-linear transformations. This type of transformation is actually a set of locally defined rigid transformations. Thus, the interpolation can be calculated directly for the regions where the transformations are defined. However, for regions where the transformations are not defined, the interpolation should be calculated according to a set of local transformations close to that region. Mathematically, the locally affine transformations model can be defined as:

$$T(x) = \begin{cases} G_i(x), & x \in V_i, i = 1 \dots n \\ \textbf{interpolate}\{G_i(x_i) | i = 1, \dots, n\}, & x \notin \bigcup_{i=1}^{n} V_i \end{cases} \tag{3-8}$$

where $\{G_i\}$ are local affine transformations which are describing the local regions $\{V_i\}$.

Similarity measurement methods can be thought of as methods that quantify the *quality* of the transformation by determining the similarity between the reference image and the transformed image. Most common methods are methods based on the intensity values in the image, for example: mean of squared intensity difference, cross-correlation and mutual information (MI).

Finally, the most common optimization methods are Powell's conjugate gradient ascent/descent method and gradient ascent/descent method [146], with a regularization scheme for advancing each iteration step as described in [87].

ATLAS-BASED SEGMENTATION Previous paragraphs explained the workings of the registration process. Let us now explain how the registration can be used to perform the segmentation. The anatomy of the heart, while varying between the patients, has a certain regularity, meaning that the location of certain parts of the heart follows the same pattern between the patients. We call the knowledge of those patterns *a priori knowledge*. Explicitly incorporating the a priori knowledge into the developed segmentation methods is not trivial. The atlas-based segmentation is basically the segmentation process which uses a priori knowledge of the heart by treating it like a registration problem. The

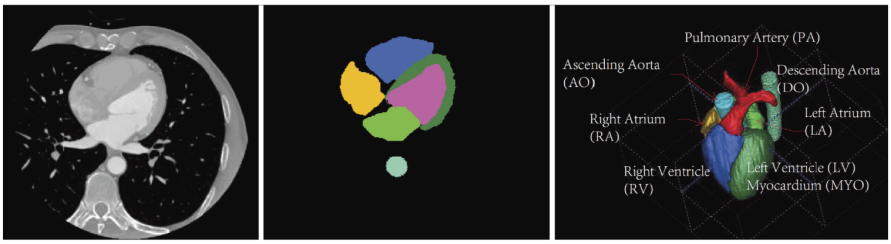

Figure 3.22: Representation of an atlas. Left: original slice, middle: desired anatomical regions are labeled – creating a slice of atlas based on the original slice, right: 3D visualization of the whole atlas. Image source: Zhuang et al. [207].

atlas is a combination of a medical image and a label map, where medical experts label (usually manually) certain anatomy in the original image. The labels now incorporate the a priori knowledge without encoding it in explicit rules. Figure 3.22 shows an example atlas.

The basic algorithm for segmenting a previously unseen medical image using an atlas-based method consists of three basic steps:

1. Register a new unseen image to the atlas. This step computes "a dense deformation field that puts the atlas into a point-to-point spatial correspondence with the target image" [9]. The spatial locations of the desired anatomy in the registered (also called transformed/deformed) image now correspond to the spatial locations of the desired anatomy in the atlas.

2. Propagate the labels from the atlas to the registered image. The registered image now contains the segmentation labels for the anatomy labeled in the atlas.

3. Un-register the image, i.e. reverse the deformation field. This step brings the segmentation labels from a spatial correspondence with the atlas to a point-to-point spatial correspondence with the input (unseen) image.

Even though the general algorithm is relatively simple, for the purpose of cardiac segmentation a lot of edge cases have to be covered. Some of them have already been mentioned, one of them being the inability of registration to handle local deformations in images. A lot of work has been published in the area of atlas-based cardiac segmentation in the recent years.

Zhuang et al. [205] developed a single-atlas based segmentation framework using enhanced locally affine registration method (LARM). Their approach enabled the preservation of the relation of intensity between local regions by computing and optimizing a global cost function.

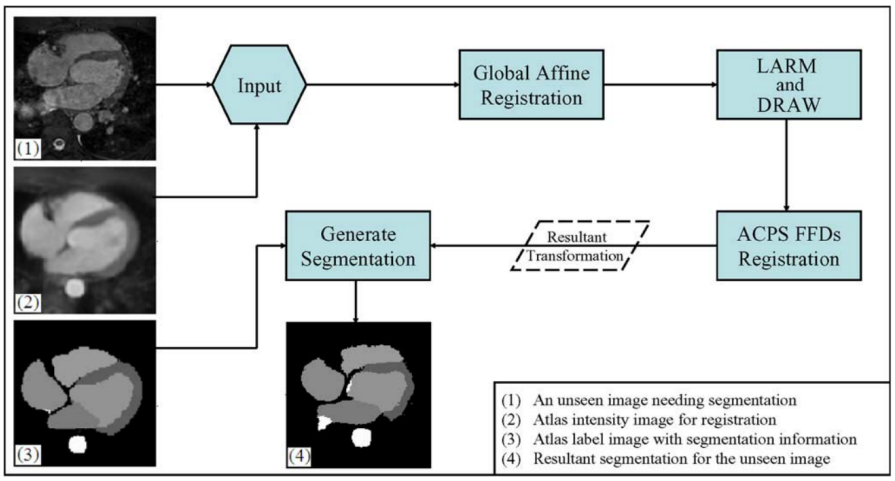

Figure 3.23: The framework for automatic whole heart segmentation based on atlas propagation. Image source: Zhuang et al. [206].

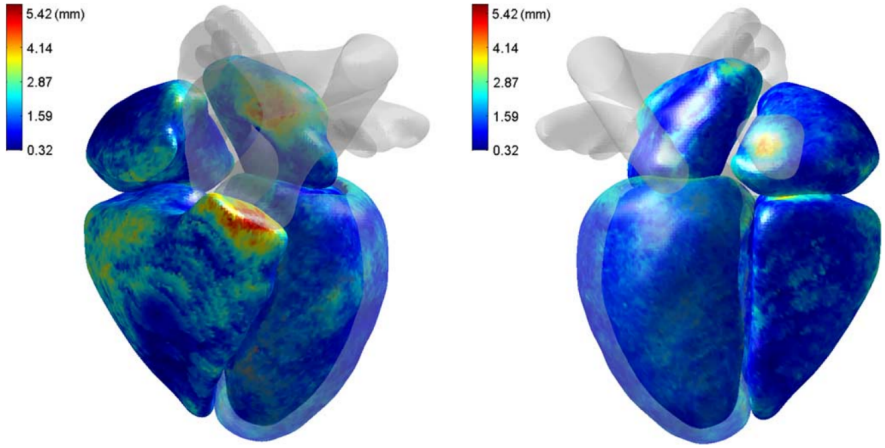

Figure 3.24: Two views showing the surface-to-surface segmentation error map. Image source: Zhuang et al. [206].

Their following improvement to the framework was the combination of the LARM approach with non-rigid transformation, published in [206], which performed the whole heart segmentation from MRI images. The approach implemented the non-rigid transformation using the free form deformations (FFDs) with adaptive control point status (ACPS). The LARM is used to initialize the cardiac substructures. With the new approach, the transformation globally deforms while local regions maintain their desired shape. This avoids the local optima during the optimization phase of the global transformation. After the successful initialization, the approach applies the ACPS FFDs registration to refine the local details. The main advantage of this approach is the ability to avoid myocardial leakage.

The last iteration of the framework [207], published in 2015., can automatically segment the heart substructure and aorta using a priori

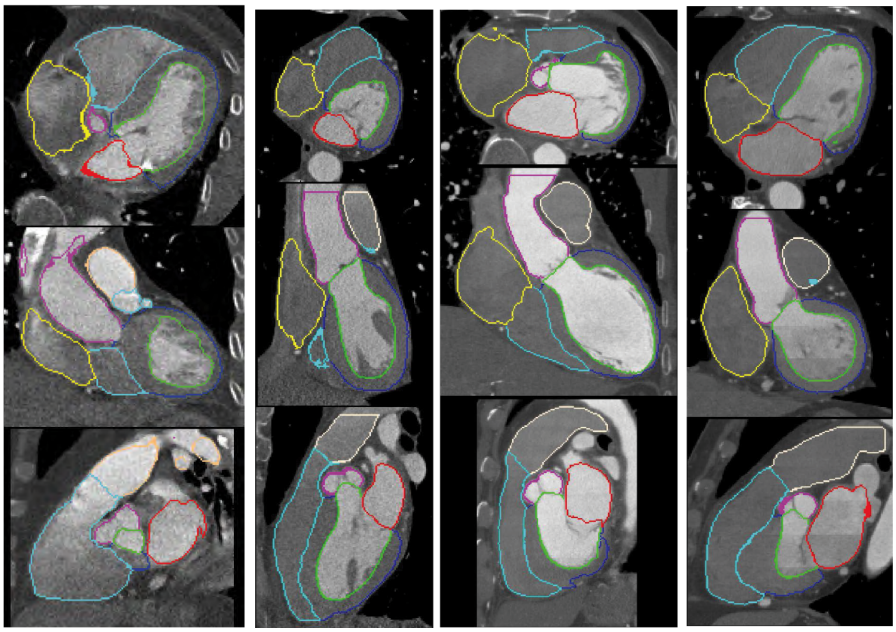

Figure 3.25: Performance of the multi-atlas segmentation (MAS) scheme proposed by Zhuang et al. Each column shows three-panel orthogonal view of a dataset. Two leftmost columns show two cases with the lowest Dice overlap for whole heart segmentation (WHS), while the rightmost two columns show datasets with median scores. Image source: Zhuang et al. [207].

anatomical information incorporated into initialization. This iteration of the framework can obtain sub-voxel segmentation accuracy as well as register local regions separately. The main limitation of this framework is the possibility of losing information about original geometrical relations, which increases the probability of the initialization step failing. Segmentation results obtained through the framework are shown in Figure 3.25.

Another approach for automatic whole heart segmentation using registration is proposed by Lorenzo-Valdes et al. in [106]. They employed a global affine registration for atlas initialization, while the fine-tuning of the details used non-rigid registration with a large number of degrees of freedom. Major disadvantage of the approach is the inability to generalize the atlas – every heart atlas can only be applied to a small number of similar images, with similar pathological data. Isgum et al. [72] proposed an approach for multi-atlas-based segmentation of the aorta and other cardiac structures. The approach introduced a concept of spatially varying weights, which estimate the success of local registrations. They also researched the possibility of reducing the computational costs by reducing the numbers of atlases.

A similar approach, introduced by Depa et al. [41], segments the left atrium with a label fusion algorithm [66]. The work of Van Rikxoort et

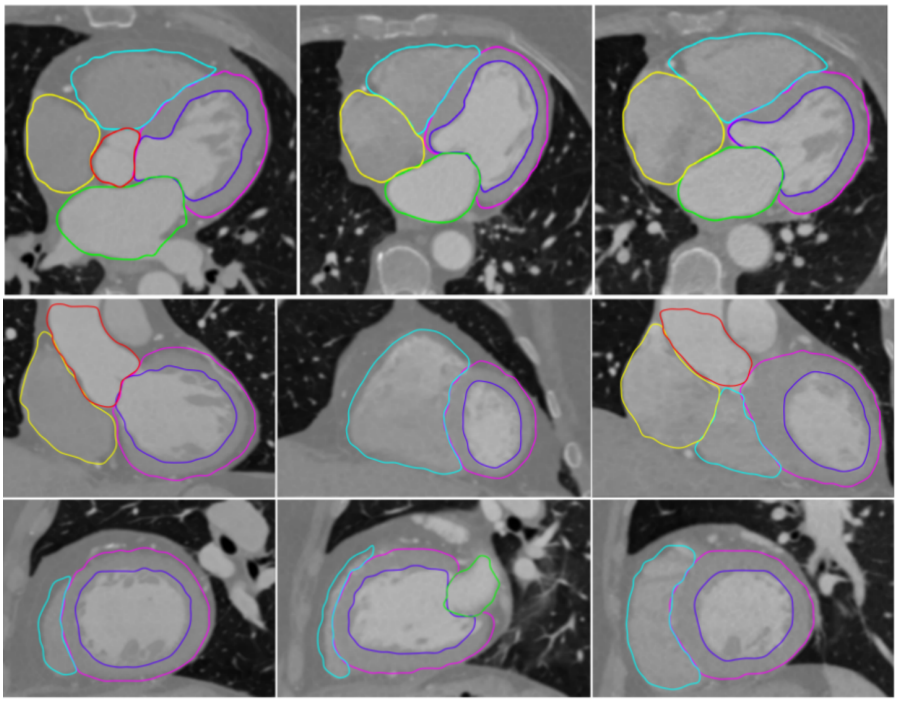

Figure 3.26: Aorta and heart multi-atlas segmentation. Image source: Kirisli et al. [86].

al. [212] introduced the automatic stopping criterion which stops registering atlases when it detects that no further improvement is possible. Multi-atlas registration approach developed by Kirisli et al. [86] uses the linear affine registration to align an image to an atlas. The result of the linear affine registration is used as an initialization for a B-spline registration. Figure 3.26 shows an example segmentation. Heinrich and Oster [67] developed discrete registration framework which improves the computational performance using continuous optimization. First, the framework linearly and nonlinearly aligns all training images to an unseen image. Afterwards, transformed segmentations from all atlases are weighted using their patch similarity.

Yang et al. [190] introduced three-step multi-atlas method for heart segmentation in CT images. First, they perform the heart localization on isotropic down-sampled images of both the patient and the atlas. The second step performs masking of the ROI and refines the segmentation using affine and B-spline registration. The third step re-runs the B-spline registration to refine the transformation from atlas to the patient's image. Finally, global fusion of the resulting segmentations generated by majority voting obtains the final WHS.

Left atrium segmentation approach proposed by Sandoval, Betancur and Dillenseger [155] used atlas-based registration followed by a region-growing step. The affine registration performed the coarse segmentation, while the region-growing step refined the segmentation

to the smallest anatomical details. Finally, another interesting approach for left atrium segmentation, similar to the Sandoval's approach, was proposed by Stender at al. [164]. The method works with both CT and MRI images, utilizing the ASMs initialized with the affine registration, followed by the atlas registration and a region-growing step.

3.4 CLUSTERING AND CLASSIFICATION TECHNIQUES

Clustering is a general technique used for dividing a set of data into a specific number of groups. Clustering is often considered an unsupervised learning strategy because it does not require explicit guidance. In the context of image processing, the clustering process groups (clusters) together image pixels of similar characteristic. The resulting clusters provide a segmentation of the image. Clustering techniques can be divided into several types:

- K-means clustering, often referred to as Hard C-means clustering [103, 113],
- mountain clustering [188],
- fuzzy C-means clustering [14] and
- subtractive clustering [31].

The K-means technique is still the most commonly used.

The term *classification* represents a technique where elements in a dataset (data observations) are assigned to one of the pre-determined classes (a label is assigned to each observation). Classification is considered a supervised learning strategy because the machine learns from already labeled (classified) data. Some of the most popular classification techniques are:

- K-nearest neighbors [5],
- support vector machines [38],
- decision trees [23],
- artificial neural networks [120].

With the advent of high computational capacity, the artificial neural network-based approaches have begun outperforming other techniques in a lot of tasks.

3.4.1 *K-means clustering*

K-means clustering algorithm tries to divide a set of data observations into k clusters, where each observation belongs to a cluster with

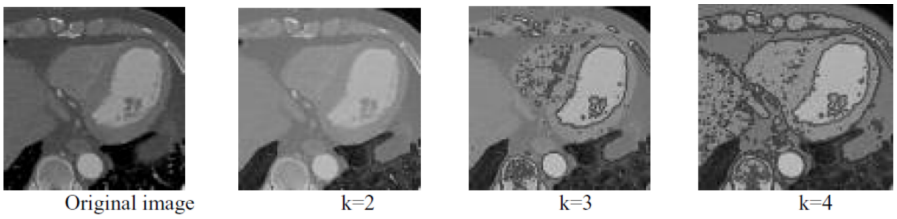

Figure 3.27: Heart segmentation using K-means clustering and graph-cuts. Image source: Yu-ke [192].

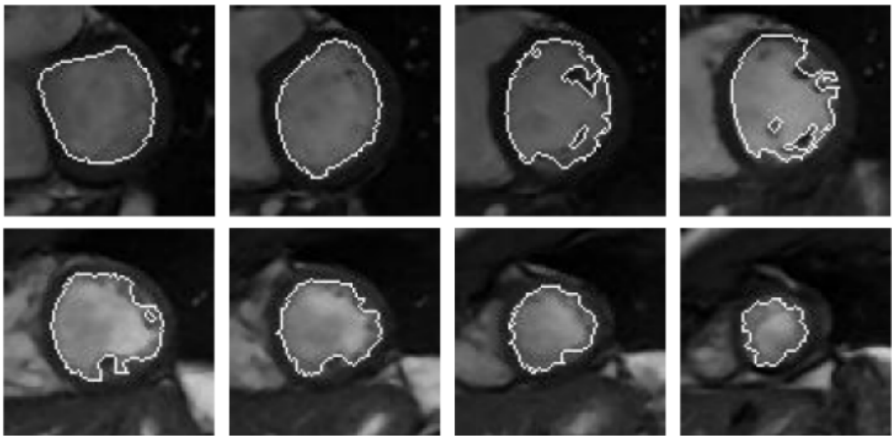

Figure 3.28: Automatic LV segmentation using K-means and graph searching. Image source: Lee [96].

the nearest mean. Clusters are defined by cluster centers. K-means algorithm tries to find cluster centers by minimizing the dissimilarity of data observations according to some cost function. Commonly used cost functions are often based on Euclidean distance. The centers of the clusters are iteratively refined until the cost function starts to converge.

The clustering approach by itself is rarely used for heart segmentation. It is mostly used as a pre-processing or pre-segmentation step. Yu-ke [192] proposed a heart segmentation method which combines the K-means clustering with graph-cuts approach. Figure 3.27 shows an example of the approach. Lee [96] proposed an automatic LV segmentation method based on K-means algorithm. The method consists of five steps: preprocessing and seed points estimation, creation of circular map via polar mapping, segmentation of the LV using K-means, graph searching to correct the errors of the K-means step, and finally inverse polar mapping to obtain the final segmentation. Figure 3.28 shows the results of the method.

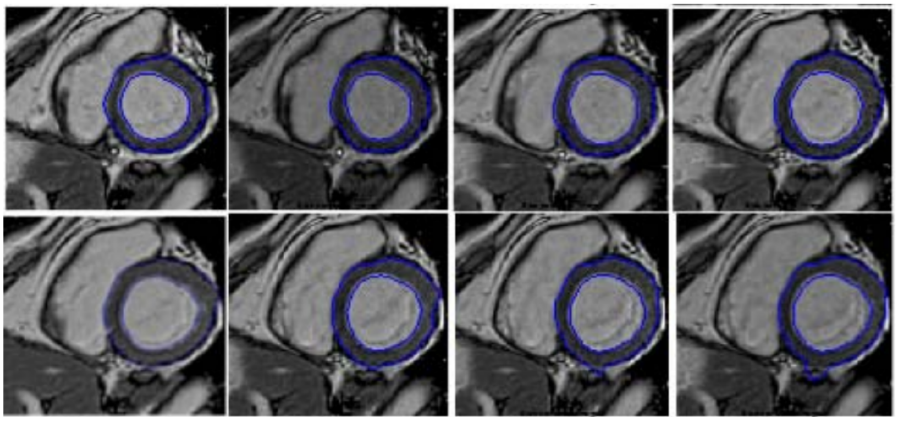

Figure 3.29: Automatic LV segmentation using graph-cuts and fuzzy C-means clustering. Image source: Wang [178].

3.4.2 *Fuzzy C-means clustering*

The basic idea of Fuzzy C-means clustering (FCM) is an adaptation of the K-means clustering, where the main difference is that in FCM an observation can belong to several clusters. The term *fuzzy* in the name refers to the fact that we attach a set of numbers (between 0 and 1) to each observation, representing a degree to which an observation belongs to each of the clusters. Thus, the observation can belong to several clusters at the same time with different degrees of membership (called the membership grade). The rest of the method is similar to K-means, with the clusters still being determined by minimizing a cost function. Still, the possibility of an observation belonging to several clusters can be beneficial for the design of heart segmentation methods. Wang et al. [178] proposed an approach for LV segmentation in MRI images which combines the FCM with the modified level set method. The level set method delineates the endocardium and estimates the bias field, which decreases the intensity inhomogeneity of the image. The combination of FCM and morphologic segmentation extracts the epicardium from the corrected image. The results can be seen in Figure 3.29.

3.4.3 *Random Forests*

Random forests algorithm, introduced by Breiman in [22], combines two earlier techniques: decision trees (also called classification and regression trees (CART)) [23] and bagging predictors [21]. Random forest classifier contains a number of decision trees and each tree is trained with a different subset of training data (bagging). The training samples are randomly assigned across trees for processing, with the samples passing through a tree from the root node to one of the leaf

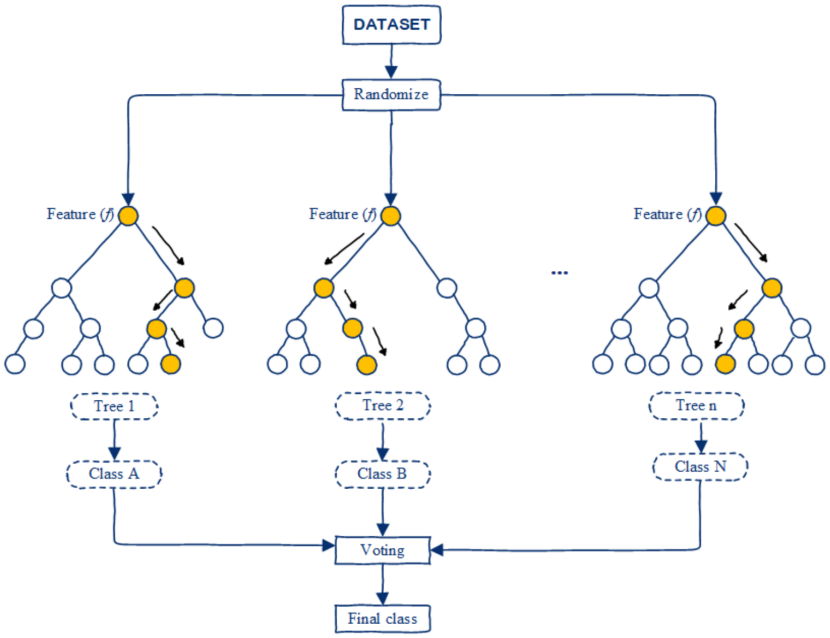

Figure 3.30: Data classification with random forests classifier. Image source: Breiman [22].

nodes. Upon entering the tree, in each node the sample encounters a binary test which compares a certain feature with a threshold. Node passes the sample to one of its children depending on the test, until the sample reaches a leaf. This concept is illustrated in Figure 3.30. Training forests helps with identification of a set of tests that are shown to best separate the data into training classes. The framework has demonstrated high performance and accuracy in a large number of general purpose classification tasks.

An example of adapting the framework to medical image segmentation was proposed by Mahapatra [114]. They proposed an automatic right ventricle segmentation method which combined superpixel segmentation [2] with random forests. First, the method determined the region of interest containing the right ventricle using the superpixel segmentation classified with random forests classifier. For the next step, the second set of random forest classifiers calculates probability values for all pixels in the determined region of interest. The calculated probability map is used as a penalty cost in the second-order Markov random-field [101] cost function. The final segmentation is obtained by optimizing the cost function using the graph cuts approach.

The work of Margeta et al. [116] used the random forests classifier to automatically segment the left atrium. Main novelty of the work concerns the reduction of training time by selective sampling of the voxels in the annotated training data. While the classifier was trained on all positive samples (voxels labeled as belonging to the LA), negative

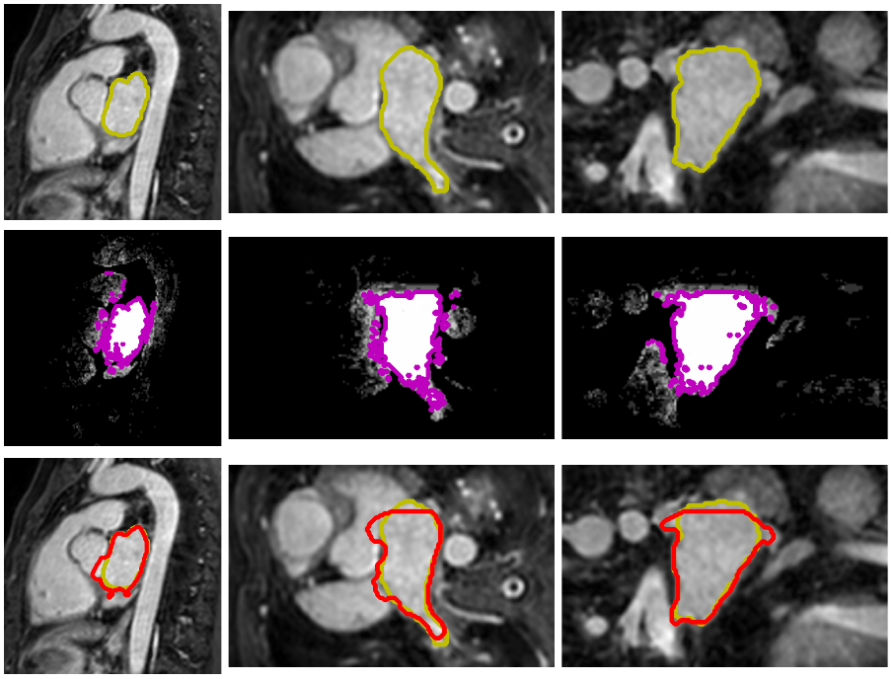

Figure 3.31: Coronal (left column), sagital (middle) and axial (right column) views of the segmentation results obtained with random forests based LA segmentation method by Margeta et al. Top row: original slice with ground truth overlaid in yellow. Middle row: atrial probability map where brighter values indicate higher probability (magenta contour = 0.6 probability). Bottom row: ground truth (yellow), final segmentation (red). Image source: Margeta et al. [116].

samples were sampled on a sparse regular grid. The final segmentation is obtained from an atrium probability map calculated for the whole volume. Figure 3.31 shows the probability map in the middle row, while Figure 3.32 shows the meshes of the final segmentation result. Main limitation of the method is a frequent misclassification of pulmonary veins.

3.4.4 *Marginal Space Learning*

Marginal Space Learning (MSL) is a generic learning-based method for efficient 3D object detection developed and proposed by Zheng and Comaniciu [198]. Here we describe the advantages of the MSL approach compared to standard approaches. Standard learning approaches for 3D object detection exhaustively search the nine-dimensional pose parameter space, since the anisotropic similarity transformation has nine degrees of freedom. The nine degrees of freedom are: three translation parameters, three rotation angles and three scales. The MSL achieves significant improvement in detection speed compared to full-space

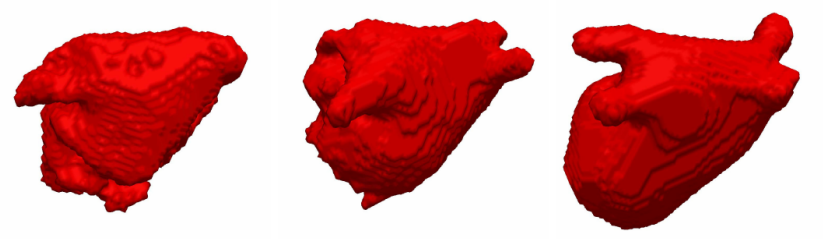

Figure 3.32: Visualization of the resulting atrial meshes obtained with the Margeta et al. method. Image source: Margeta et al. [116].

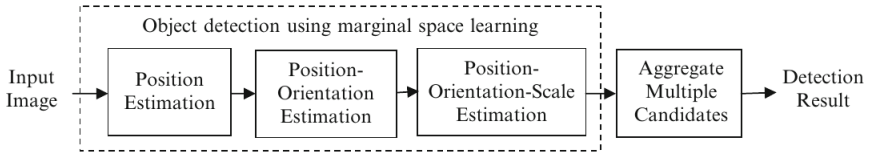

Figure 3.33: Marginal Space Learning parameter search steps. Image source: Zheng and Comaniciu et al. [198].

learning because the search is only performed in low-dimensional marginal spaces instead of the full-space exhaustive search. Parameter estimation is split into three steps: position estimation, position-orientation estimation, and position-orientation-scale estimation (as shown in Figure 3.33).

Each step increasingly narrows the search space, using a different estimator for each step. The first step (position estimation) uses an estimator trained to decide whether a position hypothesis represents a good estimate of the target object's position. The exhaustive search of the position marginal space (three-dimensional) finds a small number of best position candidates. The second step (position-orientation estimation) uses an estimator trained to decide whether a position-orientation hypothesis is a good estimate. The exhaustive search of the orientation marginal space, while searching for every position candidate retained in the previous step, finds a limited number of good position-orientation candidates. Finally, the position-orientation-scale candidates are found by using the position-orientation candidates to exhaustively search the scale marginal space.

Even though in each step the method performs an exhaustive search, only a small number of candidates are preserved for the next step. In each step the method prunes a large portion of the search space with low posterior probability, drastically increasing the efficiency. The MSL, compared to the exhaustive full-space search, can reduce the number of testing hypotheses by six orders of magnitude. The name Marginal Space Learning comes from the fact that the learning and detection is performed in a sequence of marginal spaces. Due to the pruning, the method can reliably detect a 3D anatomical structure

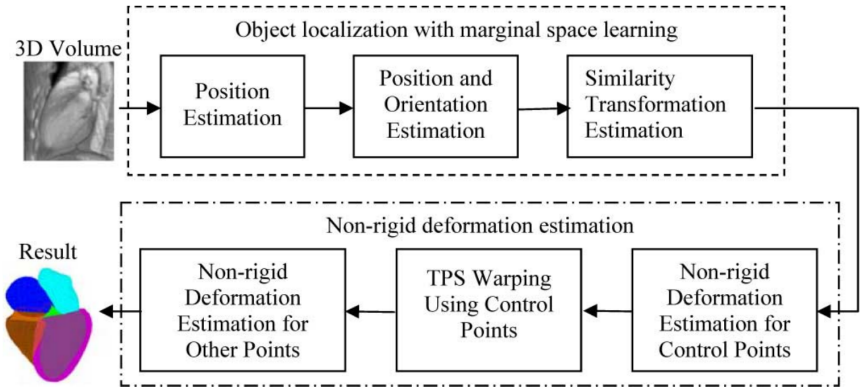

Figure 3.34: Marginal Space Learning-based whole heart segmentation framework. Image source: Zheng and Comaniciu et al. [197].

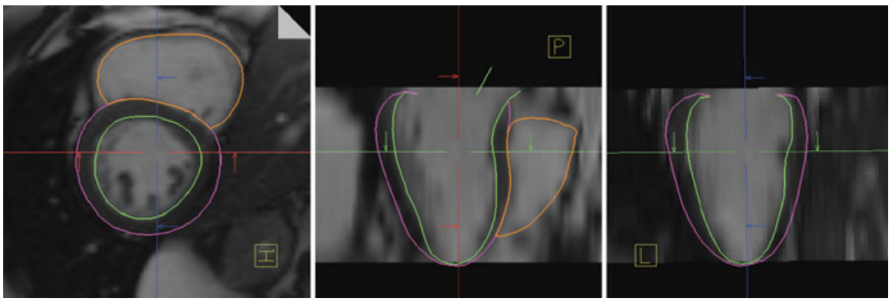

Figure 3.35: Left ventricle segmentation using Marginal Space Learning, in a method implemented by Lu et al. [108]. Image source: Zheng and Comaniciu [198].

with a speed of 0.1–0.5 s/volume on an ordinary personal computer (3.2 GHz duo-core processor and 3 GB memory) without the use of special hardware such as graphics processing units.

Some of the works using the MSL for initial segmentation have already been mentioned in this review. For example, the work by Yang et al. [189] presented an approach combining the MSL based ASM fitting with the graph-cuts refinement for the purpose of left atrium segmentation (Figures 3.11 and 3.12 in Section 3.2). Lu et al. [108] presented an MSL-based method for segmentation of the left ventricle in MRI images (Figure 3.35).

Marginal Space Learning-based approaches are capable of working in different imaging modalities. The MSL book by Zheng and Comaniciu [198] presents cases where the method is capable of handling the modalities such as X-ray fluoroscopy, 2D and 3D ultrasound, 2D and 3D MRI and 3D CT. Detailed review of the MSL approach is outside the scope of this thesis and the reader is referred to [198] for more information.

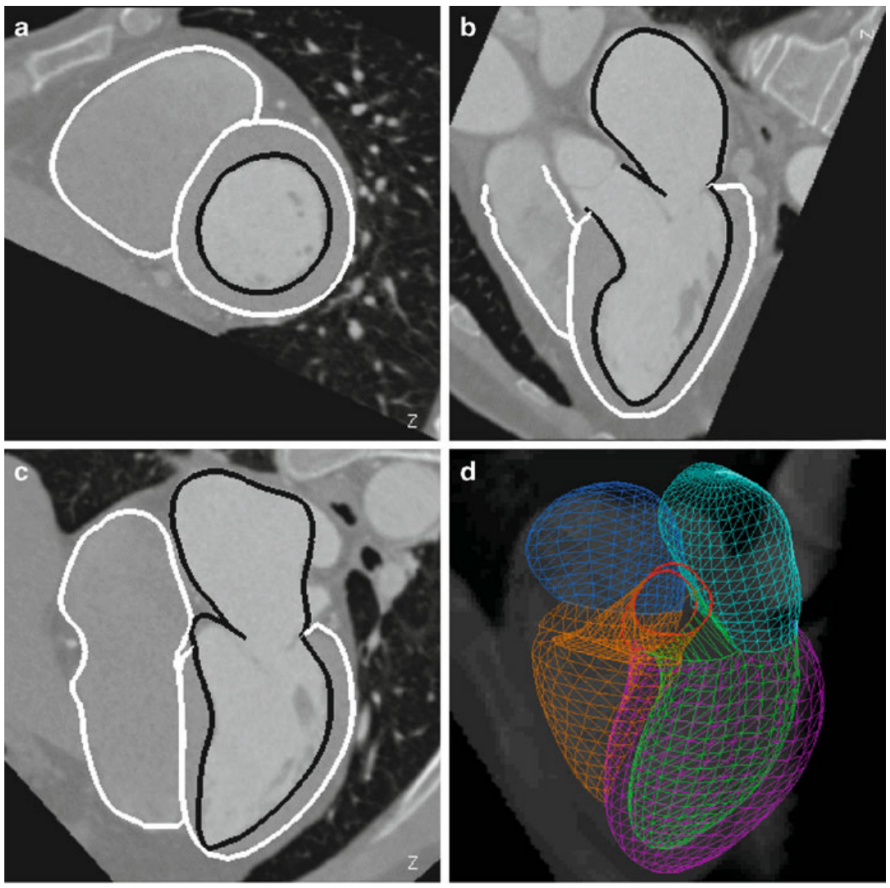

Figure 3.36: Whole heart segmentation using Marginal Space Learning. Image source: Zheng and Comaniciu [198].

One of the more important MSL-based works by Zheng et al. team was the whole heart segmentation method proposed in [197, 199]. The method is using the MSL to guide the shape deformation of an active shape model in order to fit the input image. The whole framework is shown in Figure 3.34. The third step of the MSL performs the Similarity Transformation Estimation. Afterwards, the non-rigid deformation estimation fits the model to the image. The example of the segmentation results obtained with the method are shown in Figure 3.36.

Heart isolation (segmenting the heart as a whole from a 3D image) is another technique with important clinical significance, but with more focus on the dataset visualization than on the quantification of the heart structures. It has clinical value in several applications, e.g. 3D volume visualization of coronary arteries, radiotherapy planning, and automatic calculation of the calcium score [198]. Large shape variations and weak image boundary complicate the isolation process. Zheng et al. [200] overcame those challenges by calculating the optimal mean shape from the training set, improving the shape initial-

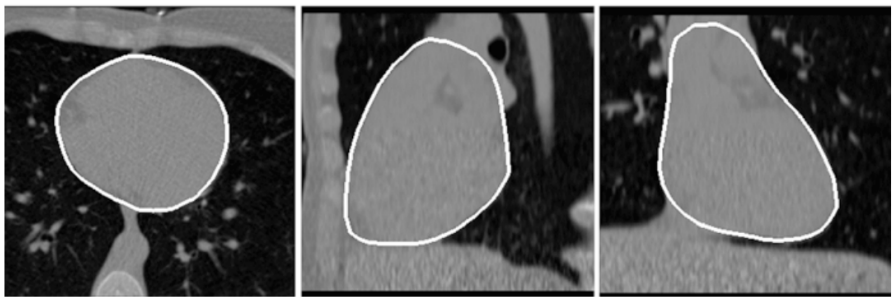

(a) Non-contrasted image

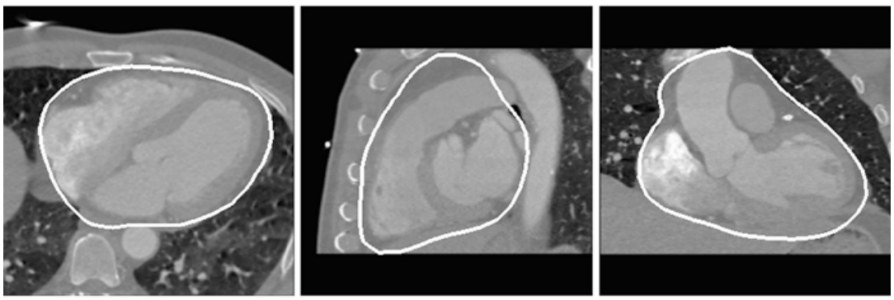

(b) Contrasted image

Figure 3.37: Transaxial, sagital and coronal views of the results of the MSL-based whole heart segmentation on both non-contrasted and contrasted CT images. Image source: Zheng and Comaniciu [198].

ization accuracy. Their later work proposed by Zhong et al. [202, 203] improved the result by removing the pulmonary veins and the left atrial appendage from the final visualization. The method has been demonstrated on both contrasted and non-contrasted CT images, as in Figure 3.37. Resulting visualization of the heart enables easy visual inspection of coronary arteries (Figure 3.38)

The shape and location of pulmonary veins, protruding from the left atrium, can vary significantly between the patients (see Section 2.1.2 and especially Figure 2.6). The approach used in [200], which calculated the optimal mean shape of the model, does not adequately cover such large anatomical variations. Consequently, Zheng et al. proposed in [201] a part-based method, which does not fit one model to the image, but fits several different models to different parts of the image. This part-based approach successfully segmented the atrium, including the pulmonary veins. This approach will be explained in more detail in Section 3.5, as it is one of approaches that successfully segments the LAA as well.

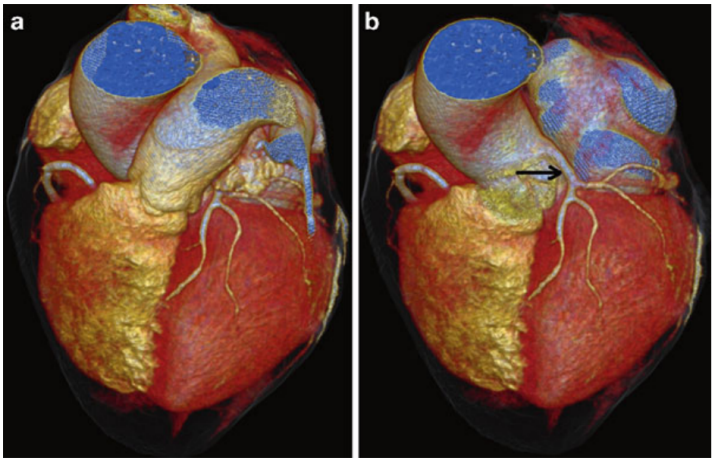

Figure 3.38: 3D volume visualization of the whole-heart segmentation results. (a) Before removal of pulmonary arteries, pulmonary veins, and left atrial appendage. (b) After removal. Image source: Zheng and Comaniciu [198].

3.4.5 *Artificial neural networks-based methods*

The concept of artificial neural networks (ANNs) was introduced in 1940s by McCulloch and Pitts [120]. The main idea behind the concept was to try to emulate the learning ability of the biological neuronal system. The basic mathematical model of ANNs consists of a parallel structure with three layers: input, hidden and output layers. Training information enters the network through the input layer and passes through one or more hidden layers until it finally reaches the output layer. Each layer transforms the input data depending on the type of the layer and the configured parameters in the network. When the input data reaches the output layer, the output of the network (i.e. the transformed input data) is compared to the correct output for that specific input data sample. The difference between the network result and the correct output is an error which is propagated back through the network, adjusting the parameters of the network. This process of adjusting the network parameters to better match the output of the network to the desired output is what we call the training or the learning of the network.

Neural networks have experienced a significant proliferation during the last decade. Ever since the seminal paper on Deep neural networks by Krizevsky et al. [90, 91], the whole field of neural network based image processing has been revived. The deep learning concept has significantly outperformed other types of methods in a large number of applications, for example in image classification [64], semantic segmentation [104], or image compression [168]. Artificial neural networks even started to outperform human experts. Rajpurkar et al.

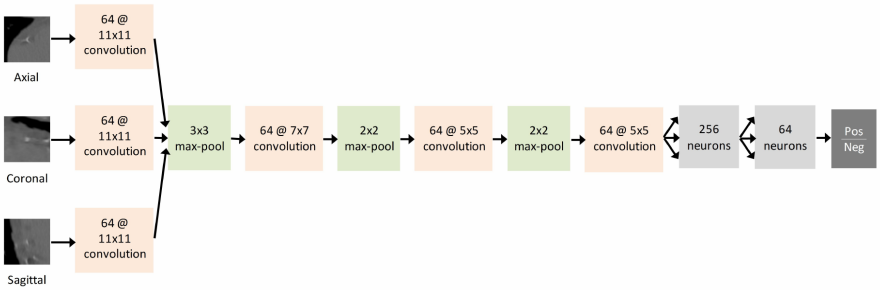

Figure 3.39: Convolutional neural network architecture for automatic LV segmentation proposed by Zreik et al. For every voxel, the input to the network are three orthogonal 48x48 patches centered around the voxel (axial, saggital and coronal neighborhoods of the voxel). The network classifies the voxel as belonging to (positive), or not belonging to the LV (negative). The convolutional neural network (CNN) has 4 convolutional layers, 3 max pooling layers, two fully connected layers and one softmax output layer. Image source: Zreik et al. [209].

[148] developed a neural network that outperforms human radiologist in detecting pneumonia from chest X-ray images. Despite the advancements in deep-learning-based methods, in the area of cardiovascular segmentation from 3D images the results were not as groundbreaking. Deep networks require massive datasets for training. Deep networks work better with very large number of data samples and small size of an individual data sample. The data available for cardiac segmentation purposes could be considered as the opposite – small number of data samples with large size of an individual sample (being a 3D image).

Shaikhina et al. [160] introduced a novel framework which enables neural network (NN) analysis in medical applications involving small datasets (despite not being focused on cardiac segmentation). The work proposed by Payer et al. [141] performs a multi-label whole heart segmentation using CNNs and anatomical label configurations. Poudel et al. [145] are using a recurrent fully convolutional neural network to perform a multi-slice MRI cardiac segmentation. Tran et al. [169] proposed an approach where a fully convolutional neural network is used for cardiac segmentation in short-axis MRI. Wolterink et al. [182] proposed an approach using a dilated convolutional neural networks for cardiovascular MR segmentation in congenital heart disease. Zreik et al. [209] proposed an approach for automatic segmentation of the left ventricle in CCTA images using CNNs. Their method used 60 CCTA datasets – 50 to train the LV localization network, five to train the segmentation network and the final five to validate the method. Dormer et al. [44] proposed a CNN based approach for heart chambers segmentation trained and validated on only 11 3D CT datasets.

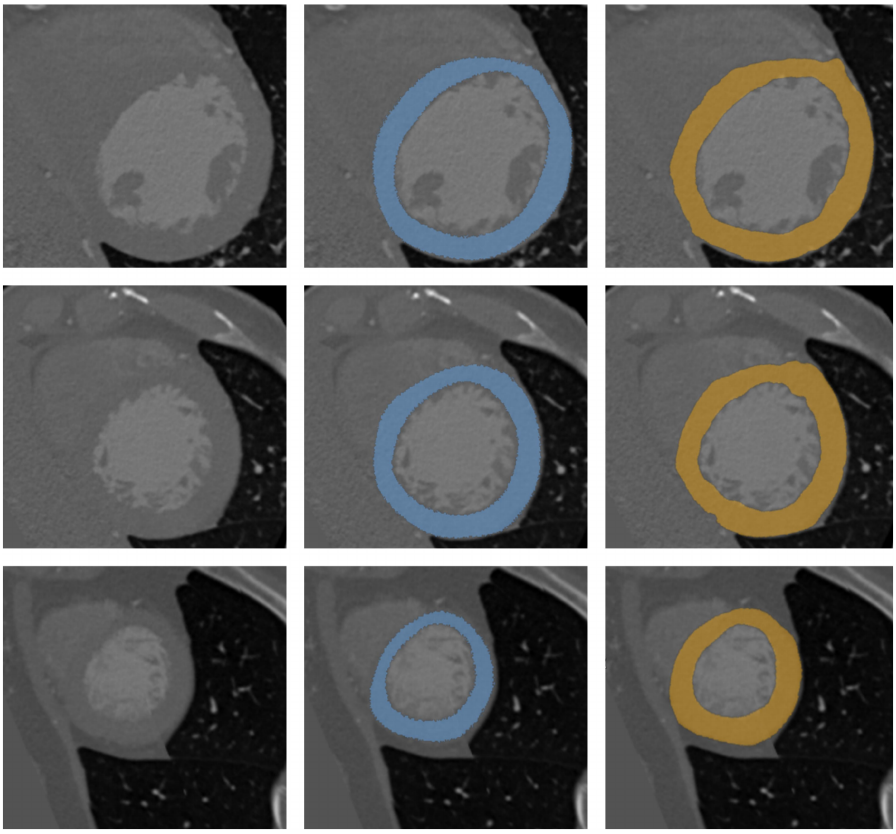

Figure 3.40: LV segmentation results by Zreik et al. Figure shows original slices (left column), ground truth annotations (middle column) and segmentation results (right column). Image source: Zreik et al. [209].

All of these approaches demonstrate the feasibility of the CNNs for the purpose of cardiac segmentation, but they do not outperform the more established methods, especially the atlas-based and model-based methods presented in previous sections.

3.5 LEFT ATRIAL APPENDAGE SEGMENTATION APPROACHES

Throughout the previous four sections we presented a wide review of the work published in the area of cardiac segmentation. In this section we cover only the approaches which segment or analyze the left atrial appendage, whether directly or indirectly.

The area of left atrial appendage segmentation is generally under-researched. To the best of our knowledge, a relatively few automatic and semi-automatic LAA analysis and segmentation methods have been published. Even though a number of methods concerning the left atrium segmentation have been proposed, almost all of those methods either discard or ignore the appendage.

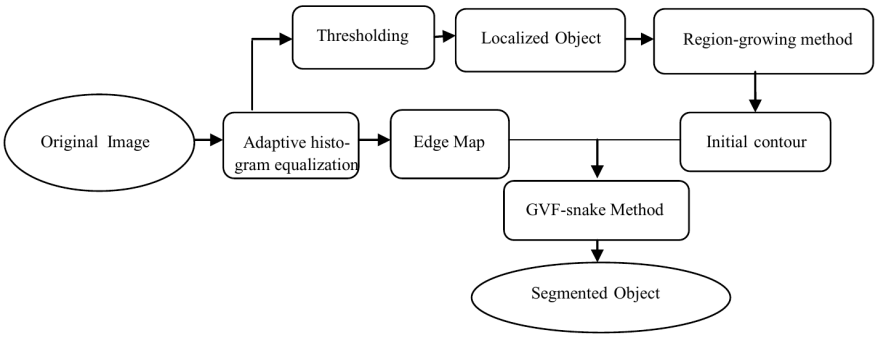

Figure 3.41: The general framework of the left atrium segmentation method proposed by Daoudi et al. Image source: Daoudi et al. [39].

In the next subsection (Section 3.5.1) we will briefly summarize major LA segmentation methods. Finally, in the Section 3.5.2 we will explain in greater detail the state-of-the-art algorithms for LAA segmentation.

3.5.1 *Left atrium segmentation methods*

In this subsection we briefly present the algorithms for left atrium segmentation. We will comment on each algorithms' treatment of the LAA .

The algorithm proposed by Daoudi et al. [39] performs the LA segmentation using an active contours-based algorithm. Their proposed algorithm works in 2D space, segmenting the atrium per slice. The method works on thresholded CT images and determines the correct threshold for the image automatically. They determine the threshold with gray level histogram analysis, after contrast correction with adaptive histogram equalization. The object in the image with the largest volume is chosen as the location of left atrium. In all of their training images the left atrium is located in the middle of the image and has the largest volume – the method relies upon this characteristic of the dataset for the localization step.

After obtaining the threshold and the seed point (the centroid of the LA volume determined in the previous step), the method detects the initial contour for the active contours step using the modified region growing methods. The region growing method does not grow the region in the binary thresholded image, but uses the grayscale values of the image. Starting with the seed point, the region is grown only in the homogeneous areas of the image, where the homogeneity is determined according the previously determined threshold. Finally, gradient vector flow (GVF) Snakes algorithm [187] segments the atrium. Figure 3.41 shows the method diagram.

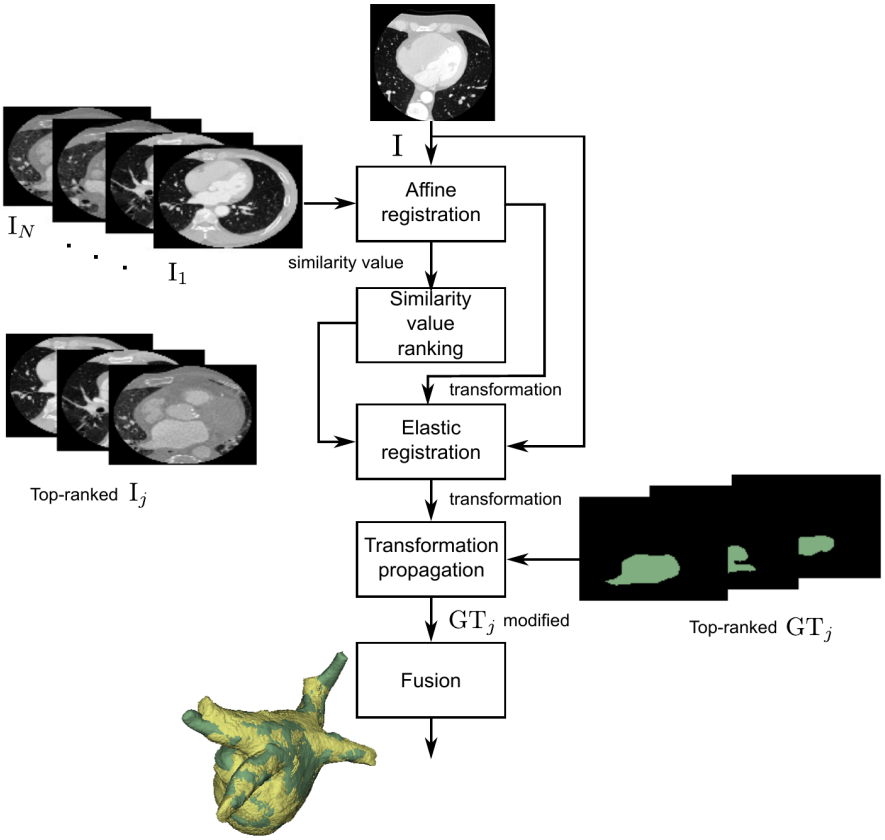

Figure 3.42: The general framework of the left atrium segmentation method proposed by Sandoval et al. The multi-atlas based approach uses the affine registration to evaluate the similarity between the input image and the atlas dataset. After atlas ranking, the ground truth of the selected atlases are modified using the elastic registration. Finally, the labels are propagated and fused to the resulting segmentation. Image source: Sandoval et al. [155].

The strengths of the method are its speed of execution, automatic initialization of snakes and high segmentation accuracy. The drawbacks are high dependency on image quality and 2D implementation. The method does not focus on the LAA segmentation and it is unclear from the paper how much of the LAA is added to the segmentation during the region-growing step, since LAA and LA are connected and the intensity values of the contrasted blood in the LAA region will be similar to the values inside the LA.

The algorithm proposed by Sandoval et al. [155] performs a fully automatic left atrium segmentation based on multi-atlas registration and region-growing. Figure 3.42 shows the method flow diagram. The method is using affine registration to rank atlases to the input image. The atlases are ranked using three similarity measures: sum of squared differences, normalized correlation coefficient and mutual information.

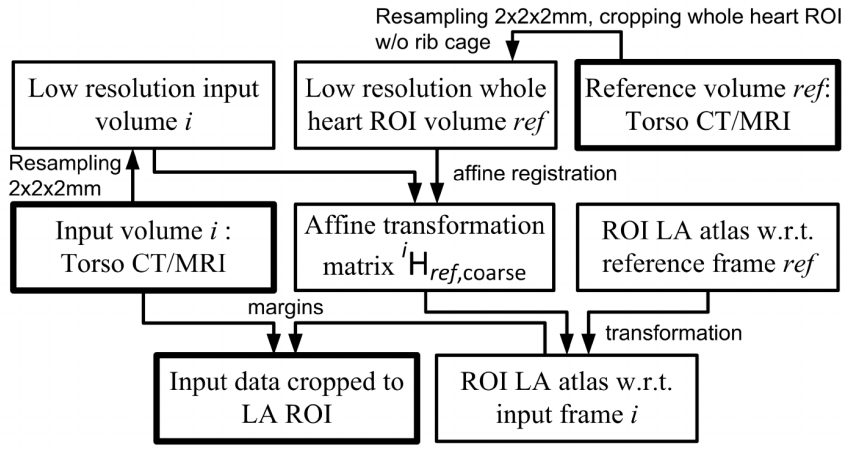

(a) LA detection flow

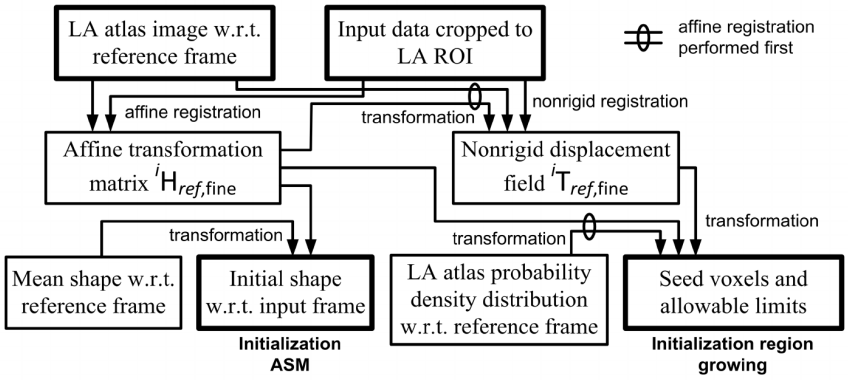

(b) Segmentation initialization

Figure 3.43: Flow diagrams of Stender et al. approach. Image source: Stender et al. [164].

Labels are propagated to the selected atlas using the majority-voting fusion. Next, the method erodes the fused label image and refines the segmentation using the eroded image as the initialization for the region-growing step. The dilated fused label image is used as a ROI to constrain the region growing. The region-growing step allows the method to adapt to the peculiarities of each patient. The same method works on both CT and MRI modalities, but uses different fusion rules.

The main strengths of the method are the use of the apriori anatomical information and the robustness due to multiple atlases. However, the method is computationally expensive, the global measure in atlas ranking is unfavourable for PVs and the region-growing has challenges in inhomogeneous regions. The method segments only a small part of the LAA, probably due to the dilated ROI not encompassing the whole appendage.

Stender et al. [164] developed two segmentation methods capable of working with both CT and MRI modalities. The first algorithm is

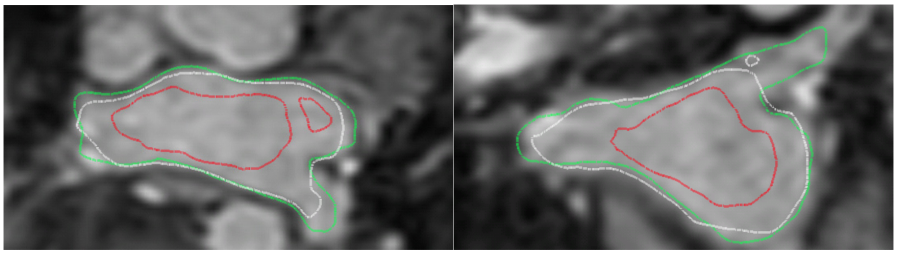

Figure 3.44: Segmentation results of statistical region growing method on an MRI volume in axial (left) and coronal (right) cutting planes. Red contour: initialized seed voxels. White contour: segmentation results. Green contour: ground truth. Image source: Stender et al. [164].

based on statistical shape models (SSM), while the second one uses region-growing. Both algorithms work fully automatically, using the same atlas information for initialization. First, the method creates two modality specific atlases, one for the CT and the other for the MRI images. Then, one of the images is selected as a reference and the remaining images are mapped in the dataset onto the reference image using the affine registration. After histogram equalization, the images were merged into a mean volume used as a template.

Figure 3.43a shows workflow for detection of the LA ROI, used by both methods. Basically, the method selects the ROI in the reference image, registers the new image to the reference image and propagates the ROI to the new image. The whole process is done on isotropically down-sampled images to improve performance. The detected ROI is then used as an initialization for both methods. Figure 3.43b shows the segmentation initialization for both methods. The first method (SSM-based) used the transformation obtained in the detection step to propagate the average mesh. The mesh was subsequently adapted by following the gradient features of the input image. A valid instance of the deformed mesh was obtained using the statistical constraints of the model. The second method used the voxels with high probability of being inside the atrium as seed points for region growing. The probability was determined from the probability density distribution of the mean volume template.

The main strength of the region-growing-based method is that it can handle anatomical variations of pulmonary veins. The main drawback is that it leaks to LV if the mitral valve is open or barely visible. On the other hand, the SSM-based method does not suffer from mitral valve leakage, but cannot handle the anatomical variability without sufficiently large training dataset. The region-growing-based method does segment a part of the LAA in some of the datasets, while the SSM-based method does not. That is to be expected, since the region growing will at least partially grow into the appendage.

The algorithm proposed by Margeta et al. [116] performs a fully automatic left atrium segmentation based on random decision forests. The proposed method consists of two steps. In the first step the structure of the decision forests is trained on all available datasets, then the trained forest is used to separate the atrial voxels from the background voxels in a previously unseen image. Each voxel was associated with several features such as: local features based on mean intensity of the voxel neighborhood; context rich features which capture strong contrast changes and long-range intensity relationships; distance to blood pool contours; and tubularity features encoding the vesselness information using a multiscale vesselness filter [156]. The method was trained on 10 provided datasets, using a leave-one-out cross-validation to select the best parameters for the forests.

The online phase, which performs the segmentation of the previously unseen image, creates a probability map – each voxel is assigned a probability of belonging to the left atrium. Thresholding the probability map creates the final segmentation. The online phase takes around a minute to fully segment the LA in a new image. Figure 3.31 on page 62 shows the calculated probability maps, while Figure 3.32 on page 63 shows the final meshes. The strength of the method is the fact that the training is done with few assumptions, everything is learned directly from the training datasets. Main limitation of the approach manifest in frequent misclassification of PVs. Due to the really small training dataset (only 10 images), the method could not handle variable LA anatomies present in the validation dataset. The method also does not attempt to segment the LAA , nor does the paper mention the LAA at all. The method does not have any assumptions regarding the LAA, the training datasets do not include the labels for the LAA and the method penalizes the voxels according to the vesselness measure – all of that points to the method not being suitable for the LAA segmentation tasks.

The algorithm proposed by Zuluaga et al. [210] performs a fully-automatic left atrium segmentation based on multi-atlas segmentation propagation. The method selects the best atlases for propagation with a cross-correlation metric. The approach registers the input image to all atlases in the atlas database. The registration is performed in two stages to avoid the registration bias introduced by the structures surrounding the heart. Figure 3.45 shows the framework of the proposed approach (steps 1-3 belong to first stage, steps 4 and 5 to second stage). The goal of the first stage is to define a ROI as a binary mask which removes the structures surrounding the heart. First, the input image is registered to the intensity images of the atlases using affine registration (step 1 in figure). After applying the obtained transformations to the label images of the atlases (step 2), the majority voting is used to

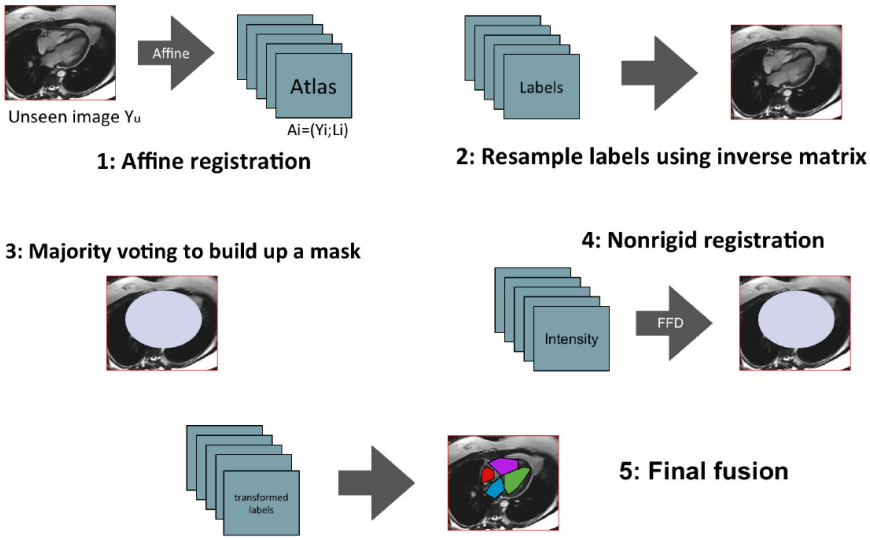

Figure 3.45: The framework for multi-atlas whole heart segmentation proposed by Zuluaga et al. See the text for the description of the steps. Image source: Zuluaga et al. [210].

create a fused label image (step 3). The second phase uses a non-rigid free form deformation registration to align the atlases to the masked input image (step 4). Finally, the resulting segmentation is obtained by fusing the labels from the registered atlases (step 5). Labels are fused from the most suitable atlases using the STEPS algorithm [26]. Suitable atlases were determined after ranking them using the strategy based on Locally Normalized Cross Correlation.

The approach is robust due to multiple atlases information, but depends on the quality and morphology of training set and it's computationally expensive. Due to the label fusion approach from multiple atlases, the approach does not segment the LAA as the LAA labels were not present in the Left Atrium Segmentation Challenge (LASC) images.

3.5.2 *LAA segmentation algorithms*

This subsection covers the state-of-the-art methods for the segmentation of the left atrial appendage. As we previously stated, to the best of our knowledge there are only a few LAA segmentation methods published in the literature.

The only two fully automatic methods we are aware of were proposed by Zheng et al. [197, 201] and evaluated in the LASC challenge [167]. The methods are referred to as SIE-PMB and SIE-MRG in the challenge, and we use the same labels throughout the text.

Zheng et al. (SIE-PMB) [197] uses a multi-part based approach to automatically segment the left atrium, including the LAA and the

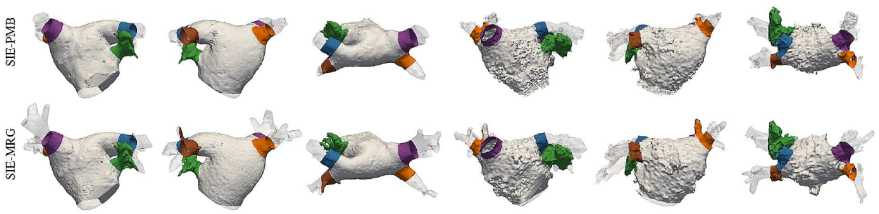

Figure 3.46: Results for both Zheng et al. methods (SIE-PMB and SIE-MRG) on two CT datasets from the LASC challenge. Dataset B007 (three leftmost columns) is a high quality dataset and the dataset B013 (three rightmost columns) is a low quality dataset. Main LA region is shown in white, other anatomical regions are color coded by the standardisation framework. The segmented LAA region is given in green color. Transparent meshes are the parts of the original segmentation results truncated by the standardization framework. Image source: Tobon-Gomez et al. [167].

pulmonary veins. The approach automatically detects the LA ROI and fits the multi-part based model to left atrium. The multi-part model is divided into six parts: LA body, LAA part and one part for each pulmonary vein. Individual models are fitted using Marginal Space Learning (MSL) and later merged into a consolidated mesh. During the MSL pose estimation phase, the statistical shape constraints were enforced to improve detection robustness.

This method was trained on an in-house CT dataset consisting of 457 cardiac CT scans, compared to previously described LASC approaches which mostly used the provided LASC datasets for training. This is the largest training dataset reported in the literature at the time of publication, and to the best of our knowledge it remains one of the largest ever reported. The size of the datasets required for training is the main limitation of the method. Also, the method does not extract the proximal side branches of PVs and does not handle extremely rare anatomical variations of the PVs. The main strength of this approach is the computational efficiency: the approach performs the complete LA segmentation in 3 seconds on a multi-core CPU. Additionally, it is very robust to image noise and artefacts (being able to handle even the C-arm CT images) and accurately determines the position of the mitral valve.

We were unable to determine if the SIE-PMB[197] method submitted to the LASC challenge was modified from the original approach published in 2008 [197]. The original paper performs the whole heart segmentation and does not explicitly mention the handling of LAA during the process. Due to the proprietary nature of the method, our main source is the LASC benchmark paper by Tobon-Gomez et al. [167]. However, the segmentation results of the method provided by the Challenge organizers' include the appendage as well.

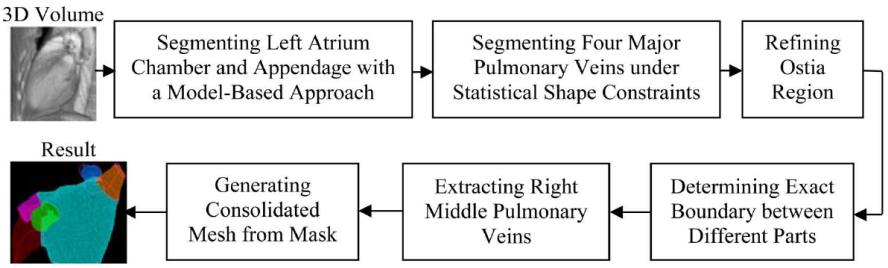

(a) System diagram of the method

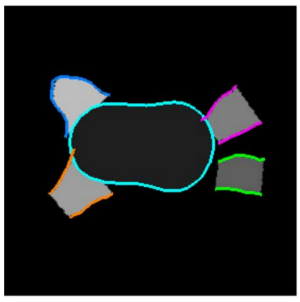

(b) Mesh and mask after parts fitting

(c) Mask after resolving the gaps between parts

(d) Mask after segmenting the RMPV

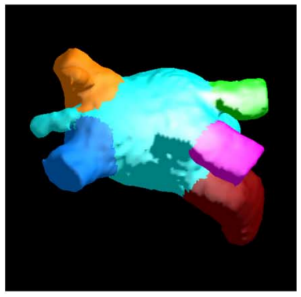

(e) Final mesh

Figure 3.47: Workflow of the SIE-MRG method (a) and intermediate results (b-e). Image source: Zheng et al. [201].

Zheng et al. [201] (SIE-MRG) is also based on multi-part based approach using Marginal Space Learning. The method workflow is shown in Figure 3.47a. Multi-part models in this approach include: the LA chamber, appendage, and four major PVs. The part based approach allows the method to use simpler models for each LA part and fit them individually (Figure 3.47). Model fitting is performed with MSL-based approach. Segmentation refinement (after fitting) is performed using region growing based on adaptive thresholds, followed by removal of the leakage using graph cuts (Figure 3.47b). Refinement step resolves the gaps between LA parts resulting from the fitting of the individual models and refines the ostia regions (Figure 3.47c). This approach handles the anatomical variation where some patients may contain an extra right middle PV (see Section 2.1.2 and Figure 2.6). The RMPV is not

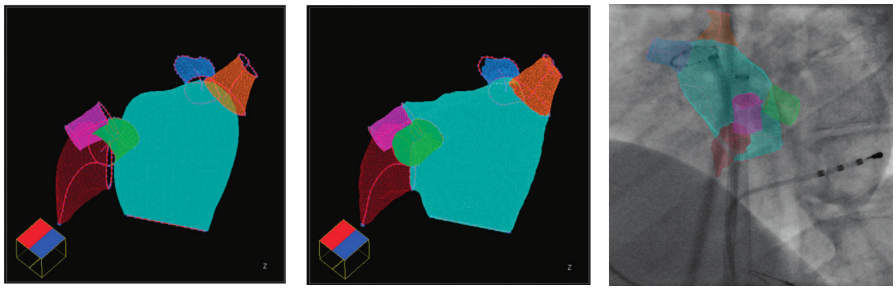

(a) (b) (c)

Figure 3.48: Meshes of the part-based LA model. (a) Meshes for the separate LA parts. (b) Final mesh after fitting and refinement. (c) The final model can be overlaid onto fluoroscopic images to provide visual guidance during surgery. Part-based meshes include: the LA chamber mesh (cyan), the appendage (dark red), left inferior pulmonary vein (green), left superior pulmonary vein (magenta), right inferior pulmonary vein (orange) and right superior pulmonary vein (blue). Image source: Zheng et al. [201].

segmented using a model based approach. Instead, the method uses a graph-cuts algorithm constrained by the already segmented major right pulmonary veins (Figure 3.47d). The graph-cuts algorithm was performed on a down-sampled volume to increase the performance.

Similarly to the SIE-PMB [197] method, we were unable to determine if the SIE-MRG [201] method submitted to the LASC challenge was modified from the original approach published in 2014 [201]. The original paper performs the LA segmentation from non-gated C-arm CT scans, while this approach works on ECG-gated multi-slice cardiac CT images. Same as before, due to the proprietary nature of the method, our main source is the LASC benchmark paper by Tobon-Gomez et al. [167]. However, some notable differences in the method between the benchmark paper and the original paper exist. Most important difference is that in this version of the method the segmentation of pulmonary veins is not model-based, but based on region-growing. Only the LA chamber and the LAA segmentations are model-based.

The main strength of the method is the ability to handle rare anatomical variations in patients, especially variations in the configuration of the PVs. The method correctly extracts the proximal side branches of PVs (due to the region-growing step) and correctly determines the position of mitral valve plane (due to the model-based LA chamber segmentation). However, the method requires sufficient contrast inside the LA and the PVs, contrary to the SIE-PMB[197] method which is shown to work even on non-contrasted images.

Compared to the SIE-PMB[197] method, this approach has an advantage when segmenting the appendage. The region-growing-based

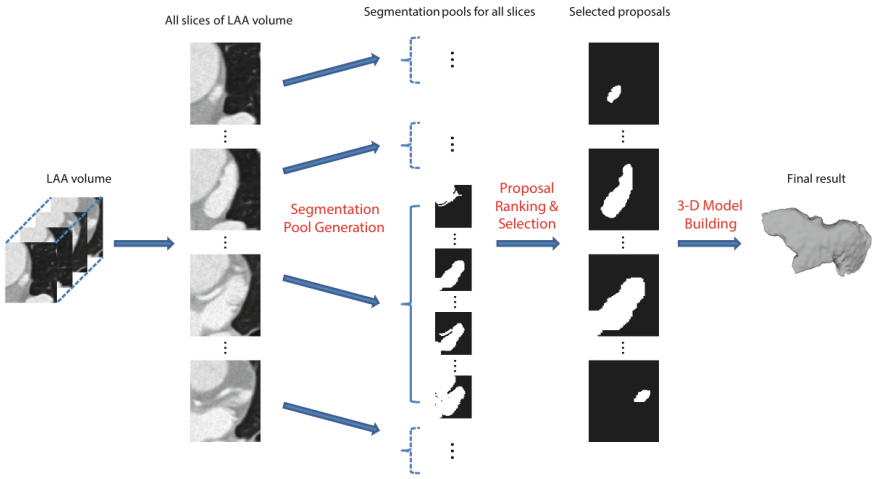

Figure 3.49: Flowchart of the LAA segmentation method proposed by Wang et al. Image source: Wang et al. [177].

refinement allows this approach to better capture the varying morphology of the LAA, as well as the trabeculations inside the LAA. Two examples of the segmented LAA and the differences in the resulting meshes can be seen in Figure 3.46. It should be noted that, because the LAA was not included in the LASC ground truth datasets, neither of the methods were evaluated on the accuracy of the LAA segmentation.

Zhong et al. [202, 203] used a model-based approach for whole heart segmentation and removal of pulmonary veins and the appendage. The goal of this approach was to remove all structures obstructing the visualization of coronary arteries. The segmented appendage was only a side result, to be removed from the final segmentation.

The method proposed by Wang et al. [177] segments the LAA from 3D cardiac computed tomography angiography (CTA) images using an approach based on ranking 2D segmentation proposals. The flowchart of the proposed method is shown in Figure 3.49. The method uses a semi-automatic approach which requires manual determination of the LAA bounding box from four manually selected points. The first step of the method processes all slices of the determined LAA volume and for each slice creates a pool of segmentation proposals. A trained random forest regressor picks the best segmentation proposal for each slice. Finally, best proposals are merged into a 3D volume using spatial continuity to correct possible segmentation errors.

The pool of segmentation proposals for each slice is created using a graph-cut method. The main advantage of the graph-cut method over the model-based approach is that it does not have any shape constraints, as it is purely driven by the image. However, the final result of the graph-cut approach is strongly dependent on the configuration parameter λ. The correct λ value is not the same for all images and

Figure 3.50: Generated segmentation proposals. The small magenta squares in the leftmost image represent different foreground seed points (seed hypothesis) for the graph-cut method. The bold blue lines surrounding the image represent the negative (background) seeds. For every seed hypothesis, the method creates a set of segmentation proposals with different λ values (λ increases from left to right). The image shows two generated proposal sets for two seed hypotheses (orange arrows). Image source: Wang et al. [177].

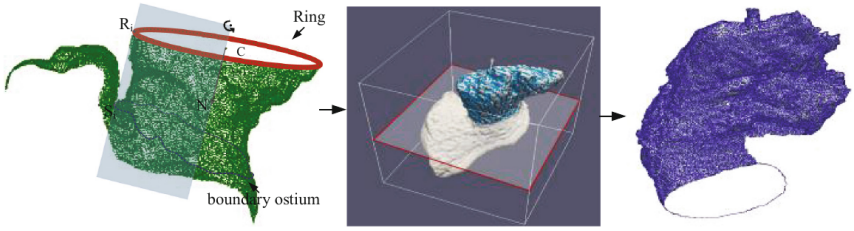

Figure 3.51: LAA delineation according to a plane determined from the maximum curvature boundary. Image source: Jin et al. [74].

determining the correct value is not a trivial task. Thus, the proposed method creates a pool of segmentation proposals using different λ values and different seed hypotheses for each slice. Figure 3.50 shows the generation of segmentation proposals.

The method achieves high Dice coefficient overlap (95.12%) with ground truth segmentations. Evaluation was performed on 60 CTA datasets using a four-fold cross-validation. The method takes about 3.5 minutes on a 4 CPU system (4 Intel Core i7 CPUs at 4.0GHz) to perform the segmentation.

The method proposed by Jin et al. [74] uses the segmentation method by Wang et al. [177] to create a model of the LAA neck and aid in occlusion procedure planning. Building of the model of the LAA neck is based on the segmentation results of maximal volume phase from a CT image. The method automatically detects the LAA ostium, establishes the standard coordinate system centered in the ostium and calculates the neck dimensions. The ostium is detected as a smooth closed bound-

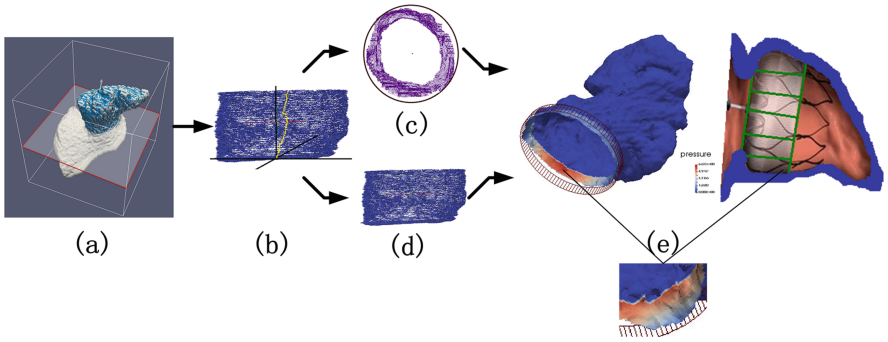

Figure 3.52: LAA neck modelling process. (a) Determining the delineation plane. (b) Traversing the slices. (c) Determining the bottom slice of the model. (d) Determining the neck height. (e) Generating the neck model where the colors represent the tensions of the closure devices. Image source: Jin et al. [74].

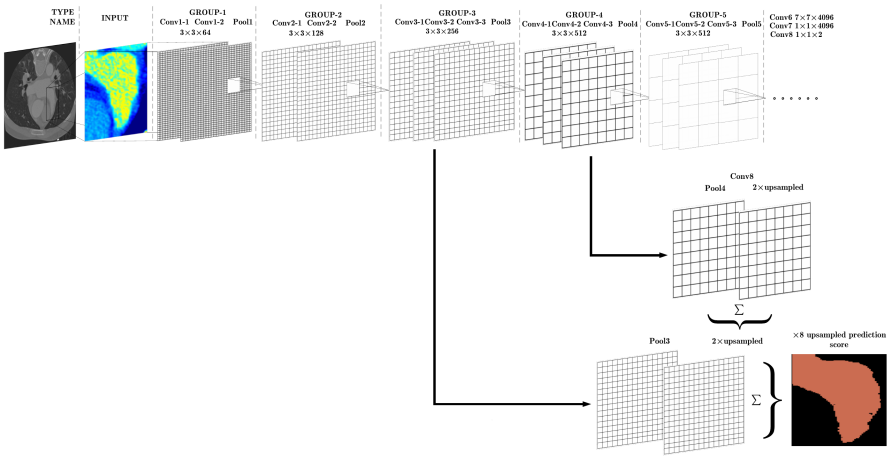

Figure 3.53: Details of the network configuration. The network combines abstract, high-level semantic features with low-level spatial information. Image source: Jin et al. [73].

ary of the highest surface curvature located in the transitional region between the LA and the appendage. After obtaining the boundary, the appendage is delineated from the left atrium according to the plane defined by the boundary. The method creates a coordinate system with the origin in the geometric centroid of the boundary. Finally, the method creates a cylinder which will model the tension of the LAA surface after placing the device (see Figure 3.52). This model will assist the clinician in choosing the occluder of the appropriate size. The method is evaluated on 100 CT datasets and 3 pig hearts. The post-procedural follow-up of 67 patients indicated the 97.01% success rate of occluder device implantation (only two failed implantation cases).

Another method proposed by Jin et al. [73] performs the LAA segmentation using fully convolutional neural networks and conditional

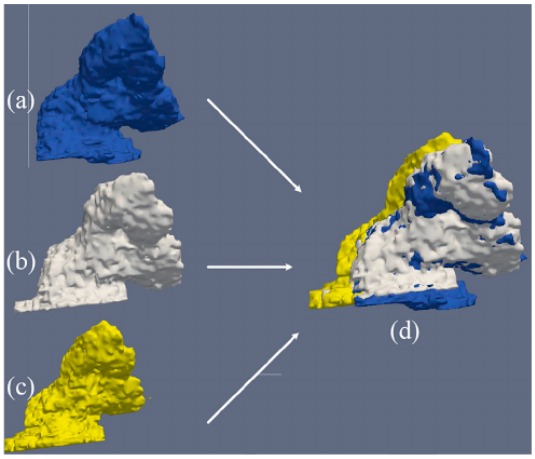

Figure 3.54: Fusion of LAA segmentation in different phases of cardiac cycle. Image source: Jin et al. [76].

random fields. This method is an improvement of the Wang et al. [177] segmentation method and uses the similar approach. After manual determination of the LAA bounding box (same as [177]), the method segments the appendage in each 2D slice of the ROI.

Slices are pre-processed with histogram equalization to increase contrast and a multi-scale method [77, 147] to enhance the CT image. Subsequently, gray-level images are converted to 3-channel RGB pseudo color images to enhance the resolution of local features. The pre-processed pseudo color 2D slices are the input to the CNN (architecture in Figure 3.53) which outputs 2D probability maps of the regions containing the appendage. The final segmentation step merges the 2D probability maps using the 3D conditional random fields [32] into a final 3D volume.

The method is evaluated on 150 CCTA datasets obtained with Philips 256 slice scanner, using five-fold cross-validation. Four medical experts carried out the ground truth segmentations to avoid observer bias. The method achieves high Dice overlap to ground truth of 94.76%. The performance of the method is significantly improved (compared to [177]) and the segmentation of a LAA volume takes less than 35 seconds. However, the method requires powerful GPU card – the evaluation was carried out using an NVIDIA Tesla K80 GPU.

Jin et al. also proposed two 4D based LAA analysis methods. The first method [76] performs the segmentation of 4D CT LAA images for diagnosis of atrial fibrillation using their graph-cuts based segmentation method [177]. The method builds a 3-D model of each time instance of the sequence. The method assists in the diagnosis of the atrial fibrillation in a few ways: by calculating the volume of 3D models in different phases of the cardiac cycle; by generating the "volume-phase" curve (showing the change of LAA volume throughout

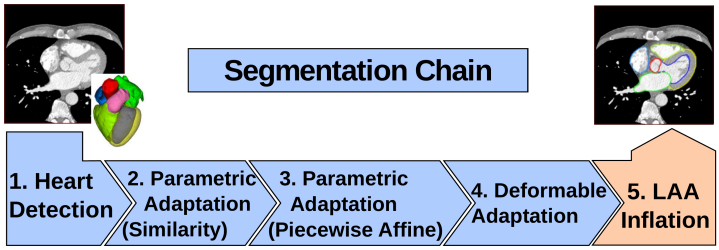

Figure 3.55: Flowchart of the LAA segmentation method proposed by Grasland-Mongrain et al. Image shows the chain of modules which perform the segmentation. Image source: Grasland-Mongrain et al. [59].

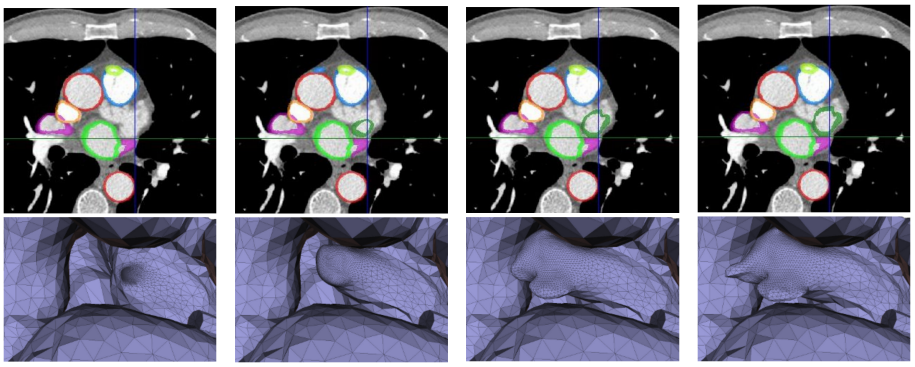

(a) Before growing (b) $\alpha = 0.2$ (c) $\alpha = 1$ (d) $\alpha = 2$

Figure 3.56: Inflation of the deformable LAA model. Contours in the top images show: LAA (dark green), LA (bright green), myocardium (yellow). Bottom images: front view of the 3D mesh. Image source: Grasland-Mongrain et al. [59].

the cycle); and obtain important dynamic LAA metrics. Finally, multivariate logistic regression analysis of the obtained metrics calculates the risk of thrombus formation, while the SVM-based model predicts the AF diagnosis.

The second method [75] uses the 4D CCTA images to detect substances inside the LAA using spatio-temporal motion analysis. The method extracts the optical flow field for all adjacent phases in a cardiac cycle. The cardiac cycle of 20 phases results in 19 optical flow fields. Using the nearest neighbor interpolation, the method generates the motion trajectory of the key voxels throughout the cycle. Hierarchical clustering tree finds the corresponding classification for every trajectory track. Changes in classifications between the tracks correspond to the division of substances in the appendage. Finally, time-frequency analysis of the trajectories enables the detection of different substances inside the appendage, including the thrombi in different states of formation.

Method proposed by Grasland-Mongrain et al. [58, 59] is an adaptation of the whole heart segmentation method proposed by Ecabert et al. [47] (explained in more detail in Section 3.3.1). First, the heart is localized and segmented with shape-constrained deformable models (ASM-based approach from [47] – first four modules in Figure 3.55). The model-based approach segments the heart chambers and determines the position of the appendage (the position of the LA -LAA interface). In the last step of the chain (Figure 3.55), the segmentation of the appendage is performed by inflating the mesh at the LA -LAA interface into the appendage.

Triangulation of the mesh at the LA -LAA interface with high resolution ensures reasonable triangle size when the mesh is inflated. The inflation is guided by minimizing external and internal energy to fit the exact shape of the appendage. The external energy (*region-based* energy) is calculated according to the voxel gray values in the image. This region-based energy decides whether the mesh has to inflate or deflate based on the voxel intensity information at the center of the triangle. This energy pushes the mesh towards the appendage edges defined by the edges between the contrasted blood in the appendage and the background. The internal energy is used to preserve a regular triangle distribution during the inflation. In standard ASM methods the internal energy is computed by comparing the deforming mesh to a fixed reference shape. In this case, the calculation of the internal energy is using the deforming mesh at a previous iteration as a reference shape.

Let $E_{internal}$ and $E_{external}$ be the internal and external energies described in the above paragraph, respectively. The energy guiding the deformation is defined as:

$$E = \alpha \cdot E_{external} + E_{internal} \tag{3-9}$$

with α as weighting factor controlling the deformation. Mesh adaptation is performed by iterating the mesh inflation and the minimization of the Eq. (3-9) until a steady state is reached. Figure 3.56 shows the LAA meshes inflated with different α values.

The method has been evaluated on images from 17 patients. The inflation of the mesh has problems reaching the tip of the appendage, as well as undersegmenting the appendage. Also, the value of α parameter has to be balanced. The value of α being too large can lead to deformations in the wrong directions, while it being too small results in undersegmentation. The method authors preferred the undersegmentation to the incorrectly twisted LAA mesh.

3.6 CONCLUSION

In this chapter we gave a broad overview of the methods used for segmentation of the heart in cardiovascular images of various imaging modalities. We divided the methods into four major categories: the PDE-based methods, graph-based techniques, model-based segmentation techniques and clustering and classification approaches. We discussed their advantages, disadvantages and the applicability to the task the thesis is attempting to solve – the pre-procedural planning of the left atrial appendage occlusion procedure. Consequently, we gave a detailed overview of methods focused on the segmentation of the left atrium and the left atrial appendage. We pointed to the limited number of published methods concerning the left atrial appendage segmentation. To the best of our knowledge, only a few methods have been published in the literature to date. Majority of the published methods are implemented using a variation of machine learning approach. The limitation of the model-based and atlas-based segmentation methods for the LAA segmentation tasks manifests primarily in the inability of the model to represent all the variations in the shape of the LAA. The most popular machine learning approaches today (CNNs and similar) are under-performing in this area, as they require massive training datasets. The datasets available today are quite limited in size. Consequently, at this time we believe that the heuristics-based methods have a slight advantage compared to the CNN-based approaches. However, the machine-learning-based methods (and especially CNN-based methods) could probably outperform all other approaches with the appearance of sufficiently large training datasets.

4

LAA CENTERLINE DETECTION

In this chapter we propose a novel LAA centerline detection method. The centerline detection is the first step in the whole chain of image processing techniques proposed in this thesis for supporting the pre-procedural planning of the left atrial appendage occlusion.

The detected centerline forms as a basis for both the LAA segmentation (explained in Chapter 5) and the automatic localization of the LAA orifice (explained in Chapter 6). The proposed method detects the centerline using only one seed point inside the appendage. We perform the automatic localization of the left atrium during the centerline detection. The ending point for the centerline is determined automatically and represents the center of the left atrium. Two main advantages of the proposed centerline detection method are: 1) minimal user interaction – the method requires only one seed point and 2) stand-alone operation without relying on other image processing methods – the method does not require the segmented LAA as an input. The contribution presented in this chapter is a novel method for the detection of the LAA centerline and localization of the center of the left atrium.

The detected centerlines are validated by calculating the Hausdorff distance to the centerlines manually extracted from the LAA skeleton. The results demonstrate a low calculated Hausdorff distance indicating a potential for clinical use. Additionally, the results of the method are indirectly validated in the two subsequent chapters, because both the LAA segmentation and orifice localization methods use the detected centerline as the input. The result a the localization of the left atrium is validated visually by our medical expert. The work presented in this chapter is published in a journal paper [100] and presented in an international conference [99]. The skeletonization method used for validation is published in [8].

4.1 INTRODUCTION

The method proposed in this chapter performs the detection of the centerline using only two inputs: a seed point placed inside the LAA; and a threshold value. The result of the proposed method – the detected centerline – is used as an input to both the segmentation and the orifice localization methods explained in the later chapters.

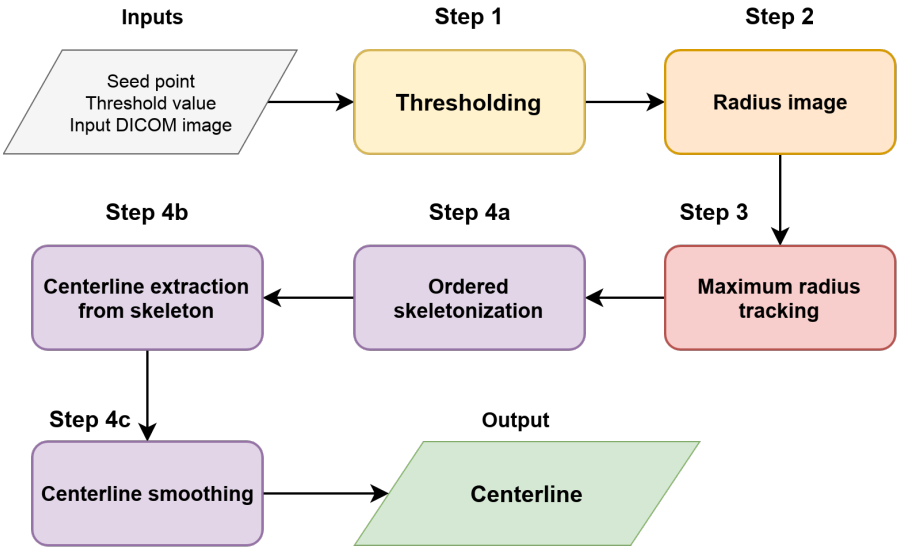

Figure 4.1: Flow diagram of the proposed centerline detection method

To the best of our knowledge, there is only one published LAA segmentation method based on the LAA centerline proposed by Morais et al. [126]. However, their method segments the LAA in a 3D TEE image from a manually created centerline. The user manually places several points in the image which determine the centerline. On the other hand, in the current literature there are no reported methods focused specifically on the detection of the centerline through the LAA. For that reason our proposed method is validated on the centerlines extracted from the skeleton of the segmented LAA. We perform the skeletonization of the ground truth segmentation of the appendage and manually extract the part of the skeleton representing the ground truth centerline. Ground truth centerlines are validated by a medical expert. The ground truth creation is explained in more detail in the Results section (Section 4.6).

The main two features of the proposed centerline detection method are: (1) the method automatically localizes the center of the left atrium which serves as the ending point of the centerline; and (2) the result of the method is an ordered set of points from the seed point to the center of left atrium, allowing for easier traversal along the centerline. The second feature is important for the orifice localization method explained in Chapter 6.

The proposed method consists of the following steps depicted in the Figure 4.1:

1. Thresholding produces a binary mask image using the provided threshold value. The LAA centerline will be detected in the binary mask image in subsequent steps.

2. Radius image is created by calculating the distance transform of the binary mask. Radius image is used to improve the performance of the next step – maximum radius tracking – by precomputing the radii of the maximum inscribed spheres in every voxel in the mask image.

3. Maximum radius tracking algorithm – this step finds the path from the seed point to the left atrium along the center of the LAA by tracking the voxels with the largest maximum inscribed sphere radii.

4. Centerline extraction is used to extract the centerline from the tracked path and create a smooth centerline curve. This step consists of three parts:

   a) Ordered skeletonization is used for the thinning of the maximum radius path – removes blobs of voxels and enables easier extraction of the centerline.

   b) Extraction of the centerline from the created skeleton results in an ordered one-voxel wide line from the seed point to the center of the left atrium.

   c) Smoothing the extracted centerline improves the orifice localization results (Chapter 6) by minimizing the change of direction vectors along the centerline.

The following sections will explain every step from the above in more detail. It should be noted at this point that the first step in the method (the thresholding) significantly affects the results of the segmentation method explained in the following chapter. However, in this chapter we will only explain the effects of the thresholding operation on the centerline detection method. The effects of the thresholding operation on the segmentation method will be explored in Section 5.2 in the next chapter.

4.2 THRESHOLD SELECTION

In this section we explain in more detail how the threshold selection affects the centerline detection results. The threshold value should be chosen by a trained medical professional based on the patient's cardiovascular anatomy and the quality of the input image (the distribution of the contrasted blood in the heart as well as the presence of noise). The purpose of the thresholding step is to create a binary mask image containing the correct amount of the LAA anatomy in the foreground of the image. All other steps process and analyze the anatomy that was *masked* by thresholding. Since the centerline is detected as a curve along the center of the LAA anatomy in the foreground of the mask

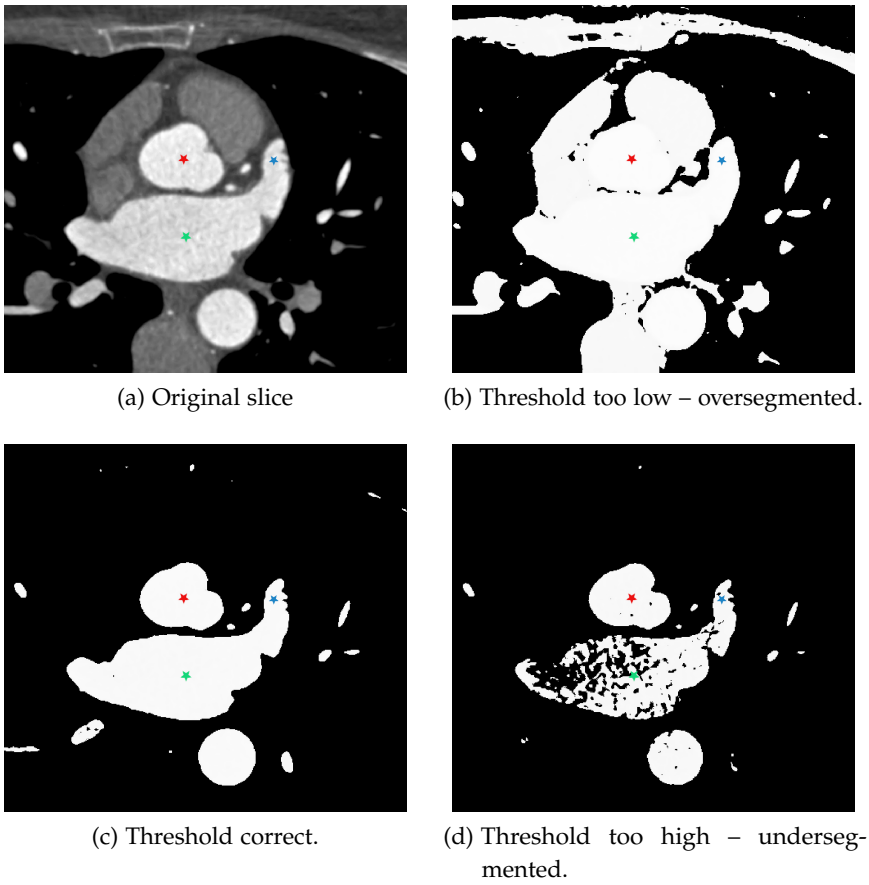

(a) Original slice

(b) Threshold too low – oversegmented.

(c) Threshold correct.

(d) Threshold too high – undersegmented.

Figure 4.2: The example of a single slice from the mask image created with different threshold values. Blue star represents the seed point inside the LAA.

image, choosing the incorrect threshold value can negatively affect the performance of the method. Still, it should be noted that our proposed methods are designed to be relatively robust to the selected threshold value (see section 4.7 for more details).

The user selects the threshold value for the dataset with a simple slider by visual inspection of 2D slices. A simple guideline for selecting the threshold value is: the chosen threshold value should be the largest value where the whole LAA is still in the foreground of the mask image, but there is a clear delineation between the parts of the heart. Moreover, the user should set the threshold to mask the contrasted blood in the image. The heart muscle should not be part of the foreground in the correctly thresholded image, especally the muscle of heart chambers. Figure 4.2 shows the effects of thresholding on a single slice. Correct threshold is shown in the Figure 4.2c. It is evident from the figure that the LAA (blue star) is correctly masked and that the left atrium (green star) is clearly delineated from the aorta (red star). This allows the centerline detection method to find a path in the mask image,

Figure 4.3: One slice of radius image quantized to 20 grayscale levels. Brighter intensity in the image denotes higher radii, darker intensity denotes lower radii.

along the center of the LAA, connecting the blue star (seed point) with the green star (center of the LA). If the chosen threshold is too low (Figure 4.2b) the image gets oversegmented, the parts of the heart are not clearly delineated and the centerline detection method can have problems localizing the left atrium. On the other hand, high levels of noise present in CCTA images can also result in holes in thresholded image if the threshold value is too high. Figure 4.2d shows the problem with holes in binary image formed inside the contrasted region due to noise.

It should be noted that the centerline detection method is more sensitive to the appearance of holes in the mask image (undersegmentation) than to the oversegmentation. Still, the proposed method is robust to the threshold selection and unless the selected threshold value is very inaccurate, the selected threshold value will not disrupt the functioning of the centerline detection. The threshold value has a lot greater effect on the extent of the LAA anatomy that will be segmented than on the accuracy of the detected centerline.

4.3 RADIUS IMAGE

In this section we explain how the radius image is created and its effects on the performance of subsequent steps in the method. We calculate the radius image for every dataset. Radius image is calculated from the thresholded image using the Euclidean distance transform. The intensity value of every voxel in the radius image represents the shortest distance from that voxel to the background. We can imagine

the voxel intensity value as the radius of the largest sphere centered in that voxel where all voxels inside the sphere are in the foreground (i.e. the largest inscribed sphere). Subsequent steps in the proposed method are based on finding the spherical neighborhoods of a certain criteria. In this way the radius of a spherical neighborhood centered in a voxel can be determined by a simple lookup of an intensity value from the radius image.

Let us define the radius image more formally. Let B be the set of all background voxels $\mathbf{v_B}$ in the thresholded image. The intensity value of each voxel $\mathbf{v} \in \mathbb{Z}^3$ in the radius image will be:

$$r(\mathbf{v}) = \begin{cases} min(d(\mathbf{v}, \mathbf{v_B})) \; ; \; \mathbf{v} \notin B, \mathbf{v_B} \in B \\ 0 \; ; \; \text{otherwise} \end{cases}, \tag{4-1}$$

where $d(\mathbf{v}, \mathbf{v_B})$ is the Euclidean distance between voxels $\mathbf{v}$ and $\mathbf{v_B}$. Figure 4.3 illustrates one slice from a dataset with calculated distances to the nearest background voxel. We calculate radius image using Maurer Distance Map method [118] generalized to N-dimensional spaces implemented inside SimpleITK framework [107]. Perfomance of radius image calculation is additionaly improved by extracting only the connected component in the thresholded image which contains the seed point. This way radii do not have to be calculated for unconnected anatomical structures in the image (e.g. ribcage).

4.4 MAXIMUM RADIUS TRACKING

In this section we explain the first step in the centerline detection method – the maximum radius tracking – whose goal is to find a path from the seed point placed in the LAA to the center of left atrium. The center of the left atrium is determined automatically. The centerline is detected by extracting the voxels belonging to the centerline from the detected path. The method works by iteratively tracking the voxels with the maximal radii of the largest inscribed spheres, starting from the seed point placed in the LAA and ending somewhere near the center of the left atrium. Since we only use one seed point, we track the maximum radius voxels for a predefined number of iterations N. The ending point of the path (the center of the left atrium) is then selected among the tracked points along the path. We discard all the tracked voxels added after the selected ending point (the located center of the LA). The resulting path between the seed point and the ending point will extend approximately through the center of the LAA. Voxel radii values tested during the tracking are looked up as the voxel's intensity values from the radius image. The algorithm of the

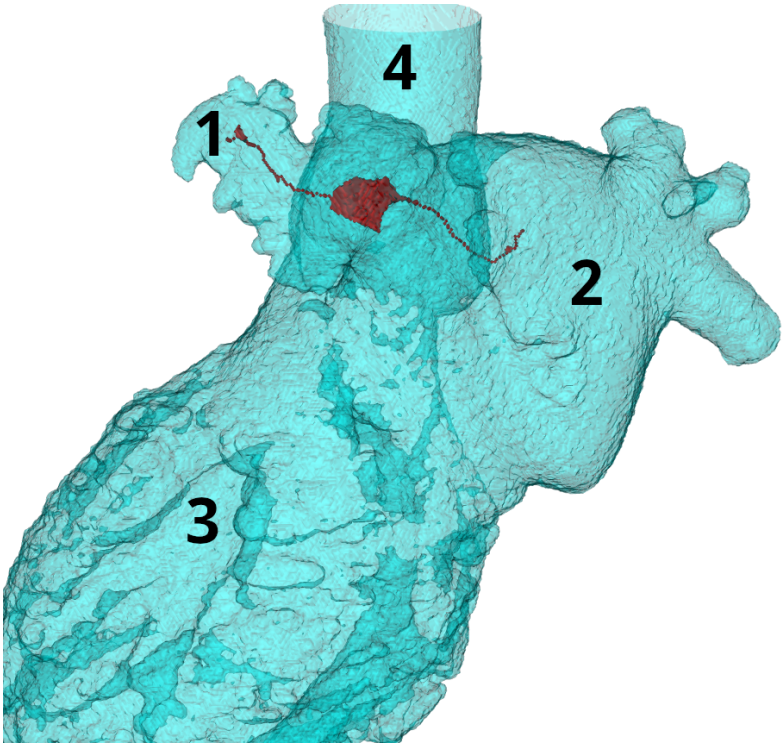

Figure 4.4: Example of a result of the maximum radius tracking method – the detected maximum radius path (red). Parts of the heart marked with numbers are: (1) the LAA, (2) the left atrium, (3) the left ventricle and (4) the aorta.

method is presented in the Algorithm 4.1, while the formal definition of the method follows.

Let $S(\mathbf{v})$ be a set of voxels belonging to the maximum inscribed sphere in the mask image centered at voxel $\mathbf{v} \in \mathbb{Z}^3$:

$$S(\mathbf{v}) = \left\{ \mathbf{q} \in \mathbb{Z}^3 \mid d(\mathbf{v}, \mathbf{q}) \leq r(\mathbf{v}) \right\}, \tag{4-2}$$

where $r(\mathbf{v})$ is a radius of the maximum inscribed sphere contained in the radius image, as defined in (4-1). The maximum radii tracking is iteratively performed for N iterations and consists of the following steps:

1. The initial step (performed only once): Let us denote with P^i the set of voxels in which the search for the highest radii value is performed (in a given iteration step i). The initial search set P^1 will be the set of voxels within the maximum inscribed sphere of the first seed point $\mathbf{v}_{seed}$:

$$P^1 = S(\mathbf{v}_{seed}). \tag{4-3}$$

2. In the search set P^i we locate the voxel with the highest value in the radius image $\mathbf{v}^i_{\mathbf{rmax}}$:

$$\mathbf{v}^i_{\mathbf{rmax}} = \arg\max_{\mathbf{v} \in P^i} r(\mathbf{v}), \tag{4-4}$$

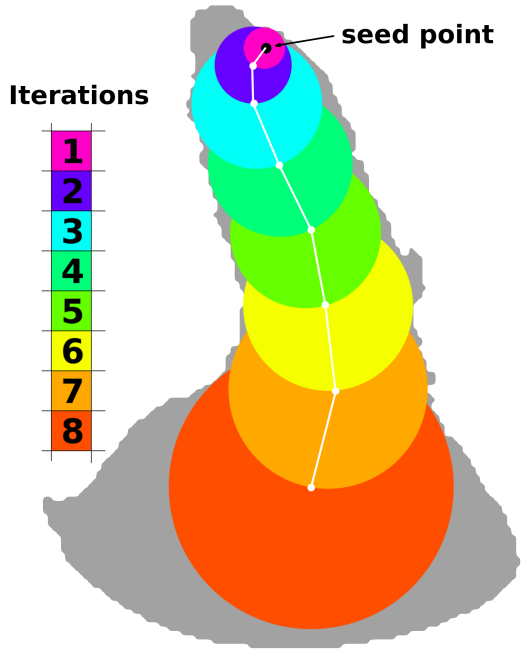

Figure 4.5: Centerline tracking by iterative selection of maximum radii voxels in the largest inscribed spherical neighborhood. This image was reported in our work: [100]

and we add it to the output set of tracked maximum radii voxels T^i:

$$T^i = T^{i-1} \cup L(\mathbf{v}^{i-1}_{\mathbf{rmax}}, \mathbf{v}^{i}_{\mathbf{rmax}}), \tag{4-5}$$

where T^{i-1} indicates the tracked maximum radii voxel set from the previous iteration (in the initial iteration this set is an empty set) and $L(\mathbf{v}^{i-1}_{\mathbf{rmax}}, \mathbf{v}^{i}_{\mathbf{rmax}})$ is the set of voxels on the line segment between the previous and current maximum radii voxel.

3. We extend the search set P^i to include the set of voxels defined by the maximum inscribed sphere of the newly added voxel $\mathbf{v}^{i}_{\mathbf{rmax}}$ to the output set T^i:

$$P^i = P^{i-1} \cup S(\mathbf{v}^{i}_{\mathbf{rmax}}), \tag{4-6}$$

where P^{i-1} indicates the search voxel set from the previous iteration step.

The general idea of the algorithm is illustrated in Figure 4.5. Masked LAA region is represented with gray area. Each colored circle in the figure represents a sphere in 3D space, while white dots represent the selected voxels $\mathbf{v}_{\mathbf{rmax}}$ in each iteration. Color codes for each iteration

are given in the legend on the left side of the figure). The initial search set P in Figure 4.5 is illustrated by the circle (representing a sphere in 3D) generated in the first iteration (color code 1). The initial search set P contains voxels from the seed voxel's sphere. In first iteration we find the maximum radius voxel $\mathbf{v_{rmax}}$ in the initial search set P and add it to the output set T. We also add the voxels on the line connecting it with seed voxel. The search set P is extended by the sphere of the found maximum radius voxel. This means that the search set P has grown and includes the first two spheres (color codes 1 and 2). New maximum radius voxel is found in the extended search set P and added to the output set T. The search set P is again extended by the sphere of a newly found maximum radius voxel. This process is repeated for N iterations. The robustness of the algorithm to the seed point placement is discussed in more detail in the Discussion section of this chapter 4.7.

After running the tracking for N iterations we find a voxel in T with the largest radius. This voxel represent the center of LA. Let the voxel in T with largest radius be defined as:

$$\mathbf{v_C} = \arg\max_{\mathbf{v}\in T} r(\mathbf{v}). \tag{4-7}$$

Finally, all voxels added to T after $\mathbf{v_C}$ are removed from T. To reiterate, even though the tracking algorithm has run for N iterations, the final detected path (set T) does not have N elements. We have discarded from T all voxels added after adding the $\mathbf{v_C}$ voxel, which is now considered the center of left atrium. The tracking is performed for a predefined number of iterations in order to avoid the need for setting the second seed point. The goal is to run the iterative tracking long enough to allow the maximum radius path to leave the LAA and enter the left atrium. There are no negative side-effects of letting the tracking running longer than necessary, except for a small performance penalty.

4.4.1 *Anatomical widening*

Due to the variable anatomy of the LAA, on some datasets the tracking can enter an anatomical widening. We explain in this subsection the handling of such a widening by the tracking algorithm. We could say that the shape of the LAA is generally tubular, even if the tube is often very deformed. The centerline through the LAA would then represent the line along that tube, through its center. The result of the maximum radius tracking will be a set of voxels approximately along the center of the LAA resembling a centerline. Note that maximum radius path is not a line, it is a set of voxels which at certain segments are often wider than one pixel, thus we refer to it as path. Still, since the points of the actual LAA centerline are later extracted from the path, we can

Algorithm 4.1 Tracking maximum radii voxels algorithm

$P^1 = S(\mathbf{v}_{seed})$ according to (4-2)
$T^1 \leftarrow \emptyset$
for $i = 1$ until $i = N$ **do**
  Find $\mathbf{v}^i_{\mathbf{rmax}}$ in P^i according to (4-4)
  Append $\mathbf{v}^i_{\mathbf{rmax}}$ to T^i according to (4-5)
  Append $S(\mathbf{v}_{\mathbf{rmax}})$ to P according to (4-6)
end for
$T \leftarrow T^N$
Find $\mathbf{v}_C$ according to (4-7)
for each $\mathbf{v} \in T$ **do**
  if $\mathbf{v}$ added after $\mathbf{v}_C$ **then**
    remove $\mathbf{v}$ from T
  end if
end for

say that the detected path resembles the centerline. The term *radius along the LAA* represents the radius of voxels along that LAA centerline. In case of the illustration on Figure 4.5, the radius along the LAA would represent the radius of each point along the white line.

Often patients have large variations of the radius along the LAA. Even though the radius along the LAA is increasing from the tip to the orifice, rarely will the increase be slow and consistent (like in the example in Figure 4.5). The width along the LAA can change unpredictably and LAA can contain additional branches or lobes which complicate the detection of the maximum radius path. The width of the anatomy along the LAA will vary until the centerline reaches the left atrium (see the result of the maximum radii voxel tracking in Figure 4.6b). Figure 4.6 illustrates the handling of the widening along the LAA. When the algorithm enters the widening it will iteratively add to the output path T all the large radius voxels in the widening. When all the large radius voxels have been added to T and the next maximum radius voxel is the voxel outside of the widening, the path tracking will continue towards the left atrium. Figure 4.6a illustrates the order in which the voxels are added to T. Figure 4.6b shows the detected path T from one of our datasets. Red voxels in the figure are voxels which belong to the output of the tracking method – the voxel set T. Red dashed circle shows the handling of such widening inside the LAA.

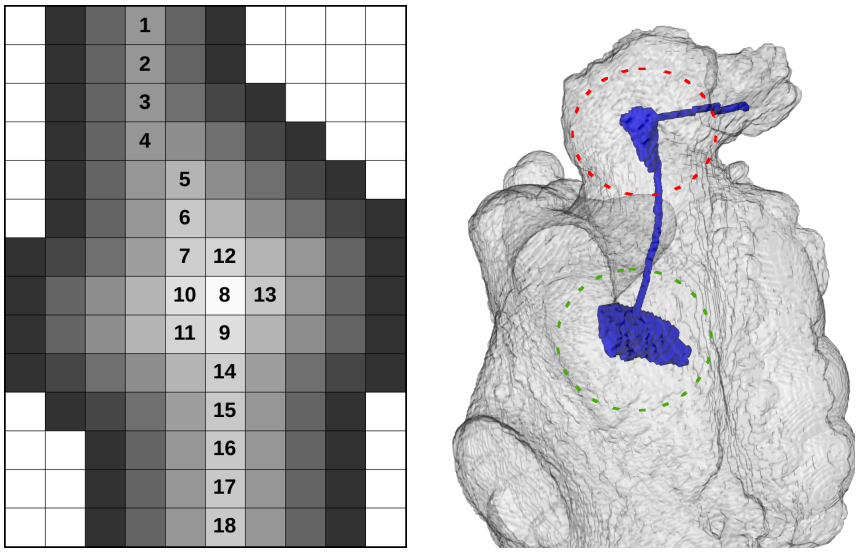

(a) (b)

Figure 4.6: Example of a widening in the anatomy during the maximum radii tracking. (a) Illustration of the order of voxels added to the tracked maximum voxel radii, where pixel gray value represents the radius value. (b) Example of tracked maximum radius path (blue) after N iterations. Red and green circles are widenings in the LAA anatomy, handled according to the illustration (a) in this figure.

4.4.2 *Left atrium localization*

Radii of voxels inside the left atrium will smoothly and consistently increase towards the LA center, due to a generally spherical internal shape of the atrium. Consequently, after the path enters the left atrium, the voxel tracking routine will proceed directly towards the voxel with the largest radius in the left atrium. The method will add the voxel with the largest radius in the LA to the path and continue adding smaller voxels around it until the number of iterations runs out. The intuition behind this is the same as with handling of the widening. The left atrium has a generally spherical shape and the center of the LA has a very large number of voxels with large radii. Thus, from the perspective of the tracking method, the LA is treated as a very large anatomical widening. Green circle in Figure 4.6b shows the handling of a widening after the tracking reaches the LA center. The method will continue adding voxels in the center to the path until the number of iterations runs out. Due to the size and shape of the left atrium, the method will not continue the tracking to some other part of the heart before the number of iterations runs our.

After the number of iterations runs out, a single voxel in the path T will have the largest radius of all the voxels in the path. We denoted

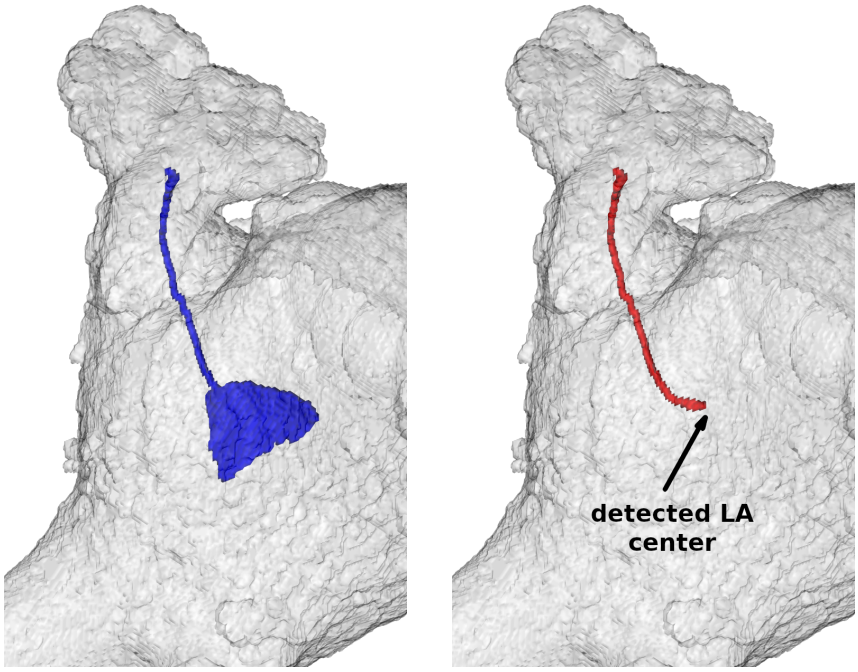

(a) (b)

Figure 4.7: Localization of the LA center. (a) Maximum radius path T before discarding voxels in the LA center. (b) Maximum radius path when all voxels added to T after $\mathbf{v_C}$ are discarded.

that voxel as $\mathbf{v_C}$ as per (4-7). We set that voxel as the location of the center of left atrium. All voxels added after that center voxel are voxels in its neighborhood and have a radius value smaller than the center voxel. We can safely discard all such voxels and use the center voxels location as the location of the LA center and the ending point of the maximum radius path. Figure 4.7 shows the path T before (blue) and after (red) the removal of all voxels added after $\mathbf{v_C}$.

The number of iterations N for the method is set to a predefined value depending on the image size. For our datasets we set the value of $N = 4000$. In almost all of our tests the maximum radius voxel in path was found in under 1000 iterations, while in only two tests the number of iterations was around 1500. The performance of the method remains stable (the method converges) after some N, thus it is important to set N to a value large enough to reach convergence. However, even significantly overestimating the number of iterations N required for convergence will not have any negative effects on the tracking result (the detected path). In other words, after the tracking converges to a voxel with the largest radius in the left atrium, the voxels added to the path in subsequent iterations do not affect the final result (the final detected path). Consequently, we can safely set the number of iterations N to a value considerably larger than the

value that the tracking would require to achieve convergence. The performance penalty will be small even if we significantly overestimate N, as the computational cost of the tracking is considerably lower than the subsequent methods in the proposed LAA segmentation framework. We have run tests with up to $N = 10000$ iterations and the tracking still behaves appropriately, i. e. the method converges to the same voxel in the LA center regardless of the number of iterations.

All things considered, we propose to pre-configure the number of iterations parameter to $N = 4000$ for several reasons:

- This value is more than enough for our datasets.
- It provides enough iterations to reach convergence even if the atrial anatomy of a new patient is significantly different from the ones in our dataset.
- The incurred performance penalty is small.
- Finally, we do not have to require the user to configure one additional parameter, but allow her the opportunity to do so if the dimensions of the input image differ significantly from the images in our dataset.

4.5 CENTERLINE EXTRACTION

In this section we explain how the detected maximum radius path is used for centerline extraction. As stated in the previous section, maximum radius tracking method determines the set of voxels in the image from seed point to the center of left atrium which defines the path for the centerline. Second part of the centerline detection method (centerline extraction) extracts from the maximum radius path the set of ordered voxels which represent the centerline. Afterwards, the extracted centerline is smoothed and used as input for the LAA orifice localization method (described in the next chapter).

The centerline extraction step is based on the work published in [8]. The centerline extraction step of the centerline detection method consists of three parts:

1. Ordered skeletonization of the maximum radius path.
2. Extraction of the longest path in skeleton – the centerline.
3. Centerline smoothing.

We explain each of these parts in the following subsections.

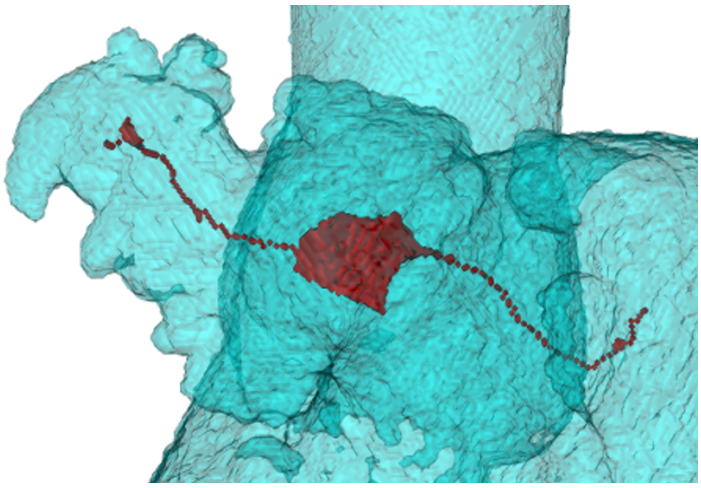

(a) Maximum radius path

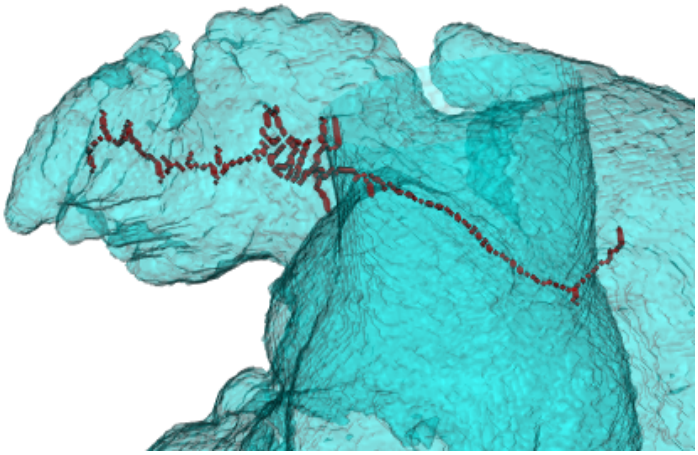

(b) Created skeleton

Figure 4.8: Skeleton created by ordered skeletonization. [100]

4.5.1 *Ordered skeletonization*

In this subsection we explain how we process the tracked maximum radius path in order to create the skeleton which contains the centerline. We use the ordered skeletonization to create a one-voxel wide line of voxels connecting the seed point with the center of left atrium. Ordered skeletonization is the process of iterative thinning of a binary image. The method iteratively discards voxels until the remaining skeleton is one-voxel wide line. Resulting skeleton image contains the LAA centerline in its central part, but it also contains stubs and multiple paths which are byproduct of skeletonization process, as visible in Figure 4.8. The centerline will be extracted from the skeleton in the next step.

The ordered skeletonization process consists of the following steps:

- Computing the Euclidean distance transform of the input image. The input image is the tracked maximum radius path image as shown in Figure 4.8a. In this case we are computing squared Euclidean distance transform, where the intensity value of every voxel in the output image is the squared distance of the voxel to the nearest background voxel in the input image. Details of the Euclidan distance transform are explained in section 4.3.
- Sorting of voxels into an ascending distance value ordered list.
- Removing the redundant voxels according to the voxel redundancy criteria proposed in [8]. The redundancy criteria states that a voxel v is redundant if all foreground voxels in its 26-neighborhood belong to the same connected component. Iterating through the list, we are discarding any voxel that fulfills this criteria.

Since the ordered skeletonization method works on binary images, redundant voxels are discarded by setting their label to background (zero gray value):

$$s(\mathbf{v}) = \begin{cases} 0, & \mathbf{v} \text{ is redundant} \\ g(\mathbf{v}), & \text{otherwise} \end{cases}, \tag{4-8}$$

where $g(\mathbf{v})$ is the voxel gray value in the input image. Skeletonization removes redundant voxels while preserving connectivity of all other voxels.

After the ordered skeletonization the center part of the resulting skeleton image is the LAA centerline. However, skeleton image also contains stubs and multiple paths which are byproduct of skeletonization process, as visible in Figure 4.8b, which have to be removed. In the figure the skeletonization method removed a large cluster of voxels in the widening of the LAA. However, multiple stubs and loops in the skeleton will complicate further processing. For that reason we remove the stubs and loops by extracting the longest path in the skeleton.

4.5.2 *Extraction of the longest path in skeleton*

In this subsection we explain how the longest path extraction is performed. The extraction of the longest path in skeleton results in an ordered set of voxels, starting from the seed voxel to the center of the left atrium and forming a centerline through the LAA. This centerline (after smoothing) is used for LAA orifice localization described in the next chapter.

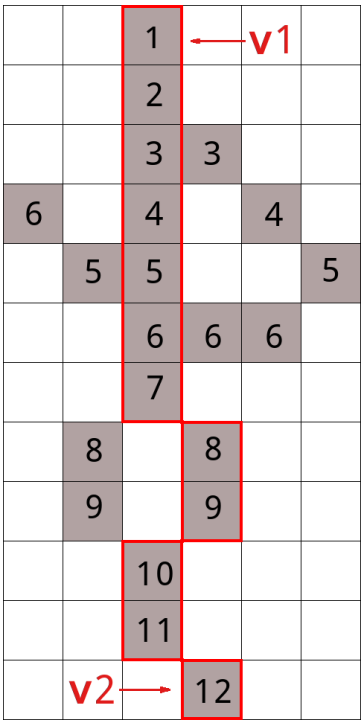

Figure 4.9: 2D example of extraction and ordering of voxels in skeleton. This method also removes stubs and multiple paths.

We extract the voxels forming the centerline by searching for the shortest path between two farthest voxels inside skeleton. The search for the longest path is perfomed in three passes.

- The first pass performs the search for the farthest voxel starting from the seed voxel, assigning the seed voxel the label value of 1. All 26-neighbors in skeleton are given the label value of 2. In each iteration unlabeled neighbors of a voxel labeled in the previous iteration are assigned a value of $label + 1$. After the first pass all voxels in skeleton image have a label representing the distance in number of steps from the seed voxel. Voxel with largest label value is the voxel that is farthest from the seed point. In this case farthest means the number of steps needed to traverse the skeleton to get from seed voxel to that voxel, not in the sense of Euclidean distance. Let denote that voxel as $\mathbf{v}_1$.

- In the second pass we perform the same labeling again, this time starting from $\mathbf{v}_1$ voxel. Now the $\mathbf{v}_1$ voxel has the label value of 1, while the new voxel with the largest label value will be the voxel that is farthest from $\mathbf{v}_1$. Let denote that voxel as $\mathbf{v}_2$. The $\mathbf{v}_2$ voxel will not necessarily be the seed voxel, but it will be very close to seed voxel, inside the LAA.

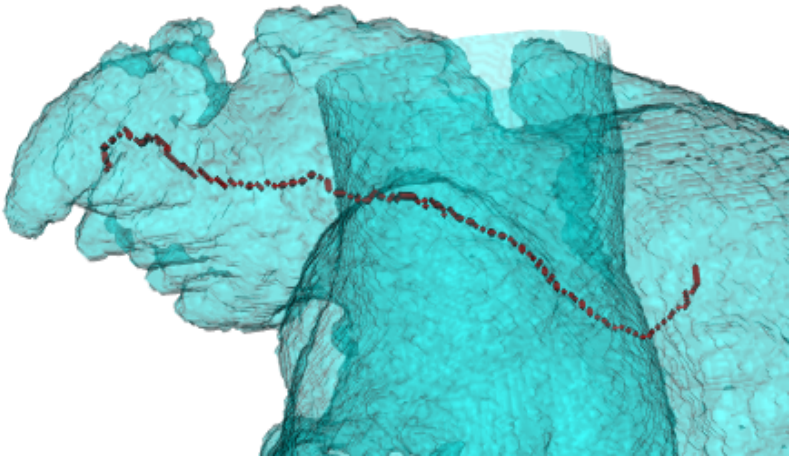

(a) Centerline extracted from the skeleton

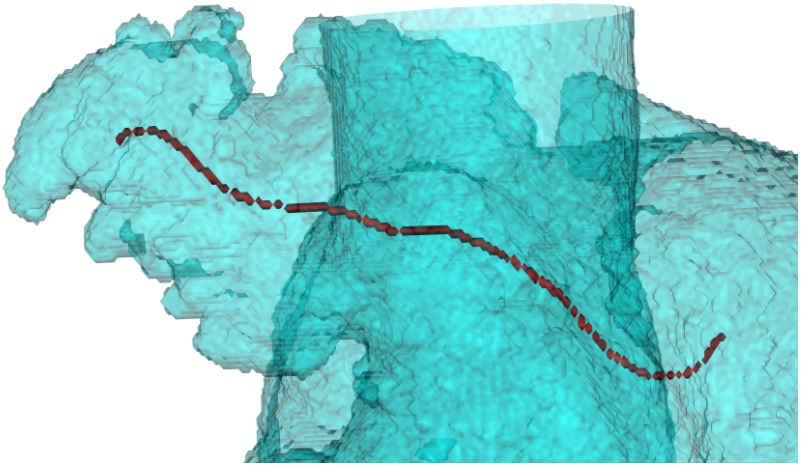

(b) Centerline after smoothing

Figure 4.10: Detected centerline: a) before smoothing, b) after smoothing. This image was reported in our work: [100]

- The extraction of ordered set of voxels representing the extracted centerline C_e is performed in the final pass. The extraction of the ordered path from $\mathbf{v}_2$ to $\mathbf{v}_1$ is preformed by traversing the labels backwards, starting with $\mathbf{v}_2$, and iteratively adding to C_e the 26-neighbor of the current voxel with the smallest label. The extraction is illustrated in Figure 4.9 and represents the extraction of shortest path between two farthest voxels in skeleton. Also, extracted voxels in path are now ordered from $\mathbf{v}_2$ (near the seed voxel) towards $\mathbf{v}_1$ (the center of the LA). This extracted ordered set of voxels represents the extracted centerline. It should be noted that at this point in the method the centerline consists of elements with discrete coordinates (voxels). Figure 4.10a shows the extracted centerline in one image from our datasets.

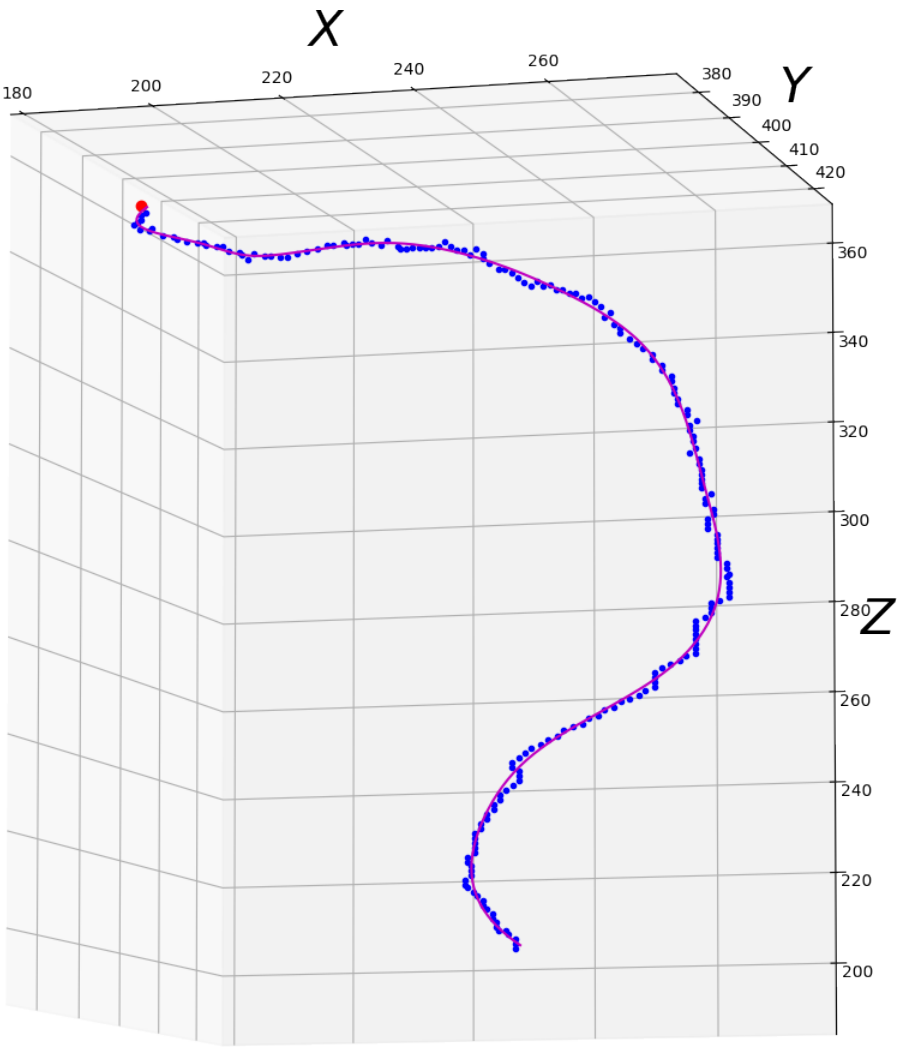

Figure 4.11: Centerline smoothing: (blue) voxels of the extracted centerline C_e, (magenta) smooth centerline C, (red point) seed point.

4.5.3 *Centerline smoothing*

The final step for centerline detection is smoothing of the extracted centerline C_e. The purpose of the centerline smoothing step in the detection method is to improve the results of the LAA orifice localization method presented in the next chapter. A smooth centerline allows better orifice localization because the localization method depends on directional vectors at each point along the centerline. Thus, the use of the smooth centerline avoids large changes in direction during the calculation of directional vectors. Figure 4.11 shows the voxel values from the extracted centerline (blue) and the final smoothed centerline (magenta).

The centerline smoothing is performed by fitting a smooth curve to the voxels of the extracted centerline. The curve fitting calculation uses

the implementation described in [43]. For simplicity, let us consider a two-dimensional example of curve fitting where original data values y_r, $r = 1, \ldots, m$, and x_r, $r = 1, \ldots, m$ belong to the dependent variable y and independent variable x, respectively. The goal of curve fitting is to fit to the y_r a function $y(x) := y(x; \boldsymbol{\theta})$ of known form but dependent on the vector of parameters $\boldsymbol{\theta}$. The fitting is performed by determining the parameters in vector $\boldsymbol{\theta}$ such that $y(x_r) \simeq y_r$. Since the resulting function will be an approximation to the original data it will be specified through what is called the *approximation criterion*.

The curve fitting is mostly done using polynomials or spline functions. We use spline functions because they are more flexible. Contrary to polynomials, they are well suited for smoothing as well as for interpolation. Also, they work well regardless of the number and the position of the data points. Additional bonus is the availability of spline based curve fitting and interpolation functionalities for almost all popular scientific programming packages.

Employing splines as the approximation functions, requires specifying the following parameters of the vector $\boldsymbol{\theta}$:

- the degree k of the spline,
- the number and position of the knots λ_i,
- the coefficients c_i which form the spline.

According to [43], cubic splines (degree $k = 3$) are recommended because they give a good compromise between efficiency and quality of fit. The smoothing is performed according to *the smoothing criterion* described in [43]. We determine a spline of degree $k = 3$ by finding the solution for the constrained minimization problem presented in the following equations.
Minimize

$$\eta := \sum_{i=1}^{g} \left(s^{(k)}(\lambda_i +) - s^{(k)}(\lambda_i -) \right)^2, \tag{4-9}$$

subject to the constraint

$$\delta := \sum_{r=1}^{m} \left(w_r (y_r - s(x_r)) \right) \leq S. \tag{4-10}$$

In the above equations g denotes the initial number of knots of the spline, function s denotes the spline, w_r denotes the weight for every data point $r = 1, \ldots, m$, while S is a specified number denoting the desired smoothness of the curve. In order to get some intuition about the above equations, we can interpret η as a measure of non-smoothness of $y(x)$ and δ as a measure of closeness of fit (least-squares criterion, a well known and general approximation criterion). Thus, η will be

larger the more wiggly the graph of $y(x)$ looks, while the δ will be smaller the closer $y(x)$ fits the data values y_r. The solution of the above equations is an approximation of the curve which makes a compromise between the following two objectives:

- find a curve with a smooth behaviour (η should be as small as possible),
- find a curve which appropriately approximates the data values (δ should not be too large).

These two objectives are often contradictory and the parameter S (called the *smoothing factor*) determines the trade-off between the smooth behaviour of the curve and the fitting of the curve to the real data values.

After the curve fitting is performed, we have a parametric curve representing the centerline. Finally, we create the smooth centerline as a set of points in 3D space by sampling the fitted parametric curve. The number of samples can be configured depending on the input image size. In our case the number of samples is 300, determined experimentally.

4.6 RESULTS

In this section we present the results of the proposed centerline detection method. The method is evaluated on 17 CCTA images of real patients, where the detected centerlines are validated by calculating the Hausdorff distance to the ground truth centerlines. All images were acquired using a Siemens Somatom 64-slice scanner for the purpose of Coronary CT Angiography. All patients have given their informed consent for the inclusion in the study. The patient data is presented in Table 5.1.

To the best of our knowledge, no other centerline detection method is specialized to handle the variable anatomy of the LAA. Hence, we validate our centerline detection method against the ground truth centerlines extracted manually from ground truth segmentations for the images in our dataset. Evaluation against the ground truth centerlines is performed with the following procedure and illustrated in Figure 4.12:

1. The LAA in every dataset is manually segmented by a medical expert (a cardiovascular surgeon). Ground truth segmentations were created using the ITK-SNAP software [194]. The expert selected the appropriate threshold and used the Geodesic active contours method [27] implemented in ITK-SNAP [107] to segment the LAA. Finally, the segmentation was manually corrected

Table 4.1: Validation dataset (17 patients)

	N	%
Patient age		
Under 35	3	17.65%
35 - 44	2	11.76%
45 - 54	2	11.76%
55 - 64	6	35.29%
65 and older	4	24.53%
Patient gender		
Male	6	35.29%
Female	11	64.71%

using the paintbrush tool. Example of a manually segmented LAA is shown in Figure 4.12a.

2. We perform an ordered skeletonization of the ground truth segmentation with the method presented in [8]. The skeletonization method is described in more detail in section 4.5.1, but here the input to the skeletonization is the ground truth segmentation instead of the maximum radius path. The result is the skeleton shown in the Figure 4.12b.

3. We manually extract the part of the skeleton from the seed point up to the center of the LAA orifice. The extracted part of the skeleton is the ground truth centerline. The example of the extracted ground truth centerline is shown in the Figure 4.12c.

4. We discard the part of our detected centerline that extends after the LAA orifice plane selected by our medical expert. The accuracy of the part of the centerline located outside the LAA does not affect the results of the segmentation and analysis methods, described in the following chapters. Therefore, we do not validate that part of the centerline. Figure 4.12d shows our detected centerline in green and the ground truth centerline in blue.

Figure 4.13 shows another comparison between our detected centerline and the ground truth centerline, with and without the skeleton. It should be noted that the ground truth segmentation used for skeletonization extends a little into the left atrium. Both the ground truth segmentation and the skeleton are delineated with the plane selected by the medical expert as the location of the LAA orifice. Parts located

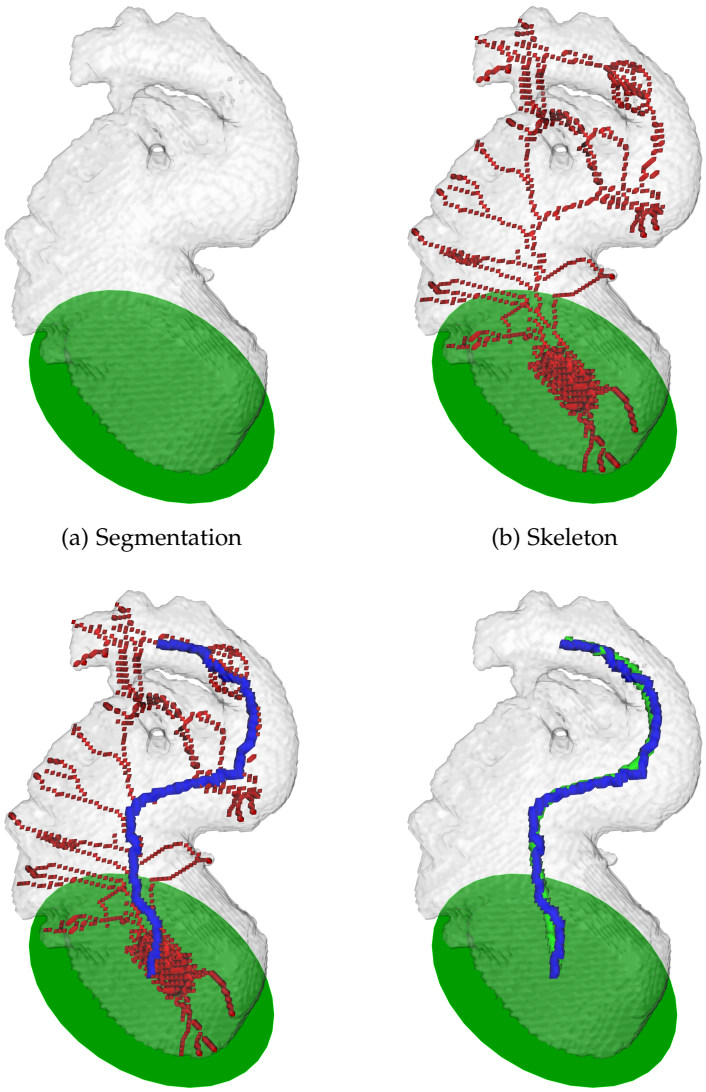

(a) Segmentation (b) Skeleton

(c) Ground (d) Our vs. ground

Figure 4.12: The ground truth centerline extraction process.

inside the left atrium are discarded after delineation. This is why the part of the skeleton near the orifice plane is wider.

Finally, we calculate the Hausdorff distance [45] between our detected centerline and the ground truth centerline. This metric, commonly used in computer vision, measures how far two subsets of a metric space are from each other. An intuitive, but slightly informal, explanation of the metric could be: given that both our centerline and the ground truth centerline are comprised of points in 3D space, for every point in one centerline we can find the distance to its closest point in the other centerline. The Hausdorff distance then represents the greatest of all the distances. In other words, two centerlines will be

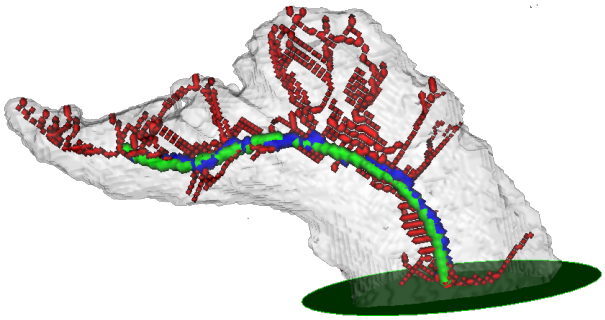

(a) With skeleton

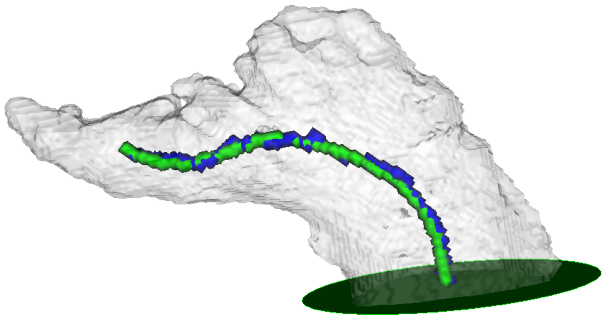

(b) Without skeleton

Figure 4.13: Centerline validation example with/without skeleton.

close in Hausdorff distance if every point on either centerline is close to some point on the other centerline.

A formal definition of the Hausdorff distance follows. Let C be the set of all points $\mathbf{p} \in \mathbb{R}^3$ comprising the final smooth centerline. Similarly, let G be the set of all points $\mathbf{q} \in \mathbb{R}^3$ comprising the ground truth centerline. We define their Hausdorff distance $d_H(C, G)$ as:

$$d_H(C, G) = \max\{\sup_{\mathbf{p}\in C} \inf_{\mathbf{q}\in G} d(\mathbf{p}, \mathbf{q}), \sup_{\mathbf{q}\in G} \inf_{\mathbf{p}\in C} d(\mathbf{p}, \mathbf{q})\}, \tag{4-11}$$

where sup represent the supremum of a set, the inf represents the infimum of a set, while $d(\mathbf{p}, \mathbf{q})$ represents the Euclidean distance between two points.

We proposed the Hausdorff distance between the centerlines as an appropriate metric for the validation of the proposed method, because it indicates the absolute distance between the two centerlines. As this metric is very sensitive to outliers, achieving low Hausdorff distance between the two centerlines indicates that the distance between the centerlines is small along the whole centerline.

The proposed method achieves an average Hausdorff distance of 3.3944 voxels (2.0376mm). The calculated Hausdorff distances for all datasets are presented in the Table 4.2. The table shows two metrics: the distance in voxels and the distance in millimeters. The reason being

that different input DICOM images have different spacing depending on the patients anatomy, the settings used while imaging and the imaging device. Some of the results are shown in the Figure 4.14.

The achieved results represent an acceptable distance to the ground truth centerline from a clinical standpoint. The occlusion is still a relatively novel procedure mostly performed by specialized medical centers. According to the current guidelines, the margins within which the clinicians interpret the measurement when sizing the device are considerable. The procedure requires significant expertise, as well as subjectivity, when interpreting the measurements.

For example, an average LAA length is measured at $48 \pm 12.1mm$ [179]. Interestingly, measurements of the LAA orifice diameters in CCTA images differ almost $5mm$ depending on the modality (26.5 ± 5.8 and $21.7 \pm 5.7mm$ measured in 2D oblique and 3D view). In terms of selecting the device of the appropriate size for the occlusion, the manufacturer guidelines recommend upsizing of the device (w.r.t. maximal ostial diameter) by $2 - 6mm$ for ACP/Amulet device and 5-35% for the WATCHMAN device [158]. Additionally, measurements between different modalities also significantly differ. Mean maximal depth measurement (LAA length) for CCTA differed from the TEE-obtained and fluoroscopy-obtained measurements by $3.1 \pm 5.8mm$ and $6.5 \pm 7.8mm$, respectively [158]. Maximal diameter measurements of the orifice in CCTA images were consistently $1 - 2mm$ larger compared to TEE, and $2 - 4mm$ larger compared to fluoroscopy [158]. After the procedure, peri-device leak of $< 5mm$ does not require anti-coagulation therapy (meaning that it is not consider a significant enough risk for thrombus formation) [69]. Finally, Spencer et al. [162] showed that mean LAA dimensions can increase by $\sim 2mm$ depending on the patients state of hydration.

All things considered, we believe that an average distance of $\sim 2mm$ demonstrated by our method is well within the margins of error the clinicians performing the procedure are used to.

4.7 DISCUSSION

In this chapter we explain in more detail the effects of the user determined input parameters on the results of the presented centerline detection method. The method finds a path from the selected seed point to the center of the left atrium and extracts the centerline. The centerline will be used as input in the LAA segmentation and the LAA orifice localization methods presented in the next two chapters. As previously mentioned, the method requires only two parameters: a threshold value and a single seed point inside the LAA. Both types of input are intuitive to the trained medical users.

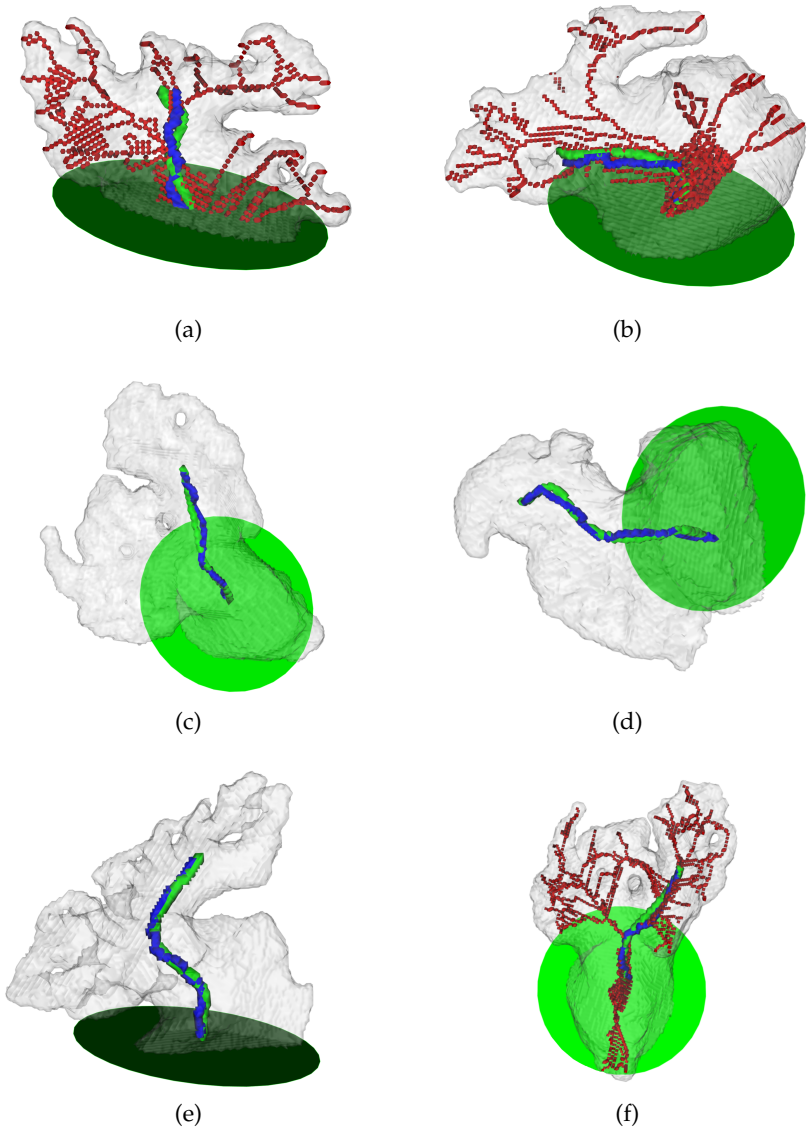

(a) (b) (c) (d) (e) (f)

Figure 4.14: Example centerline detection results.

4.7.1 *Threshold value selection*

The threshold for centerline detection is selected in a manner common for medical software: by visual selection where the effect of a particular value is directly displayed to the user. The thresholding step effectively performs a pre-segmentation, creating a binary mask, and all following steps are performed by analyzing the mask image. Both the centerline detection method and the methods for segmentation and orifice localization use the heart anatomy masked in the thresholding step. However, the proposed method is designed to be robust to the selected threshold.

Table 4.2: Hausdorff distance per dataset between the ground truth centerline and our detected centerline.

Dataset	Hausdorff distance [voxels]	Hausdorff distance [mm]
1	2.6982	1.4784 mm
2	4.5253	2.6278 mm
3	4.0821	2.6658 mm
4	3.1481	1.6816 mm
5	4.1648	2.3498 mm
6	5.9860	3.6761 mm
7	2.9396	1.6175 mm
8	2.4173	1.3752 mm
9	4.1313	2.3116 mm
10	2.5649	1.3641 mm
11	2.5724	1.5120 mm
12	2.6778	2.4533 mm
13	3.5771	1.8862 mm
14	3.1923	1.6979 mm
15	2.5117	1.3937 mm
16	3.7950	2.2668 mm
17	2.7213	2.2813 mm
Avg:	3.3944	2.0376 mm

The maximum radius tracking method is very robust to over-segmentation (Figure 4.2b). The method works best when there is a clear delineation in the mask image between the left atrium and both the left ventricle and the aorta. Still, the method will perform adequately even if the image is oversegmented. The method tracks the largest radii in the image and for anatomical reasons the radii near the LV and near the aorta will be smaller then in the center of the LA. Even if the masked image leaks between the LA and the aorta, the tracked path will not leave the LA beacuse the radii inside the leak is always a lot smaller than the radii in the center of the LA. Also, the grayscale intensity of the mitral valve compared to the contrasted blood will create a narrowing between the LA and the LV, resulting in a decreased radii values. Thus, the maximum radius path will not leave the left atrium.

The maximum radius tracking method is less robust to selection of a too high threshold value. The problem with too high threshold is the manifestation of holes in the mask image (as evident in the Figure 4.2d in the left atrium). The holes mainfest in both the LAA and the left atrium. The location of holes has the biggest effect on the method results. If holes were located near the LAA orifice, the radii of voxels near the holes would be a lot smaller than it should be according to patient's anatomy. In which case the tracking could have problems following the largest radii, exiting the LAA and finding the center of the left atrium. However, if the threshold is set so high that the masked LAA contains holes, there probably won't be any leaks. Thus, the tracking will stay inside the LAA until the number of iterations runs out.

All things considered, it is very unlikely for the trained user to select the threshold value so incorrectly that the method fails to detect the centerline.

4.7.2 *Seed points*

The selection of seed points is performed with a click in a desired location in 2D slices. The process is similar to placing a segmentation bubble in ITK-SNAP. The seed point should be placed deep in the LAA, near the tip. The location of the seed point will not disrupt the maximum radius tracking method. The maximum radius path will always find its way out of the LAA and in to the LA. However, the length of the LAA covered by the detected centerline does depend on the seed point location. The detected path will not extend throughout the whole LAA, unless the seed point is placed near the tip of the LAA.

It is possible that the LAA has a widening near the tip, due to its very irregular anatomical shape. If the starting seed point is placed near that widening, the tracking could go in the wrong direction – towards the tip instead of towards the LA. The tracking will add all the largest radii in that widening to T. However, at some point the largest radius voxel in the search set P will be the voxel which will continue the tracking towards the LA. Theoretically, the only way the algorithm could fail to reach the LA is if the widening near the tip also has a significant leak. It that case the tracking could go through the leak and enter some other anatomical structure, potentially one of the pulmonary veins. Radii in pulmonary veins are often larger than in the LAA and the algorithm would not return to the LAA . It should be noted that this case never occurred with our datasets. If the leak near the tip is large enough for the tracking algorithm to pass through the leak, the threshold value is probably very incorrectly set.

4.7.3 *Implementation details*

The centerline smoothing algorithm we explained in Section 4.5.3 is defined for 2D images. However, in our case the real data values are three-dimensional, so the curve fitting implementation we use is generalized to N-dimensional spaces. Our implementation is using the curve fitting methods from the `scipy.interpolate` package from Scientific Python (SciPy) package [79]. The main advantage of this smoothing method is that it does not require any user interaction. All the parameters can be appropriately predetermined. The weights w_r for all data values are the same because our input data is already an ordered one-voxel wide centerline. The smoothness of the curve is more important than the fitting error (δ), so the parameter S is relatively large. The SciPy documentation recommends value for S in the range between $[m - \sqrt{2 * m}, m + \sqrt{2 * m}]$, thus for our datasets we are using the lowest value in that range: $S = m - \sqrt{2 * m}$. We previously specified that we are using the cubic splines, thus the parameter $k = 3$. The final configured parameter is the initial number of knots g which is set to 5. The method will increase the number of knots if necessary.

4.8 CONCLUSION

In this chapter we proposed a novel method for the left atrial appendage centerline extraction. The method requires two inputs from a trained user: threshold and a seed point inside the LAA. Proposed method finds a path in the thresholded (mask) image between the seed point and the center of the LA and extracts the centerline. The centerline will be used as an input in the segmentation and orifice detection methods explained in the next two chapters. The proposed detection method is validated on 17 ground truth centerlines extracted from CCTA images manually segmented by a medical expert. The validation performed by calculating the Hausdorff distance to the ground truth centerlines showed an excellent performance of the method, with a consistently small error, which was in most of the cases bellow $2mm$ – such error is well within the margins of error proposed by current procedural guidelines for the procedure. Hence, we cen conclude that the proposed method shows potential for clinical use in the planning of the LAA occlusion procedure.

5

CENTERLINE-BASED LAA SEGMENTATION

In this chapter we will propose a novel method for semi-automatic left atrial appendage (LAA) segmentation. Left atrial appendage segmentation is an important step during the LAA closure procedure planing. Accurate measurements are required for planning the procedure. Accurate segmentation can aid physicians in determining the measurements, the feasibility of the closure procedure, as well as determining the correct type and size of the occlusion device for each patient. Additional benefit of the accurate segmentation is the ability to choose the correct device size and type using a 3D printed model of the LAA [84, 136]. Physicians can test devices of different sizes to determine the best fit. Computer methods for left atrial appendage segmentation are still relatively underdeveloped. To the best of our knowledge there are only few published methods dealing with LAA segmentation. Related methods are described in the section 5.1, while the detailed overview of available methods is provided in section 3.5.2, along with their advantages and disadvantages. All described methods are machine learning based. The main challenge with the machine learning based methods (such as the methods described above) is the reproducibility of the results without access to the training datasets.

The main advantage of our method, compared to other state-of-the-art methods, is the invariance to the type and dimensions of the input image used for segmentation. The segmentation is performed by extracting the LAA from a binary image, created from the user selected threshold value. Thus, the method can work with binary images created from any type of 3D image (e.g., binary images created with active contours, or images from MRI). The only requirement is that the input binary image contains the LAA and at least a part of the left atrium. The main contribution proposed in this chapter is a novel left atrial appendage segmentation method based on the LAA centerline path. The main input to the method is the detected centerline proposed in the previous chapter. The results indicate good potential for surgical planning. The work described in this chapter appeared in the proceedings of in the international conference [99], and a journal paper in Science Citation Index [100].

5.1 INTRODUCTION

Medical image segmentation methods represent one the most important applications in the area of medical image processing. Their goal is to partition the image into regions and extract relevant medical information. When applied to the left atrial appendage analysis, the goal of image segmentation methods is to provide physicians with relevant information about the shape and the anatomy of the LAA. In this section, we provide an overview of different approaches to LAA segmentation available in the literature. To the best of our knowledge, only a small number of LAA segmentation methods exist. However, in the last few years, there was a noticeable increase in the number of the proposed methods.

A common segmentation approach, often used in whole heart segmentation [48, 200, 203], is based on adapting an existing model (ASM) to segment a new image. Despite the popularity of model-based approach in whole heart segmentation (WHS), model-based segmentation of the LAA is complicated due to the considerable variability in the shape, size and orientation of the LAA in the heart. Grasland-Mongrain et al. [58, 59] proposed an LAA segmentation method based on shape-constrained deformable models. The method is an upgrade to an already existing framework [47] capable of localizing and segmenting the whole heart. Using the segmentation result from the framework, the method grows the mesh of the LAA-LA interface and inflates it into the LAA .

Two similar approaches have been proposed by Zheng et al. [197, 201] and to the best of our knowledge, these are the only two fully automatic approaches available. Both methods use multi-part models, where individual models are fitted using marginal space learning [198] and later merged into a consolidated mesh. However, one approach [197] fits six individual models (atrial chamber, the appendage, and four pulmonary veins) to image and refines the segmentation using graph-cuts, while the other approach [201] fits only two individual models (atrial chamber and the appendage), but segments the PVs and refines the segmentation using region-growing based on adaptive thresholds.

An approach based on per-slice 2D segmentation has been proposed by Wang et al. [177]. Within a selected ROI the method generates a number of segmentation proposals for every 2D slice, ranks the proposals using a trained random forest regressor and fuses the best proposals into a 3D volume. Jin et al. [73] proposed a method which follows the same general idea, except it creates the 2D per-slice segmentations using a fully convolutional network and merges them into a 3D volume using 3D conditional random fields [32]. The same

group proposed two additional methods based on the Wang et al. [177] segmentation approach. The first method [74] creates a model of the LAA neck from the segmentation result. The second method performs the LAA segmentation in an input 4D CCTA image and builds a 3D model of every time instance in the image in order to diagnose atrial fibrillation.

The limitation of all of the approaches presented so far is that they require large fully labeled datasets for training. Finally, Morais et al. [126] proposed a centerline based LAA segmentation approach which works in 3D TEE images. The approach initializes a model from a manually created centerline, grows the model using fast contour growing and determines the segmentation from refined model.

In this chapter we develop a novel semi-automatic method for the segmentation of the LAA which is capable of obtaining an accurate LAA segmentation from an input image of any size and modality and does not require training phase. The method requires only two input parameters: threshold value and a point inside the left atrial appendage. The proposed method works directly in 3D space of CCTA contrasted images. After the segmentation, we allow the user to select the location of the LAA orifice. The user selects the orifice as a delineation plane between the appendage and the LA. Finally, we perform an additional segmentation refinement step based on the selected delineation plane.

The proposed method consists of the following steps depicted in the Figure 5.1:

1. Thresholding – Produces a binary mask image using the provided threshold value. The LAA will be extracted from the binary mask image in subsequent steps.

2. Radius image generation – Radius images are calculated by applying to the distance transform to the binary image as was explained in Section 4.3 .

3. Centerline detection – Detects the centerline from the seed point to the center of the left atrium, which will be used to initialize the segmentation. The centerline detection method was detailed in Chapter 4.

4. Initial segmentation. This step reconstructs an approximate LAA volume from the detected centerline by adding to the initial segmentation image the largest maximum inscribed sphere of every point in the centerline.

5. Fine segmentation. An original decreasing radii segmentation algorithm is employed here to grow the initial segmentation towards the border regions of the LAA and LA anatomy. At this

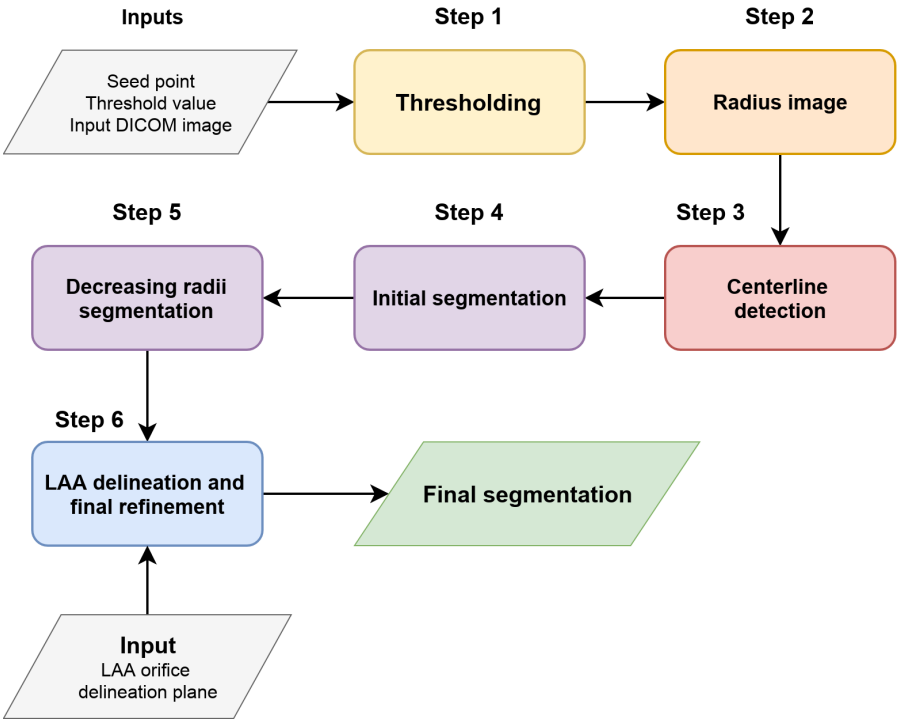

Figure 5.1: Proposed semi-automatic LAA segmentation method flow diagram.

point the segmentation contains both the LAA and a part of left atrium.

6. Delineation – This final step is performed after an additional input from the user in order to determine the LAA orifice. The user selects the delineation plane on the visualized segmentation. We extract the LAA and perform the segmentation refinement by adding the LAA components adjacent to the segmentation, which the decreasing radii segmentation step failed to segment.

The overall method allows the user to accurately segment the LAA with minimal interaction and select the location of the LAA orifice directly on the visualized segmentation. In the final step, the user selects the delineation plane by selecting three 3D points on the segmentation result from the previous step. Selected points form a plane dividing the appendage from the left atrium. The LA is discarded from the segmentation and only the LAA is refined.

5.2 THRESHOLD SELECTION

In this section we explain in more detail how the threshold selection affects the segmentation results. We also explain what are leaks in the thresholded image and their effect on the segmentation results. It

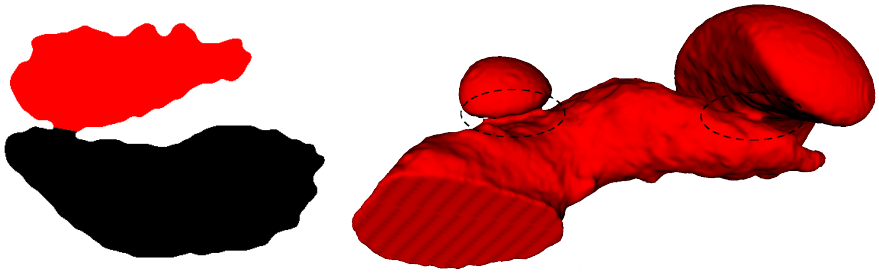

(a) Example leak (b) Leak effects on segmentation

Figure 5.2: Example of leaks in mask image due to thresholding. (a) Example of leak in one slice (LAA – red, pulmonary vein – black) (b) The effect of leaks on interactive segmentation using Geodesic active contours in ITK-SNAP software. Dashed ellipses show locations where the segmentation leaked.

should be noted that the thresholding step affects both the centerline detection results and the later segmentation results. The effect of the selected threshold on the centerline detection step is explained in Section 4.2. This section will focus on how the thresholding affects the segmentation step of the method. The purpose of the thresholding step is to create a binary mask which contains the LAA. It should be noted that at this point the appendage is still not delineated from the rest of the heart. The thresholding determines which part of the appendage will be segmented – the rest of the method extracts only the appendage from the binary mask.

The user selects the threshold value for the dataset with a simple slider by visual inspection of 2D slices. Since our proposed method extracts the LAA from the binary image, the volume of the LAA extracted during the subsequent segmentation steps depends on the selected threshold value. A simple guideline for selecting the threshold value is: the chosen threshold value should be the largest value where the whole LAA is still in the foreground of the mask image. Any part of the LAA not in the foreground of the mask image after thresholding will not be a part of the final segmentation. Still, the proposed method is robust to the threshold selection and unless the selected threshold value is very inaccurate, the selected threshold value will not disrupt the functioning of the segmentation method. Threshold value mostly determines the extent of the LAA anatomy that will be segmented. The rest of this section describes the effects of the selected threshold value on the segmentation results.

There is a significant difference in intensity values in CCTA images between the areas of the heart that do and do not contain contrasted blood. However, because of vast differences in shape, size and location of the LAA in the heart it is possible that after thresholding the

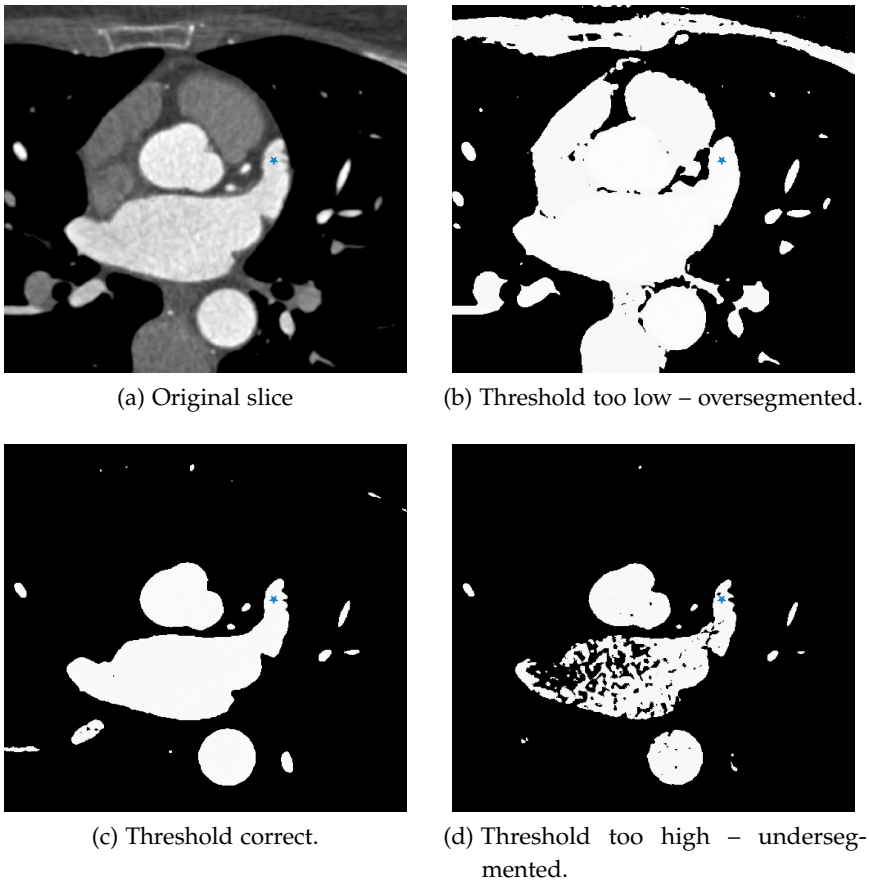

(a) Original slice

(b) Threshold too low – oversegmented.

(c) Threshold correct.

(d) Threshold too high – undersegmented.

Figure 5.3: The effects of different threshold values on oversegmentation and undersegmentation. Blue star represents the seed point inside the LAA

LAA appears connected to other anatomical structures, most often to one of pulmonary veins. Occurrence of such connection in the mask image is called a leak and illustrated in Figure 5.2a. The example of a segmentation problem due to leaks is shown in 5.2b. Still, threshold based segmentation methods are often used because they are visually very intuitive to users and there is only one parameter they need to configure – the threshold value. There is an inherent trade-off when using thresholding based segmentation. If the threshold value is too high, leaks can be avoided but the resulting segmentation will be undersegmented compared to the real LAA anatomy. If the threshold is too low, oversegmentation occurs and leaks become a significant problem for segmentation algorithms. Additionally, heart moves while imaging and the borders in the image get blurred, which increases the oversegmentation or undersegmentation problem. Figure 5.3 shows the effects of thresholding on a single slice. High level of noise present in CCTA images can also result in holes in thresholded image if the

(a) Grayscale (b) Threshold 173 (c) Threshold 274 (d) Threshold 410 (e) Threshold 535

Figure 5.4: The effects of different threshold values on segmentation of the blurry border regions in the LAA.

threshold value is too high. Figure 5.4d shows the problem with holes in binary image formed inside the contrasted region due to noise.

Our proposed method is designed to be robust to leaks in the mask image. The method will accurately extract the LAA even with leaks present in the image. Thus, the user should always select the threshold value in such a way that the anatomy they wish to segment is in the foreground of the mask image. Figure 5.4 shows the effects of the threshold values on the anatomy which will be included in the segmented image. For each threshold in the figure the proposed method will correctly extract the LAA from the mask image. Thus, the selected threshold value depends on the extent of the anatomy the user wants to include in the final segmentation. The user does not have to try to avoid the leaks in the mask image by setting the threshold value higher than necessary. The rest of the steps in the method will ensure that the LAA is extracted from the binary mask without leaking to other areas.

The same mask image is used for all steps in the segmentation method, meaning that all steps in the method use the same threshold value. We have to balance between the effects of the selected threshold on the centerline detection and on the segmentation. However, the centerline detection method is very robust to the selected threshold value, as explained in the Section 4.2. Thus, we will always choose the threshold value which will result in a better segmentation, while counting on the centerline detection methods robustness to accurately detect the centerline.

5.3 DECREASING RADII SEGMENTATION

In this section we present a novel, leak resistant segmentation method which works by improving an initial segmentation toward the border regions with decreasing radii. The method extensively uses the radius

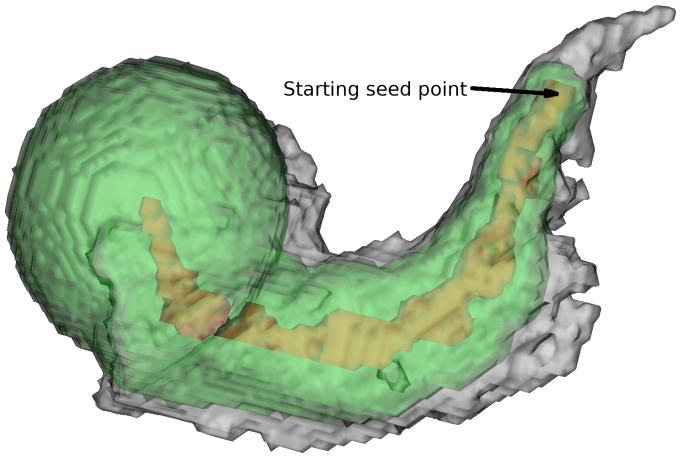

Figure 5.5: Initial segmentation (green) created from maximum radius path (orange). White color represents the real boundaries of the LAA . This image was reported in our own work: Leventić et al. [99].

image (see Section 4.3), because the whole method is based on adding to the segmentation the spheres of a certain criteria. First, we create an initial segmentation which contains regions with the largest radii in an anatomical structure. Next, the method iteratively grows the initial segmentation towards border regions of the anatomy where the radii of voxels is decreasing. The only requirement for the method is the initial segmentation image to initialize the region growing. Finally, we stop the iterative growing when all the border regions of the anatomy have been segmented. The initial segmentation image should contain the voxels with largest radius in the area we want to segment. Thus, the method does not have to be used exclusively for LAA segmentation. For example, atrium segmentation shown in white in Figure 5.9 (created for the visualization purposes) is segmented using the method proposed in this section.

5.3.1 *Initial segmentation*

Initial segmentation is used as a starting segmentation for the Decreasing radii segmentation method. The goal with creating the initial segmentation is to segment a large part of the LAA while making sure that none of the leaks have been segmented. The initial segmentation is created using either the maximum radius path or the detected centerline as the input, both of which are explained in detail in the previous chapter. Both the maximum radius path and the centerline are represented as a set of voxels, containing voxels in the center of the LAA all along its length. Thus, both sets of voxels are a valid input to the method. Let T denote a set of all voxels of the chosen input. We

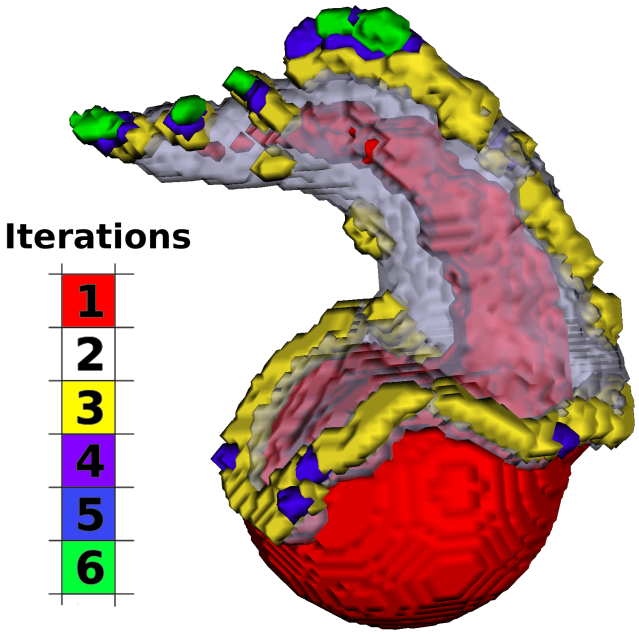

Figure 5.6: Iterations of the decreasing radii segmentation. Color code 1 represents initial segmentation. This image was reported in our own work: Leventić et al. [99].

create the initial segmentation by adding to the initial segmentation set I the maximum inscribed sphere for every voxel in T

$$I = \bigcup_{\mathbf{v} \in T} S(\mathbf{v}). \tag{5-1}$$

where $S(\mathbf{v})$ is defined in (4-2). Figure 5.5 shows the initial segmentation in green color. The maximum radius path, used for creating the initial segmentation, is shown in orange color. The real LAA shape is shown in white.

5.3.2 *Segmentation algorithm*

In this subsection we propose a novel method for leak resistant segmentation based on the initial LAA segmentation. The method will iteratively grow the initial segmentation towards the edges of the LAA. Growing is performed by adding spheres where the radii inside spheres decreases. The radii of the voxels in the LAA will gradually decrease as the segmentation approaches the edges of the anatomy. We do not grow the segmentation towards the regions of the anatomy where the radii are increasing, as those areas are usually regions inside the leaks or regions where the segmentation is entering another, larger anatomical structure (in this case the left atrium). For successful segmentation the initial segmentation has to contain LAA regions with the

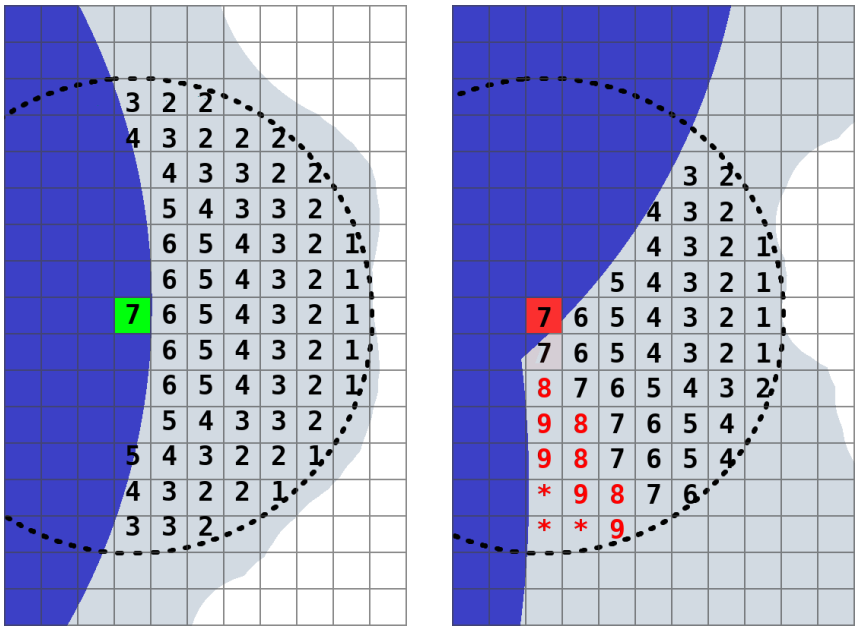

(a) Sphere added to segmentation (b) Sphere not added to segmentation

Figure 5.7: Decreasing radii segmentation: conditions for adding the sphere. (a) Voxels in the spherical neighborhood of the current voxel will be added to the segmentation because all of them have the radius value lower than the radius value of the current voxel. (a) None of the voxels in the spherical neighborhood of the current voxel will be added to the segmentation because some of them have the radius value higher than the radius value of the current voxel. This image was reported in our own work: Leventić et al. [100]

largest radii values. Figure 5.6 shows the iterations in the segmentation process of one of our datasets. Each iteration is shown in a different color, with the initial segmentation being the iteration 1. For easier visualization the segmentation in the figure is limited to 5 additional iterations. The initial segmentation used for this example is shown in Figure 5.5 in green color.

Decreasing radii segmentation runs iteratively for all voxels at the edge of segmentation while at least one sphere in an iteration has been added to the segmentation. Algorithm stops after the iteration in which no voxels have been added to the segmentation. The algorithm iteratively tests all the voxels at the edge (boundary) of the current segmentation. For each boundary voxel the algorithm tries to determine whether the spherical neighborhood of the voxel should be added to the segmentation. Next, the algorithm adds a spherical neighborhood of the voxel to the segmentation if the radii of all voxels in the unsegmented part of that neighborhood are less than or equal to the radius of currently observed voxel (the radius of the voxel at the center of the sphere). Formal explanation of the method follows.

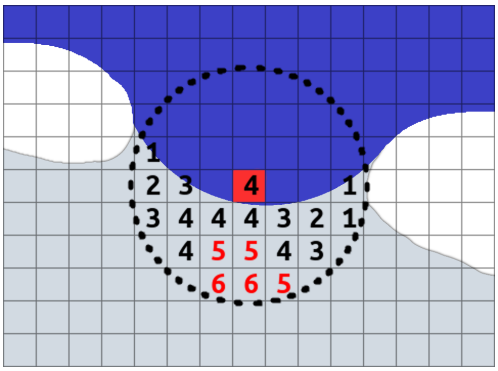

Figure 5.8: Segmentation leaks are characterized as regions in which the values of maximum radii increase. Because of this, the decreasing radii segmentation method will prevent the leak regions from being added to the segmentation. This image was reported in our own work: Leventić et al. [100]

Let H^i denote a set of all segmented voxels in an iteration i. Let $N_{26}(\mathbf{v})$ be the 26-neighborhood of voxel $\mathbf{v}$ – a set of 26 voxels – all the nearest (first) neighbors of $\mathbf{v}$ horizontally, vertically and diagonally in 3D.

In first iteration the method starts with the set of segmented voxels containing only voxels from the initial segmentation: $H^1 = I$. For an iteration i the voxels on the edge (boundary) of the set of segmented voxels H^i are defined as:

$$E^i = \left\{ \mathbf{v} \in H^i \;\middle|\; \exists \mathbf{q} \in N_{26}(\mathbf{v}),\ \mathbf{q} \notin H^i \right\}. \tag{5-2}$$

Let us denote the set of unsegmented voxels centered at voxel $\mathbf{v}$ within the maximum inscribed sphere $S(\mathbf{v})$ with:

$$U^i(\mathbf{v}) = \left\{ \mathbf{q} \;\middle|\; \mathbf{q} \in S(\mathbf{v}),\ \mathbf{v} \in H^i,\ \mathbf{q} \notin H^i \right\}, \tag{5-3}$$

For every edge voxel $\mathbf{v} \in E^i$ we add to segmentation H^i all unsegmented voxels inside its spherical neighborhood $U^i(\mathbf{v})$ if the radii of all those voxels in $U^i(\mathbf{v})$ are smaller or equal to the maximum radius value of the given voxel $r(\mathbf{v})$:

$$A^i(\mathbf{v}) = \begin{cases} U^i(\mathbf{v}) \,;\, \forall \mathbf{q} \in U^i(\mathbf{v}) :\ r(\mathbf{q}) \leq r(\mathbf{v}) \\ \quad \emptyset \,;\, \text{otherwise} \end{cases} \tag{5-4}$$

$$A^i = \bigcup_{\mathbf{v} \in E^i} A^i(\mathbf{v}). \tag{5-5}$$

Voxels A^i are added to the segmentation for the next iteration:

$$H^{i+1} = H^i \cup A^i. \tag{5-6}$$

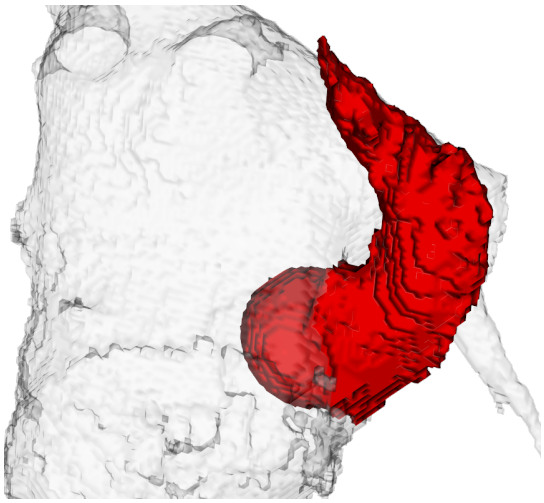

Figure 5.9: The result of running the decreasing radii segmentation method: Segmented LAA (red), left atrium (white).

The algorithm stops when no new voxels were added to segmentation in an iteration, i.e. when $H^{i+1} = H^i$.

Figure 5.7 illustrates the conditions for adding a sphere to the segmentation. An example where the spherical neighborhood will be added to the segmentation is shown in Figure 5.7a. The voxel at the center of the neighborhood has a radius value of 7. All voxels in the unsegmented part of the neighborhood have radii smaller than 7. Thus, the condition given in (5-4) will be fulfilled and the voxels in the unsegmented part of the sphere will be added to the segmentation. Figure 5.7b illustrates an example where the spherical neighborhood will not be added to the segmentation. We can see from the figure that the radii of voxels in the lower part of the neighborhood (red values) are larger than the radius of the voxel at the center of the neighborhood. Thus, the condition in (5-4) is not fulfilled and in this example no voxels will be added to the segmentation.

An important property of the proposed method is its resistance to leaks. The leaks are characterised by one narrow section which connects two wide anatomical structures. An illustration of the method's robustness to leaks is given in the Figure 5.8. The figure shows a spherical neighborhood of a voxel inside a leak. Some of the unsegmented voxels in the neighborhood (red) are larger than the radius of the sphere. These voxels belong the the anatomical structure the segmentation is leaking into. The spherical neighborhood of this voxel will not be added to the segmentation because the radii of red voxels is larger than the radius of the voxel at the center of the neighborhood. The segmentation will not leak through to the other anatomical structure whenever the radii of voxels inside the leak are smaller than the radius of that other anatomical structure.

In order to be able to easily distinguish between different intermediary result images in the segmentation process, we call the segmentation image created from maximum radius path in section 5.3.1 the *initial segmentation image*. The segmentation result created in this section using decreasing radii method is called the *fine segmentation image*, while the final segmentation image explained in following section is called *final segmentation image*. Figure 5.9 shows the result of running the decreasing radii segmentation method (the fine segmentation image). The resulting segmentation is shown in red. Left atrium shown in the figure in white is added for visualization purposes (left atrium segmentation is not a part of the proposed method). The segmented LAA in the figure is not correctly delineated from the left atrium. We can see a large sphere of the segmentation protruding to the left atrium. However, at this point the region belonging to the LAA is properly segmented and we have to delineate and further refine the segmentation. We allow the user to select the delineation plane and refine the segmentation according to the selected plane. The plane selection and segmentation refinement is explained in the next section.

5.4 DELINEATION AND REFINEMENT

This section explains how we create the final segmentation. First we visualize the resulting fine segmentation image and present it to the user. User determines the delineation plane between the LAA and the left atrium by selecting three points on the visualized segmentation. At this point we are sure that most of the LAA has been properly segmented. Visualized segmentation also contains a part of the left atrium. Visualized segmentation provides enough information about the LAA anatomy to the user to be able to properly select the delineation plane. The user selects three points representing the plane from the user interface (UI) of the application. The user can freely interact with the segmentation in order to find the optimal delineation plane. Figure 5.10a shows the delineation plane selected by the user. Plane is determined by three points represented in the figure with small red, green, and blue spheres (red point is not visible from this angle). We perform one final refinement step after the user confirms the chosen delineation plane. Refinement is performed through the following steps:

1. Remove from the fine segmentation image all voxels in the delineation plane.

2. Discard the part of the segmentation belonging to the left atrium by extracting from the segmentation only the connected com-

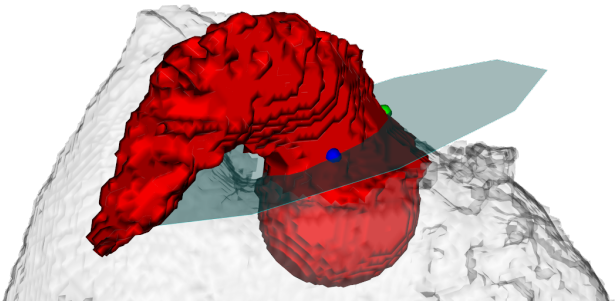

(a) Delineation plane selected. Plane is determined by selecting three points on the segmentation (red, blue and green)

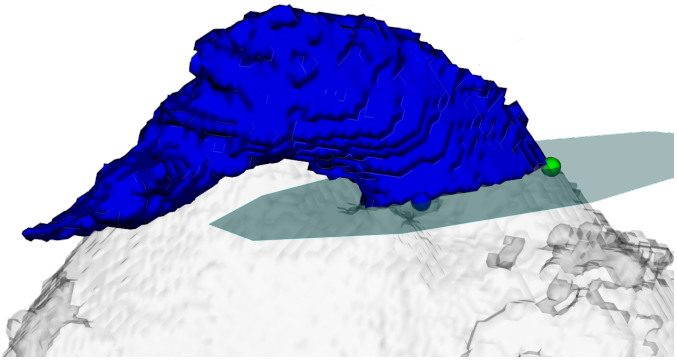

(b) Final segmentation after delineation and refinement

Figure 5.10: Selection of the delineation plane between the LAA and the LA and the final segmentation result according to the selected plane.

ponent containing first seed point (the seed point placed in the LAA). We call this image the extracted segmentation image.

3. Find all the connected components in the mask image while setting the LAA from the extracted segmentation image to a distinct label. The largest component in the image (containing the whole heart except for the extracted part) will have a different label. However, depending on the dataset, it is possible that connected components labeling will create additional components which were disconnected from the rest of the heart by the extracted LAA.

4. Add to the final segmentation image all the components connected to the extracted LAA with the volume and the bounding box smaller than the extracted segmentation.

The final segmentation result is shown in the Figure 5.10b. Most of the time the components that got disconnected from the rest of the heart will be parts of the LAA that the decreasing radii segmentation algorithm failed to segment. The components are probably a part of the LAA if the components are connected to the extracted segmentation

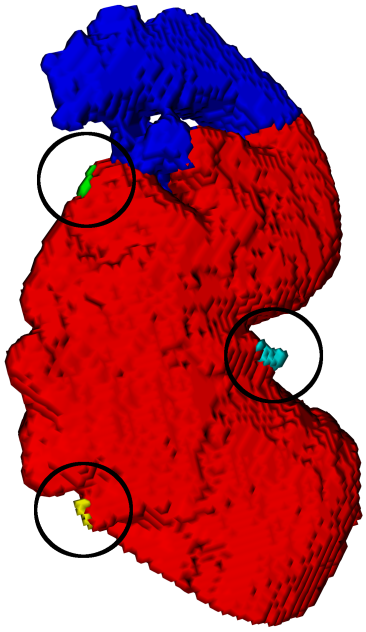

Figure 5.11: Adding of additional components after delineation. Extracted segmentation shown in red, added components shown in other colors. This image was reported in our own work: Leventić et al. [100]

and not connected to the rest of the heart. However, depending on the selected threshold and the patients anatomy, it is possible for the segmentation to disconnect a part of the vein. When that happens the component containing part of the vein not connected to the rest of the heart will be connected to the extracted segmentation. Such components are not a part of the LAA and should not be added to the final segmentation. We check that the volume and the bounding box size of the component are both smaller than that of the extracted segmentation. Checking the volume will prevent adding the component containing the rest of the heart to the segmentation. Checking the bounding box will prevent adding the disconnected part of the veins, which are often long and narrow. Their volume will be smaller than the extracted segmentation, but their bounding box size probably will not be. It should be noted that in our experiments the breaking up of veins only happens when the selected threshold value is not optimal. Figure 5.11 shows the components added in the refinement step (different dataset than previous figures).

5.5 RESULTS

The segmentation results were evaluated on 17 CCTA images, against manually segmented ground truth segmentations by two medical

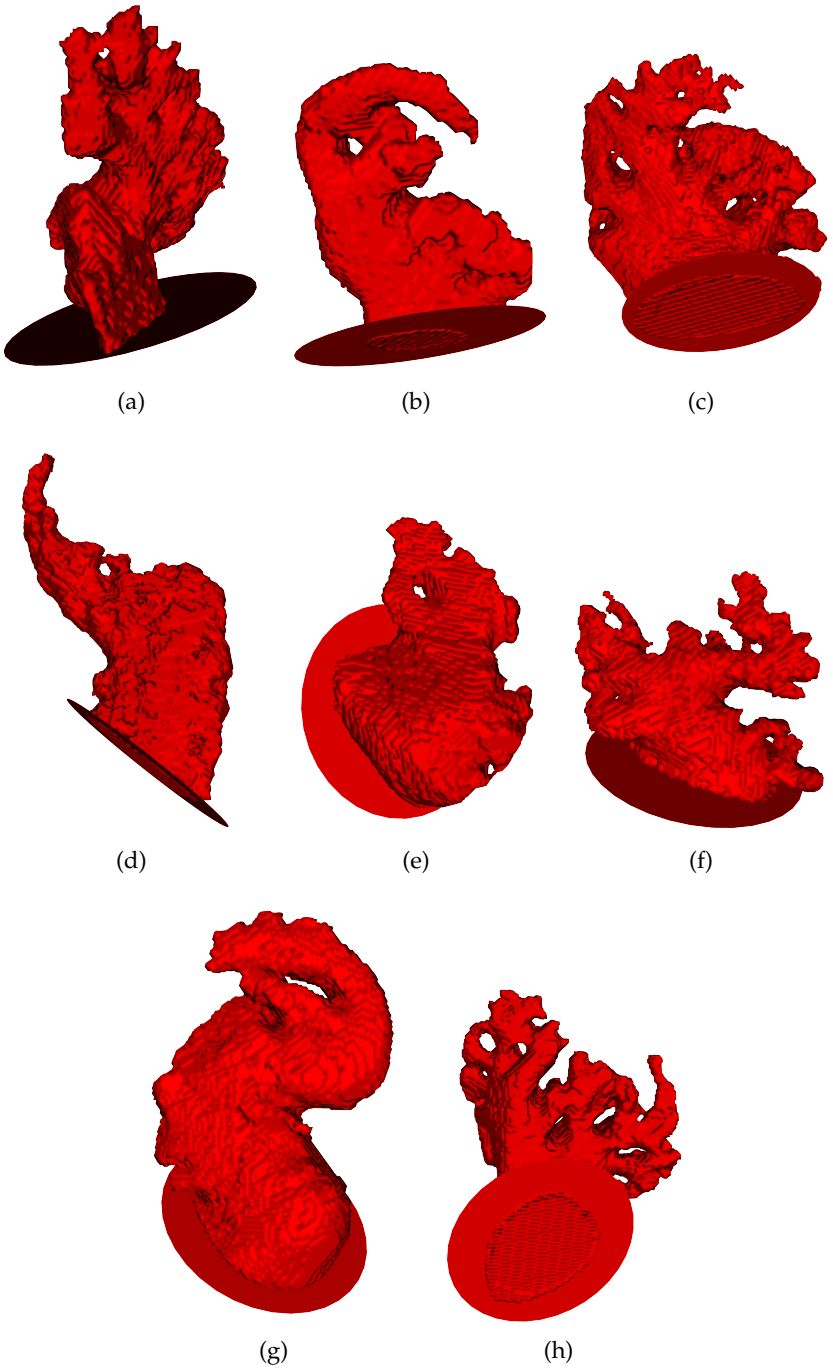

Figure 5.12: Examples of LAA segmentation results. This image was reported in our own work: Leventić et al. [100]

Table 5.1: Validation dataset (17 patients)

	N	%
Patient age		
Under 35	3	17.65%
35 - 44	2	11.76%
45 - 54	2	11.76%
55 - 64	6	35.29%
65 and older	4	24.53%
Patient gender		
Male	6	35.29%
Female	11	64.71%

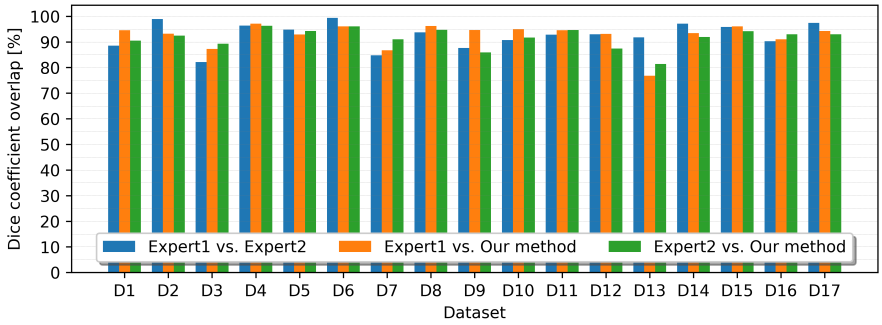

Figure 5.13: Plot of dice coefficients overlap. This image was reported in our own work: Leventić et al. [100]

experts: a cardiovascular surgeon and a radiologist. All images were acquired using a Siemens Somatom 64-slice scanner for the purpose of Coronary CT Angiography. All patients have given their informed consent for the inclusion in the study. The patient data is presented in Table 5.1. Ground truth segmentations were created using the ITK-SNAP software [194]. Doctors selected the appropriate threshold and used the Geodesic active contours method [27] implemented in ITK-SNAP to segment the LAA. Finally, doctors manually corrected the segmentation using the paintbrush tool. During the ground truth creation twelve out of 17 datasets had extensive leaks due to the selected threshold and required extensive corrections. Creation of ground truth segmentations required on average 10 minutes per doctor per dataset, with the shortest dataset creation lasting around 5 minutes and the longest 17 minutes.

Table 5.2: Dice coefficients overlap (n=17). Table shows dice overlap between segmentations of the two consulted medical experts (E1, E2) and the overlap of segmentation results with our method between each of the experts' segmentations.

Dataset	dice(E1, E2)	dice(E1, our)	dice(E2, our)
D1	88.50%	**94.58%**	90.51%
D2	**98.94%**	93.24%	92.43%
D3	82.16%	87.28%	**89.32%**
D4	96.37%	**97.11%**	96.29%
D5	**94.78%**	92.87%	94.29%
D6	**99.35%**	96.07%	96.03%
D7	84.77%	86.73%	**91.03%**
D8	93.74%	**96.25%**	94.72%
D9	87.65%	**94.61%**	85.91%
D10	90.71%	**94.90%**	91.66%
D11	92.85%	94.56%	**94.60%**
D12	92.94%	**93.15%**	87.42%
D13	**91.76%**	76.78%	81.41%
D14	**97.09%**	93.41%	91.96%
D15	95.85%	**96.07%**	94.15%
D16	90.30%	91.02%	**92.98%**
D17	**97.40%**	94.25%	92.94%
Avg:	92.66%	92.52%	91.63%

5.5.1 *Evaluation*

Figure 5.12 shows the resulting segmentations from eight of our datasets. We performed the evaluation of the method by calculating the dice coefficient overlap between our segmentation results and each of the two ground truth segmentations. For every voxel $\mathbf{v} \in \mathbb{Z}^3$ let G be the set of all voxels in the ground truth segmentation, and let R be the set of all voxels in our resulting segmentation. The dice coefficient is calculated according to the following formula:

$$dice(G, R) = \frac{2 * |G \cap R|}{|G| + |R|} \tag{5-7}$$

The proposed method achieved an average dice coefficient overlap of 92.52% and 91.63% against the ground truth segmentations by first and second expert, respectively. Dice coefficient overlap between the two

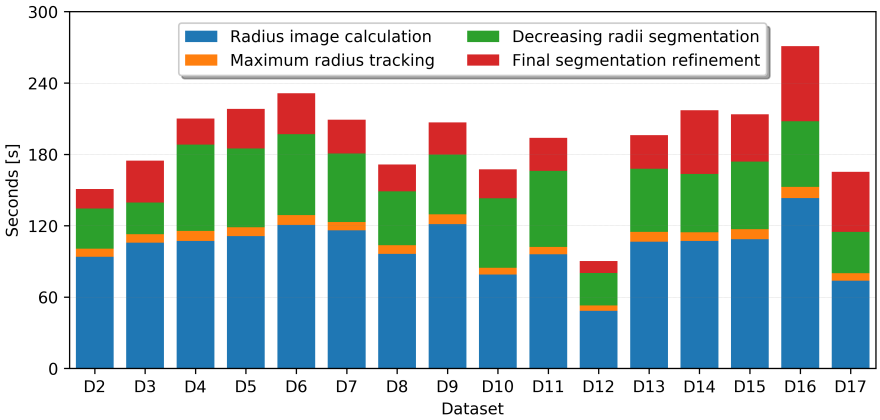

Figure 5.14: Method runtime per step. Thresholding and initial segmentation steps are ommited because they are finished in under a second.

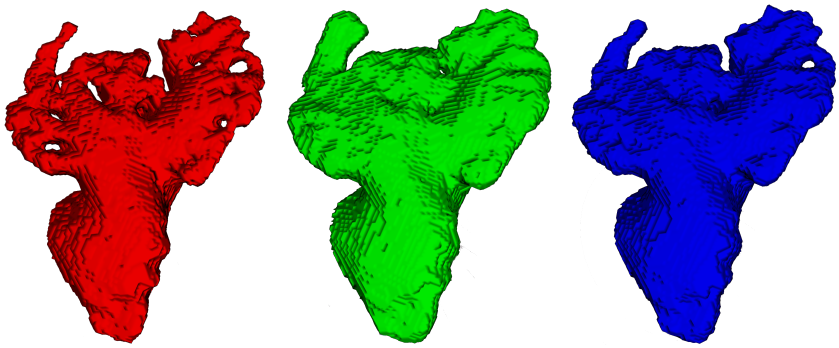

(a) Our segmentation (b) Expert 1 (c) Expert 2

Figure 5.15: Effects of threshold selection on the resulting segmentation

ground truth segmentations is only marginally better at 92.66%. Our method demonstrated segmentation accuracy very close to human experts. Dice coefficients overlap is shown in Table 5.2, as well as Figure 5.13.

The runtime of our method depends on the image size and the patient anatomy. The method runtime for our datasets was, in most cases, between 3 and 4 minutes. The runtime depends both on the image size and on the patient's anatomy. Figure 5.14 shows the runtime per dataset for each step of the segmentation methods.

5.6 DISCUSSION

In this section we propose an interpretation of the results and explain in more detail the requirements for the input parameters and the effects of the various inputs on the segmentation results. We also discuss the robustness of the method to the types of input images.

First, we would like to point out an interesting fact about the results visible in Table 5.2. The overlap of the two human experts' segmentations is highest between themselves in only seven cases. In six cases the first expert agrees more with our result than with the second expert. Similarly, in four cases the second expert agrees more with our result than with the first expert. Thus, in ten out of seventeen cases one of the experts agrees more with our result, than with the other expert. However, even more interesting is the fact that in seven out of those ten cases both experts agree more with our result, then between themselves.

One possible reason for this could be tied to the process of creating the ground truth segmentations. Both experts used the Snakes method in ITK-SNAP to create initial segmentations. Even though they manually refined the segmentations and fixed the leaks using the paintbrush tool, a significant part of the anatomy included in the ground truths depended on the initial thresholds that experts chose for the snakes. Since our algorithm is also threshold-based, on probable reason for this overlap is that our chosen threshold was sometimes closer to the threshold of one and sometimes of the other expert.

5.6.1 *Input requirements*

The user has to provide two inputs to our method: a seed point and a threshold value. Afterwards, user can select the desired delineation plane as the location of the LAA orifice. Both method inputs, as well as the selection of the plane, are intuitive to the trained medical users.

For the threshold selection, we follow an approach that is generally recommended for medical software: the user selects the desired threshold value for the dataset with a simple slider, while visually observing the effects a particular threshold value has on the image. The guidelines for the threshold selection were presented in section 5.2. High threshold value will undersegment the border regions and LAA trabeculations. Low threshold value will result in leaks in the thresholded image. Our method is specifically designed to be robust to leaks i.e. oversegmentation.

We can also conclude that our method correctly extracts the LAA anatomy from the mask image regardless of the chosen threshold value. From the anatomical perspective, our method will correctly segment the LAA even with suboptimal threshold selected. The resulting segmentation will contain most of the LAA and its shape will still be accurately segmented. Figure 5.15 shows the effects of the selected threshold on the result. In this case our chosen threshold was higher than both thresholds selected by the experts, as evident in the presence of trabeculations in our segmentation manifesting as holes.

Our method extracted the correct LAA anatomy despite the presence of holes by from trabeculations.

Both centerline detection and decreasing radii steps in the method are very robust to oversegmentation. Still, when the selected threshold value is too low the leaks will create complications for the final segmentation refinement step. When a part of the LAA close to the tip of the LAA leaks to some other anatomical structure the refinement step will probably fail to add it to the segmentation. The reason is that refinement step adds small components neighboring the already segmented LAA. If a part of LAA not segmented by decreasing radii segmentation leaks, it will probably be connected to the component containing the rest of the heart. Thus, the volume of that component will be larger than the LAA volume and the refinement step will fail to add that component to the segmentation.

5.6.2 *Input images*

The proposed method is robust to the type and size of the input images. The method does not have predefined constraints on the type of input images. Due to the first step in the method being thresholding, all other steps in the method are designed to extract the LAA from the binary mask created by thresholding step. As long as the region in the image containing the appendage has intensity values different enough for the masking to be possible, the created binary mask image will be usable by the method. The binary mask image can be created, for example, as an output from some other algorithm (active contours, level sets, clustering, etc.), or using some other type of image (e.g. MRI).

Additionally, the performance of the proposed method does not depend on the dimensions of the input image. We do not require the image to be of any particular resolution. Thus, it is possible to perform the segmentation only on a selected ROI from the original image. The ROI has to contain the LAA and large part of the left atrium for the method to function properly. The reason being that the tracking step moves towards the voxels with the larger radii. Limiting the performance to ROI could potentially improve the computational efficiency of the method.

5.7 CONCLUSION

In this chapter we presented a novel method for left atrial appendage segmentation, which requires requires minimal user interaction. The proposed method finds a path, in the thresholded (mask) image, from the seed point to the center of LA and extracts the LAA. Afterwards,

the user selects the delineation plane between left atrium and the appendage and we run an additional refinement step according to the selected delineation plane. Finally, the refined segmentation is presented to the user. The proposed segmentation method is validated on 17 CCTA images manually and independently segmented by two medical experts.

Segmentation results show high overlap with ground truth segmentations performed by medical experts. Our segmentation method achieves only marginally lower overlap to ground truth than the overlap of two ground truths between themselves. Moreover, numerical results show that the average overlap area between our segmentation results and any of the two expert delineations is very similar to their mutual overlap. The two (ground truth) segmentations yielded an average dice overlap of 92.66% on the seventeen tested images. The overlap between our result and the expert segmentations was only 1% smaller when compared to one expert and only 0.14% smaller when compared to the other expert. Furthermore, in ten out of seventeen cases our result agreed better with some of the experts then they among themselves. This indicates a good potential of the proposed method for clinical use in the planning of the LAA occlusion procedure.

6

LAA ORIFICE LOCALIZATION

In Chapter 4 and Chapter 5 we presented novel methods for the LAA centerline detection and the LAA segmentation. However, the methods presented in those chapters require the user to determine the orifice location manually. Orifice localization is an important step in the surgical planning of the LAA closure procedure. It is important to obtain accurate measurements of the orifice, since the occluder devices are placed inside the orifice to effectively separate bloodflow between the LAA and the rest of the heart. As explained in Chapter 2 the occluder devices are available on the market in a number of predefined sizes. The correct occluder device to be used for the closure procedure has to be selected according to each patient's heart anatomy. The goal of the method presented in this chapter is to determine the orifice location automatically using the segmentation result from Chapter 5 and the centerline from Chapter 4. Automatic localization and measurement of the orifice aids the medical doctors in selecting the device of the appropriate size for the planning of the procedure. In this chapter we propose a novel method for the localization of the LAA orifice for the purpose of the occluder placement. The main contribution is a novel method which performs the localization of the LAA orifice using the segmentation image and the LAA centerline. After the localization, we calculate important parameters for the planning of the closure procedure. We calculate and present to the user the shape, diameters and circumference of the orifice. The validation of the determined orifice location is performed against the orifice locations determined manually by a medical expert. The work presented in this chapter is published in a journal paper [100].

6.1 INTRODUCTION

The purpose of the proposed method is to localize the LAA orifice as a plane delineating the LAA from the left atrium and propose the location for the occluder placement. The orifice is defined as the narrowest part in the LAA neck, following the definition proposed by [175]. We calculate the delineation plane by analyzing the cross-sectional areas along the centerline. The criteria for the delineation is the last point on the centerline where the cross-sectional area decreases, after which the areas along the centerline start to significantly increase.

We know from the cardiovascular anatomy that the volume of the LA is significantly larger than the volume of LAA [33], while the interior of the LA is of a relatively spherical shape. Therefore, the cross-sectional area inside the LA will be larger than the cross-sectional area inside the appendage. Moreover, the magnitudes of the cross-sectional areas along the centerline will significantly differ depending on which part of the centerline the area is calculated.. Areas along the part of the centerline located inside the LAA will vary unpredictably due to the irregular shape of the appendage. However, once the centerline leaves the appendage and enters the left atrium, the calculated areas along the centerline will start to significantly increase. Our method tries to determine the point on the centerline where the areas have increased enough that the centerline is now inside the left atrium. When the algorithm determines that the centerline has entered the LA , we search backwards from that point towards the seed point and choose the first narrowing of the anatomy as the LAA orifice. For this analysis we propose a novel method called Weighted rising slopes algorithm. The LAA orifice detected in this way follows the definition of the orifice proposed in [175]. The proposed method consists of two steps:

- Calculation of minimal areas along the centerline – i.e., the minimal cross-sectional area in each point on the centerline; and
- Search for the smallest area among the calculated areas that occurs right before the left atrium.

6.2 CALCULATION OF AREAS ALONG CENTERLINE

In this section we explain how we calculate the cross-sectional areas along the centerline in order to be able to determine the narrowing in the LAA anatomy and thus the location of the orifice. The input for this method is the detected LAA centerline as explained in the previous chapter. The centerline C is a curve in 3D space which consists of N positions $\mathbf{p} \in \mathbb{R}^3$.

Let $\mathbf{p}(i)$ denote a position on the LAA centerline C with index $i \in \{1, ..., N\}$. For each position $\mathbf{p}(i)$ we calculate the curve tangent in that position, represented by vector $\mathbf{n}(i)$:

$$\mathbf{n}(i) = \mathbf{p}(i+1) - \mathbf{p}(i-1). \tag{6-1}$$

The vector $\mathbf{n}(i)$ represents the centerline direction vector in a particular position. We calculate the cross-sectional areas along the centerline where the centerline direction at each centerline position is the normal of the cross-sectional plane. A cross-sectional plane $\psi(i)$ at index i is a plane defined by the position $\mathbf{p}(i)$ along the centerline and the directional vector $\mathbf{n}(i)$ as the plane's normal. Let us denote the area of

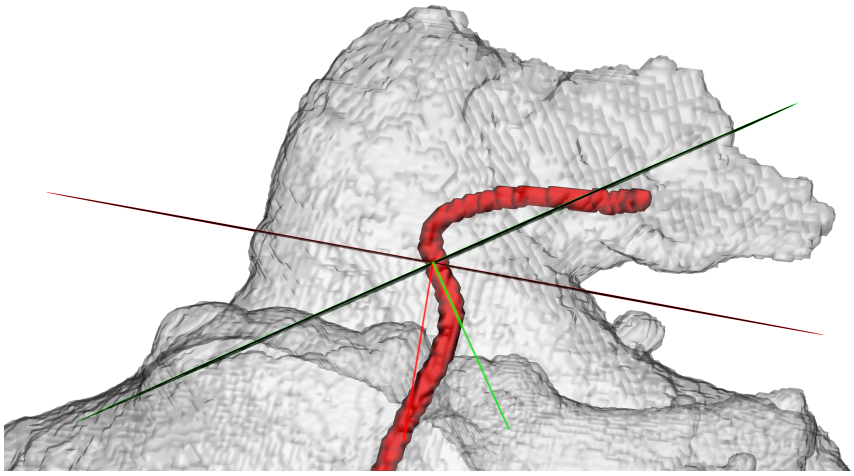

Figure 6.1: Planes at position $\mathbf{p}(i)$. Green plane $\psi(i)$ is a plane orthogonal to the centerline direction vector $\mathbf{n}(i)$ where the cross-sectional area $a(i)$ is not minimal. Red plane is a plane in that point where the cross-sectional area is minimal.

the cross-sectional plane $\psi(i)$ at position $\mathbf{p}(i)$ with $a(\psi(i))$. The area of the cross-sectional plane $\psi(i)$ will be the area of the region defined by the intersection of the discrete positions of the plane $\psi(i)$ and the segmentation set H:

$$a(\psi(i)) = |D(\psi(i)) \cap H|, \tag{6-2}$$

where $D(\psi(i))$ denotes the set of discretized positions of plane $\psi(i)$.

Next, we should be able to determine the narrowing of the LAA neck and localize the orifice by analysing the calculated cross-sectional areas along the centerline. However, often the cross-sectional plane orthogonal to the centerline direction (defined by a normal $\mathbf{n}(i)$) does not actually represent a cross-section of the LAA. An example is illustrated in Figure 6.1, where the plane orthogonal to the centerline direction (green plane) does not create a cross-section through the appendage, but the left atrium as well. The centerline cannot always properly represent the variations in shape of LAA edges. Still, our analysis is based on the areas of the appendage cross-sections along the centerline. To surpass this problem, at each position along the centerline we search for the minimal cross-sectional area by testing a number of planes with different normals. For each centerline position we select the plane where the area of the cross-section with that plane is minimal. The example is shown as a red plane in Figure 6.1. It is evident in the figure that the cross-section defined by the red plane, as opposed to the green plane, is a minimal area cross-section of the LAA, even though it is not exactly orthogonal to the direction of the centerline.

Algorithm 6.2 Calculation of new plane normals

1: **for** $\alpha \in \{0.5, 1, 1.5, 2, ..., 40\}$ **do**
2: $\quad \mathbf{n}(i, \alpha) =$ rotate $\mathbf{n}(i)$ by α around $\mathbf{p}(i)$
3: $\quad$ **for** $\beta \in \{0, 2, 4, ..., 358\}$ **do**
4: $\quad\quad \mathbf{n}(i, \alpha, \beta) =$ rotate $\mathbf{n}(i, \alpha)$ by β around $\mathbf{n}(i)$
5: $\quad\quad \Psi(i) \leftarrow \psi(i, \alpha, \beta)$
6: $\quad$ **end for**
7: **end for**

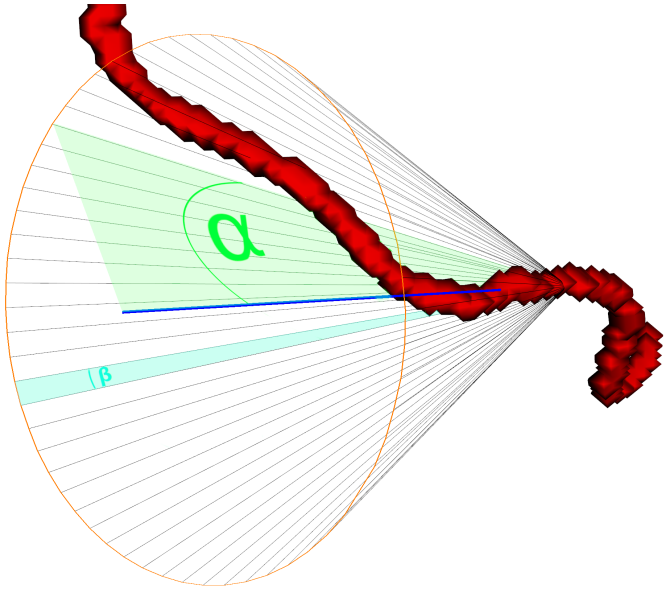

Figure 6.2: Angles of directional vectors rotation.

We find the planes with minimal areas by modifying the normals for the planes up to 40 degrees and rotating them in full circle. Particularly, we calculate a number of directional vectors by modifying and rotating the $\mathbf{n}(i)$ according to the Algorithm 6.2. Each new directional vector $\mathbf{n}(i, \alpha, \beta)$ represents a normal of a plane $\psi(i, \alpha, \beta)$ to be tested for the minimal cross-sectional area. Figure 6.2 illustrates the creation of new normals. The centerline is represented with red color, while the blue line represents the directional normal $\mathbf{n}(i)$. Angles α and β are shown in green and blue, respectively. Every new normal $\mathbf{n}(i, \alpha, \beta)$ is created by rotating the vector $\mathbf{n}(i)$ (blue line) by α around $\mathbf{p}(i)$ and then rotating by β around $\mathbf{n}(i)$. Let $\Psi(i)$ denote the set of all planes $\psi(i, \alpha, \beta)$ created using the algorithm 6.2. Using (6-2), we calculate areas for all planes in $\Psi(i)$ and denote the set of all calculated areas as:

$$A(i) = \{a(\psi) | \psi \in \Psi(i)\}. \tag{6-3}$$

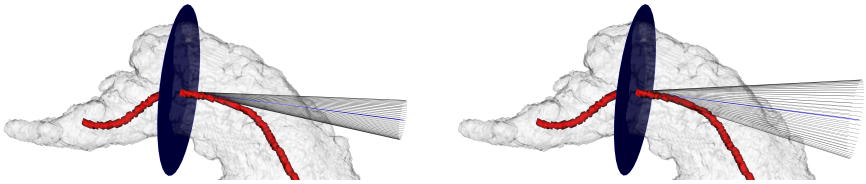

(a) $\alpha = 5°$, $\Delta\beta = 6°$

(b) $\alpha = 10°$, $\Delta\beta = 6°$

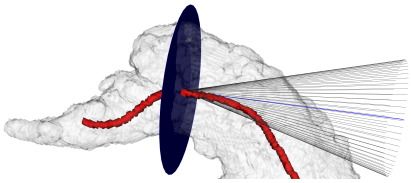

(c) $\alpha = 15°$, $\Delta\beta = 6°$

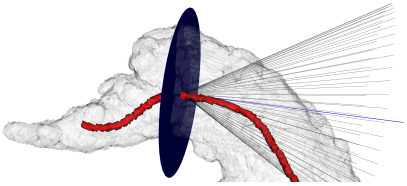

(d) $\alpha = 30°$, $\Delta\beta = 6°$

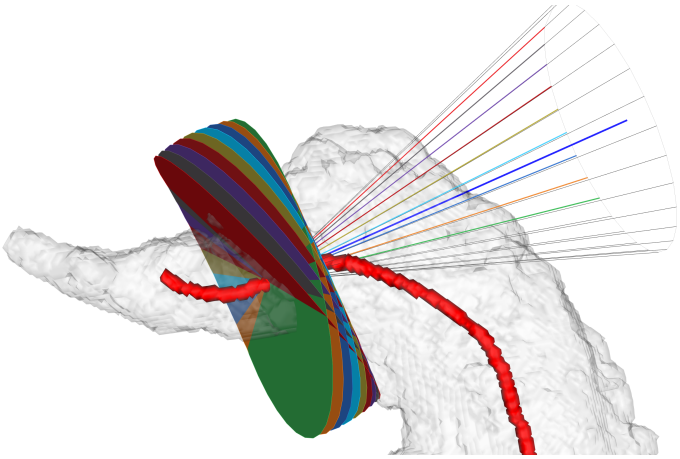

(e) $\alpha = 20°$, $\Delta\beta = 12°$

Figure 6.3: Creation of planes with different angles. (a-d) Normal $\mathbf{n}(i)$ and its corresponding plane $\psi(i)$ are shown in blue, while black lines show created new normals $\mathbf{n}(i, \alpha, \beta)$. (e) Normal $\mathbf{n}(i)$ in blue, planes $\psi(i, \alpha, \beta)$ and normals $\mathbf{n}(i, \alpha, \beta)$ in different colors.

Finally, the minimal cross-sectional area at index i is defined as:

$$a(i) = min(A(i)). \tag{6-4}$$

Figures 6.3(a-d) show different steps in creating the normals used in the search for minimal areas. For each position on the centerline, we find all normals of up to 40° and calculate the areas of candidate cross-sections defined by those normals. Each subfigure in Figure 6.3 shows normals created with a different angle α. In the figure we introduce the parameter $\Delta\beta$ which represents the change of angle β between each candidate normal. Our algorithm uses $\Delta\beta = 2$, meaning that for every α we find 180 normals in a full circle. For better visibility, we created the figures with larger $\Delta\beta$ angle (smaller number of normals in a full circle rotation). Figure 6.3e shows a few of created planes

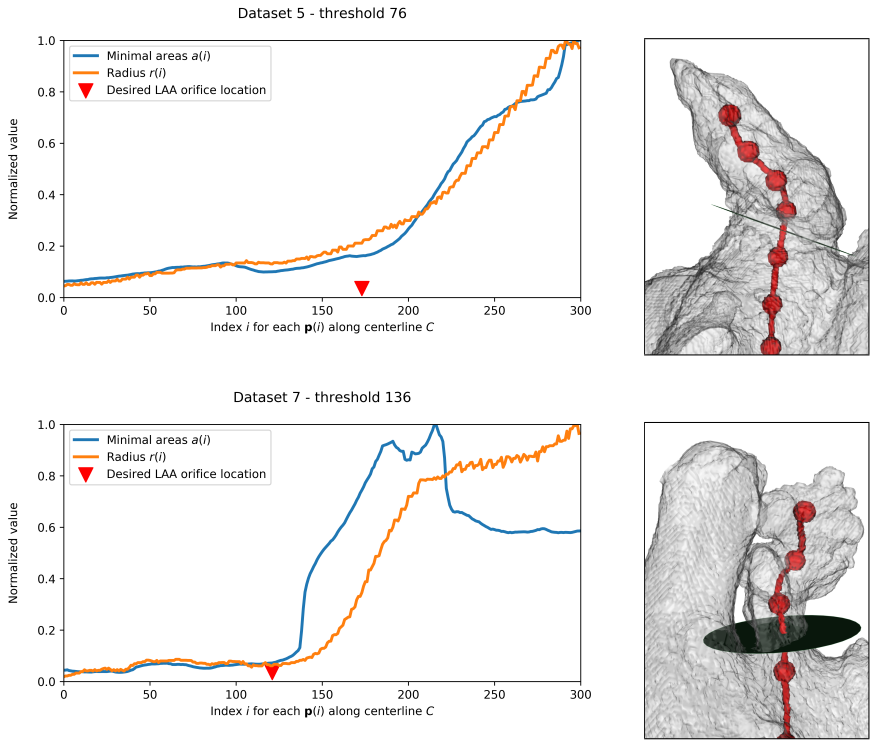

Figure 6.4: Plots of minimal areas and change in radius along the centerline. The plots also indicate the desired position of the LAA orifice (red wedge on graph and the delineation plane in the render). Knots on centerlines in the renders are placed every 50 indices and correspond to the ticks of the plots' x-axis.

and their corresponding normals (the plane-normal pairs are given in same colors). The rotation angles α and β have been determined experimentally. The final area $a(i)$ is the minimum area calculated from the candidate cross-sections. The plot of minimal areas along the centerline $a(i)$ is illustrated in Figure 6.4. We are interested in the rate of change of the area and radius – that is why the Figure shows normalized values on y-axis.

6.3 WEIGHTED RISING SLOPES

In this section we propose a novel method for LAA orifice localization. The method analyzes the calculated areas and proposes the delination plane between the appendage and the left atrium. As explained earlier, according to [175] the location of the orifice is defined as the narrowest part of the neck of the LAA. The neck of the appendage is the part of the appendage just before the left atrium. Hence, we need to find the local minima of the highest growth in the cross-sectional area $a(i)$. The highest growth in cross-sectional areas will be present inside the left atrium, and the local minima before this highest growth will

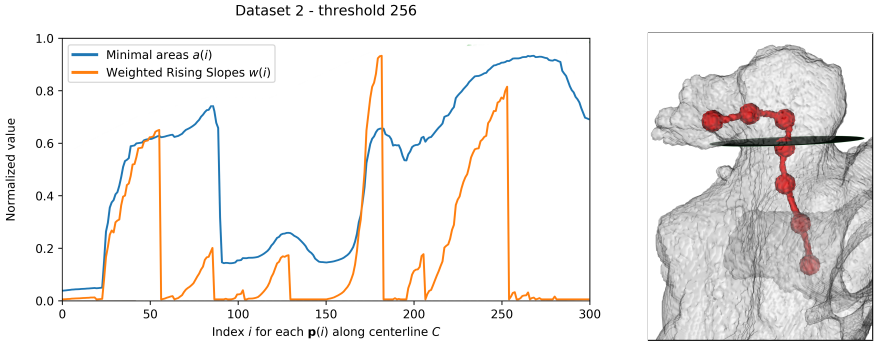

Figure 6.5: Plot of weighted rising slopes for Dataset 2. Local minimum before the maximum value of $w(i)$ indicates the position of the LAA orifice (at index $i = 148$).

be the narrowing of the LAA neck. The growth also has to be the most dominant one in its surrounding to account for growth of cross-sectional area due to LAA shape. Our proposed weighted rising slopes $w(i)$ method represents the rate of change in minimal area $a(i)$ along the centerline C. Figure 6.5 shows the weighted rising slopes with orange line.

The weighted rising slopes function is positive only on the intervals where the minimal area $a(i)$ is increasing because we want to know the rate of increase of the area along the centerline. On intervals where $a(i)$ is decreasing the function $w(i)$ is set to zero. Within the intervals where $a(i)$ is increasing let $m(i)$ be the index of the closest local minimum before the index i. We calculate $w(i)$ in the following way:

$$w(i) = \sqrt{(m(i) - i)^2 + (a(m(i)) - a(i))^2}. \tag{6-5}$$

Peaks of $w(i)$ represent locations along the centerline C where the areas $a(i)$ had the largest uninterrupted growth. Most often those locations are inside the LA. The rapid increase in area values after the centerline enters the LA is visible in $a(i)$ plots (Figure 6.4). We choose the location of the maximum value of $w(i)$ as the location inside the left atrium. The last location where $w(i) = 0$ before the maximum value of $w(i)$ is the location of the last decrease in cross-sectional area. That location represents the last narrowing of the anatomy before the largest growth of the calculated cross-sectional areas (widening of the anatomy). Hence, the location of the last $w(i) = 0$ before the location of the maximum $w(i)$ value is proposed as location of the LAA orifice. Considering the plot of $w(i)$ on Figure 6.5, the proposed location of the orifice is at index $i = 148$. The proposed location is the last location where $w(i) = 0$, before the location of $\max(w(i))$ at index $i = 182$.

The weighted rising slopes formula (6-5) shows that the value of $w(i)$ increases with the length of uninterrupted growth in area values

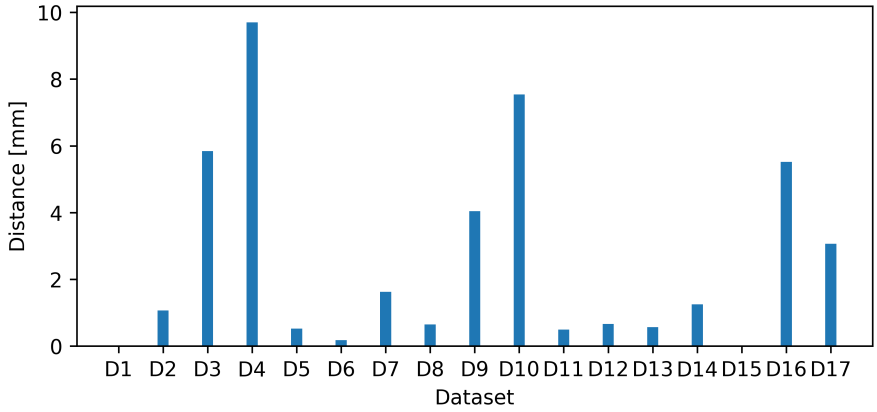

Figure 6.6: Plot of distances between the center points of the proposed LAA orifice plane and the delineation plane determined by the medical expert.

along the centerline. Rare cases are possible where, due to the LAA shape, there will be a sharp rise in calculated areas inside the LAA, resulting in peaks of $w(i)$. Observing the Figure 6.5 we can see a local maximum at index $i = 54$. The location of this local maximum is inside the LAA. The location at $i = 182$ is still the global maximum located inside the atrium and the method will still correctly propose the orifice location. On the other hand, the values in the radius image will always be small inside the LAA and large inside the LA. We want to penalize the peaks occurring inside the LAA to make sure that the largest peak will be inside the LA. Therefore, we introduce another discrete function called *radius weighted rising slopes*, which we denote as $w_r(i)$. We will penalize the values of $w(i)$ inside the LAA by scaling them with radius values along the centerline. In essence, the radius value of each voxel is the radius of the maximum inscribed sphere centered in that voxel, or a distance to the nearest background voxel in the thresholded image. The radius values are explained in more detail in section 4.3. Let the $r(i)$ be the radius of the voxel from radius image at location i. In this case the $w_r(i)$ is as follows:

$$w_r(i) = w(i) \cdot r(i). \tag{6-6}$$

Scaling the $w(i)$ with the radius values along the centerline ensures that even if the calculated area inside the LAA gets very large, the resulting weights will still be smaller inside the LAA than inside the LA. Figure 6.7 shows 3 datasets with calculated $r_w(i)$ and proposed orifice locations.

Table 6.1: Distance in mm between center points of our proposed location for LAA orifice and the desired location determined by a medical expert.

Dataset	Distance	Dataset	Distance
D1	0.00 mm	D10	7.54 mm
D2	1.07 mm	D11	0.50 mm
D3	5.84 mm	D12	0.67 mm
D4	9.70 mm	D13	0.57 mm
D5	0.53 mm	D14	1.25 mm
D6	0.18 mm	D15	0.00 mm
D7	1.62 mm	D16	5.52 mm
D8	0.65 mm	D17	3.07 mm
D9	4.04 mm		
Average distance: 2.51 mm			
Median distance: 1.07 mm			

6.4 RESULTS AND DISCUSSION

In this section we present the results of the proposed LAA orifice localization method. The method is validated on 17 CCTA datasets against the locations of the orifice determined by a medical expert. Visualizations of the proposed and the desired delineation planes for several datasets are presented in Figure 6.7. The average distance between our proposed location and the desired location is $2.51mm$. Median distance in our datasets is $1.07mm$. Distances between the proposed and the desired location are presented in Figure 6.6 and shown in Table 6.1 on page 145. The results show that in most cases the desired orifice location is either the location proposed by our method, or a location very close to our proposed location.

However, in some cases our method makes a larger error. Notably, these are the datasets D4 and D10 in Table 6.1. We believe that distances demonstrated by our method are well within the margins of error the clinicians performing the procedure are used to. Additionally, the manufacturer's guidelines for positioning of the occlusion device provide a lot of room for subjective decisions. For example, with the WATCHMAN device, the guidelines for positioning and sizing of the device state that the *landing zone* is determined in "a plane from the left coronary artery to a point $1-2cm$ distal to the limbus of the left upper pulmonary vein" [193].

While this type of guidelines suggests that the margin of error for positioning is up to a centimeter, we consider the errors on D4 and D10 outside the margin of error. The case with the largest error (D4) is shown in Figure 6.7 at the botom. The reason of the error is because our localization algorithm is not suitable for the type of morphology present in these two appenadages. As we are not aware of an objective criterion for the determination of the LAA ostium, our detection algorithm is searching for a narrowing in the neck of the LAA – proposed by Walker et al. [175] and described in Section 6.3. The cases like the D4 do not have such narrowing in the neck, but deeper in the orifice. Thus, our algorithm finds the narrowing deeper in the appendage, increasing the error.

Nevertheless, even when the method makes an error, we allow the user to correct the desired plane along the centerline in both directions. The calculated cross-sectional areas and dimensions along the centerline provide the user with important information about the orifice shape and diameters at each point of the centrline.

Finally, The search for the smallest cross-sectional area along the appendage centerline is not performed along the whole centerline. At the point where the centerline enters the atrium, the area significantly increases and varies due to the shape of the atrium and its connected structures (vessels). In order to avoid the unneeded analysis of the cross-sections in the atrium (to improve speed and accuracy of the computation), we define here criteria for choosing the centerline position at which we stop the search for the minimal area. We observed that the maximum radius inside the LA is always at least twice as large as the radius anywhere inside the LAA. Therefore, we stop the search for minimal areas when the radius along the centerline becomes larger than half of the maximum radius in the atrium. The left side of Figure 6.7 shows the plot of calculated areas $a(i)$ and radius weighted rising slopes $w_r(i)$ for the visualized segmentation.

6.5 CONCLUSION

In this chapter we proposed a novel method for the localization of the left atrial appendage orifice in the CCTA image. The method works on the input from the methods proposed in the previous two chapters: the LAA segmentation result and the detected LAA centerline. The proposed method detects the narrowing inside the LAA neck and proposes the delineation plane as the location of the orifice. The method is validated on the 17 ground truth locations determined by a medical expert. The ground truth locations are determined as delineation planes between the atrium and the appendage. The localization result is evaluated as a distance between the proposed plane and the plane

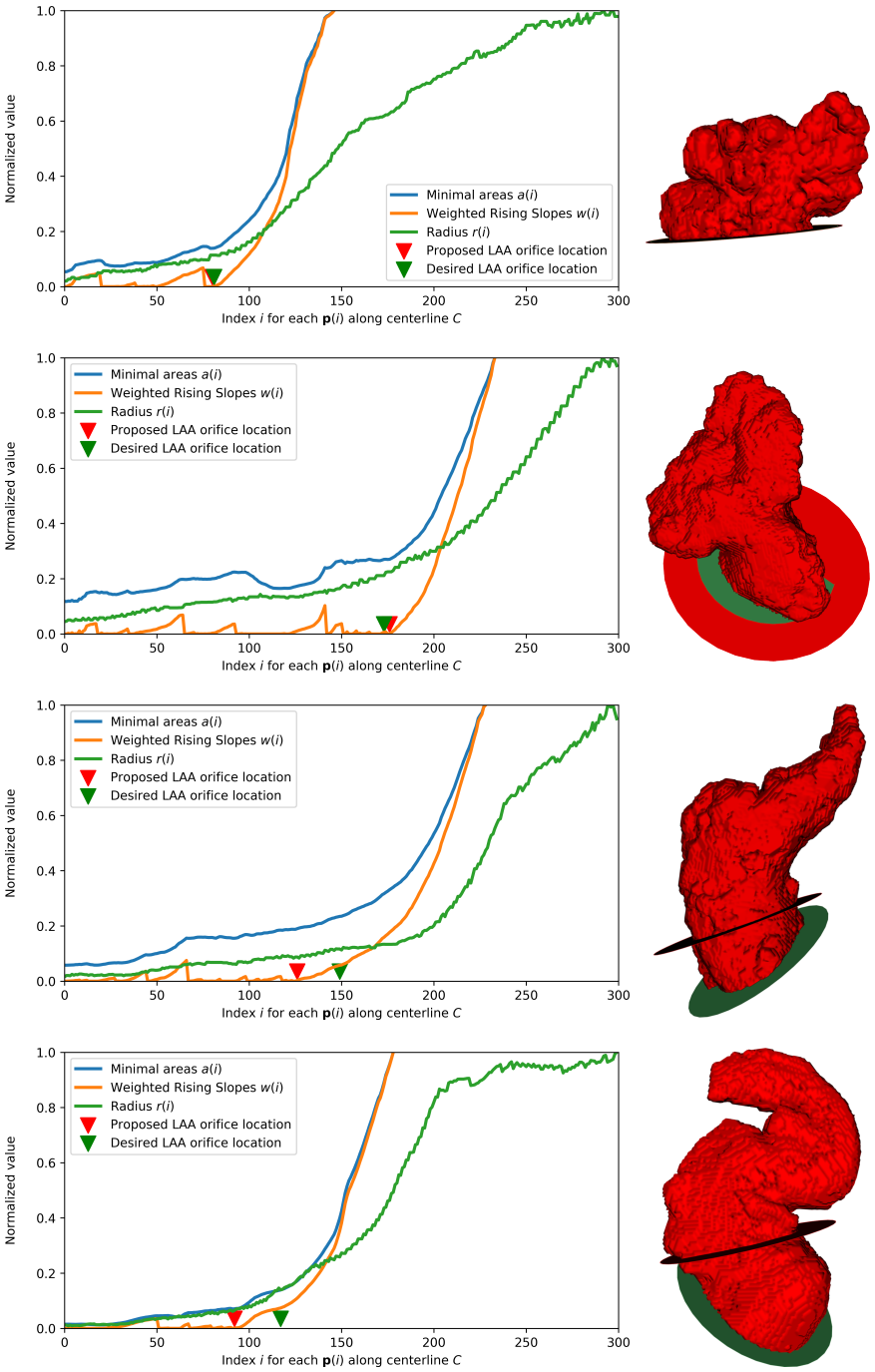

Figure 6.7: LAA orifice localization results. Rows: (1) No error; (2) Small error; (3) Medium error; (4) Large Error.

determined by the expert. The average distance between the ground truth and our proposed location is 2.54 mm. The proposed method achieves high localization accuracy indicating the potential in surgical planning for the LAA closure procedure.

7

CONCLUSIONS

This thesis developed novel image processing methods for the segmentation and the analysis of the left atrial appendage in cardiovascular images. The goal was to define a solid methodology and to develop efficient and robust methods that can support the physician in the pre-procedural planning of the left atrial appendage occlusion procedure.

Determining the correct measurements of the ostium of the appendage and determining the correct type of the morphology from the visualized segmentation result are of crucial importance in these clinical procedures. The main challenge was in developing reliable and computationally efficient methods to extract accurate and clinically relevant information about the appendage from the cardiovascular CT images. To be acceptable for clinical practice, the approach has to offer certain control to the medical expert, however without too many tunable parameters, hence the type of the desired user interactions may not be neglected.

During the literature review we have determined the anatomical landmarks which can predict the feasibility of the occlusion procedure for a certain patient. We had to decide which of the landmarks that are possible to determine from the pre-procedural CT image are the most important for the occlusion procedure planning. With the goal of aiding the physicians in the planning of the procedure, we opted to develop methods which can offer considerable time savings to the physicians. Driven by this motivation, we developed three particular methods, devoted to the problems of the centerline detection of the left atrial appendage, the segmentation of the appendage and the the localization of the LAA orifice. Each of the developed methods allows the physician to easily measure and determine a set of necessary LAA parameters – parameters which are directly needed for the planning of the occlusion procedure.

A centerline detection method aids the physician in determining the length of the appendage and the length of the dominant lobe. The length of the appendage is an important parameter for choosing the correct type of the device. Inadequate length of the appendage is an exclusion criterion for some of the devices: for example, the length of the appendage smaller than the width of the appendage excludes the use of a Watchman device for the procedure. The length can be easily measured from the centerline of the appendage. Currently, in most pre-procedural planning software suites the physician measures

the length of the appendage either directly in 2D slices, or from the manually created centerline. The software often allows the physician to manually construct the centerline by manually placing the points of the centerline in the image, which is often subjective and error prone.

In Chapter 4 we introduced a novel left atrial appendage centerline detection method. The method requires minimal interaction (only two input parameters). The method detects the centerline by tracking the voxels with largest radii of maximal inscribed spheres. The tracking step detects the path from the seed point to the center of the left atrium. The detected path contains blobs of voxels along the path. We implemented the extraction step which extracts the centerline from the detected path using the skeletonization approach and Dijkstra's longest shortest path algorithm. The length of the LAA is determined from the extracted centerline. In order to prove the accuracy of our method, we have validated the extraction method by measuring the Hausdorff distance between the centerline created by a medical professional and the centerline detected with out method. The validation demonstrated a small Hausdorff distance of the detected centerline from the ground truth centerline, indicating a small error and a large correspondence between the two lines.

Segmentation methods are needed to facilitate determining the type of the morphology of the appendage (shape). Presence of a certain type of the morphology is an exclusion criterion for the occlusion procedure with some devices. However, determining the morphology from a 2D image is subjective and dependent on the angle of the reconstruction. Our goal was to develop an objective method which will segment the appendage in a timely manner with minimal interaction from the physician.

In Chapter 5 we introduced a novel centerline based left atrial appendage segmentation method. The proposed method uses the result of the previous step – the detected centerline – in order to extract the appendage from the mask image. The main technical contribution of this chapter is the Decreasing radii segmentation, a novel region-growing method which grows the initial segmentation towards the border areas of the anatomy. The proposed method is robust to the threshold selection and to the leaks which often appear in thresholded images. We validated the method against the ground truth segmentations created by two medical experts. The method demonstrated high Dice overlap against both of the ground truth segmentations, indicating a possibility of clinical use.

Localization of the orifice is meant to aid the physician in sizing the occluder device. The term "sizing the device" actually means choosing the device of the correct diameter size for a given patient. The devices are available on the market in a set of predefine sizes.

Manual measurements of the appendage ostium diameter from 2D images are error prone and subjective.

In Chapter 6 we introduced a novel method for the localization of the LAA orifice. Our proposed method determines the location of the orifice by analysing the cross-sectional areas along the centerline. The orifice is defined as a narrowing in the neck of the appendage. Our algorithm finds the largest increase in cross-sectional areas when the centerline enters the left atrium. The location of the last minimal cross-sectional area before this largest increase is defined as a location of the orifice. The results of the orifice detection are validated against the ground truth orifice locations determined by a medical expert. The distance between our detected locations of the orifice and the locations determined by a medical expert are small, indicating a possible use for orifice detection. The detected orifice is represented as a plane in 3D space delineating the appendage from the left atrium. After the delineation, the physician can easily measure the minimal and maximal diameters – the parameters needed for the occluder device sizing.

In terms of publications, the work presented in this thesis was published in two A1 journals. Additionally, the work appeared in the proceedings of four international conferences. Future work on this topic will continue in two directions: towards making the segmentation method automatic, and towards LAA analysis in 4D images. Addition of the time dimension to the analysis will provide additional information which should enable applications such as detection of the presence of thrombus in the LAA and modelling of the blood flow in the LAA , both of which provide important information to physicians.

BIBLIOGRAPHY

[1] Philip I. Aaronson, Jeremy P. T. Ward, and Michelle J. Connolly. *The Cardiovascular System at a Glance*. English. 4 edition. Chichester, West Sussex ; Malden, MA: Wiley-Blackwell, Nov. 2012. ISBN: 978-0-470-65594-8 (cit. on pp. 9, 13).

[2] Radhakrishna Achanta, Appu Shaji, Kevin Smith, Aurelien Lucchi, Pascal Fua, and Sabine Süsstrunk. „SLIC Superpixels Compared to State-of-the-Art Superpixel Methods." In: *IEEE transactions on pattern analysis and machine intelligence* 34.11 (2012), pp. 2274–2282 (cit. on p. 61).

[3] David Adalsteinsson and James A. Sethian. „A Fast Level Set Method for Propagating Interfaces." In: *Journal of computational physics* 118.2 (1995), pp. 269–277. URL: http://www.sciencedirect.com/science/article/pii/S0021999185710984 (visited on 11/24/2015) (cit. on p. 40).

[4] N Al-Saady, O Obel, and A Camm. „Left Atrial Appendage: Structure, Function, and Role in Thromboembolism." In: *Heart* 82.5 (Nov. 1999), pp. 547–554. ISSN: 1355-6037. URL: https://www.ncbi.nlm.nih.gov/pmc/articles/PMC1760793/ (visited on 11/04/2018) (cit. on pp. 17, 18).

[5] N. S. Altman. „An Introduction to Kernel and Nearest-Neighbor Nonparametric Regression." In: *The American Statistician* 46.3 (Aug. 1992), pp. 175–185. ISSN: 0003-1305. DOI: 10.1080/00031305.1992.10475879 (cit. on p. 58).

[6] Robert M. Anderson, James M. Fritz, and James E. O'Hare. „The Mechanical Nature of the Heart as a Pump." In: *American Heart Journal* 73.1 (Jan. 1967), pp. 92–105. ISSN: 0002-8703. DOI: 10.1016/0002-8703(67)90313-4 (cit. on p. 16).

[7] Ben Appleton. „Optimal Geodesic Active Contours: Application to Heart Segmentation." In: *APRS Workshop on Digital Image Computing*. Australian Pattern Recognition Society, 2003, pp. 27–32 (cit. on pp. 40, 41).

[8] D. Babin, A. Pižurica, L. Velicki, V. Matić, I. Galić, H. Leventić, V. Zlokolica, and W. Philips. „Skeletonization Method for Vessel Delineation of Arteriovenous Malformation." In: *Computers in Biology and Medicine* 93 (Feb. 2018), pp. 93–105. ISSN: 0010-4825. DOI: 10.1016/j.compbiomed.2017.12.011 (cit. on pp. 87, 99, 101, 107).

[9] M. Bach Cuadra, V. Duay, and J.-Ph. Thiran. „Atlas-Based Segmentation." en. In: *Handbook of Biomedical Imaging: Methodologies and Clinical Research*. Ed. by Nikos Paragios, James Duncan, and Nicholas Ayache. Boston, MA: Springer US, 2015, pp. 221–244. ISBN: 978-0-387-09749-7. DOI: 10.1007/978-0-387-09749-7_12. URL: https://doi.org/10.1007/978-0-387-09749-7_12 (visited on 12/05/2018) (cit. on p. 54).

[10] Jing-Wen Bai, Ping-An Li, and Ke-Hao Wang. „Automatic Whole Heart Segmentation Based on Watershed and Active Contour Model in CT Images." In: *Computer Science and Network Technology (ICCSNT), 2016 5th International Conference On*. IEEE, 2016, pp. 741–744 (cit. on p. 37).

[11] Yves-Laurent Bayard et al. „PLAATO (Percutaneous Left Atrial Appendage Transcatheter Occlusion) for Prevention of Cardioembolic Stroke in Non-Anticoagulation Eligible Atrial Fibrillation Patients: Results from the European PLAATO Study." eng. In: *EuroIntervention: Journal of EuroPCR in Collaboration with the Working Group on Interventional Cardiology of the European Society of Cardiology* 6.2 (June 2010), pp. 220–226. ISSN: 1969-6213. DOI: 10.4244/ (cit. on p. 32).

[12] Michael Behnes et al. „Percutaneous Closure of Left Atrial Appendage Affects Mid-Term Release of MR-proANP." En. In: *Scientific Reports* 7.1 (Aug. 2017), p. 9028. ISSN: 2045-2322. DOI: 10.1038/s41598-017-08999-4 (cit. on p. 17).

[13] Roy Beigel, Nina C. Wunderlich, Siew Yen Ho, Reza Arsanjani, and Robert J. Siegel. „The Left Atrial Appendage: Anatomy, Function, and Noninvasive Evaluation." In: *JACC: Cardiovascular Imaging* 7.12 (Dec. 2014), pp. 1251–1265. ISSN: 1936-878X. DOI: 10.1016/j.jcmg.2014.08.009 (cit. on p. 19).

[14] James C. Bezdek, Robert Ehrlich, and William Full. „FCM: The Fuzzy c-Means Clustering Algorithm." In: *Computers & Geosciences* 10.2-3 (1984), pp. 191–203 (cit. on p. 58).

[15] Joseph L. Blackshear and John A. Odell. „Appendage Obliteration to Reduce Stroke in Cardiac Surgical Patients with Atrial Fibrillation." In: *The Annals of Thoracic Surgery* 61.2 (Feb. 1996), pp. 755–759. ISSN: 0003-4975. DOI: 10.1016/0003-4975(95)00887-X (cit. on pp. 17, 18).

[16] Blausen Medical Communications, Inc. *Cardiovascular System By Blausen Medical Communications, Inc. - Donated via OTRS, See Ticket for Details, CC BY 3.0*, 2013. URL: https://commons.wikimedia.org/w/index.php?curid=26986298 (cit. on p. 11).

[17] Blausen.com staff. „Medical Gallery of Blausen Medical 2014." In: *WikiJournal of Medicine* 1.2 (2014), p. 10. ISSN: 2002-4436. DOI: 10.15347/wjm/2014.010 (cit. on pp. 14, 25, 27–29).

[18] Alberto Bouzas-Mosquera, Francisco J. Broullón, Nemesio Álvarez-García, Elizabet Méndez, Jesús Peteiro, Teresa Gándara-Sambade, Oscar Prada, Víctor X. Mosquera, and Alfonso Castro-Beiras. „Left Atrial Size and Risk for All-Cause Mortality and Ischemic Stroke." In: *CMAJ : Canadian Medical Association Journal* 183.10 (July 2011), E657–E664. ISSN: 0820-3946. DOI: 10.1503/cmaj.091688 (cit. on p. 15).

[19] Y. Boykov, O. Veksler, and R. Zabih. „Fast Approximate Energy Minimization via Graph Cuts." In: *IEEE Transactions on Pattern Analysis and Machine Intelligence* 23.11 (Nov. 2001), pp. 1222–1239. ISSN: 0162-8828. DOI: 10.1109/34.969114 (cit. on p. 42).

[20] Yuri Y. Boykov and M.-P. Jolly. „Interactive Graph Cuts for Optimal Boundary & Region Segmentation of Objects in ND Images." In: *Computer Vision, 2001. ICCV 2001. Proceedings. Eighth IEEE International Conference On*. Vol. 1. IEEE, 2001, pp. 105–112 (cit. on pp. 42, 43).

[21] Leo Breiman. „Bagging Predictors." In: *Machine learning* 24.2 (1996), pp. 123–140 (cit. on p. 60).

[22] Leo Breiman. „Random Forests." In: *Machine learning* 45.1 (2001), pp. 5–32 (cit. on pp. 60, 61).

[23] Leo Breiman, Jerome Friedman, Charles J. Stone, and R. A. Olshen. *Classification and Regression Trees*. en. Taylor & Francis, Jan. 1984. ISBN: 978-0-412-04841-8 (cit. on pp. 58, 60).

[24] Loren P. Budge, Katherine M. Shaffer, J. Randall Moorman, Douglas E. Lake, John D. Ferguson, and J. Michael Mangrum. „Analysis of in Vivo Left Atrial Appendage Morphology in Patients with Atrial Fibrillation: A Direct Comparison of Transesophageal Echocardiography, Planar Cardiac CT, and Segmented Three-Dimensional Cardiac CT." en. In: *Journal of Interventional Cardiac Electrophysiology* 23.2 (Nov. 2008), pp. 87–93. ISSN: 1383-875X, 1572-8595. DOI: 10.1007/s10840-008-9281-7 (cit. on pp. 3, 18, 19, 31).

[25] José Angel Cabrera, Farhood Saremi, and Damián Sánchez-Quintana. „Left Atrial Appendage: Anatomy and Imaging Landmarks Pertinent to Percutaneous Transcatheter Occlusion." en. In: *Heart* 100.20 (Oct. 2014), pp. 1636–1650. ISSN: , 1468-201X. DOI: 10.1136/heartjnl-2013-304464 (cit. on pp. 3, 17, 20, 32, 33).

[26] M. Jorge Cardoso, Kelvin Leung, Marc Modat, Shiva Keihaninejad, David Cash, Josephine Barnes, Nick C. Fox, and Sebastien Ourselin. „STEPS: Similarity and Truth Estimation for Propagated Segmentations and Its Application to Hippocampal Segmentation and Brain Parcelation." English. In: *Medical Image Analysis* 17.6 (Aug. 2013), pp. 671–684. ISSN: 1361-8415. DOI: 10.1016/j.media.2013.02.006 (cit. on p. 75).

[27] Vicent Caselles, Ron Kimmel, and Guillermo Sapiro. „Geodesic Active Contours." In: *International journal of computer vision* 22.1 (1997), pp. 61–79. URL: http://link.springer.com/article/10.1023/A:1007979827043 (visited on 06/12/2015) (cit. on pp. 40, 106, 131).

[28] Vicent Caselles, Francine Catté, Tomeu Coll, and Françoise Dibos. „A Geometric Model for Active Contours in Image Processing." In: *Numerische mathematik* 66.1 (1993), pp. 1–31. URL: http://link.springer.com/article/10.1007/BF01385685 (visited on 11/11/2015) (cit. on p. 40).

[29] Ruben Castaneda. *These Are the Most Common Congenital Heart Defects*. 2018. URL: https://health.usnews.com/health-care/patient-advice/articles/2018-06-26/8-of-the-most-common-congenital-heart-defects (visited on 12/13/2018) (cit. on p. 27).

[30] Tony F. Chan, Luminita Vese, and others. „Active Contours without Edges." In: *Image processing, IEEE transactions on* 10.2 (2001), pp. 266–277. URL: http://ieeexplore.ieee.org/xpls/abs_all.jsp?arnumber=902291 (visited on 11/11/2015) (cit. on pp. 40, 41).

[31] Stephen L. Chiu. „Fuzzy Model Identification Based on Cluster Estimation." In: *Journal of Intelligent & fuzzy systems* 2.3 (1994), pp. 267–278 (cit. on p. 58).

[32] Patrick Ferdinand Christ, Mohamed Ezzeldin A. Elshaer, Florian Ettlinger, Sunil Tatavarty, Marc Bickel, Patrick Bilic, Markus Rempfler, Marco Armbruster, Felix Hofmann, and Melvin D'Anastasi. „Automatic Liver and Lesion Segmentation in CT Using Cascaded Fully Convolutional Neural Networks and 3D Conditional Random Fields." In: *International Conference on Medical Image Computing and Computer-Assisted Intervention*. Springer, 2016, pp. 415–423 (cit. on pp. 82, 116).

[33] Luc Christiaens, Nicolas Varroud-Vial, Paul Ardilouze, Stéphanie Ragot, Jean Mergy, Benjamin Bonnet, Daniel Herpin, and Joseph Allal. „Real Three-Dimensional Assessment of Left Atrial and Left Atrial Appendage Volumes by 64-Slice Spiral Computed Tomography in Individuals with or without

Cardiovascular Disease." In: *International Journal of Cardiology* 140.2 (Apr. 2010), pp. 189–196. ISSN: 0167-5273. DOI: 10.1016/j.ijcard.2008.11.055 (cit. on p. 138).

[34] Sumeet S. Chugh et al. „Worldwide Epidemiology of Atrial Fibrillation: A Global Burden of Disease 2010 Study." en. In: *Circulation* (Dec. 2013), CIRCULATIONAHA.113.005119. ISSN: 0009-7322, 1524-4539. DOI: 10.1161/CIRCULATIONAHA.113.005119 (cit. on p. 31).

[35] Timothy F. Cootes, Gareth J. Edwards, and Christopher J. Taylor. „Active Appearance Models." In: *IEEE Transactions on Pattern Analysis & Machine Intelligence* 6 (2001), pp. 681–685 (cit. on p. 49).

[36] Timothy F. Cootes and Chris J. Taylor. *Statistical Models of Appearance for Computer Vision*. Technical report, University of Manchester, 2004 (cit. on p. 49).

[37] Timothy F. Cootes, Christopher J. Taylor, David H. Cooper, and Jim Graham. „Active Shape Models-Their Training and Application." In: *Computer vision and image understanding* 61.1 (1995), pp. 38–59 (cit. on p. 45).

[38] Corinna Cortes and Vladimir Vapnik. „Support-Vector Networks." en. In: *Machine Learning* 20.3 (Sept. 1995), pp. 273–297. ISSN: 1573-0565. DOI: 10.1007/BF00994018 (cit. on p. 58).

[39] Abdelaziz Daoudi, Saïd Mahmoudi, and Mohammed Amine Chikh. „Automatic Segmentation of the Left Atrium on CT Images." en. In: *Statistical Atlases and Computational Models of the Heart. Imaging and Modelling Challenges*. Ed. by Oscar Camara, Tommaso Mansi, Mihaela Pop, Kawal Rhode, Maxime Sermesant, and Alistair Young. Lecture Notes in Computer Science. Springer Berlin Heidelberg, 2014, pp. 14–23. ISBN: 978-3-642-54268-8. DOI: 10.1007/978-3-642-54268-8_2 (cit. on pp. 39, 70).

[40] Xiang Deng, Yuanjie Zheng, Yunlong Xu, Xiaoming Xi, Ning Li, and Yilong Yin. „Graph Cut Based Automatic Aorta Segmentation with an Adaptive Smoothness Constraint in 3D Abdominal CT Images." In: *Neurocomputing* (2018) (cit. on p. 44).

[41] Michal Depa, Mert R. Sabuncu, Godtfred Holmvang, Reza Nezafat, Ehud J. Schmidt, and Polina Golland. „Robust Atlas-Based Segmentation of Highly Variable Anatomy: Left Atrium Segmentation." In: *International Workshop on Statistical Atlases and Computational Models of the Heart*. Springer, 2010, pp. 85–94 (cit. on p. 56).

[42] Luigi Di Biase et al. „Does the Left Atrial Appendage Morphology Correlate With the Risk of Stroke in Patients With Atrial Fibrillation? Results From a Multicenter Study." English. In: *Journal of the American College of Cardiology* 60.6 (Aug. 2012). WOS:000307071400009, pp. 531–538. ISSN: 0735-1097. DOI: 10.1016/j.jacc.2012.04.032 (cit. on p. 22).

[43] Paul Dierckx. *Curve and Surface Fitting with Splines /*. Oxford [England] : Clarendon ; 1993. ISBN: 978-0-19-853441-9 (cit. on p. 105).

[44] James D. Dormer, Ling Ma, Martin Halicek, Carolyn M. Reilly, Eduard Schreibmann, and Baowei Fei. „Heart Chamber Segmentation from CT Using Convolutional Neural Networks." In: *Medical Imaging 2018: Biomedical Applications in Molecular, Structural, and Functional Imaging*. Vol. 10578. International Society for Optics and Photonics, 2018, 105782S (cit. on p. 68).

[45] M. Dubuisson and A. K. Jain. „A Modified Hausdorff Distance for Object Matching." In: *Proceedings of 12th International Conference on Pattern Recognition*. Vol. 1. Oct. 1994, 566–568 vol.1. DOI: 10.1109/ICPR.1994.576361 (cit. on p. 108).

[46] Olivier Ecabert, Jochen Peters, Cristian Lorenz, Jens von Berg, Mani Vembar, Krishna Subramanyan, G. Lavi, and J. Weese. „Towards Automatic Full Heart Segmentation in Computed-Tomography Images." In: *Computers in Cardiology, 2005*. IEEE, 2005, pp. 223–226. URL: http://ieeexplore.ieee.org/xpls/abs_all.jsp?arnumber=1588077 (visited on 11/10/2015) (cit. on p. 46).

[47] Olivier Ecabert et al. „Automatic Model-Based Segmentation of the Heart in CT Images." In: *Medical Imaging, IEEE Transactions on* 27.9 (2008), pp. 1189–1201. URL: http://ieeexplore.ieee.org/xpls/abs_all.jsp?arnumber=4505365 (visited on 11/10/2015) (cit. on pp. 46–48, 84, 116).

[48] Olivier Ecabert, Jochen Peters, Matthew J. Walker, Thomas Ivanc, Cristian Lorenz, Jens von Berg, Jonathan Lessick, Mani Vembar, and Jürgen Weese. „Segmentation of the Heart and Great Vessels in CT Images Using a Model-Based Adaptation Framework." In: *Medical Image Analysis* 15.6 (2011), pp. 863–876. URL: http://www.sciencedirect.com/science/article/pii/S1361841511000910 (visited on 10/15/2015) (cit. on pp. 47, 48, 116).

[49] Eleanor Stevens, Eva Emmett, Yanzhong Wang, Christopher McKevitt, and Charles DA Wolfe. *The Burden of Stroke in Europe Report | King's College London for the Stroke Alliance for Europe*.

en-US. Tech. rep. 2017. URL: http://strokeeurope.eu/ (visited on 06/08/2018) (cit. on p. 30).

[50] E. Falk. „Why Do Plaques Rupture?" eng. In: *Circulation* 86.6 Suppl (Dec. 1992), pp. III30–42. ISSN: 0009-7322 (cit. on p. 26).

[51] Martin A. Fischler and Robert C. Bolles. „Random Sample Consensus: A Paradigm for Model Fitting with Applications to Image Analysis and Automated Cartography." In: *Communications of the ACM* 24.6 (1981), pp. 381–395 (cit. on p. 47).

[52] Dominik Fritz, Daniel Rinck, Roland Unterhinninghofen, Ruediger Dillmann, and Michael Scheuering. „Automatic Segmentation of the Left Ventricle and Computation of Diagnostic Parameters Using Regiongrowing and a Statistical Model." In: *Medical Imaging 2005: Image Processing*. Vol. 5747. International Society for Optics and Photonics, 2005, pp. 1844–1855 (cit. on pp. 48, 50).

[53] Dominik Fritz, Daniel Rinck, Rüdiger Dillmann, and Michael Scheuering. „Segmentation of the Left and Right Cardiac Ventricle Using a Combined Bi-Temporal Statistical Model." In: *Medical Imaging 2006: Visualization, Image-Guided Procedures, and Display*. Vol. 6141. International Society for Optics and Photonics, 2006, p. 614121 (cit. on pp. 48, 49).

[54] Gareth Funka-Lea, Yuri Boykov, Charles Florin, M.-P. Jolly, Romain Moreau-Gobard, Rana Ramaraj, and Daniel Rinck. „Automatic Heart Isolation for CT Coronary Visualization Using Graph-Cuts." In: *Biomedical Imaging: Nano to Macro, 2006. 3rd IEEE International Symposium On*. IEEE, 2006, pp. 614–617. URL: http://ieeexplore.ieee.org/xpls/abs_all.jsp?arnumber=1624991 (visited on 11/10/2015) (cit. on pp. 42, 43).

[55] Giuseppe Carone and Declan Costello. „Can Europe Afford to Grow Old?" en-US. In: *Finance and Development | F&D* 43.3 (2006). URL: http://www.imf.org/external/pubs/ft/fandd/2006/09/carone.htm (visited on 06/08/2018) (cit. on p. 30).

[56] Orly Goitein, Noam Fink, Ilan Hay, Elio Di Segni, Victor Guetta, David Goitein, Yafim Brodov, Eli Konen, and Michael Glikson. „Cardiac CT Angiography (CCTA) Predicts Left Atrial Appendage Occluder Device Size and Procedure Outcome." en. In: *The International Journal of Cardiovascular Imaging* 33.5 (May 2017), pp. 739–747. ISSN: 1569-5794, 1573-0743. DOI: 10.1007/s10554-016-1050-6 (cit. on p. 32).

[57] Martin E. Goldman, Lesly A. Pearce, Robert G. Hart, Miguel Zabalgoitia, Richard W. Asinger, Robert Safford, Jonathan L. Halperin, Stroke Prevention in Atrial Fibrillation Investiga-

tors, and others. „Pathophysiologic Correlates of Thromboembolism in Nonvalvular Atrial Fibrillation: I. Reduced Flow Velocity in the Left Atrial Appendage (The Stroke Prevention in Atrial Fibrillation [SPAF-III] Study).” In: *Journal of the American Society of Echocardiography* 12.12 (1999), pp. 1080–1087. URL: http://www.sciencedirect.com/science/article/pii/S0894731799701057 (visited on 04/20/2017) (cit. on p. 3).

[58] Pol Grasland-Mongrain. „Segmentation of the Left Atrial Appendage from 3D Images.” PhD thesis. Master Thesis. ENS Cachan, 2009. URL: http://polgm.free.fr/travail/stage_philips/Report/report_PolGM_Philips.pdf (visited on 04/24/2017) (cit. on pp. 84, 116).

[59] Pol Grasland-Mongrain, Jochen Peters, and Olivier Ecabert. „Combination of Shape-Constrained and Inflation Deformable Models with Application to the Segmentation of the Left Atrial Appendage.” In: *Biomedical Imaging: From Nano to Macro, 2010 IEEE International Symposium On*. IEEE, 2010, pp. 428–431. URL: http://ieeexplore.ieee.org/abstract/document/5490319/ (visited on 04/24/2017) (cit. on pp. 83, 84, 116).

[60] Dorothy M. Greig, Bruce T. Porteous, and Allan H. Seheult. „Exact Maximum a Posteriori Estimation for Binary Images.” In: *Journal of the Royal Statistical Society. Series B (Methodological)* (1989), pp. 271–279 (cit. on p. 42).

[61] Damien Grosgeorge, Caroline Petitjean, J.-N. Dacher, and Su Ruan. „Graph Cut Segmentation with a Statistical Shape Model in Cardiac MRI.” In: *Computer Vision and Image Understanding* 117.9 (2013), pp. 1027–1035 (cit. on pp. 43, 44).

[62] Ashraf Hamdan, Patrick Asbach, Ernst Wellnhofer, Christoph Klein, Rolf Gebker, Sebastian Kelle, Harald Kilian, Alexander Huppertz, and Eckart Fleck. „A Prospective Study for Comparison of MR and CT Imaging for Detection of Coronary Artery Stenosis.” In: *JACC: Cardiovascular Imaging* 4.1 (Jan. 2011), pp. 50–61. ISSN: 1936-878X. DOI: 10.1016/j.jcmg.2010.10.007 (cit. on p. 2).

[63] Robert G. Hart, Oscar Benavente, Ruth McBride, and Lesly A. Pearce. „Antithrombotic Therapy To Prevent Stroke in Patients with Atrial FibrillationA Meta-Analysis.” In: *Annals of internal medicine* 131.7 (1999), pp. 492–501. URL: http://annals.org/aim/article/712969/antithrombotic-therapy-prevent-stroke-patients-atrial-fibrillation-meta-analysis (visited on 04/20/2017) (cit. on pp. 18, 31).

[64] Kaiming He, Xiangyu Zhang, Shaoqing Ren, and Jian Sun. „Deep Residual Learning for Image Recognition." In: *Proceedings of the IEEE Conference on Computer Vision and Pattern Recognition*. 2016, pp. 770–778 (cit. on p. 67).

[65] *Heart Basics - Highland Hospital - University of Rochester Medical Center*. URL: https://www.urmc.rochester.edu/highland/departments-centers/cardiology/basics/heart-basics.aspx (visited on 12/13/2018) (cit. on pp. 28, 30).

[66] Rolf A. Heckemann, Joseph V. Hajnal, Paul Aljabar, Daniel Rueckert, and Alexander Hammers. „Automatic Anatomical Brain MRI Segmentation Combining Label Propagation and Decision Fusion." In: *NeuroImage* 33.1 (2006), pp. 115–126 (cit. on p. 56).

[67] Mattias P. Heinrich and Julien Oster. „MRI Whole Heart Segmentation Using Discrete Nonlinear Registration and Fast Non-Local Fusion." In: *International Workshop on Statistical Atlases and Computational Models of the Heart*. Springer, 2017, pp. 233–241 (cit. on p. 57).

[68] Siew Yen Ho, José Angel Cabrera, and Damian Sanchez-Quintana. „Left Atrial Anatomy Revisited." en. In: *Circulation: Arrhythmia and Electrophysiology* 5.1 (Jan. 2012), pp. 220–228. ISSN: 1941-3149, 1941-3084. DOI: 10.1161/CIRCEP.111.962720 (cit. on p. 15).

[69] David R. Holmes, Vivek Y. Reddy, Zoltan G. Turi, Shephal K. Doshi, Horst Sievert, Maurice Buchbinder, Christopher M. Mullin, Peter Sick, Protect AF Investigators, and others. „Percutaneous Closure of the Left Atrial Appendage versus Warfarin Therapy for Prevention of Stroke in Patients with Atrial Fibrillation: A Randomised Non-Inferiority Trial." In: *The Lancet* 374.9689 (2009), pp. 534–542. URL: http://www.sciencedirect.com/science/article/pii/S014067360961343X (visited on 10/15/2015) (cit. on pp. 32, 110).

[70] Chester Hyman. „The Concept of End Arteries and Diversion of Blood Flow." en. In: *Investigative Ophthalmology & Visual Science* 4.6 (Dec. 1965), pp. 1000–1003. ISSN: 1552-5783. URL: https://iovs.arvojournals.org/article.aspx?articleid=2125092 (visited on 11/03/2018) (cit. on p. 15).

[71] *Immunology - Inhibiting Atherosclerosis Inflammation*. en. URL: https://www.albert.io/learn/immunology/innate-immunity--1/chronic-inflammation-as-a-cause-of-atherosclerosis/inhibiting-atherosclerosis-inflammation?page=1 (visited on 12/13/2018) (cit. on p. 26).

[72] I. Isgum, M. Staring, A. Rutten, M. Prokop, M.A. Viergever, and B. van Ginneken. „Multi-Atlas-Based Segmentation With Local Decision Fusion—Application to Cardiac and Aortic Segmentation in CT Scans." In: *IEEE Transactions on Medical Imaging* 28.7 (July 2009), pp. 1000–1010. ISSN: 0278-0062, 1558-254X. DOI: 10.1109/TMI.2008.2011480 (cit. on p. 56).

[73] C. Jin, J. Feng, L. Wang, J. Liu, H. Yu, J. Lu, and J. Zhou. „Left Atrial Appendage Segmentation Using Fully Convolutional Neural Networks and Modified Three-Dimensional Conditional Random Fields." In: *IEEE Journal of Biomedical and Health Informatics* PP.99 (2018), pp. 1–1. ISSN: 2168-2194. DOI: 10.1109/JBHI.2018.2794552 (cit. on pp. 81, 116).

[74] Cheng Jin, Heng Yu, Jianjiang Feng, Lei Wang, Jiwen Lu, and Jie Zhou. „Left Atrial Appendage Neck Modeling for Closure Surgery." en. In: *Statistical Atlases and Computational Models of the Heart. ACDC and MMWHS Challenges*. Lecture Notes in Computer Science. Springer, Cham, Sept. 2017, pp. 32–41. ISBN: 978-3-319-75540-3 978-3-319-75541-0. DOI: 10.1007/978-3-319-75541-0_4 (cit. on pp. 80, 81, 117).

[75] Cheng Jin, Heng Yu, Jianjiang Feng, Lei Wang, Jiwen Lu, and Jie Zhou. „Detection of Substances in the Left Atrial Appendage by Spatiotemporal Motion Analysis Based on 4D-CT." en. In: *Statistical Atlases and Computational Models of the Heart. ACDC and MMWHS Challenges*. Ed. by Mihaela Pop, Maxime Sermesant, Pierre-Marc Jodoin, Alain Lalande, Xiahai Zhuang, Guang Yang, Alistair Young, and Olivier Bernard. Lecture Notes in Computer Science. Springer International Publishing, 2018, pp. 42–50. ISBN: 978-3-319-75541-0 (cit. on p. 83).

[76] Cheng Jin, Jianjiang Feng, Lei Wang, Heng Yu, Jiang Liu, Jiwen Lu, and Jie Zhou. „Left Atrial Appendage Segmentation and Quantitative Assisted Diagnosis of Atrial Fibrillation Based on Fusion of Temporal-Spatial Information." en. In: *Computers in Biology and Medicine* 96 (May 2018), pp. 52–68. ISSN: 00104825. DOI: 10.1016/j.compbiomed.2018.03.002 (cit. on p. 82).

[77] D. J. Jobson, Z. Rahman, and G. A. Woodell. „A Multiscale Retinex for Bridging the Gap between Color Images and the Human Observation of Scenes." In: *IEEE Transactions on Image Processing* 6.7 (July 1997), pp. 965–976. ISSN: 1057-7149. DOI: 10.1109/83.597272 (cit. on p. 82).

[78] Marie-Pierre Jolly. „Automatic Segmentation of the Left Ventricle in Cardiac MR and CT Images." In: *International Journal of Computer Vision* 70.2 (2006), pp. 151–163 (cit. on p. 44).

[79] Eric Jones, Travis Oliphant, Pearu Peterson, and others. „SciPy: Open Source Scientific Tools for Python." In: (2001). URL: http://www.scipy.org/ (cit. on p. 114).

[80] Dongwoo Kang, Jonghye Woo, Piotr J. Slomka, Damini Dey, Guido Germano, and C.-C Jay Kuo. „Heart Chambers and Whole Heart Segmentation Techniques: Review." In: *Journal of Electronic Imaging* 21.1 (2012), pp. 010901–1. ISSN: 1017-9909. DOI: 10.1117/1.JEI.21.1.010901 (cit. on p. 35).

[81] Ho Chul Kang, Bohyoung Kim, Jeongjin Lee, Juneseuk Shin, and Yeong-Gil Shin. „Automatic Left and Right Heart Segmentation Using Power Watershed and Active Contour Model without Edge." en. In: *Biomedical Engineering Letters* 4.4 (Dec. 2014), pp. 355–361. ISSN: 2093-9868, 2093-985X. DOI: 10.1007/s13534-014-0164-9 (cit. on pp. 41, 42).

[82] Kenichi Kaseno, Hiroshi Tada, Keiko Koyama, Masaaki Jingu, Shigeki Hiramatsu, Miki Yokokawa, Koji Goto, Shigeto Naito, Shigeru Oshima, and Koichi Taniguchi. „Prevalence and Characterization of Pulmonary Vein Variants in Patients With Atrial Fibrillation Determined Using 3-Dimensional Computed Tomography." In: *The American Journal of Cardiology* 101.11 (June 2008), pp. 1638–1642. ISSN: 0002-9149. DOI: 10.1016/j.amjcard.2008.01.053 (cit. on p. 17).

[83] Michael Kass, Andrew Witkin, and Demetri Terzopoulos. „Snakes: Active Contour Models." In: *International journal of computer vision* 1.4 (1988), pp. 321–331. URL: http://link.springer.com/article/10.1007/BF00133570 (visited on 06/12/2015) (cit. on pp. 35–37).

[84] Houman Khalili, Ralph E. Gentry, Melissa A. Stevens, Steven L. Almany, Subhash Banerjee, David E. Haines, and George S. Hanzel. „Rapid and Affordable 3-Dimensional Prototyping for Left Atrial Appendage Closure Planning." en. In: *Circulation: Cardiovascular Interventions* 10.2 (Feb. 2017), e004710. ISSN: 1941-7640, 1941-7632. DOI: 10.1161/CIRCINTERVENTIONS.116.004710 (cit. on p. 115).

[85] Paulus Kirchhof et al. „2016 ESC Guidelines for the Management of Atrial Fibrillation Developed in Collaboration with EACTS." In: *European Heart Journal* 37.38 (Oct. 2016), pp. 2893–2962. ISSN: 0195-668X. DOI: 10.1093/eurheartj/ehw210 (cit. on pp. 29–31).

[86] Hortense A. Kirisli, Michiel Schaap, Stefan Klein, Lisan A. Neefjes, Annick C. Weustink, Theo Van Walsum, and Wiro J. Niessen. „Fully Automatic Cardiac Segmentation from 3D CTA Data: A Multi-Atlas Based Approach." In: *Medical Imaging 2010: Image*

Processing. Ed. by Benoit M. Dawant and David R. Haynor. Vol. 7623. International Society for Optics and Photonics, 2010, p. 762305. DOI: 10.1117/12.838370 (cit. on p. 57).

[87] Stefan Klein, Marius Staring, and Josien PW Pluim. „Evaluation of Optimization Methods for Nonrigid Medical Image Registration Using Mutual Information and B-Splines." In: *IEEE transactions on image processing* 16.12 (2007), pp. 2879–2890 (cit. on p. 53).

[88] M. M. J. Koppert, P. M. J. Rongen, M. Prokop, B. M. ter Haar Romeny, and H. C. van Assen. „Cardiac Left Atrium CT Image Segmentation for Ablation Guidance." In: *2010 IEEE International Symposium on Biomedical Imaging: From Nano to Macro*. Apr. 2010, pp. 480–483. DOI: 10.1109/ISBI.2010.5490304 (cit. on p. 39).

[89] Miika Korhonen, Antti Muuronen, Otso Arponen, Pirjo Mustonen, Marja Hedman, Pekka Jäkälä, Ritva Vanninen, and Mikko Taina. „Left Atrial Appendage Morphology in Patients with Suspected Cardiogenic Stroke without Known Atrial Fibrillation." In: *PLOS ONE* 10.3 (Mar. 2015), e0118822. ISSN: 1932-6203. DOI: 10.1371/journal.pone.0118822 (cit. on p. 31).

[90] Alex Krizhevsky, Ilya Sutskever, and Geoffrey E. Hinton. „ImageNet Classification with Deep Convolutional Neural Networks." In: *Proceedings of the 25th International Conference on Neural Information Processing Systems - Volume 1*. NIPS'12. USA: Curran Associates Inc., 2012, pp. 1097–1105. URL: http://dl.acm.org/citation.cfm?id=2999134.2999257 (visited on 12/07/2018) (cit. on p. 67).

[91] Alex Krizhevsky, Ilya Sutskever, and Geoffrey E. Hinton. „ImageNet Classification with Deep Convolutional Neural Networks." en. In: *Communications of the ACM* 60.6 (May 2017), pp. 84–90. ISSN: 00010782. DOI: 10.1145/3065386 (cit. on p. 67).

[92] Dominik Kutra, Axel Saalbach, Helko Lehmann, Alexandra Groth, Sebastian Dries, Martin Krueger, Olaf Dössel, and Jürgen Weese. „Automatic Multi-Model-Based Segmentation of the Left Atrium in Cardiac MRI Scans." In: *Medical Image Computing and Computer-Assisted Intervention–MICCAI 2012* (2012), pp. 1–8. URL: http://www.springerlink.com/index/L8G833H880Q746G1.pdf (visited on 10/15/2015) (cit. on p. 16).

[93] Matt LaBarberra and Rob Donnino. *Noninvasive Cardiac Imaging: Coronary CT Angiography – Clinical Correlations*. en-US. 2008. URL: https://www.clinicalcorrelations.org/2008/03/26/noninvasive-cardiac-imaging-coronary-ct-angiography/ (visited on 11/26/2018) (cit. on p. 2).

[94] Dhanunjaya Lakkireddy et al. „Left Atrial Appendage Closure and Systemic Homeostasis: The LAA HOMEOSTASIS Study." eng. In: *Journal of the American College of Cardiology* 71.2 (Jan. 2018), pp. 135–144. ISSN: 1558-3597. DOI: 10.1016/j.jacc.2017.10.092 (cit. on p. 17).

[95] S. Lankton and A. Tannenbaum. „Localizing Region-Based Active Contours." In: *IEEE Transactions on Image Processing* 17.11 (Nov. 2008), pp. 2029–2039. ISSN: 1057-7149. DOI: 10.1109/TIP.2008.2004611 (cit. on p. 37).

[96] Hae-Yeoun Lee. „Automatic LV Segmentation with K-Means Clustering and Graph Searching on Cardiac MRI." In: *World Academy of Science, Engineering and Technology, International Journal of Medical, Health, Biomedical, Bioengineering and Pharmaceutical Engineering* 9.3 (2015), pp. 292–295 (cit. on p. 59).

[97] Hrvoje Leventić, Časlav Livada, and Irena Galić. „Cardiac CT Image Enhancement for 3D Heart Registration and Visualization." In: *Proceedings ELMAR-2015*. IEEE, 2015, pp. 229–232. URL: http://ieeexplore.ieee.org/abstract/document/7334535/ (visited on 02/15/2017) (cit. on p. 39).

[98] Hrvoje Leventić, Časlav Livada, Irena Galić, Vladimir Zlokolica, Lazar Velicki, Danilo Babin, Ratko Obradović, and Bogoljub Mihajlović. „4D CT Cardiac Image Enhancement for Subjective Medical Quality Perception of the Left Ventricle." English. In: *MIPS2015 Book of Abstracts*. Ghent, Belgium, Jan. 2015, pp. 60–60. URL: http://bib.irb.hr/prikazi-rad?\&rad=901863 (visited on 10/29/2017) (cit. on p. 39).

[99] Hrvoje Leventić, Danilo Babin, Lazar Velicki, Irena Galić, and Vladimir Zlokolica. „Semi-Automatic Left Atrial Appendage Segmentation from 3D CCTA Images." English. In: *Proceedings ELMAR-2017*. Zadar, Croatia: IEEE, Jan. 2017, pp. 39–42. ISBN: 978-953-184-230-3. URL: http://bib.irb.hr/prikazi-rad?rad=901698 (visited on 10/27/2017) (cit. on pp. 87, 115, 122, 123).

[100] Hrvoje Leventić, Danilo Babin, Lazar Velicki, Daniel Devos, Irena Galić, Vladimir Zlokolica, Krešimir Romić, and Aleksandra Pižurica. „Left Atrial Appendage Segmentation from 3D CCTA Images for Occluder Placement Procedure." In: *Computers in Biology and Medicine* 104 (Jan. 2019), pp. 163–174. ISSN: 0010-4825. DOI: 10.1016/j.compbiomed.2018.11.006 (cit. on pp. 87, 94, 100, 103, 115, 124, 125, 129–131, 137).

[101] Zhi-Jun Liao and Jie-Yu Zhao. „Exact Optimization for a Class of Second Order Markov Random Field via Graph Cuts." In:

2005 International Conference on Machine Learning and Cybernetics. Vol. 9. Aug. 2005, 5512–5516 Vol. 9. DOI: 10.1109/ICMLC.2005.1527918 (cit. on p. 61).

[102] Časlav Livada, Hrvoje Leventić, and Irena Galić. „Image Segmentation Using Active Contour Models and Partial Differential Equations." In: *Proceedings ELMAR-2014*. IEEE, 2014, pp. 1–4. URL: http://ieeexplore.ieee.org/abstract/document/6923348/ (visited on 02/15/2017) (cit. on pp. 38, 39).

[103] S. Lloyd. „Least Squares Quantization in PCM." In: *IEEE Transactions on Information Theory* 28.2 (Mar. 1982), pp. 129–137. ISSN: 0018-9448. DOI: 10.1109/TIT.1982.1056489 (cit. on p. 58).

[104] Jonathan Long, Evan Shelhamer, and Trevor Darrell. „Fully Convolutional Networks for Semantic Segmentation." In: *Proceedings of the IEEE Conference on Computer Vision and Pattern Recognition*. 2015, pp. 3431–3440 (cit. on p. 67).

[105] Cristian Lorenz, I.-C. Carlsen, Thorsten M. Buzug, Carola Fassnacht, and Jürgen Weese. „Multi-Scale Line Segmentation with Automatic Estimation of Width, Contrast and Tangential Direction in 2D and 3D Medical Images." In: *CVRMed-MRCAS'97*. Springer, 1997, pp. 233–242 (cit. on p. 39).

[106] Maria Lorenzo-Valdés, Gerardo I. Sanchez-Ortiz, Raad Mohiaddin, and Daniel Rueckert. „Atlas-Based Segmentation and Tracking of 3D Cardiac MR Images Using Non-Rigid Registration." In: *International Conference on Medical Image Computing and Computer-Assisted Intervention*. Springer, 2002, pp. 642–650 (cit. on p. 56).

[107] Bradley C. Lowekamp, David T. Chen, Luis Ibáñez, and Daniel Blezek. „The Design of SimpleITK." In: *Frontiers in Neuroinformatics* 7 (2013). ISSN: 1662-5196. DOI: 10.3389/fninf.2013.00045 (cit. on pp. 92, 106).

[108] Yingli Lu, Perry Radau, Kim Connelly, Alexander Dick, and Graham A. Wright. „Segmentation of Left Ventricle in Cardiac Cine MRI: An Automatic Image-Driven Method." In: *Functional Imaging and Modeling of the Heart*. Springer, 2009, pp. 339–347. URL: http://link.springer.com/chapter/10.1007/978-3-642-01932-6_37 (visited on 11/22/2015) (cit. on p. 64).

[109] „Lumen (Anatomy)." en. In: *Wikipedia* (Apr. 2018). Page Version ID: 834127676. URL: https://en.wikipedia.org/w/index.php?title=Lumen_(anatomy)\&oldid=834127676 (visited on 12/13/2018) (cit. on p. 25).

[110] Patrick J. Lynch. *Coronary Arteries, CC BY-SA 3.0*. 2010. URL: https://commons.wikimedia.org/wiki/File:Coronary_arteries.svg (cit. on p. 15).

[111] Patrick J. Lynch and Carl Jaffe. *Heart Left Atrial Appendage Transesophageal Echocardiography View - CC BY 2.5*. 2006. URL: https://commons.wikimedia.org/wiki/File:Heart_left_atrial_appendage_tee_view.jpg (cit. on p. 17).

[112] Fei Ma, Jiquan Liu, Bin Wang, and Huilong Duan. *Automatic Segmentation of the Full Heart in Cardiac Computed Tomography Images Using a Haar Classifier and a Statistical Model*. en. Text. Sept. 2016. DOI: info:doi/10.1166/jmihi.2016.1916. URL: https://www.ingentaconnect.com/contentone/asp/jmihi/2016/00000006/00000005/art00028 (visited on 12/02/2018) (cit. on p. 48).

[113] J. MacQueen. „Some Methods for Classification and Analysis of Multivariate Observations." EN. In: *Proceedings of the Fifth Berkeley Symposium on Mathematical Statistics and Probability, Volume 1: Statistics*. The Regents of the University of California, 1967. URL: https://projecteuclid.org/euclid.bsmsp/1200512992 (visited on 12/06/2018) (cit. on p. 58).

[114] Dwarikanath Mahapatra. „Automatic Cardiac Segmentation Using Semantic Information from Random Forests." In: *Journal of digital imaging* 27.6 (2014), pp. 794–804 (cit. on p. 61).

[115] Deepa Mangalat, Andreas Kalogeropoulos, Vasiliki Georgiopoulou, Arthur Stillman, and Javed Butler. „Value of Cardiac CT in Patients With Heart Failure." In: *Current cardiovascular imaging reports* 2.6 (Dec. 2009), pp. 410–417. ISSN: 1941-9066. DOI: 10.1007/s12410-009-0052-3 (cit. on p. 2).

[116] Ján Margeta, Kristin McLeod, Antonio Criminisi, and Nicholas Ayache. „Decision Forests for Segmentation of the Left Atrium from 3D MRI." In: *International Workshop on Statistical Atlases and Computational Models of the Heart*. Springer, 2013, pp. 49–56 (cit. on pp. 61–63, 74).

[117] Edith M. Marom, James E. Herndon, Yun Hyeon Kim, and H. Page McAdams. „Variations in Pulmonary Venous Drainage to the Left Atrium: Implications for Radiofrequency Ablation." en. In: *Radiology* 230.3 (Mar. 2004), pp. 824–829. ISSN: 0033-8419, 1527-1315. DOI: 10.1148/radiol.2303030315 (cit. on pp. 16, 17).

[118] Calvin R. Maurer Jr., Rensheng Qi, and Vijay Raghavan. „A Linear Time Algorithm for Computing Exact Euclidean Distance Transforms of Binary Images in Arbitrary Dimensions." In:

IEEE Trans. Pattern Anal. Mach. Intell. 25.2 (Feb. 2003), pp. 265–270. ISSN: 0162-8828. DOI: 10.1109/TPAMI.2003.1177156 (cit. on p. 92).

[119] Mayo Clinic. *Atrial Fibrillation - Symptoms and Causes*. en. URL: https://www.mayoclinic.org/diseases-conditions/atrial-fibrillation/ (visited on 12/15/2018) (cit. on p. 31).

[120] Warren S. McCulloch and Walter Pitts. „A Logical Calculus of the Ideas Immanent in Nervous Activity." en. In: *The bulletin of mathematical biophysics* 5.4 (1943), pp. 115–133. ISSN: 1522-9602. DOI: 10.1007/BF02478259 (cit. on pp. 58, 67).

[121] Merriam-Webster.com. *Ostium*. en. 2018. URL: https://www.merriam-webster.com/dictionary/ostium (visited on 11/04/2018) (cit. on p. 16).

[122] Merriam-Webster.com. *Posterior*. en. 2018. URL: https://www.merriam-webster.com/dictionary/posterior (visited on 11/04/2018) (cit. on p. 15).

[123] Steven C. Mitchell, Boudewijn PF Lelieveldt, Rob J. Van Der Geest, Hans G. Bosch, J. H. C. Reiver, and Milan Sonka. „Multistage Hybrid Active Appearance Model Matching: Segmentation of Left and Right Ventricles in Cardiac MR Images." In: *IEEE Transactions on medical imaging* 20.5 (2001), pp. 415–423 (cit. on p. 51).

[124] Steven C. Mitchell, Johan G. Bosch, Boudewijn PF Lelieveldt, Rob J. Van der Geest, Johan HC Reiber, and Milan Sonka. „3-D Active Appearance Models: Segmentation of Cardiac MR and Ultrasound Images." In: *IEEE transactions on medical imaging* 21.9 (2002), pp. 1167–1178 (cit. on p. 50).

[125] Oliver K. Mohrs, Rainer Schraeder, Steffen E. Petersen, Detlef Scherer, Bernd Nowak, Hans-Ulrich Kauczor, and Thomas Voigtlaender. „Percutaneous Left Atrial Appendage Transcatheter Occlusion (PLAATO): Planning and Follow-Up Using Contrast-Enhanced MRI." In: *American Journal of Roentgenology* 186.2 (Feb. 2006), pp. 361–364. ISSN: 0361-803X. DOI: 10.2214/AJR.04.1875 (cit. on p. 32).

[126] P. Morais, S. Queirós, P. De Meester, W. Budts, J. L. Vilaça, J. M. R. S. Tavares, and J. D'hooge. „Fast Segmentation of the Left Atrial Appendage in 3D Transesophageal Echocardiographic Images." In: *IEEE Transactions on Ultrasonics, Ferroelectrics, and Frequency Control* (2018), pp. 1–1. ISSN: 0885-3010. DOI: 10.1109/TUFFC.2018.2872816 (cit. on pp. 88, 117).

[127] David Mumford and Jayant Shah. „Optimal Approximations by Piecewise Smooth Functions and Associated Variational Problems." In: *Communications on pure and applied mathematics* 42.5 (1989), pp. 577–685. URL: http://onlinelibrary.wiley.com/doi/10.1002/cpa.3160420503/full (visited on 11/12/2015) (cit. on p. 41).

[128] Niyada Naksuk, Deepak Padmanabhan, Vidhushei Yogeswaran, and Samuel J. Asirvatham. „Left Atrial Appendage." en. In: *JACC: Clinical Electrophysiology* 2.4 (Aug. 2016), pp. 403–412. ISSN: 2405500X. DOI: 10.1016/j.jacep.2016.06.006 (cit. on p. 19).

[129] National Heart, Lung and Blood Institute. *Cardiomyopathy*. URL: https://www.nhlbi.nih.gov/health-topics/cardiomyopathy (visited on 12/01/2018) (cit. on pp. 27, 28).

[130] Melanie Nichols, Nick Townsend, Peter Scarborough, and Mike Rayner. *European Cardiovascular Disease Statistics*. English. 2012. ISBN: 978-2-9537898-1-2 2-9537898-1-2 (cit. on p. 1).

[131] Alan Noble, Robert Johnson, Alan Thomas, and Paul Bass. *The Cardiovascular System*. 2nd (Second) edition. Systems of the Body. Elsevier Health Sciences, Feb. 2010. ISBN: 978-0-7020-5082-4 (cit. on pp. 9, 11).

[132] Michelle C. Odden, Pamela G. Coxson, Andrew Moran, James M. Lightwood, Lee Goldman, and Kirsten Bibbins-Domingo. „The Impact of the Aging Population on Coronary Heart Disease in the U.S." In: *The American journal of medicine* 124.9 (Sept. 2011), 827–833.e5. ISSN: 0002-9343. DOI: 10.1016/j.amjmed.2011.04.010 (cit. on p. 30).

[133] OpenStax College. *Pulmonary Circuit - Illustration from the Anatomy & Physiology, Connexions Web Site. http://cnx.org/content/col11496/1.6/, Jun 19, 2013., CC BY 3.0*, URL: https://commons.wikimedia.org/w/index.php?curid=30148269 (cit. on p. 12).

[134] Sebastian Ordas, Estanislao Oubel, Rubén Leta, Francesc Carreras, and Alejandro F. Frangi. „A Statistical Shape Model of the Heart and Its Application to Model-Based Segmentation." In: *Medical Imaging 2007: Physiology, Function, and Structure from Medical Images*. Vol. 6511. International Society for Optics and Photonics, 2007, 65111K (cit. on pp. 48, 49).

[135] Stefan H. Ostermayer et al. „Percutaneous Left Atrial Appendage Transcatheter Occlusion (PLAATO System) to Prevent Stroke in High-Risk Patients With Non-Rheumatic Atrial FibrillationResults From the International Multi-Center Feasibility Trials." In: *Journal of the American College of Cardiology* 46.1 (July

2005), pp. 9–14. ISSN: 0735-1097. DOI: 10.1016/j.jacc.2005.03.042 (cit. on pp. 18, 32).

[136] James M. Otton, Roberto Spina, Romina Sulas, Rajesh N. Subbiah, Neil Jacobs, David W. M. Muller, and Brendan Gunalingam. „Left Atrial Appendage Closure Guided by Personalized 3D-Printed Cardiac Reconstruction." In: *JACC: Cardiovascular Interventions* 8.7 (June 2015), pp. 1004–1006. ISSN: 1936-8798. DOI: 10.1016/j.jcin.2015.03.015 (cit. on p. 115).

[137] Sidakpal Panaich and Jr. Holmes David R. *Left Atrial Appendage Occlusion*. 2017. URL: http\%3a\%2f\%2fwww.acc.org\%2flatest-in-cardiology\%2farticles\%2f2017\%2f01\%2f31\%2f13\%2f08\%2fleft-atrial-appendage-occlusion (visited on 02/16/2018) (cit. on p. 32).

[138] Nikos Paragios and Rachid Deriche. „Geodesic Active Regions and Level Set Methods for Motion Estimation and Tracking." In: *Computer Vision and Image Understanding* 97.3 (2005), pp. 259–282. URL: http://www.sciencedirect.com/science/article/pii/S1077314204001213 (visited on 11/24/2015) (cit. on p. 40).

[139] Nikos Paragios, Olivier Mellina-Gottardo, and Visvanathan Ramesh. „Gradient Vector Flow Fast Geodesic Active Contours." In: *Computer Vision, 2001. ICCV 2001. Proceedings. Eighth IEEE International Conference On*. Vol. 1. IEEE, 2001, pp. 67–73. URL: http://ieeexplore.ieee.org/xpls/abs_all.jsp?arnumber=937500 (visited on 11/11/2015) (cit. on p. 40).

[140] Jai-Wun Park et al. „Left Atrial Appendage Closure with Amplatzer Cardiac Plug in Atrial Fibrillation: Initial European Experience." en. In: *Catheterization and Cardiovascular Interventions* 77.5 (Apr. 2011), pp. 700–706. ISSN: 15221946. DOI: 10.1002/ccd.22764 (cit. on p. 32).

[141] Christian Payer, Darko Štern, Horst Bischof, and Martin Urschler. „Multi-Label Whole Heart Segmentation Using CNNs and Anatomical Label Configurations." In: *International Workshop on Statistical Atlases and Computational Models of the Heart*. Springer, 2017, pp. 190–198 (cit. on p. 68).

[142] Pietro Perona and Jitendra Malik. „Scale-Space and Edge Detection Using Anisotropic Diffusion." In: *IEEE Transactions on Pattern Analysis and Machine Intelligence* 12.7 (1990), pp. 629–639. ISSN: 0162-8828. DOI: 10.1109/34.56205 (cit. on p. 39).

[143] Caroline Petitjean et al. „Right Ventricle Segmentation from Cardiac MRI: A Collation Study." eng. In: *Medical Image Analysis* 19.1 (Jan. 2015), pp. 187–202. ISSN: 1361-8423. DOI: 10.1016/j.media.2014.10.004 (cit. on p. 39).

[144] Eric Pierce. *Diagram of the Human Heart by By Wapcaplet - Own Work, CC BY-SA 3.0*, 2006. URL: https://commons.wikimedia.org/w/index.php?curid=830253 (cit. on p. 10).

[145] Rudra PK Poudel, Pablo Lamata, and Giovanni Montana. „Recurrent Fully Convolutional Neural Networks for Multi-Slice MRI Cardiac Segmentation." In: *Reconstruction, Segmentation, and Analysis of Medical Images*. Springer, 2016, pp. 83–94 (cit. on p. 68).

[146] Michael JD Powell. „An Efficient Method for Finding the Minimum of a Function of Several Variables without Calculating Derivatives." In: *The computer journal* 7.2 (1964), pp. 155–162 (cit. on p. 53).

[147] Z. Rahman, D. J. Jobson, and G. A. Woodell. „Multi-Scale Retinex for Color Image Enhancement." In: *Proceedings of 3rd IEEE International Conference on Image Processing*. Vol. 3. Sept. 1996, 1003–1006 vol.3. DOI: 10.1109/ICIP.1996.560995 (cit. on p. 82).

[148] Pranav Rajpurkar et al. „CheXNet: Radiologist-Level Pneumonia Detection on Chest X-Rays with Deep Learning." In: (Nov. 2017). URL: http://arxiv.org/abs/1711.05225 (visited on 12/07/2018) (cit. on p. 68).

[149] V. Y. Reddy, D. Holmes, S. K. Doshi, P. Neuzil, and S. Kar. „Safety of Percutaneous Left Atrial Appendage Closure: Results From the Watchman Left Atrial Appendage System for Embolic Protection in Patients With AF (PROTECT AF) Clinical Trial and the Continued Access Registry." en. In: *Circulation* 123.4 (Feb. 2011), pp. 417–424. ISSN: 0009-7322, 1524-4539. DOI: 10.1161/CIRCULATIONAHA.110.976449 (cit. on p. 32).

[150] Vivek Y. Reddy, Sven Möbius-Winkler, Marc A. Miller, Petr Neuzil, Gerhard Schuler, Jens Wiebe, Peter Sick, and Horst Sievert. „Left Atrial Appendage Closure With the Watchman Device in Patients With a Contraindication for Oral Anticoagulation." en. In: *Journal of the American College of Cardiology* 61.25 (June 2013), pp. 2551–2556. ISSN: 07351097. DOI: 10.1016/j.jacc.2013.03.035 (cit. on p. 32).

[151] Mohammad Rouhani and Angel Sappa. „Non-Rigid Shape Registration: A Single Linear Least Squares Framework." In: Oct. 2012, pp. 264–277. DOI: 10.1007/978-3-642-33786-4_20 (cit. on p. 52).

[152] Olivier Rousseau and Yves Bourgault. „Heart Segmentation with an Iterative Chan-Vese Algorithm." Nov. 2008. URL: https:

//hal.archives-ouvertes.fr/hal-00403627 (visited on 12/02/2018) (cit. on p. 42).

[153] Daniel Rueckert, Alejandro F. Frangi, and Julia A. Schnabel. „Automatic Construction of 3-D Statistical Deformation Models of the Brain Using Nonrigid Registration." In: *IEEE transactions on medical imaging* 22.8 (2003), pp. 1014–1025 (cit. on p. 48).

[154] Daniel Rueckert, Maria Lorenzo-Valdes, Raghavendra Chandrashekara, G. L. Sanchez-Ortiz, and Raad Mohiaddin. „Non-Rigid Registration of Cardiac MR: Application to Motion Modelling and Atlas-Based Segmentation." In: *Biomedical Imaging, 2002. Proceedings. 2002 IEEE International Symposium On*. IEEE, 2002, pp. 481–484 (cit. on p. 51).

[155] Zulma Sandoval, Julián Betancur, and Jean-Louis Dillenseger. „Multi-Atlas-Based Segmentation of the Left Atrium and Pulmonary Veins." In: *International Workshop on Statistical Atlases and Computational Models of the Heart*. Springer, 2013, pp. 24–30 (cit. on pp. 57, 71).

[156] Yoshinobu Sato, Shin Nakajima, Hideki Atsumi, Thomas Koller, Guido Gerig, Shigeyuki Yoshida, and Ron Kikinis. „3D Multi-Scale Line Filter for Segmentation and Visualization of Curvilinear Structures in Medical Images." en. In: *CVRMed-MRCAS'97*. Ed. by Jocelyne Troccaz, Eric Grimson, and Ralph Mösges. Lecture Notes in Computer Science. Springer Berlin Heidelberg, 1997, pp. 213–222. ISBN: 978-3-540-68499-2 (cit. on p. 74).

[157] Shalin Savalia and Vahid Emamian. „Cardiac Arrhythmia Classification by Multi-Layer Perceptron and Convolution Neural Networks." In: *Bioengineering* 5.2 (May 2018). ISSN: 2306-5354. DOI: 10.3390/bioengineering5020035 (cit. on p. 29).

[158] Jacqueline Saw, Peter Fahmy, Ryan Spencer, Roshan Prakash, Patrick Mclaughlin, Savvas Nicolaou, and Michael Tsang. „Comparing Measurements of CT Angiography, TEE, and Fluoroscopy of the Left Atrial Appendage for Percutaneous Closure." en. In: *Journal of Cardiovascular Electrophysiology* 27.4 (Apr. 2016), pp. 414–422. ISSN: 1540-8167. DOI: 10.1111/jce.12909 (cit. on pp. 4, 32, 110).

[159] James Albert Sethian. *Level Set Methods and Fast Marching Methods: Evolving Interfaces in Computational Geometry, Fluid Mechanics, Computer Vision, and Materials Science*. Vol. 3. Cambridge university press, 1999. URL: https://www.google.com/books?hl=hr\&lr=\&id=ErpOoynE4dIC\&oi=fnd\&pg=PR1\&dq=sethian+\&ots=N_hiB_Z_I7\&sig=EXYor31b11Grh2wAtpUk85K96_Q (visited on 11/24/2015) (cit. on p. 40).

[160] Torgyn Shaikhina and Natalia A. Khovanova. „Handling Limited Datasets with Neural Networks in Medical Applications: A Small-Data Approach." In: *Artificial Intelligence in Medicine* 75 (Jan. 2017), pp. 51–63. ISSN: 0933-3657. DOI: 10.1016/j.artmed.2016.12.003 (cit. on p. 68).

[161] Shafiullah Soomro, Farhan Akram, Asad Munir, Chang Ha Lee, and Kwang Nam Choi. *Segmentation of Left and Right Ventricles in Cardiac MRI Using Active Contours*. en. Research Article. 2017. DOI: 10.1155/2017/8350680. URL: https://www.hindawi.com/journals/cmmm/2017/8350680/abs/ (visited on 11/26/2018) (cit. on pp. 38, 39).

[162] Ryan J. Spencer et al. „Changes in Left Atrial Appendage Dimensions Following Volume Loading During Percutaneous Left Atrial Appendage Closure." en. In: *JACC: Cardiovascular Interventions* 8.15 (Dec. 2015), pp. 1935–1941. ISSN: 1936-8798, 1876-7605. DOI: 10.1016/j.jcin.2015.07.035 (cit. on p. 110).

[163] Mikkel B. Stegmann and Dorthe Pedersen. „Bi-Temporal 3D Active Appearance Models with Applications to Unsupervised Ejection Fraction Estimation." In: *Medical Imaging 2005: Image Processing*. Vol. 5747. International Society for Optics and Photonics, 2005, pp. 336–351 (cit. on p. 50).

[164] Birgit Stender, Oliver Blanck, Bo Wang, and Alexander Schlaefer. „Model-Based Segmentation of the Left Atrium in CT and MRI Scans." In: *International Workshop on Statistical Atlases and Computational Models of the Heart*. Springer, 2013, pp. 31–41 (cit. on pp. 58, 72, 73).

[165] P. Su, K. P. McCarthy, and S. Y. Ho. „Occluding the Left Atrial Appendage: Anatomical Considerations." en. In: *Heart* 94.9 (Sept. 2008), pp. 1166–1170. ISSN: 1355-6037, 1468-201X. DOI: 10.1136/hrt.2006.111989 (cit. on p. 21).

[166] T. Tabata, T. Oki, H. Yamada, A. Iuchi, S. Ito, T. Hori, T. Kitagawa, I. Kato, H. Kitahata, and S. Oshita. „Role of Left Atrial Appendage in Left Atrial Reservoir Function as Evaluated by Left Atrial Appendage Clamping during Cardiac Surgery." eng. In: *The American Journal of Cardiology* 81.3 (Feb. 1998), pp. 327–332. ISSN: 0002-9149 (cit. on p. 17).

[167] C. Tobon-Gomez et al. „Benchmark for Algorithms Segmenting the Left Atrium From 3D CT and MRI Datasets." In: *IEEE Transactions on Medical Imaging* 34.7 (July 2015), pp. 1460–1473. ISSN: 0278-0062. DOI: 10.1109/TMI.2015.2398818 (cit. on pp. 18, 75, 76, 78).

[168] George Toderici, Damien Vincent, Nick Johnston, Sung Jin Hwang, David Minnen, Joel Shor, and Michele Covell. „Full Resolution Image Compression with Recurrent Neural Networks." In: *CVPR*. 2017, pp. 5435–5443 (cit. on p. 67).

[169] Phi Vu Tran. „A Fully Convolutional Neural Network for Cardiac Segmentation in Short-Axis MRI." In: *arXiv preprint arXiv:1604.00494* (2016) (cit. on p. 68).

[170] Marina Urena et al. „Percutaneous Left Atrial Appendage Closure With the AMPLATZER Cardiac Plug Device in Patients With Nonvalvular Atrial Fibrillation and Contraindications to Anticoagulation Therapy." In: *Journal of the American College of Cardiology* 62.2 (July 2013), pp. 96–102. ISSN: 0735-1097. DOI: 10.1016/j.jacc.2013.02.089 (cit. on p. 32).

[171] John P. Veinot, Phillip J. Harrity, Federico Gentile, Bijoy K. Khandheria, Kent R. Bailey, Jeffrey T. Eickholt, James B. Seward, A. Jamil Tajik, and William D. Edwards. „Anatomy of the Normal Left Atrial Appendage A Quantitative Study of Age-Related Changes in 500 Autopsy Hearts: Implications for Echocardiographic Examination." en. In: *Circulation* 96.9 (Apr. 1997), pp. 3112–3115. ISSN: 0009-7322, 1524-4539. DOI: 10.1161/01.CIR.96.9.3112 (cit. on p. 21).

[172] WHO. *Causes of Death*. Tech. rep. Geneva: World Health Organization, 2008 (cit. on p. 25).

[173] WHO. *Cardiovascular Diseases (CVDs)*. en. 2017. URL: https://www.who.int/news-room/fact-sheets/detail/cardiovascular-diseases-(cvds) (visited on 12/12/2018) (cit. on p. 26).

[174] WHO, World Heart Federation, and World Stroke Organization, eds. *Global Atlas on Cardiovascular Disease Prevention and Control*. 2011. ISBN: 978 92 4 156437 3. URL: http://www.who.int/cardiovascular_diseases/publications/atlas_cvd/en/ (visited on 12/12/2018) (cit. on pp. 24, 27).

[175] Daniel T. Walker, Julie A. Humphries, and Karen P. Phillips. „Anatomical Analysis of the Left Atrial Appendage Using Segmented, Three-Dimensional Cardiac CT: A Comparison of Patients with Paroxysmal and Persistent Forms of Atrial Fibrillation." en. In: *Journal of Interventional Cardiac Electrophysiology* 34.2 (Aug. 2012), pp. 173–179. ISSN: 1383-875X, 1572-8595. DOI: 10.1007/s10840-011-9638-1 (cit. on pp. 19, 137, 138, 142, 146).

[176] Dee Dee Wang et al. „Application of 3-Dimensional Computed Tomographic Image Guidance to WATCHMAN Implantation and Impact on Early Operator Learning Curve: Single-Center Experience." In: *JACC: Cardiovascular Interventions* 9.22 (Nov.

2016), pp. 2329–2340. ISSN: 1936-8798. DOI: 10.1016/j.jcin.2016.07.038 (cit. on p. 4).

[177] Lei Wang, Jianjiang Feng, Cheng Jin, Jiwen Lu, and Jie Zhou. „Left Atrial Appendage Segmentation Based on Ranking 2-D Segmentation Proposals." en. In: *Statistical Atlases and Computational Models of the Heart. Imaging and Modelling Challenges*. Springer, Cham, Oct. 2016, pp. 21–29. DOI: 10.1007/978-3-319-52718-5_3 (cit. on pp. 79, 80, 82, 116, 117).

[178] Li Wang, Yurun Ma, Kun Zhan, and Yide Ma. „Automatic Left Ventricle Segmentation in Cardiac MRI via Level Set and Fuzzy C-Means." In: *Recent Advances in Engineering & Computational Sciences (RAECS), 2015 2nd International Conference On*. IEEE, 2015, pp. 1–6 (cit. on p. 60).

[179] Yan Wang, Luigi Di Biase, Rodney P. Horton, Tuan Nguyen, Prasant Morhanty, and Andrea Natale. „Left Atrial Appendage Studied by Computed Tomography to Help Planning for Appendage Closure Device Placement." en. In: *Journal of Cardiovascular Electrophysiology* 21.9 (Sept. 2010), pp. 973–982. ISSN: 10453873. DOI: 10.1111/j.1540-8167.2010.01814.x (cit. on pp. 19, 21–23, 110).

[180] E. Lindley & B. Whisenant. „Percutaneous Left Atrial Appendage Closure: A Review of the WATCHMAN Clinical Trial Experience." en. In: *Interventional Cardiology* 7.4 (2015), pp. 333–342. ISSN:
 1755-5310 (Electronic)
1755-5302 (Print). URL: https://www.openaccessjournals.com/articles/percutaneous-left-atrial-appendage-closure-a-review-of-the-watchman-clinical-trial-experience.html (visited on 11/26/2018) (cit. on p. 3).

[181] Philip A. Wolf, Robert D. Abbott, and William B. Kannel. „Atrial Fibrillation as an Independent Risk Factor for Stroke: The Framingham Study." In: *Stroke* 22.8 (1991), pp. 983–988. URL: http://stroke.ahajournals.org/content/strokeaha/22/8/983.full.pdf (visited on 04/20/2017) (cit. on pp. 3, 18).

[182] Jelmer M. Wolterink, Tim Leiner, Max A. Viergever, and Ivana Išgum. „Dilated Convolutional Neural Networks for Cardiovascular MR Segmentation in Congenital Heart Disease." In: *Reconstruction, Segmentation, and Analysis of Medical Images*. Springer, 2016, pp. 95–102 (cit. on p. 68).

[183] World Health Organization. *The Top 10 Causes of Death Worldwide Fact Sheet*. Tech. rep. 2017. URL: http://www.who.int/mediacentre/factsheets/fs310/en/ (visited on 02/15/2018) (cit. on pp. 1, 3, 24, 30).

[184] Yuwei Wu, Yuanquan Wang, and Yunde Jia. „Adaptive Diffusion Flow Active Contours for Image Segmentation." In: *Computer Vision and Image Understanding* 117.10 (2013), pp. 1421–1435 (cit. on pp. 37, 38).

[185] Nina C. Wunderlich, Roy Beigel, Martin J. Swaans, Siew Yen Ho, and Robert J. Siegel. „Percutaneous Interventions for Left Atrial Appendage Exclusion." en. In: *JACC: Cardiovascular Imaging* 8.4 (Apr. 2015), pp. 472–488. ISSN: 1936878X. DOI: 10.1016/j.jcmg.2015.02.002 (cit. on p. 32).

[186] Chenyang Xu and Jerry L. Prince. „Generalized Gradient Vector Flow External Forces for Active Contours." In: *Signal processing* 71.2 (1998), pp. 131–139. URL: http://www.sciencedirect.com/science/article/pii/S0165168498001406 (visited on 11/11/2015) (cit. on p. 39).

[187] Chenyang Xu and Jerry L. Prince. „Snakes, Shapes, and Gradient Vector Flow." In: *Image Processing, IEEE Transactions on* 7.3 (1998), pp. 359–369. ISSN: 1057-7149. DOI: 10.1109/83.661186 (cit. on pp. 39, 70).

[188] R. R. Yager and D. P. Filev. „Approximate Clustering via the Mountain Method." In: *IEEE Transactions on Systems, Man, and Cybernetics* 24.8 (Aug. 1994), pp. 1279–1284. ISSN: 0018-9472. DOI: 10.1109/21.299710 (cit. on p. 58).

[189] Dong Yang, Yefeng Zheng, and Matthias John. „Graph Cuts Based Left Atrium Segmentation Refinement and Right Middle Pulmonary Vein Extraction in C-Arm Ct." In: *Medical Imaging 2013: Image Processing*. Vol. 8669. International Society for Optics and Photonics, 2013, 86693U (cit. on pp. 44, 45, 64).

[190] Guanyu Yang, Chenchen Sun, Yang Chen, Lijun Tang, Huazhong Shu, and Jean-louis Dillenseger. „Automatic Whole Heart Segmentation in CT Images Based on Multi-Atlas Image Registration." en. In: *Statistical Atlases and Computational Models of the Heart. ACDC and MMWHS Challenges*. Ed. by Mihaela Pop, Maxime Sermesant, Pierre-Marc Jodoin, Alain Lalande, Xiahai Zhuang, Guang Yang, Alistair Young, and Olivier Bernard. Lecture Notes in Computer Science. Springer International Publishing, 2018, pp. 250–257. ISBN: 978-3-319-75541-0 (cit. on p. 57).

[191] Kelly A. Young, James A. Wise, Peter DeSaix, Dean H. Kruse, Brandon Poe, Eddie Johnson, Jody E. Johnson, Oksana Korol, J. Gordon Betts, and Mark Womble. *Anatomy & Physiology*. English. 1st edition. OpenStax College, Jan. 2013. ISBN: 978-1-938168-13-0 (cit. on p. 15).

[192] Chen Yu-ke, Wu Xiao-ming, Cai Ken, and Ou Shan-xin. „CT Image Segmentation Based on Clustering and Graph-Cuts." In: *Procedia Engineering* 15 (2011), pp. 5179–5184 (cit. on p. 59).

[193] Cheuk-Man Yu, Ahmed A. Khattab, Stefan C. Bertog, Alex P. W. Lee, Joey S. W. Kwong, Horst Sievert, and Bernhard Meier. „Mechanical Antithrombotic Intervention by LAA Occlusion in Atrial Fibrillation." eng. In: *Nature Reviews. Cardiology* 10.12 (Dec. 2013), pp. 707–722. ISSN: 1759-5010. DOI: 10.1038/nrcardio.2013.158 (cit. on p. 145).

[194] Paul A. Yushkevich, Joseph Piven, Heather Cody Hazlett, Rachel Gimpel Smith, Sean Ho, James C. Gee, and Guido Gerig. „User-Guided 3D Active Contour Segmentation of Anatomical Structures: Significantly Improved Efficiency and Reliability." In: *NeuroImage* 31.3 (July 2006), pp. 1116–1128. ISSN: 1053-8119. DOI: 10.1016/j.neuroimage.2006.01.015 (cit. on pp. 41, 106, 131).

[195] Paul A. Yushkevich et al. „User-Guided Segmentation of Multi-Modality Medical Imaging Datasets with ITK-SNAP." en. In: *Neuroinformatics* (June 2018). ISSN: 1559-0089. DOI: 10.1007/s12021-018-9385-x (cit. on p. 41).

[196] Xuan Zhao, Yao Wang, and Gabor Jozsef. „Robust Shape-Constrained Active Contour for Whole Heart Segmentation in 3-D CT Images for Radiotherapy Planning." In: *Image Processing (ICIP), 2014 IEEE International Conference On*. IEEE, 2014, pp. 1–5 (cit. on p. 47).

[197] Y. Zheng, A. Barbu, B. Georgescu, M. Scheuering, and D. Comaniciu. „Four-Chamber Heart Modeling and Automatic Segmentation for 3-D Cardiac CT Volumes Using Marginal Space Learning and Steerable Features." In: *IEEE Transactions on Medical Imaging* 27.11 (Nov. 2008), pp. 1668–1681. ISSN: 0278-0062. DOI: 10.1109/TMI.2008.2004421 (cit. on pp. 18, 64, 65, 75, 76, 78, 116).

[198] Yefeng Zheng and Dorin Comaniciu. *Marginal Space Learning for Medical Image Analysis: Efficient Detection and Segmentation of Anatomical Structures*. Springer Science & Business, 2014 (cit. on pp. 62–67, 116).

[199] Yefeng Zheng, Adrian Barbu, Bogdan Georgescu, Michael Scheuering, and Dorin Comaniciu. „Fast Automatic Heart Chamber Segmentation from 3D CT Data Using Marginal Space Learning and Steerable Features." In: *Computer Vision, 2007. ICCV 2007. IEEE 11th International Conference On*. IEEE, 2007, pp. 1–8. URL: http://ieeexplore.ieee.org/xpls/abs_

all.jsp?arnumber=4408925 (visited on 08/30/2013) (cit. on p. 65).

[200] Yefeng Zheng, Fernando Vega-Higuera, Shaohua Kevin Zhou, and Dorin Comaniciu. „Fast and Automatic Heart Isolation in 3D CT Volumes: Optimal Shape Initialization." In: *International Workshop on Machine Learning in Medical Imaging*. Springer, 2010, pp. 84–91 (cit. on pp. 65, 66, 116).

[201] Yefeng Zheng, Dong Yang, Matthias John, and Dorin Comaniciu. „Multi-Part Modeling and Segmentation of Left Atrium in C-Arm CT for Image-Guided Ablation of Atrial Fibrillation." In: *IEEE Transactions on Medical Imaging* 33.2 (2014), pp. 318–331. ISSN: 0278-0062, 1558-254X. DOI: 10.1109/TMI.2013.2284382 (cit. on pp. 66, 75, 77, 78, 116).

[202] Hua Zhong, Yefeng Zheng, Gareth Funka-Lea, and Fernando Vega-Higuera. „Segmentation and Removal of Pulmonary Arteries, Veins and Left Atrial Appendage for Visualizing Coronary and Bypass Arteries." In: *Computer Vision and Pattern Recognition Workshops (CVPRW), 2012 IEEE Computer Society Conference On*. IEEE, 2012, pp. 24–30 (cit. on pp. 66, 79).

[203] Hua Zhong, Yefeng Zheng, Gareth Funka-Lea, and Fernando Vega-Higuera. „Automatic Heart Isolation in 3D CT Images." In: *Medical Computer Vision. Recognition Techniques and Applications in Medical Imaging*. Springer, 2013, pp. 165–180. URL: http://link.springer.com/chapter/10.1007/978-3-642-36620-8_17 (visited on 10/15/2015) (cit. on pp. 66, 79, 116).

[204] Yan Zhou, Wei-Ren Shi, Wei Chen, Yong-lin Chen, Ying Li, Li-Wen Tan, and Dai-Qiang Chen. „Active Contours Driven by Localizing Region and Edge-Based Intensity Fitting Energy with Application to Segmentation of the Left Ventricle in Cardiac CT Images." In: *Neurocomputing* 156 (2015), pp. 199–210 (cit. on p. 37).

[205] Xiahai Zhuang, Kawal Rhode, Simon Arridge, Reza Razavi, Derek Hill, David Hawkes, and Sebastien Ourselin. „An Atlas-Based Segmentation Propagation Framework Using Locally Affine Registration–Application to Automatic Whole Heart Segmentation." In: *Medical Image Computing and Computer-Assisted Intervention–MICCAI 2008*. Springer, 2008, pp. 425–433. URL: http://link.springer.com/chapter/10.1007/978-3-540-85990-1_51 (visited on 11/10/2015) (cit. on p. 54).

[206] Xiahai Zhuang, Kawal S. Rhode, Reza S. Razavi, David J. Hawkes, and Sebastien Ourselin. „A Registration-Based Propagation Framework for Automatic Whole Heart Segmentation of Cardiac MRI." In: *Medical Imaging, IEEE Transactions on* 29.9

(2010), pp. 1612–1625. URL: http://ieeexplore.ieee.org/xpls/abs_all.jsp?arnumber=5444972 (visited on 11/10/2015) (cit. on p. 55).

[207] Xiahai Zhuang, Wenjia Bai, Jingjing Song, Songhua Zhan, Xiaohua Qian, Wenzhe Shi, Yanyun Lian, and Daniel Rueckert. „Multiatlas Whole Heart Segmentation of CT Data Using Conditional Entropy for Atlas Ranking and Selection." en. In: *Medical Physics* 42.7 (July 2015), pp. 3822–3833. ISSN: 0094-2405. DOI: 10.1118/1.4921366 (cit. on pp. 54–56).

[208] Massimo Zoni-Berisso, Fabrizio Lercari, Tiziana Carazza, and Stefano Domenicucci. „Epidemiology of Atrial Fibrillation: European Perspective." In: *Clinical Epidemiology* 6 (June 2014), pp. 213–220. ISSN: 1179-1349. DOI: 10.2147/CLEP.S47385 (cit. on p. 31).

[209] Majd Zreik, Tim Leiner, Bob D. de Vos, Robbert W. van Hamersvelt, Max A. Viergever, and Ivana Isgum. „Automatic Segmentation of the Left Ventricle in Cardiac CT Angiography Using Convolutional Neural Network." In: *arXiv preprint arXiv:1704.05698* (2017) (cit. on pp. 68, 69).

[210] Maria A. Zuluaga, M. Jorge Cardoso, Marc Modat, and Sébastien Ourselin. „Multi-Atlas Propagation Whole Heart Segmentation from MRI and CTA Using a Local Normalised Correlation Coefficient Criterion." en. In: *Functional Imaging and Modeling of the Heart*. Ed. by Sébastien Ourselin, Daniel Rueckert, and Nicolas Smith. Lecture Notes in Computer Science. Springer Berlin Heidelberg, 2013, pp. 174–181. ISBN: 978-3-642-38899-6 (cit. on pp. 74, 75).

[211] Marit de Jong, H. Bart van der Worp, Yolanda van der Graaf, Frank L. J. Visseren, and Jan Westerink. „Pioglitazone and the Secondary Prevention of Cardiovascular Disease. A Meta-Analysis of Randomized-Controlled Trials." In: *Cardiovascular Diabetology* 16.1 (Oct. 2017), p. 134. ISSN: 1475-2840. DOI: 10.1186/s12933-017-0617-4 (cit. on p. 25).

[212] Eva M. van Rikxoort, Ivana Isgum, Yulia Arzhaeva, Marius Staring, Stefan Klein, Max A. Viergever, Josien PW Pluim, and Bram van Ginneken. „Adaptive Local Multi-Atlas Segmentation: Application to the Heart and the Caudate Nucleus." In: *Medical image analysis* 14.1 (2010), pp. 39–49 (cit. on p. 57).